



**HAL**  
open science

# Fatigue and corrosion-fatigue in Cr-Mo steel in biaxial tension

Vidit Gaur

► **To cite this version:**

Vidit Gaur. Fatigue and corrosion-fatigue in Cr-Mo steel in biaxial tension. Mechanics [physics]. Université Paris Saclay (COMUE), 2016. English. NNT : 2016SACLX027 . tel-01438984

**HAL Id: tel-01438984**

**<https://pastel.hal.science/tel-01438984>**

Submitted on 18 Jan 2017

**HAL** is a multi-disciplinary open access archive for the deposit and dissemination of scientific research documents, whether they are published or not. The documents may come from teaching and research institutions in France or abroad, or from public or private research centers.

L'archive ouverte pluridisciplinaire **HAL**, est destinée au dépôt et à la diffusion de documents scientifiques de niveau recherche, publiés ou non, émanant des établissements d'enseignement et de recherche français ou étrangers, des laboratoires publics ou privés.

NNT : 2016SACLX027

THÈSE DE DOCTORAT  
DE  
L'UNIVERSITÉ PARIS-SACLAY  
PRÉPARÉE À  
« ÉCOLE POLYTECHNIQUE »

ÉCOLE DOCTORALE N° 579

Sciences Mécaniques et Énergétiques, Matériaux et Géosciences

Spécialité Mécanique des solides

Par

M Vidit GAUR

Fatigue et fatigue-corrosion d'un acier au Cr-Mo en tension-biaxiale

Thèse présentée et soutenue à « École Polytechnique », le « 8 Juillet, 2016 » :

**Composition du Jury :**

|                      |  |                               |
|----------------------|--|-------------------------------|
| M Thierry Palin-Luc  | Professeur, ENSAM Bordeaux                             | Rapporteur                    |
| M Franck Morel       | Professeur, ENSAM Angers                               | Rapporteur                    |
| M Gilbert Hénaff     | Professeur, ENSMA Poitiers                             | Examinateur, <i>Président</i> |
| M Habibou Maitournam | Professeur, ENSTA Palaiseau                            | Examinateur                   |
| Mme Véronique Doquet | Directrice de recherche, Ecole Polytechnique Palaiseau | Directrice de thèse           |
| Mme Eléonore Roguet  | Ingénieur de recherche, IFPEN Rueil-Malmaison          | Invité                        |
| M Jean Kittel        | Ingénieur de recherche, IFPEN Solaize                  | Invité                        |



# Table of Contents

|  |            |
|--|------------|
| <b>Résumé</b>                                  | <b>v</b>   |
| <b>Abstract</b>                                | <b>vii</b> |
| <b>Acknowledgements</b>                        | <b>ix</b>  |
| <b>Introduction</b>                            | <b>xi</b>  |
| <b>1 Literature review</b>                     | <b>1</b>   |
| <b>Part A: Fatigue in air</b> . . . . .        | 1          |
| 1.1 Damage mechanisms . . . . .                | 1          |
| 1.1.1 Crack initiation . . . . .               | 2          |
| 1.1.2 Crack growth . . . . .                   | 6          |
| 1.1.3 Effect of biaxial tension . . . . .      | 8          |
| 1.2 Fatigue criteria . . . . .                 | 11         |
| 1.2.1 Low-cycle fatigue . . . . .              | 11         |
| 1.2.2 High-cycle fatigue . . . . .             | 12         |
| 1.2.3 Application to biaxial tension . . . . . | 20         |
| 1.3 Specimens for biaxial tension . . . . .    | 21         |
| <b>Part B: Corrosion-fatigue</b> . . . . .     | 23         |
| 1.4 Electrochemical aspects . . . . .          | 23         |
| 1.5 Polarization . . . . .                     | 23         |
| 1.5.1 Anodic polarization . . . . .            | 24         |
| 1.5.2 Cathodic polarization . . . . .          | 25         |
| 1.6 Damage mechanisms . . . . .                | 26         |
| 1.6.1 Crack initiation . . . . .               | 27         |

|          |  |           |
|----------|--|-----------|
| 1.6.2    | Crack growth . . . . .                                     | 32        |
| 1.7      | Parameters influencing corrosion-fatigue . . . . .         | 33        |
| 1.7.1    | Effect of frequency . . . . .                              | 33        |
| 1.7.2    | Effect of the R ratio . . . . .                            | 36        |
| 1.7.3    | Effect of electrode potential . . . . .                    | 36        |
| 1.7.4    | Effect of pH and Cl <sup>-</sup> ions . . . . .            | 37        |
| 1.7.5    | Effect of dissolved O <sub>2</sub> . . . . .               | 38        |
| 1.7.6    | Effect of hydrogen . . . . .                               | 38        |
| 1.8      | Effect of biaxial tension in corrosive medium . . . . .    | 40        |
|          | <b>Part C: Synthesis and open questions . . . . .</b>      | <b>42</b> |
| <b>2</b> | <b>Material characterization . . . . .</b>                 | <b>43</b> |
| 2.1      | Microstructural characterization . . . . .                 | 43        |
| 2.2      | Mechanical characterization . . . . .                      | 50        |
| <b>3</b> | <b>Finite element analysis of clip connector . . . . .</b> | <b>57</b> |
| <b>4</b> | <b>Influence of the mean stress . . . . .</b>              | <b>65</b> |
| 4.1      | Experimental procedures . . . . .                          | 65        |
| 4.2      | Experimental results . . . . .                             | 66        |
| 4.2.1    | Fatigue lives . . . . .                                    | 66        |
| 4.2.2    | Damage mechanisms . . . . .                                | 69        |
| 4.2.3    | Residual stress analyses . . . . .                         | 78        |
| 4.3      | Discussion . . . . .                                       | 81        |
| 4.3.1    | Crack initiation . . . . .                                 | 81        |
| 4.3.2    | Crack growth . . . . .                                     | 85        |
| 4.4      | Concluding remarks . . . . .                               | 91        |
| <b>5</b> | <b>Effect of biaxial tension in air . . . . .</b>          | <b>95</b> |
| 5.1      | Experimental procedures . . . . .                          | 95        |
| 5.2      | Experimental results . . . . .                             | 97        |
| 5.2.1    | Cyclic biaxial tension . . . . .                           | 97        |

|          |   |            |
|----------|---|------------|
| 5.2.2    | Reversed torsion . . . . .  | 102        |
| 5.3      | Discussion . . . . .  | 104        |
| 5.3.1    | Crack initiation . . . . .  | 104        |
| 5.3.2    | Crack growth . . . . .  | 106        |
| 5.4      | Fatigue criterion . . . . .   | 109        |
| <b>6</b> | <b>Corrosion-fatigue</b>  | <b>115</b> |
| 6.1      | Experimental procedures . . . . .   | 115        |
| 6.2      | Experimental results and discussion . . . . .                                       | 117        |
| 6.2.1    | Free corrosion . . . . .  | 117        |
| 6.2.2    | With cathodic potential . . . . .   | 123        |
|          | <b>Conclusions</b>  | <b>127</b> |
|          | <b>Perspectives</b>   | <b>131</b> |
|          | <b>Appendices</b>   | <b>133</b> |
| <b>A</b> | <b>Algorithm for stepwise integration of Paris equation for<br/>internal cracks</b> | <b>135</b> |
| <b>B</b> | <b>Murakami's <math>\sqrt{area}</math> model</b>                                    | <b>137</b> |
|          | <b>REFERENCES</b>   | <b>139</b> |



# Résumé

Les connecteurs clips utilisés pour assembler les joints de riser pour le forage pétrolier offshore subissent un chargement cyclique dû aux vagues. 90% de la durée de service est passée en mode connecté (riser fixé en haut et en bas) qui implique une amplitude modérée, mais une contrainte moyenne élevée ( $R = 0,7$ ), alors que 10% est passé en mode déconnecté (riser suspendu à la plateforme) caractérisé par une plus grande amplitude, mais une faible contrainte moyenne ( $R = 0,2$ ). Des calculs numériques réalisés avec une loi de comportement elasto-plastique identifiée sur l'acier qui constitue les connecteurs montrent qu'un chargement cyclique de tension biaxiale en phase prévaut dans la zone critique de la structure. Les effets de contrainte moyenne et de biaxialité doivent donc tous deux être pris en compte pour un design approprié. Les critères de fatigue multiaxiale proposés dans la littérature sont basés sur des données de traction et torsion combinées et ne discriminent pas bien l'influence de la tension biaxiale de celle d'une contrainte moyenne. L'objectif de cette étude est donc de caractériser séparément ces deux effets.

Pour étudier les effets de la contrainte moyenne, des essais de fatigue uniaxiale ont été menés sur un acier 2,5% Mo-1% Cr avec différents rapports  $R$ . Les durées de la vie, ainsi que la pente de la courbe S-N diminuent avec l'augmentation de  $R$ , et la limite d'endurance suit la parabole de Gerber. À faible contrainte moyenne et amplitude de contrainte relativement élevée, les fissures s'amorcent en surface, tandis que pour des rapports  $R$  élevés et des amplitudes plus faibles, les fissures s'amorcent à partir de défauts internes ou coupant la surface. Cette transition est analysée à partir de calculs élasto-plastiques des champs de contrainte et déformation autour des défauts. Les fissures internes se propagent sous un faible  $\Delta K$  qui s'avère indépendant de  $R$ , ce qui est attribué à la quasi absence d'effets de fermeture.

Pour étudier l'effet d'un taux de biaxialité positif, des essais cycliques de tension et pression interne combinées avec diverses proportions de chaque chargement ont été effectués sur des échantillons tubulaires, à un ratio  $R$  fixe (0,25). Un taux de biaxialité modéré ( $B = 0,25$  et 0,5) a un effet bénéfique sur la vie de fatigue, attribué principalement à un retard de l'initiation des fissures, alors que la tension équibiaxiale a un effet légèrement

nuisible, attribué à un “pseudo effet de taille” (probabilité plus grande qu’une microfissure se propage le long de deux plans principaux équivalents au lieu d’un seul).

De facettes intergranulaires révélatrices de fragilisation par l’hydrogène consécutive à une ségrégation d’impuretés lors du traitement thermique de l’acier ont été observées sur les surfaces de rupture. Les évolutions de la fraction de rupture intergranulaire avec  $\Delta K$  et la charge biaxialité suggèrent une possible réduction de la vitesse de fissuration à  $B = 0$  et 0.5, mais l’effet néfaste de la tension équibiaxiale n’a pu être attribuée à une accélération de la propagation.

Plusieurs des critères de fatigue les plus populaires échouent à décrire toutes les données de cette étude. En particulier, les critères d’endurance qui comprennent un terme linéaire de contrainte moyenne ou de tension hydrostatique ne parviennent pas à prédire les variations non linéaires de la limite d’endurance de ce matériau avec le rapport  $R$  et le rapport de biaxialité. Aussi, un nouveau critère de fatigue a été proposé sur la base de la parabole de Gerber. Il décrit bien l’évolution de la limite d’endurance sous les effets combinés d’une contrainte moyenne positive et d’un taux de biaxialité positif.

Pour étudier l’influence d’un milieu corrosif (solution à 3,5% NaCl) sur les durées de vie en fatigue, des essais de tension et pression interne combinées en diverses proportions ont été conduits sous deux types de conditions: 1) corrosion libre et 2) protection cathodique.

En corrosion libre, l’eau salée réduit fortement les durées de vie et supprime la limite d’endurance. Cela est dû à la formation de piqûres de corrosion, qui favorisent l’amorçage précoce et multiple de fissures. La tension équibiaxiale n’accentue pas l’effet nocif de l’eau salée. Les durées de vie en fatigue uniaxiale et biaxiale sont en effet presque les mêmes, malgré des mécanismes de fissuration différents: décohésion fragile transgranulaire dans le cas uniaxial mais principalement intergranulaire en tension biaxiale.

La protection cathodique annule l’effet néfaste de l’eau salée pour tous les taux de biaxialité, en dépit d’un net accroissement de la fragilisation par l’hydrogène des joints de grains. Les surfaces de rupture deviennent presque complètement intergranulaires indépendamment du taux de biaxialité, tandis qu’à l’air, le taux de rupture intergranulaire ne dépassait pas 45%.

# Abstract

The clip connectors used to join the riser tubes for offshore oil drilling undergo cyclic loading due to sea waves. 90% of the service life is spent in the “connected mode” with a high mean stress ( $R = 0.7$ ) and 10% in the “disconnected mode” with a lower mean stress ( $R = 0.2$ ). Finite element computations revealed in-phase biaxial tension in the critical areas of the clip connector along with high mean stresses. Thus, both the mean stress effect and the biaxiality effect are needed to be addressed for a proper design of these structures. However, most of the multiaxial fatigue criteria are based on tension-torsion fatigue data and do not discriminate the influence of biaxial tension from that of a mean stress. This study investigates separately these two effects.

For investigating the mean stress effect, uniaxial fatigue tests were run on a 2.5%Cr-1%Mo steel with various R ratios ( $\sigma_{\min}/\sigma_{\max}$ ). The fatigue lives, as well as the slope of the S-N curves were found to decrease with increasing R, and the endurance limit to follow Gerber’s parabola. At low R ratios and thus relatively high stress ranges, fatigue cracks were found to initiate from the surface, while for high R ratios, and thus low stress ranges, cracks initiated from internal or surface-cutting defects. This transition was analyzed based on elastic-plastic computations of stress and strain fields around the defects. The threshold for internal fatigue crack growth from defects was found to be quite low and independent from the R ratio. This was attributed to a nearly closure-free propagation.

To investigate the effect of positive stress biaxiality, combined cyclic tension and internal pressure tests with various proportions of each loading were run on tubular specimens, at a fixed R ratio (0.25). Moderate stress biaxialities ( $B = 0.25$  and  $0.5$ ) had a beneficial effect on fatigue lives, attributed mainly to a retardation of crack initiation, while equibiaxial tension had a slightly detrimental effect, attributed to a “pseudo size effect”: higher probability for an incipient crack to grow along two possible planes, compared to a single one.

Intergranular facets associated with temper and hydrogen embrittlement were observed on the fracture surfaces. The evolutions of their surface fraction with  $\Delta K$  and load

biaxiality suggested a possible reduction in crack growth rate at moderate biaxialities, but the detrimental effect of equibiaxial tension could not be explained in terms of crack growth rate.

Several popular fatigue criteria failed to describe all fatigue data. Endurance criteria that include a linear mean stress term or contain a hydrostatic tension term fail to predict the variations of the endurance limit of this material with the R ratio and biaxiality ratio. Thus, a new fatigue criterion based on Gerber's parabola has been proposed. It captures the evolution of the endurance limit under the combined effects of a positive mean stress and positive biaxiality.

To investigate the influence of corrosive medium (3.5% NaCl) on fatigue lives combined cyclic tension and internal pressure tests with various proportions of each loading were run under two types of test conditions: 1) free corrosion and 2) cathodic protection.

In free corrosion, salt water strongly reduced the fatigue lives and suppressed the endurance limit. This was due to the formation of corrosion pits that favor early, multiple crack initiations. The detrimental effect of salt water was not enhanced by equibiaxial tension, which also did not modify the aspect ratio and density of corrosion pits. Fatigue lives in uniaxial and biaxial tension were nearly the same, although the crack growth mechanism was different: transgranular brittle decohesion in uniaxial loading and mostly intergranular in biaxial tension.

Cathodic protection cancelled the detrimental effect of salt water for all biaxialities, in spite of a clear enhancement of H-induced embrittlement of the grain boundaries. The fracture surfaces were nearly fully intergranular, irrespective of load biaxialities, while in air the proportion of intergranular fracture never exceeded 45%.

# Acknowledgements

First, I would like to express my sincere thanks to my PhD supervisor (Dr. Doquet) for her consistent support and understanding throughout the work, not only in professional life but also in personal life. She was a great source of motivation for me. I would also like to thank my promoter of this thesis from our industrial partner (IFPEN): Mr. Emmanuel, Dr. Eléonore and Dr. Jean, who have consistently provided useful advices to this work from time to time, especially for the part devoted to corrosion, thanks to Dr. Jean Kittel.

I would like to thank all the jury members of my PhD defense, who took out time of their schedule for me and the reporters (Dr. Thierry Palin-Luc and Dr. Franck Morel) for their useful advices for the improvement of this manuscript.

I would also like to thank my lab (LMS) where I carried out this thesis and my employer (IFPEN) for providing funds for this work.

I would also like to thank the lab technicians especially Mr. Erik Guimbretière, Mr. Vincent De Greef, Mr. Alexandre Tanguy, Mr. Simon Hallias, Mr. Jean-Christophe and also, Dr. Eva Hériprié, who helped me during my thesis with various experimental equipment and trained me to use them. Thanks to all of them.

Also, the lab LAMPA, Arts et Mtiers ParisTech (Angers) and Dr. Charles Mareau for allowing to do a part of my experimental work there and providing useful advice on measurements of residual stresses that I performed there.

Thanks to the secretariat of LMS and IFPEN, that made the administrative procedures easier during my thesis and thereby, making my life a lot comfortable so that I can concentrate on my work.

And, last but not the least, my parents and family members who supported me throughout my life and encouraged me to go through this PhD framework.

Thanks to all for your support and help.



# Introduction

## Industrial context

World energy consumption has increased by two fold since the energy crises of the 1970s. More than 80% of this energy is obtained from fossil fuels. This consumption is still increasing day by day. Other than looking for other sources of energy, companies are also trying to increase the efficiency of fuel extraction from known sources. Of all the known sources, oil is of particular concern because of its limited reserves available throughout the world with most of the countries being importer of oil. The oil reserves are exhausting at a faster rate with limited number of substitutes available. Global oil consumption has nearly tripled since 1965, with fastest consumption in developing countries. The present study concerns the oil extraction process. In order to increase the production of oil from oil reserves, efforts have been made for deeper offshore drilling through riser tubes and that too in harsher environments (Guesnon et al., 2002; Désamais et al., 2007). The design of offshore structures has to integrate a reliable assessment of their durability under complex cyclic loadings. In order to facilitate deep water drilling the riser tubes have to be connected by means of an assembly called “Clip-Riser™ assembly”.

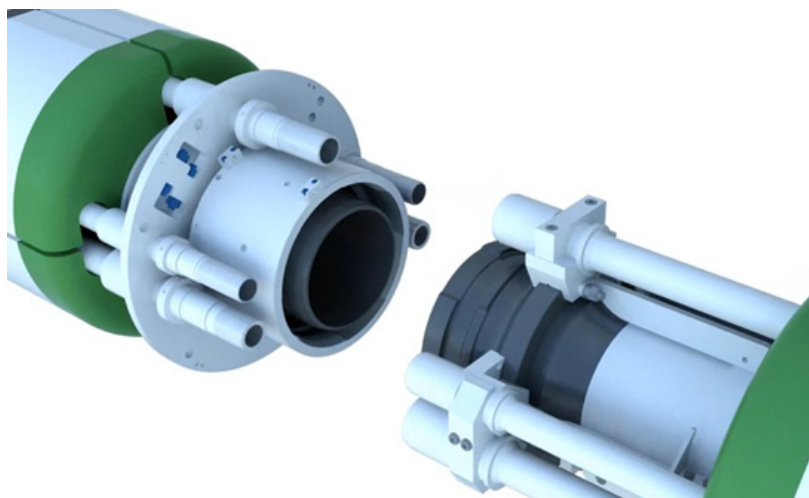


**Figure 1:** Clip-Riser™ connector.

Institut Français du Pétrole et Energies Nouvelles (IFPEN) designed an efficient clip riser that allows fast and secure connection and de-connection time, without any preloading as compared to flanged-type connectors. A typical Clip-Riser™ connector designed by IFPEN is shown in figure 1 and a 3D model of Clip-Riser™ tube assembly with clip connector (or lock ring, which is the component of interest in present study) is shown in figure 2. Clip connector has a wedge like structure along the circumference and another set with 45° offset along the longitudinal direction that provides quick and secure locking action.

A Clip-Riser™ joint is typically 75 feet (22.86 m) long and approximately 133 joints are required for 3028 m (10000 ft) drilling. A riser assembly in drilling process is subjected to quite a complex loading. The forces experienced by a riser tube in working condition are depicted in figure 3. When immersed in sea water, the assembly not only experiences external pressure from sea water but also the internal pressure of fluid flowing through it as well as the weight of the riser assembly, buoyancy force, and sea waves and currents, which induce cyclic bending with a random amplitude. Hence fatigue comes into picture. A simulated spectrum of sea wave amplitude generated from recorded data over a span of time at a harbor and the corresponding tension load experienced by the riser assembly is shown in figure 4. The high mean load comes from the fact that the riser tubes are in pre-tension while the variation in load is induced by sea waves.

Hence, there is need to characterize and model the fatigue behavior of the steel which constitutes the connectors in representative stress states, which will be shown to correspond to in-phase biaxial tension with high mean stresses.

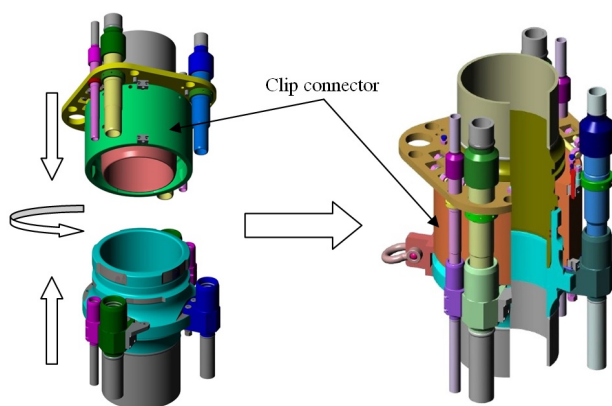


**Figure 2:** Clip riser assembly.

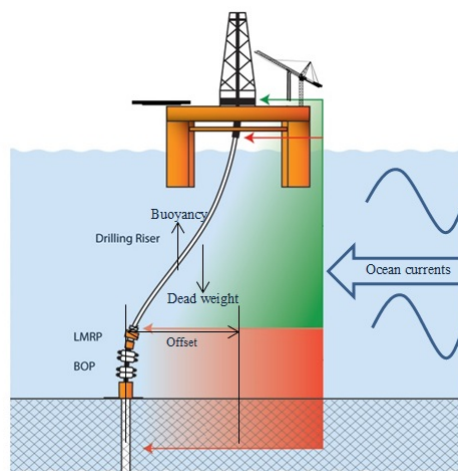


**Figure 3:** Mechanics of clip riser in operation.

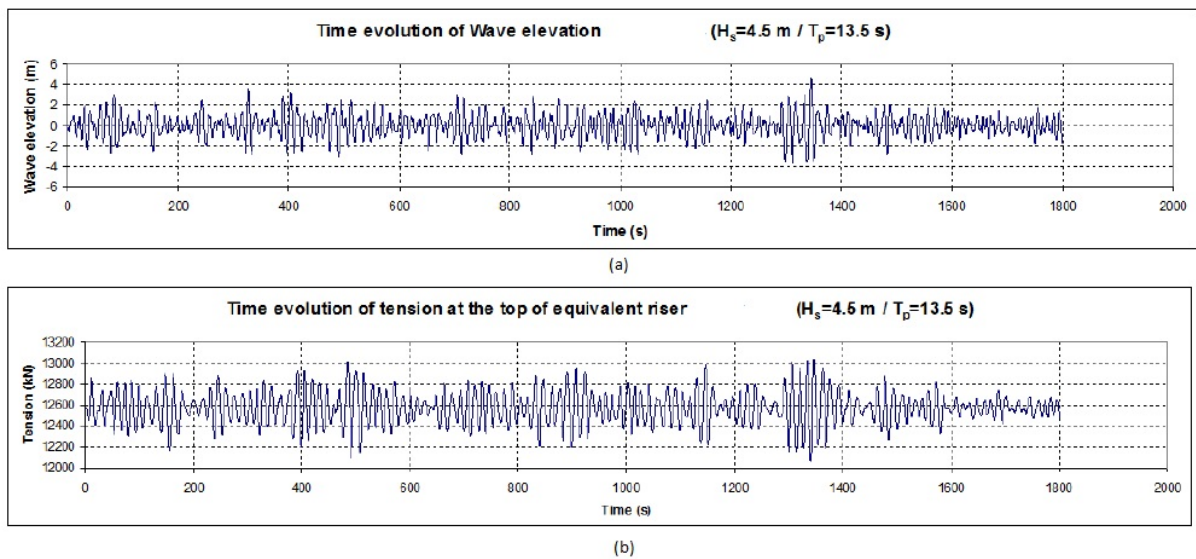


**Figure 4:** (a) Simulated Sea wave amplitude with the help of data recorded over a span of time (b) Corresponding variation of load on riser.

Even though the clip connectors are provided with a protective coating, this coating can get damaged while operating, allowing a direct contact between steel and sea water. The literature shows that a significant depreciation in fatigue life can occur due to a corrosive environment. This depreciation thus needs to be assessed under representative stress states as well.

## Scientific questions

The majority of experimental studies devoted to multiaxial fatigue focused on tension/compression and torsion tests. Data concerning biaxial cyclic tension are limited and sometimes contradictory, as it will be shown in the literature review presented in part A of chapter 1. Many multiaxial fatigue criteria are based on tension-torsion and some recent studies (Koutiri et al., 2013) have shown that such criteria do not give good results under biaxial-tension loadings.

The primary aim of the study was thus to formulate and identify an accurate and reliable fatigue criterion, for the type of stress states currently encountered in offshore structures, to be implemented in a finite element code thereafter.

Second, the life debit in corrosion-fatigue is generally evaluated from uniaxial tests, which might underestimate the detrimental effect under biaxial loading. The high hydrostatic

stress encountered in offshore structures might enhance any environment-induced reduction of their resistance to fatigue that involves hydrogen ingress into the metal, as discussed in the literature review presented in part B of chapter 1.

## Structure of the manuscript

While chapter 1 has been devoted to literature surveys on multiaxial fatigue in air and corrosion fatigue, respectively, chapter 2 focuses on the steel constituting the clip connector, which was characterized in terms of micro-structure and the constitutive equations.

FE simulations of service load conditions on clip connector assembly were done and the stress states in critical areas were analyzed, in order to determine relevant experimental conditions for the fatigue tests, as described in chapter 3.

The mean stress effect under uniaxial loading was then investigated and modeled. The changes in damage mechanisms associated with a change in mean stress were analyzed and has been described in chapter 4.

Then, biaxial fatigue tests were run under repeated tension and internal fluid pressure on tubular specimens, with various proportions of each loading so as to evaluate the influence of load biaxiality on the fatigue life and damage mechanism at fixed mean stress. This part of the work has been discussed in chapter 5.

To re-evaluate the potential life debit due to contact with sea water under representative loading states, uniaxial and biaxial fatigue tests were performed in salt water, with or without cathodic protection, and the results were analyzed in relation with the observed damage mechanisms. This part of the work has been reported in chapter 6.

A synthesis of all results has finally been presented and suggestions for further work has been made.

# Chapter 1

## Literature review

### Part A: Fatigue in air

While fatigue studies for uniaxial cases (pure bending or pure tension) have been of much focus before 1975, multiaxial fatigue has been key area of interest for researchers for more than 30 years since many structures experiencing fatigue in real operations undergo multiaxial loadings (bending-torsion, tension-torsion or tension-tension).

#### 1.1 Damage mechanisms

In general, in high-cycle fatigue, the fatigue damage can be divided into four stages:

- Crack initiation stage (number of cycles to form microcracks, generally on the surface).
- Microcracks growth in strong interaction with microstructural barriers, with an alternation of fast transgranular propagation and arrest periods.
- Macrocracks propagation stage (smooth propagation of engineering size cracks, following the Paris law)
- Unstable propagation leading to fracture

There is no general agreement on the definition of crack initiation. The number of cycles for crack initiation,  $N_i$ , can be assumed to correspond to the creation of a crack of

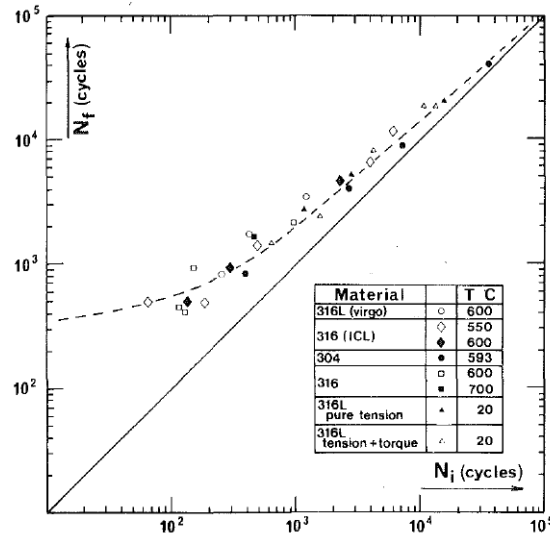


**Figure 1.1:** Total fatigue life,  $N_f$ , as a function of number of cycles for crack initiation,  $N_i$ , (Jacquelin et al., 1983)

length  $a_0$  of about 0.1 mm, comparable to the mean grain size in many metallic materials (Forsyth, 1972). The ratio of number of cycles representing initiation stage ( $N_i$ ) to total life ( $N_f$ ) varies depending upon the loading amplitude. It represents up to 90% of the fatigue life in high cycle fatigue, figure 1.1.

### 1.1.1 Crack initiation

#### Surface crack initiation

In general, fatigue cracks get initiated from surface of specimens, as explained by Forsyth (1972), mainly because of:

- Stress concentrations at extrusions and intrusions generated by dislocations' gliding in persistent slip bands (PSBs).
- Environment effects, even just in moist air.

The application of cyclic strains (or stress) close to the endurance limit, produces persistent slip bands (PSBs), which produce surface roughness, leading to initiation of microcracks, figure 1.2a. In particular intrusion sites are likely to initiate cracks because of a stress concentration effect. Initiation is followed by a shear-driven transgranular propagation stage along a slip plane, described as “Stage I” of crack propagation, figure 1.2b. Since stage I cracks change their orientation at each grain boundary, it is quite rough.

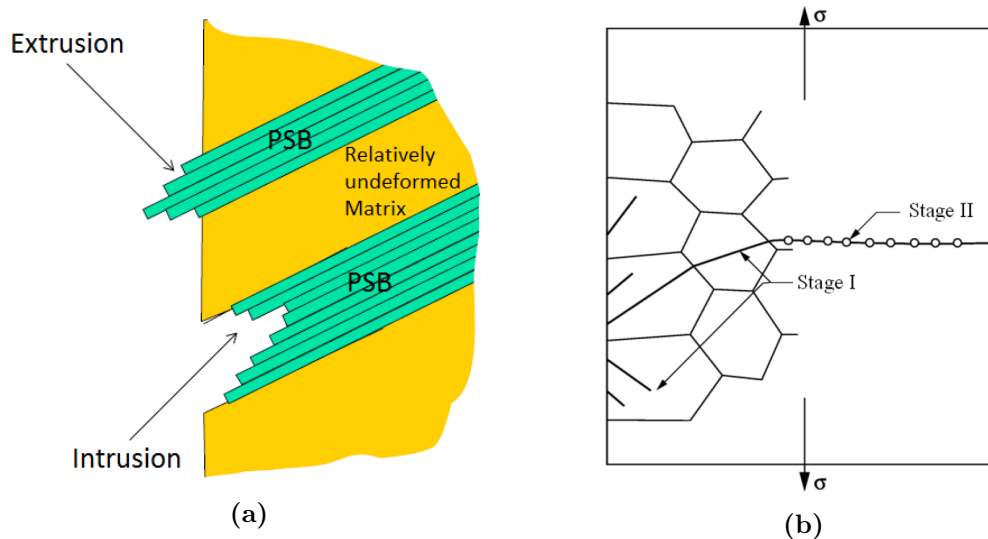
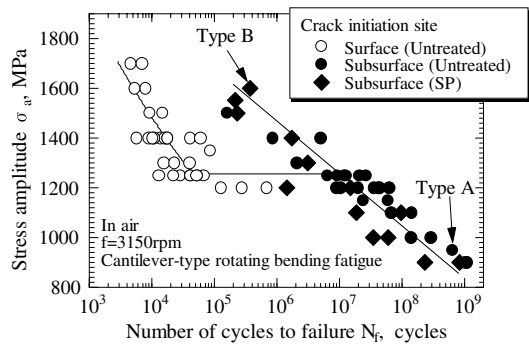


**Figure 1.2:** (a) Stage I and stage II propagation of cracks (Bathias and Pineau, 2010) (b) Intrusion-extrusion pair on surface

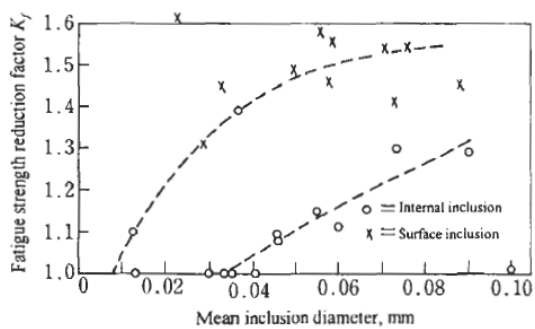
Friction between the crack face can significantly hinder their development. An opening stress which reduces friction thus triggers their propagation, while a compressive normal stress tends to slow it down. During stage I, microcracks growth shows repeated accelerations and decelerations due to interactions with grain boundaries (Zhang and Edwards, 1992) that can be modeled if crack tip plasticity and microstructure are taken into account (Bertolino et al., 2005). Some microcracks do not propagate further than the first grain boundary because of a large misorientation between neighbouring grains while some can cross microstructural barriers without any deceleration. For “microstructurally-short cracks”, continuum fracture mechanics is not the appropriate tool while for “mechanically-short cracks”, which are longer than about 5 grains but smaller than 1 or 2 mm and less dependent on microstructure, Linear Elastic Fracture Mechanics can be used, although with a different correction for closure effects than for long cracks, as explained below. In push-pull or bending, stage I is limited to a few grains in depth and is followed by “Stage II” crack growth, during which the crack propagates in mode I perpendicular to the first principal stress.

## Internal crack initiation

Cracks can also initiate from internal broken or debonded inclusions. This mechanism tends to become predominant in the very high cycle fatigue or giga-cycle fatigue domain and leads to dual S-N curves (figure 1.3(a)) with a plateau between  $5 \times 10^5$  and  $10^7$  cycles



(a)



(b)



(c)

**Figure 1.3:** (a) Dual SN curves of high carbon-chromium bearing steel typical of a transition from surface to internal crack initiation when the loading range decreases (Shiozawa et al., 2006) (b) Effect of Inclusion's size and location on fatigue strength (Duckworth and Ineson, 1963) (c) An example of a fish eye pattern.

which has long been considered as an endurance limit. However, the recent development of ultra-high frequency testing machines has shown that internal cracks initiated from defects can lead to fatigue fracture at even lower stress ranges beyond  $10^7$  to  $10^9$  cycles. The size, shape and location of the inclusions can affect the fatigue strength: the bigger the inclusions and sharper their edges, the larger is the reduction in fatigue strength, with existence of a threshold size below which no reduction on fatigue strength occurs, figure 1.3(b). For a given size and fatigue life, surface inclusions are more detrimental than internal inclusions (Duckworth and Ineson, 1963). Tensile or compressive residual stresses are often induced around the inclusions during the solidification process because of a difference in thermal expansion coefficient of matrix ( $\alpha_m$ ) and inclusions ( $\alpha_i$ ). If  $\alpha_m > \alpha_i$ , which is the case for  $\text{Al}_2\text{O}_3$  inclusions, tensile stresses are induced on the plane perpendicular to loading direction while if  $\alpha_m < \alpha_i$ , which is the case for MnS inclusions, compressive stresses appear. The elastic properties of the inclusions and their mismatch with those of the matrix also affect the stress distribution in the inclusion and around it

---

and hence change the stress concentration factor and the crack initiation site (Donnel, 1974). Murakami proposed to treat inclusions as mechanically equivalent to small defects and introduced the  $\sqrt{\text{area}}$  parameter in an empirical equation in which the endurance limit is computed as a function of the  $\sqrt{\text{area}}$  of the projection of the largest inclusion in the stressed volume on the first principal plane (Murakami, 2002).

Internal crack initiation often leads to the formation of a “fish eye” (figure 1.3(c)) pattern with the defect as the ward and the bright, non oxidized crack grown “under vacuum” until it reaches the free surface, as the white of the eye. Such patterns were first reported by Naito et al. (1984) in giga-cycle regime. The crack initiated in fish eye quickly adopts a circular shape (iso-SIF contour). Surface residual stresses play an important role in the competition between surface crack initiation and internal crack initiation (Li et al., 2012, 2014; Schijve, 1978). Compressive surface residual stresses tend to favor internal initiation. Fish eye is often accompanied by a special area around the initiation site called Optically Dark Area, ODA (Murakami et al., 2000b) or Fine Granular Area, FGA (Shiozawa et al., 2006; Sakai et al., 2006) or Granular Bright Facet, GBF (Sakai et al., 2001) in very long fatigue life regime (Li et al., 2014). Several mechanisms for crack initiation from these areas have been proposed like hydrogen assisted cracking due to hydrogen trapped by inclusions and released into the metal, reducing the threshold  $\Delta K$  for fatigue crack growth (Murakami et al., 2000a), segregation of fine carbides and subsequent formation and coalescence of microcracks (Shiozawa et al., 2010), local refinement of the micro-structure & de-bonding from matrix (Sakai et al., 2006). The reduction in grain size would reduce roughness-induced closure and thus reduces the threshold  $\Delta K$  (Petit and Sarrazin-Baudoux, 2006). The most convincing explanation for the formation of the ODA was provided by Nakamura et al. (2010). They showed that the repeated contact of bare metallic crack faces in vacuum is responsible for very high adhesion and contact stresses, leading to repeated welding and fracture of the asperities, and to a modification in their aspect after crack propagation. The local refinement of the micro-structure within the ODA would thus be a side effect and would not play any important role in crack growth.

Internal initiation can also occur from an inhomogeneous composition of the material (Ochi et al., 2002; Furuya, 2008; Li et al., 2012). The mechanism of such initiation is different from that arising from inclusion or pores. Few studies have been carried out yet to understand the mechanism of such initiations.

The initial crack growth environment after internal initiation is similar to vacuum (Nakamura et al., 2010) and plays an important role in crack kinetics, usually much slower

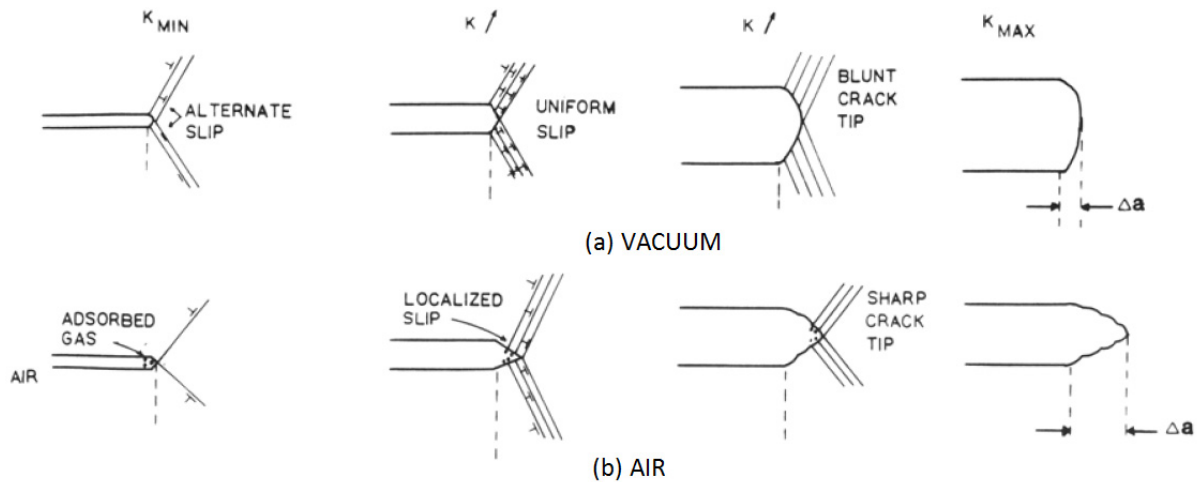


**Figure 1.4:** Schematic representation of the blunting process of crack tip as influenced by the environment (air and vacuum), (McEvily and Gonzalez Velazquez, 1992).

than in air (McEvily and Gonzalez Velazquez, 1992; Petit and Sarrazin-Baudoux, 2006). Fatigue striations are generally absent under vacuum, due to diffuse plasticity, promoting crack tip blunting, while in air, moisture adsorption and hydrogen release would favor localized crack tip plasticity, the formation of striations and faster crack growth than in vacuum as explained in figure 1.4 (McEvily and Gonzalez Velazquez, 1992). This probably partly explains why the numerous attempts to evaluate the number of cycles for internal crack growth in gigacycle fatigue by integration of mode I crack growth kinetic data obtained from lab experiments run in air (Ogawa et al., 2014) provide a negligible fraction of the fatigue life. It is thus currently admitted that VHCF (Very High Cycle Fatigue) is controlled by internal crack nucleation, which would constitute the major part of life. This conclusion however seems questionable, since it is not based on crack growth kinetics measured in vacuum.

### 1.1.2 Crack growth

Stage II crack growth is controlled by the range of mode I stress intensity factor at the crack tip. This stage of crack propagation is often characterized by the presence of striations formed by repeated plastic blunting and resharpening of the crack tip, figure 1.5. Under tension, crack faces are pulled apart generating shear stresses which induce dislocation emission and glide away from the tip, along these planes, figure 1.5(b). This results in blunting of the crack tip into a semi circle ahead of previous crack tip, figure 1.5(c). At unloading, some but not all the dislocations glide back towards the former crack tip (now located somewhat behind the current one), figure 1.5(d). Due to the difference in

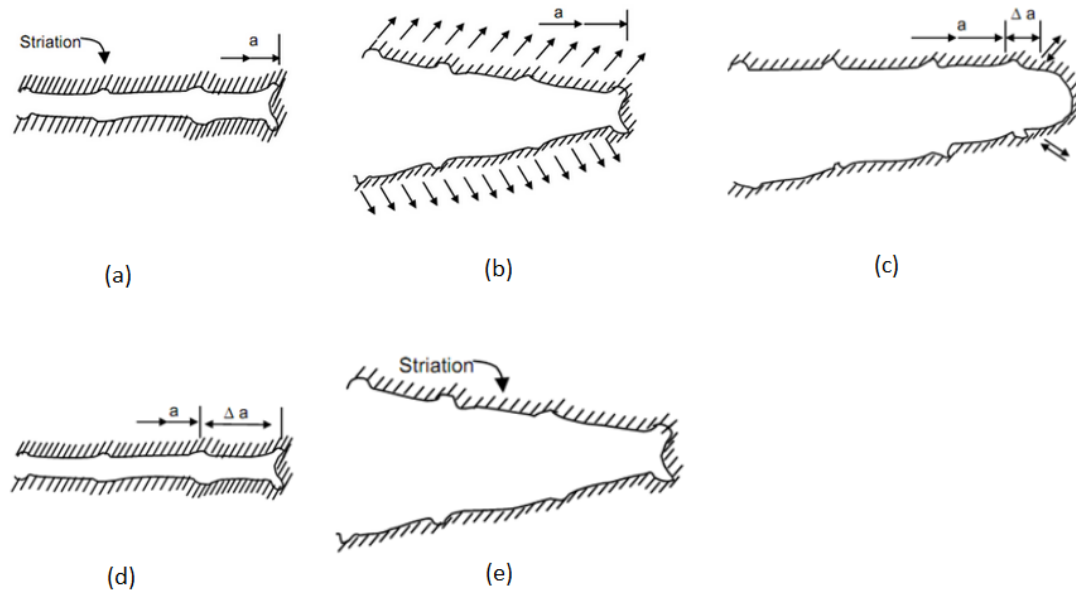


**Figure 1.5:** Stage II crack growth mechanism (a) zero load (b) small tension (c) maximum tension (d) zero load (e) small tension (next cycle), (Laird, 1967)

the number of dislocations emitted and annihilated, a small step (a striation) forms on the crack face and process repeats during each cycle. Paris law based on linear elastic fracture mechanics, relating crack growth rate ( $da/dN$ ) and stress intensity factor ( $\Delta K$ ), was initially introduced to describe the crack growth in this regime ( $A$  and  $m$  are material constants).

$$\frac{da}{dN} = A \Delta K^m \quad (1.1)$$

Elber (1970) introduced the concept of crack closure to explain the R ratio-dependence of crack growth kinetics. Fatigue crack closure phenomenon can be attributed to three basic mechanisms: plasticity-induced closure (Elber, 1971), roughness-induced closure (Suresh and Ritchie, 1982; Lin and Fine, 1982) and oxide-induced closure (Suresh et al., 1981). Plasticity induced closure arises due to the existence of a “plastic wake” behind the crack tip with some residual tensile strain restrained by the surrounded elastic material, most prevalent under plane stress conditions. But some studies have shown significant closure effects in plane strain conditions near the crack growth threshold,  $\Delta K_{th}$ , as shown in figure 1.6(a) (Suresh et al., 1981). To explain this, the other two mechanisms were evoked. Oxide induced closure effects arise from the oxide deposits formed on crack tip surfaces due to active environmental conditions (eg moisture etc.) or repeated friction between the crack faces, with a thickness comparable to the crack tip opening displacement.

The oxide-induced closure induced by repeated contact of crack faces gets reduced by a high mean stress or the presence of non-oxidizing environment ( $H_2$ ), figure 1.6(b).

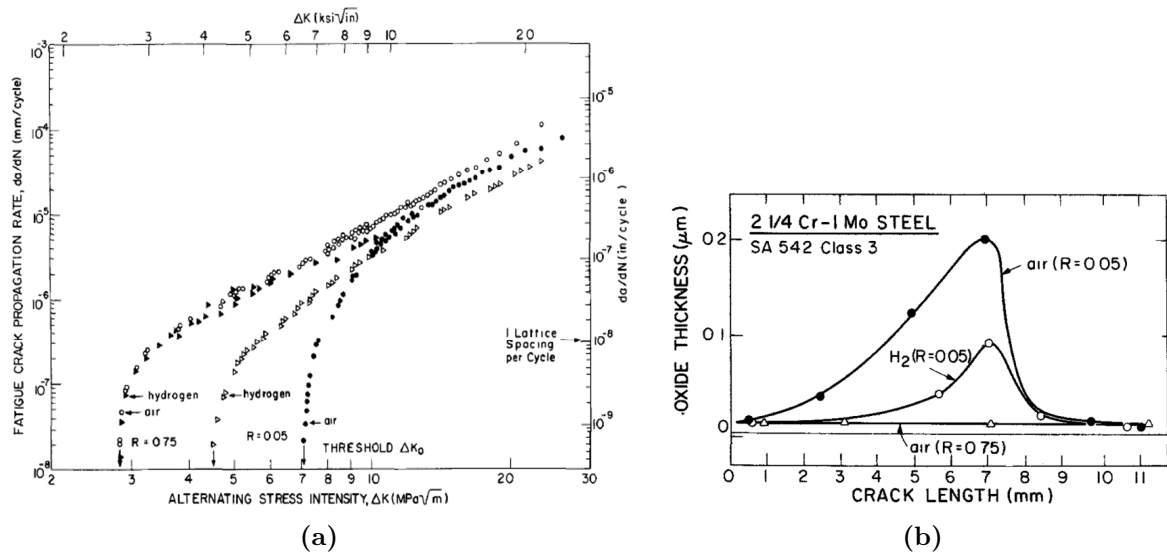


**Figure 1.6:** (a) Fatigue crack growth rate in martensitic SA542-2 steel (b) Oxide thickness as a function of crack length in different environment in SA542-3 steel (Suresh et al., 1981).

Roughness induced closure effects arise from the asperities of fracture surfaces comparable to crack opening displacements, and to significant mode II displacements (Suresh and Ritchie, 1982). To take into account closure effects,  $\Delta K$  is replaced by  $\Delta K_{\text{eff}} = K_{\text{max}} - K_{\text{op}}$ , where  $K_{\text{max}}$  is maximum stress intensity factor and  $K_{\text{op}}$  is the stress intensity factor corresponding to the nominal stress required to open the crack. When the crack growth rates measured with different R ratios are replotted versus  $\Delta K_{\text{eff}}$ , all the data fall onto a single and intrinsic curve, figure 1.7.

“Mechanically short cracks” have been extensively studied since the work published by Pearson (1975) in which they are reported to behave differently as compared to long cracks in respect to following two aspects:

- These cracks grow faster than long cracks at a given  $\Delta K$  (B to D in figure 1.8).
- They grow at  $\Delta K$  lower than threshold value for long cracks.

This behavior can be explained by lower plasticity-induced crack closure. Journet et al. (1989) proposed an exponential relationship between  $K_{\text{op}}$  and the crack length,  $a$ :

$$K_{\text{op}} = K_0(1 - e^{-ka}) \quad (1.2)$$

The use of  $\Delta K_{\text{eff}}$  eliminates the growth rate difference between long and short cracks (Ravichandran and Larsen, 1997; Verreman and Espinosa, 1997).

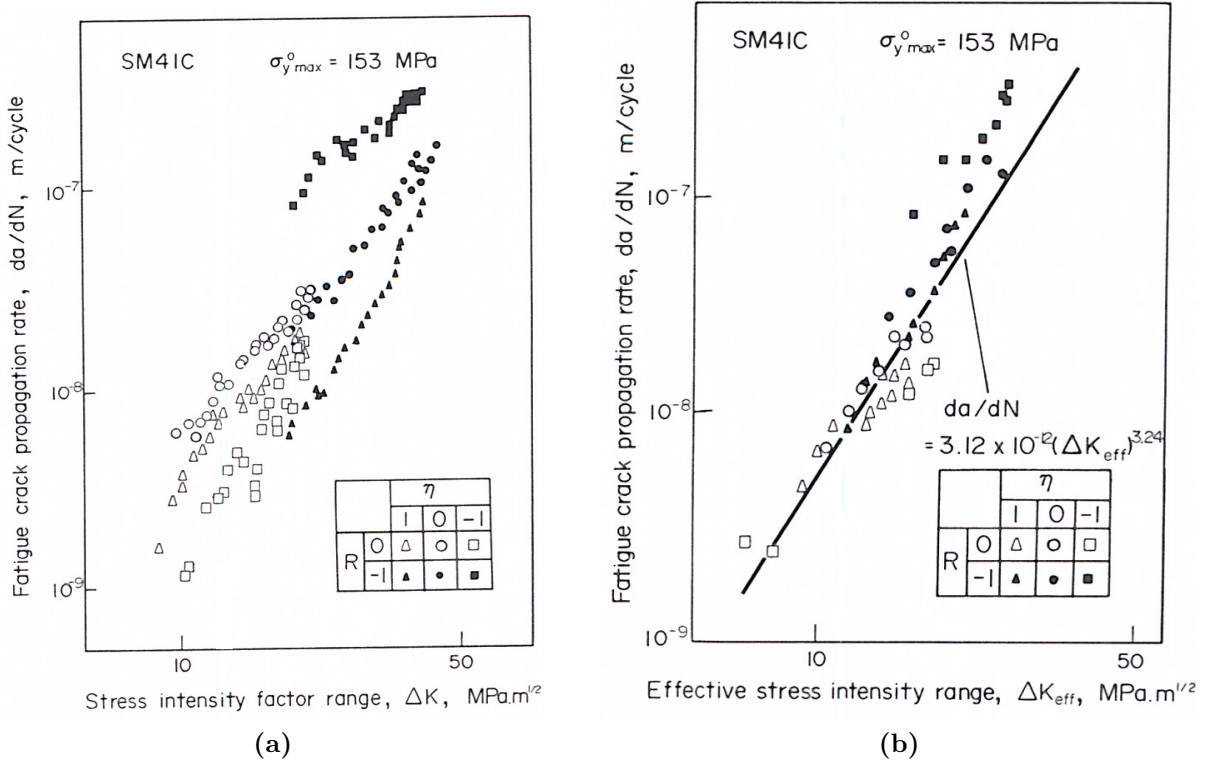


**Figure 1.7:** Correlation of crack growth rate with (a) Nominal  $\Delta K$  (b) Effective  $\Delta K$ , R is the R-Ratio and  $\eta$  is biaxiality ratio (Hoshide et al., 1981)

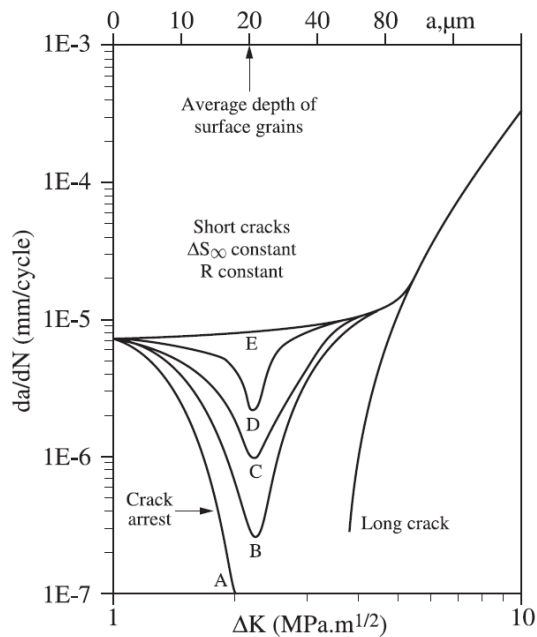


**Figure 1.8:** Propagation rates of short cracks within Al alloy 7075-T651 compared to long cracks as a function of  $\Delta K$ , (Lankford, 1985)

### 1.1.3 Effect of biaxial tension

Load biaxiality can affect the proportions of stage I or stage II in total fatigue life. In torsion, the transition from stage I to stage II is postponed and may not even occur: at large shear stress or strain ranges, the cracks continue to grow in mode II and III until fracture (Socie, 1987). By contrast, biaxial tension has been reported to produce predominantly stage II cracking (Havard and Topper, 1969).

In Spheroidal Graphite (SG) cast iron, cracks often initiate from inclusions and this process is affected by load biaxiality because stress concentration ( $K_t$ ) varies with type of loading, for e.g.  $K_t$  for 2D circular center hole is 3 under uniaxial loading, 4 under torsion loading and only 2 under equi-biaxial loading (Marquis and Karjalainen-Roikonen, 2001) and for 3D spherical internal holes, the maximum  $K_t$  varies from 2.04 under uniaxial tension to 1.36 under equibiaxial tension (Goodier, 1933).

T-stress, higher-order term in the Williams series, affects the distribution of plastic strain around the crack (Brown and Miller, 1985; McClung, 1989). There is very little difference between the plastic zone size in uniaxial tension ( $T = 0$ ) and biaxial tension ( $T > 0$ ), but under shear loading ( $T < 0$ ), it is larger (figure 1.9a). Negative T-stress has been found to accelerate crack growth (Brown and Miller, 1985). For crack growth under mode I,

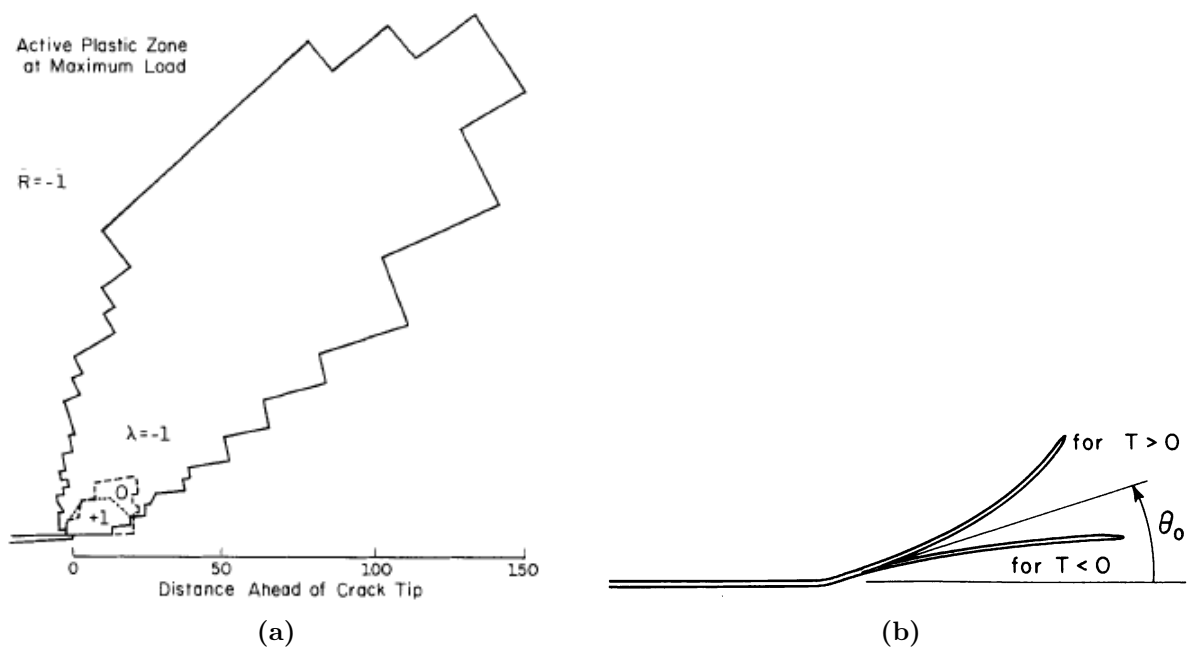


**Figure 1.9:** Effect of biaxiality ( $\lambda$ ) or T-stress ( $T$ ) on (a) distribution of plastic strain ahead of the crack tip (McClung, 1989) (b) crack path stability (Cotterell and Rice, 1980)

---

straight crack path has been shown to be stable under  $T < 0$  and unstable under  $T > 0$ , figure 1.9b (Cotterell and Rice, 1980).

Fatigue cracks in SG cast iron under biaxial tension have been reported to be more tortuous (with more branching) as compared to that in uniaxial and torsional loading (Marquis and Karjalainen-Roikonen, 2001). The same effect was reported by Kane and Doquet (2006) for 304L stainless steel (at  $R = 0$ ), and also the beneficial effect of biaxial tension on fatigue crack growth rate. As a consequence, asperity-induced closure should be more pronounced under biaxial tension.

Fatigue crack growth rates (FCGR) in AL alloy 2024-T3 (range  $10^{-5}$  to  $10^{-2}$  mm/cycle,  $R = 0.1$ ) were found to be noticeably sensitive to load biaxiality (accelerating with increase in biaxiality) under both constant amplitude as well as spectrum loading (Sunder and Ichenko, 2011). Hoshida et al. (1981) found that equibiaxial loading does not always give minimum FCGR rather it is also dependent on mean stress ( $R = 0$  or  $-1$ ).

Yuuki et al. (1989) reported no biaxiality effect on crack growth rate at low stress levels but noticeable effect at high stress levels. The existence of a threshold stress level (roughly 40% of yield strength) below which no biaxiality effect (at  $R = -1$ ) exists has been reported by McClung (1989) in growth range of  $10^{-6}$  to  $10^{-3}$  mm/cycle. Marquis and Karjalainen-Roikonen (2001) observed almost no effect of equibiaxial loading on fatigue life as compared to uniaxial one. Misak et al. (2014) found that the FCGR in aluminum alloy 7075-T6 is same in uniaxial and equibiaxial loading, although the damage mechanism was different. However, Lee and Taylor (2011) reported the beneficial effect of in-phase equibiaxial tension on the same aluminum alloy. Kamaya and Tsuji (2014) reported the beneficial effect of biaxial stress on the fatigue lives of 316 stainless steel.

In summary, many literatures exist concluding that the detrimental effect (Bonnand et al., 2011; Joshi and Shewchuk, 1970; Vansovich et al., 2015; Clàudio et al., 2014), beneficial effect (Bellett et al., 2010; Doquet and De Greef, 2012; Kane and Doquet, 2006; Lee and Taylor, 2011) or neutral effect (Marquis and Karjalainen-Roikonen, 2001; Leever et al., 1976; Kitagawa et al., 1978; Misak et al., 2014) on fatigue life and fatigue crack growth in air (depending upon  $R$  ratio and loading amplitude) under biaxial tension, leading to no general perception. There is a consensus to attribute the effects of load biaxiality on fatigue crack growth to their influence on plasticity or roughness-induced closure effects. As a consequence, parameters which take closure effects into account that is either  $\Delta K_{\text{eff}}$  or Crack opening displacement (COD) range, can be used to account for biaxiality effects.

---

## 1.2 Fatigue criteria

### 1.2.1 Low-cycle fatigue

Lots of low cycle fatigue criteria have been proposed in the literature. Only few and popular ones are discussed here. A very well know criterion is the Smith-Watson-Topper criterion ([Smith et al., 1970](#)):

$$\sigma_{N,max} \epsilon_{N,a} = \frac{(\sigma'_f)^2}{E} (2N)^{2b} + \sigma'_f \epsilon'_f (2N)^{b+c} \quad (1.3)$$

The energy term is defined on the plane undergoing the maximum normal strain amplitude. It assumes mode I cracking because of involvement of normal stress and strain terms. The material parameters are identified using the Coffin-Manson curves. [Kandil et al. \(1982\)](#) proposed another form of criterion which is based on their previous study ([Brown and Miller, 1973](#)), with the plane of maximum shear strain as the critical plane.

$$\gamma_a + 2 \left( \frac{\tau_{-1}}{\sigma_{-1}} - 0.5 \right) \left( \frac{1 + \nu}{1 - \nu} \right) \epsilon_{N,a} = \gamma'_f (2N)^c + \frac{\tau'_f}{G} (2N)^b \quad (1.4)$$

The terms  $\tau'_f/G$  &  $\gamma'_f$  are related to elastic and plastic part of strain respectively. One of the problems resulting from the criteria related to strain amplitudes alone is the non-consideration of the mean stress and stress amplitude. The KBM criterion is only applicable to proportional loadings without any additional strain hardening effect. To overcome the shortcomings of this model, [Socie et al. \(1985\)](#) introduced a term accounting for the mean normal stress, which influences crack opening, with the plane of maximum shear stress amplitude as critical plane:

$$\gamma_a + \epsilon_{N,a} + \frac{\sigma_{N,m}}{E} = \gamma'_f (2N)^c + \frac{\tau'_f}{G} (2N)^b \quad (1.5)$$

[Fatemi and Socie \(1988\)](#) made another modification by changing the normal strain term to maximum normal stress, considering the extra hardening due to the phase shift between the stresses.

$$\gamma_a \left( 1 + k \frac{\sigma_{N,max}}{\sigma_y} \right) = \gamma'_f (2N)^c + \frac{\tau'_f}{G} (2N)^b \quad (1.6)$$

The coefficient  $k$  is determined by push-pull and torsion tests data.

+

---

## 1.2.2 High-cycle fatigue

In order to determine the allowable stress limit for safety of mechanical component, many multiaxial fatigue endurance criteria exist in literature which can be divided into four different categories:

- (i) Criteria based on a critical plane approach
- (ii) Criteria based on an integral approach
- (iii) Criteria based on energy
- (iv) Criteria based on stress invariants

### Critical plane-based criteria

Experimental observations indicate that cracks nucleate and grow on specific planes called critical planes. Depending on the material and loading conditions, these planes can be either maximum shear planes or maximum tensile stress planes. Failure assessment is performed on a plane where the amplitude or value of some stress component or combination of them attains its maximum. This type of approach reflects the physical nature of fatigue damage in their formulation.

The physical basis for such type of models is that the irregular shape of micro-cracks result in interlocking and friction between crack surfaces during cyclic shear. A tensile stress perpendicular to crack surface assists crack growth by reducing these forces. However, when the mean normal stress relative to critical plane is larger than a threshold value, it does not result in further increase of fatigue damage (Kaufman and Topper, 2003; Susmel, 2008). This observation is based on the fact that once mean normal stress is high enough to fully open the micro/meso cracks, the crack faces can no longer interact with each other and shear forces are directly transmitted to crack tip favoring the mode II propagation. When the mean normal stress is lower than the threshold value, crack faces can interact, leading to a decrease in fatigue damage because crack growth is retarded by asperities on crack faces.

One of the earliest works based on critical plane approach was by Findley (1959) with damage parameter as a linear combination of maximum shear stress amplitude ( $\tau_a$ ) and maximum normal stress ( $\sigma_{N,max}$ ) acting on the critical plane (Euler angles:  $\phi^*, \theta^*$ ) which

---

is the plane of maximizing the damage function.

$$\tau_a(\phi^*, \theta^*) + \kappa_f \sigma_{N,\max}(\phi^*, \theta^*) \leq \lambda_f \quad (1.7)$$

where  $\kappa_f$  and  $\lambda_f$  are material parameters given by:

$$\kappa_f = \frac{2-w}{2\sqrt{w-1}}, \quad \lambda_f = \frac{\sigma_{-1}}{2\sqrt{w-1}}, \quad w = \frac{\sigma_{-1}}{\tau_{-1}}$$

$\sigma_{-1}$  and  $\tau_{-1}$  are the fatigue limits in fully reversed push-pull fatigue and torsional fatigue. This criterion incorrectly predicts the absence of mean shear stress effect on fatigue life, first observed by [Gough et al. \(1951\)](#). By redefining the critical plane as a plane of maximum shear stress amplitude only, [Matake \(1977\)](#) proposed another criterion with the same damage parameter as proposed by [Findley \(1959\)](#). The Matake parameters are deduced from the endurance limits in fully reversed torsion ( $\tau_{-1}$ ) and fully reversed bending ( $\sigma_{-1}$ ).

$$\kappa = 2s - 1, \quad \lambda = \tau_{-1}, \quad s = \frac{\tau_{-1}}{\sigma_{-1}}$$

It correctly predicts the absence of mean shear stress effect in torsion (true in most cases, provided the maximum von-mises stress does not the yield limit) and the effect of mean tensile/compressive stress on fatigue life ([Papadopoulos et al., 1997](#)). [McDiarmid \(1994\)](#) then modified the criterion by using different parameters while using the same damage function and critical plane (plane of maximum shear stress amplitude), employing the concept of type A and type B facets introduced by [Brown and Miller \(1973\)](#) under biaxial loading conditions, figure 1.10. Type A facets, arising from negative biaxiality ( $\lambda$ ), are cracks for which the maximum shear stress is parallel to the surface plane hence propagating along the surface. Type B facets (more severe than case A), arising from positive biaxiality ( $\lambda$ ), are cracks for which maximum shear stress is not parallel to surface hence propagating in inwards direction from surface.

$$\tau_a(\phi^*, \theta^*) + \frac{\tau_{A,B}}{2\sigma_u} \sigma_{N,\max}(\phi^*, \theta^*) \leq \tau_{A,B} \quad (1.8)$$

$$\tau_{A,B} = \tau_A \text{ OR } \tau_B$$

$\sigma_u$  is the ultimate tensile strength of material. Either of shear endurance limit,  $\tau_A$  or  $\tau_B$ , is used depending upon type of crack potentiality. Case A cracks occur in fully reversed torsion experiments giving  $\tau_A = \tau_{-1}$  with critical plane tangent to the surface of the specimen. This criterion predicts the uniqueness of fatigue torsion limit and mean tensile/compressive stress effect on fatigue limit ([Papadopoulos et al., 1997](#)). In 1973

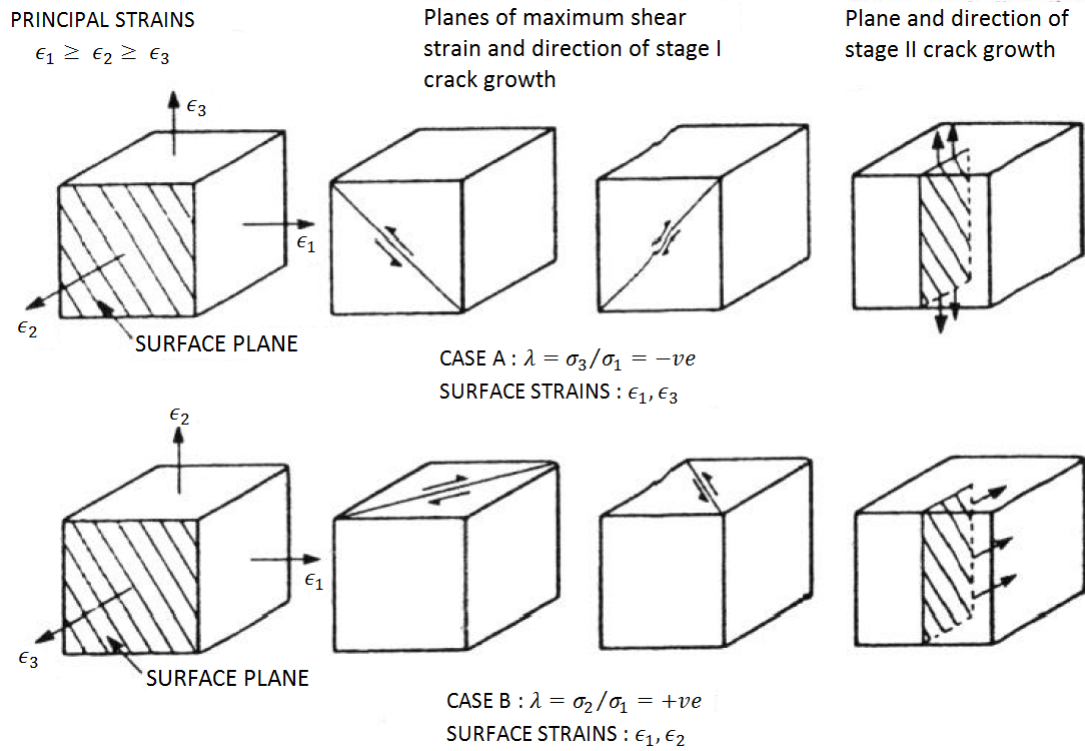


**Figure 1.10:** Planes of maximum shear and crack growth direction under biaxial loading, (Brown and Miller, 1973)

Dang-van proposed an endurance criterion using the hydrostatic stress ( $\sigma_h$ ) and mesoscopic shear stress ( $T$ ), with the critical plane ( $\vec{n}$ ) being the one which maximizes the damage parameter (Dang Van, 1973).

$$\max_{\vec{n}} \left( \max_t (a T + b \sigma_{h,\max}) \right) \leq \sigma_{-1} \quad (1.9)$$

$$\kappa = \frac{\sigma_{-1}}{\tau_{-1}}, \quad a = \kappa, \quad b = 3 - \frac{3}{2}\kappa$$

where  $\sigma_{-1}$  and  $\tau_{-1}$  are endurance limits in completely reversed tension and torsion respectively. This function establishes the Dang Van Endurance Domain but it gives poor results under non-proportional loading (Papuga and Ruzika, 2008). The method has been implemented in a number of commercial softwares and widely used for design purposes in spite of the fact that it is not able to predict multiaxial and mean stress effect simultaneously (Koutiri et al., 2013). By directly correlating the critical plane with the fracture plane (maximum normal stress amplitude plane), Liu and Mahadevan (2005) proposed a criterion including mean stress effect. The direction of the critical plane with respect to the fatigue fracture plane is given by parameter  $\alpha$ , which is the angle between the two. The critical plane orientation,  $\alpha$ , also depends upon material properties in addition to

---

stress state. [Papuga and Ruzika \(2008\)](#) proposed a criteria based on critical plane (PCr criterion) emphasizing the shear stress effect as compared to normal stress ( $a_c$  &  $b_c$  are material constants depending upon  $\kappa$ ), with the critical plane being the one maximizing the damage parameter.

$$\sqrt{a_c \tau_a^2 + b_c \left( \sigma_a + \frac{\tau_{-1}}{\sigma_0} \sigma_m \right)^2} \leq \sigma_{-1}; \quad \kappa = \frac{\sigma_{-1}}{\tau_{-1}} \quad (1.10)$$

## Integral-based criteria

In integral approach, the damage parameter is integrated over all possible orientations at a point and then compared with a critical value. In general, results produced by the critical plane approach are better than those obtained by integral approach which are more time consuming ([Papuga and Ruzika, 2008](#)). Most of the times, the expressions of such criteria are very complex. Many such criteria exist in literature: [Zenner and Richter \(1977\)](#); [Papadopoulos \(1995\)](#); [Kenmengen et al. \(1996\)](#) etc. The criterion proposed by [Liu and Zenner \(1993\)](#) is quite popular, in spite of complicated expression and involvement of lots of material parameters. Further clarification for the definition of the shear stress amplitude and mean shear stress was provided ([Zenner et al., 2000](#)) implying the dependence of torsion fatigue limit on superimposed static mean shear stress. Because of its limited performance and time cost and lack of physical meaning, such type of criteria are not the focus of this study.

## Energy-based criteria

The criteria based on strain energy per cycle can be classified into three categories:

- Criteria based on the elastic strain energy (high-cycle fatigue)
- Criteria based on the plastic strain energy (low-cycle fatigue)
- Criteria based on sum of elastic and plastic strain energy (low and high-cycle fatigue)

According to most of the authors, either elastic & plastic normal strain energy densities in the plane of maximum normal strain or shear strain energy densities in the plane of maximum shear strain should be considered as the fatigue damage parameter. However,

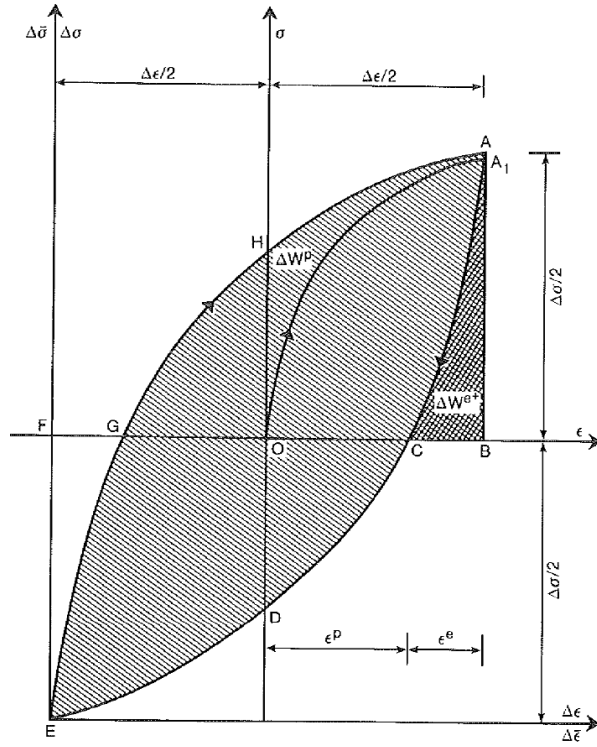


**Figure 1.11:** First loading and stabilized cyclic hysteresis loop, plastic ( $\Delta W^p$ ) and elastic ( $\Delta W^e$ ) strain energy densities (Ellyin, 1989)

application of plastic strain energy density to high cycle fatigue situations is difficult since plastic strains are small. But plastic strain energy per cycle has an advantage of being nearly constant during the fatigue life. Figure 1.11 shows the two energy components during cyclic loading. The plastic strain energy per cycle is the area EGHACDE, the area of hysteresis loop. Elastic strain energy plays a role in fatigue damage in tension only (area ACB). Glinka et al. (1995) used total strain energy density on the critical plane as a damage parameter. It was further modified so that it can predict fatigue life under multiaxial loading (Pan et al., 1999). The material constants are identified using tensile and fully reversed torsional data. The modified damage parameter can be written as:

$$W^* = \frac{\Delta\gamma}{2} \frac{\Delta\tau}{2} + k_1 k_2 \frac{\Delta\epsilon_n}{2} \frac{\Delta\sigma_n}{2} \quad ; \quad k_1 = \frac{\gamma'_f}{\epsilon'_f}, \quad k_2 = \frac{\sigma'_f}{\tau'_f} \quad (1.11)$$

$\Delta\gamma$ ,  $\Delta\epsilon_n$  and  $\Delta\tau$ ,  $\Delta\sigma_n$  are shear and normal strain/stress range on critical plane, defined as a plane of maximum shear strain amplitude,  $\gamma_{a,\max}$ .  $\gamma'_f$ ,  $\epsilon'_f$ ,  $\sigma'_f$  and  $\tau'_f$  are material parameters, identified using pure tension and pure torsion fatigue data.  $\gamma'_f$  and  $\epsilon'_f$  are shear and axial fatigue ductility coefficients while  $\sigma'_f$  and  $\tau'_f$  are shear and axial fatigue strength coefficients. For finite life prediction, the criterion can be modified using Manson-Coffin-Basquin equation. Lagoda and Macha (Lagoda et al., 1999) used maximum normal

---

strain energy density on critical plane (plane maximizing damage function):

$$W_\eta(t) = \frac{1}{2} \epsilon_\eta(t) \sigma_\eta(t) \text{Sgn}[\sigma_\eta(t), \epsilon_\eta(t)] \quad (1.12)$$

The function  $\text{Sgn}[\sigma_\eta(t), \epsilon_\eta(t)]$  includes the effect of positive and negative work done during tension and compression. For finite life prediction, the expression can be written as (with help of Manson-Coffin-Basquin equation):

$$W_{\max} = \frac{1}{2} \epsilon_{n,\max} \sigma_{n,\max} = \frac{(\sigma'_f)^2}{E} (2N)^{2b} + \sigma'_f \epsilon'_f (2N)^{b+c}$$

These type of criteria can also account for extra hardening effects under non-proportional loadings.

## Stress-based criteria

Searching a critical plane which usually takes heavy calculation time, is a drawback of critical plane approaches and integral approaches. This is overcome in stress based criteria. First and second invariants ( $I_1$ , corresponds to hydrostatic stress &  $J_2$ , corresponds to Von Mises stress) of the deviatoric stress tensor are used in damage function. Many such criteria exist in literature but only few of them are discussed here. One of the earliest and most popular criterion was proposed by ([Crossland, 1956](#)) and uses the amplitude of second stress invariant ( $J_{2,a}$ ) and maximum hydrostatic stress ( $\sigma_{h,\max}$ ) in the damage parameter:

$$\sqrt{J_{2,a}} + \kappa \sigma_{h,\max} \leq \lambda \quad ; \quad \kappa = 3 \left( \frac{\tau_{-1}}{\sigma_{-1}} - 1 \right) , \quad \lambda = \tau_{-1} \quad (1.13)$$

It predicts mean tensile/compressive load effect on fatigue strength and the absence of mean shear stress effect on fatigue strength.

[Marin \(1956\)](#) proposed to use amplitude and mean of second stress invariant ( $J_2$ ), no hydrostatic stress:

$$\left( \frac{\sqrt{3} J_{2,a}}{\sigma_{-1}} \right)^\lambda + \left( \kappa \frac{\sqrt{J_{2,m}}}{\sigma_{-1}} \right)^\mu \leq 1 \quad (1.14)$$

Generally, the values for  $\kappa$ ,  $\lambda$  and  $\mu$  are taken as  $\kappa = 1$  and  $\lambda = \mu = 2$ . This criterion incorrectly predicts a dependence of the fatigue limit on the mean torsion stress and is not able to distinguish the effect of a static tensile stress from that of a static compressive stress because of the squared terms ([Papadopoulos et al., 1997](#)).

---

Later on in 1959, Sines ([Sines, 1959](#)) proposed to use a combination of  $J_2$  amplitude and mean hydrostatic stress.

$$\sqrt{J_{2,a}} + \kappa \sigma_{h,m} \leq \lambda \quad ; \quad \kappa = 3 \left( \frac{\tau_{-1}}{\sigma_0} - 1 \right) \quad , \quad \lambda = \tau_{-1} \quad (1.15)$$

Material parameters  $\kappa$  and  $\lambda$  are identified using fully reversed torsion and repeated bending tests. Sines criterion correctly reproduces the effect of mean static torsion stress on fatigue limit and introduces a linear dependence of the bending limit upon a superimposed static normal stress ([Papadopoulos et al., 1997](#)). Sines criterion on application under fully reversed bending gives the ratio  $\tau_{-1}/\sigma_{-1}$  constant ( $= 1/\sqrt{3}$ ) for all metals which is not true ( $1/\sqrt{3} \leq \tau_{-1}/\sigma_{-1} \leq 1$  for brittle metallic alloys and  $\tau_{-1}/\sigma_{-1} \leq 1/\sqrt{3}$  for ductile metallic alloys). Expression of  $\kappa$  can be modified using Goodman relation ([Goodman, 1899](#)) ( $\sigma_a = \sigma_m = \sigma_0$ ), thereby replacing the term  $\sigma_0$  by  $\sigma_{-1}$ :

$$\frac{\sigma_a}{\sigma_{-1}} + \frac{\sigma_m}{\sigma_u} = 1 \quad (\text{Goodman Line}) \quad ; \quad \kappa = \frac{\sqrt{3}\sigma_{-1}}{\sigma_u} - 1$$

[Gonçalves et al. \(2005\)](#) used the concept of minimum circumscribed ellipsoid over the load path in five-dimensional deviatoric ( $d_i$ ) Ilyushin space. It utilizes the maximum principal stress ( $\sigma_{1,\max}$ ) over the load cycle and the distances of the center of the ellipsoid to the faces of any arbitrarily oriented rectangular prism circumscribing the stress path in the deviatoric space ( $d_i$ ), as a second load parameter.

$$a_g \sqrt{\sum_{i=1}^5 d_i^2} + b_g \sigma_{1,\max} \leq \sigma_{-1} \quad (1.16)$$

The computation is simple and fast ([Papuga and Ruzika, 2008](#)). One of the latest criteria in this category was proposed by [Vu et al. \(2010\)](#) which include mean stress effect, frequency effect and phase shift effect in multiaxial loading and combination of both stress invariants:  $I_1$  &  $J_2$  ( $\bar{\sigma}_a^D$  is the deviator of the amplitude of the stress tensor,  $\sigma_u$  is the ultimate strength and  $I_f(I_{1,a}, I_{1,mean}) = I_{1,a} + I_{1,mean}$  for  $\sigma_u < 750$  MPa; and is  $= I_{1,a} + \frac{\sigma_{-1}}{\tau_{-1}} I_{1,mean}$  for  $\sigma_u > 750$  MPa).

$$\sqrt{\gamma_1 J_2'(t)^2 + \gamma_2 J_{2,mean}^2 + \gamma_3 I_f(I_{1,a}, I_{1,mean})} \leq \beta \quad (1.17)$$

$$J_{2,mean} = \frac{1}{T} \int_0^T J_2(t) dt \quad , \quad J_2'(t) = \sqrt{\frac{1}{2} \bar{\sigma}_a^D(t) : \bar{\sigma}_a^D(t)}$$

### 1.2.3 Application to biaxial tension

Most of the existing multiaxial fatigue criteria are based on tension-torsion fatigue data and hence do not perform well tension-tension loadings. [Bonnand et al. \(2011\)](#) tried to apply the Sines and Crossland criteria under multiaxial loading (Uniaxial, tension-internal pressure (T.IP) and tension-tension (T.T)) for a finite life of 40,000 cycles on a

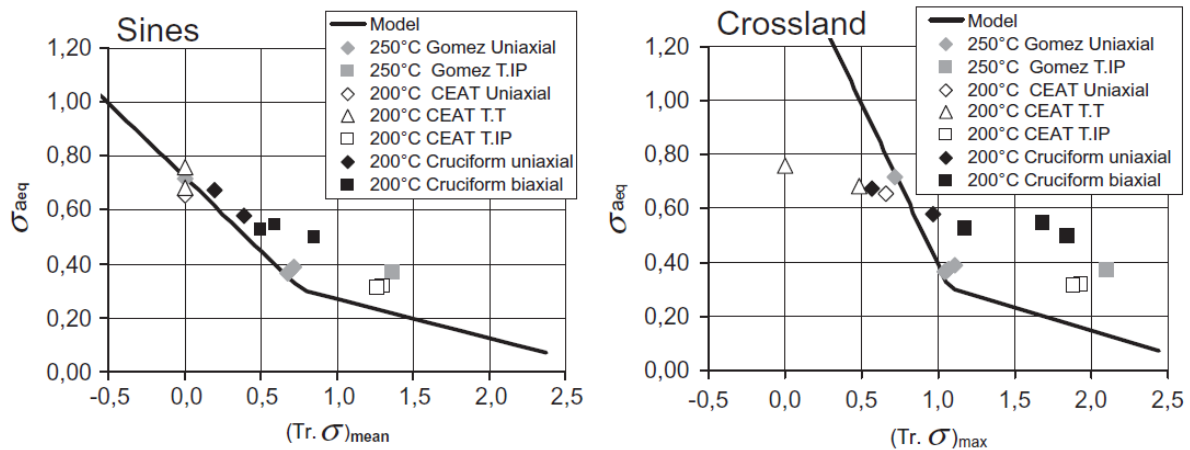


**Figure 1.12:** Comparison of Sines and Crossland criteria in multiaxial loading ([Bonnand et al., 2011](#))

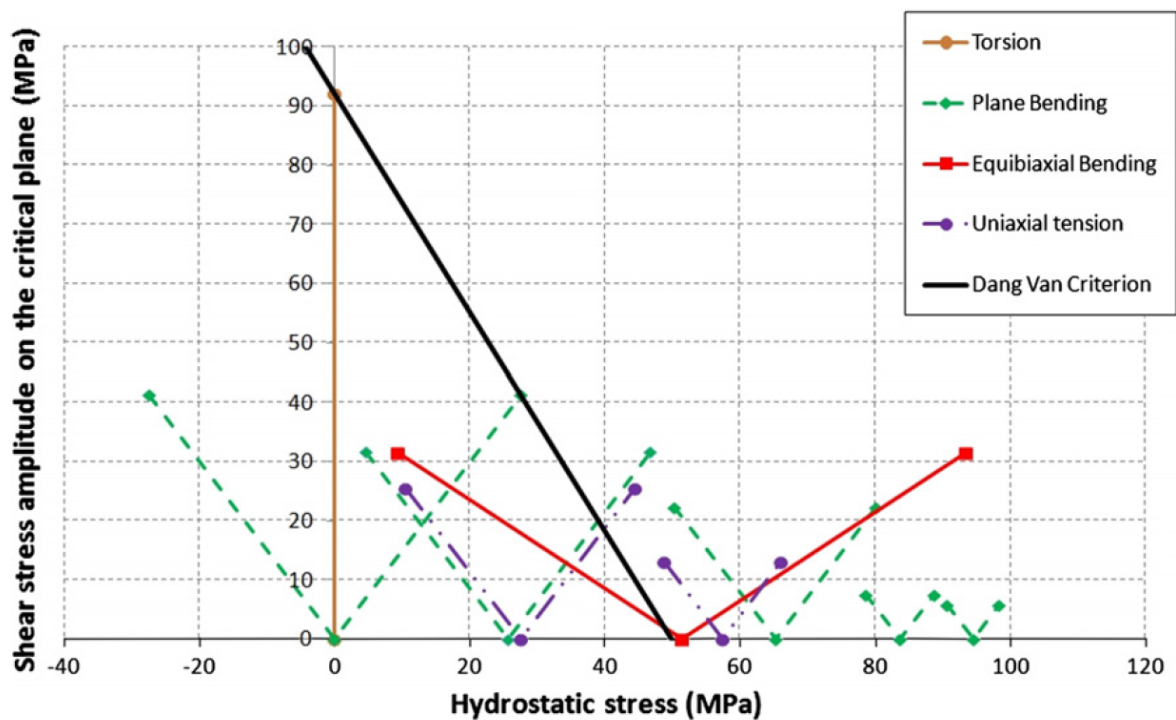


**Figure 1.13:** Dang-van diagram with loading paths at endurance limits under different loadings and mean stresses ([Koutiri et al., 2013](#))

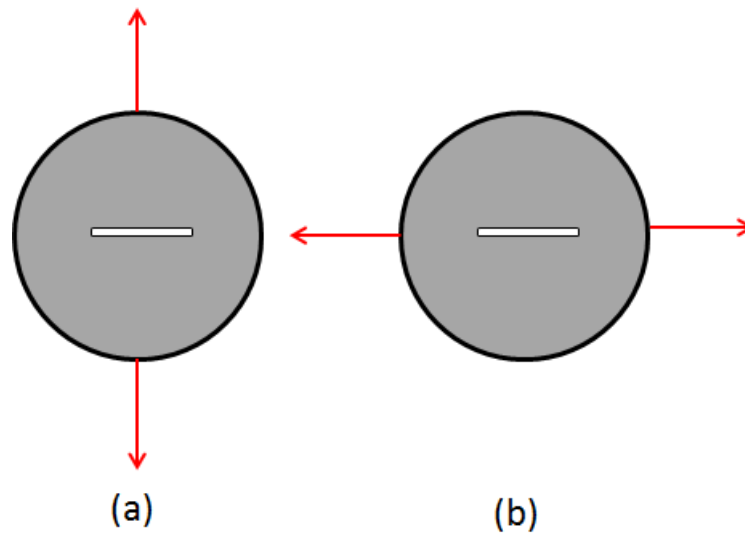


**Figure 1.14:** (a) Crack opening stress (b) T-stress on a plate with crack

titanium alloy, figure 1.12. The bi-linear fit accounts for the saturation of the mean stress effect as discussed earlier. It can be seen that both criteria give poor results with biaxial loading (tension-tension and tension-internal pressure). But it is fair to add that both these criteria were not meant for finite lives and also, testing temperatures were high. [Koutiri et al. \(2013\)](#) evaluated the pertinence of Dang-Van criterion for mean stress effect and biaxial tension loading in cast hypo-eutectic AlSi alloys, figure 1.13. It shows the loading paths at the endurance limits for different mean stresses under uniaxial bending (purple and green colors), torsion (mustard color) and biaxial tension (red color) on the Dang-van's plot. The Dang-van criterion does not capture the mean stress effect and load biaxiality effect. May be the problem with the criteria involving the hydrostatic stress is their inability to distinguish between the effect of a crack opening stress (normal to crack face) and the effect of a T-stress (parallel to crack face) as both cases gives the same trace, figure 1.14. From above discussion, it can be deduced that none of proposed criteria give satisfactory results for biaxial tension loadings and hence there is a need to find one.

### 1.3 Specimens for biaxial tension

In order to perform biaxial tension tests various kinds of specimens have been proposed: Cruciform specimens loaded in two orthogonal directions ([Bonnand et al., 2011](#); [Makinde et al., 1992](#); [Lagoda et al., 1999](#); [Tanaka et al., 1979](#); [Sunder and Ilchenko, 2011](#); [Mc-](#)

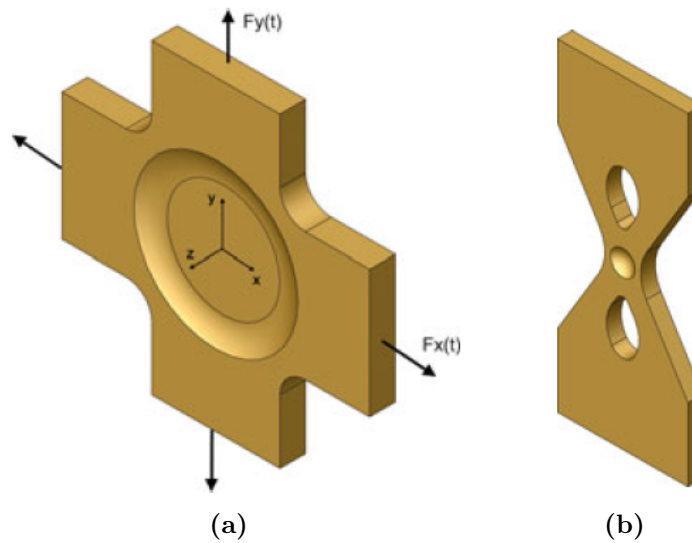


**Figure 1.15:** Specimens for biaxial tension tests (a) Cruciform type (b) specimen proposed by Bellett et al. (2010) for biaxial tension under uniaxial loading

Clung, 1989; Doudard et al., 2007; Misak et al., 2014; Lee and Taylor, 2011), tubular specimens loaded in tension and internal pressure (Brown and Miller, 1979; Marquis and Karjalainen-Roikonen, 2001; Dietmann et al., 1989; Itoh et al., 2013; Varvani-Farahani and Topper, 1997; Doquet and De Greef, 2012) and disc specimens submitted to biaxial bending (Zouani et al., 1999; Kane and Doquet, 2006; Koutiri et al., 2013; Kamaya and Tsuji, 2014; Joshi and Shewchuk, 1970). Tests on cruciform type specimens require specific and expensive multi-axis testing machines with four actuators. Secondly, specimens are large and relatively complex in shape, so that the cost and time to manufacture goes up. Thirdly, the zone in which stress and strain are uniform is usually small and test analysis demands numerical simulations and/or DIC measurements of strain fields. Biaxial tension tests on tubular specimens require a tension-pressure machine. If only internal pressure is available, then only loading cycles with a positive R ratio can be applied. Negative R ratios become possible only if external pressure can be added. If pressure is applied by a liquid, tests can be performed only at near-ambient temperatures. For higher temperatures, it is possible to pressurize a gas, but security issues become important. The disc type specimens perform good in fatigue but they are relatively larger (Kamaya and Tsuji, 2014). In addition to these, some special specimens have also been proposed to achieve biaxial stress state in uniaxial loading with a suitable geometry, figure 1.15 (Sawert, 1943; Bellett et al., 2010). In the present study, tubular specimens have been used for tension-internal pressure fatigue loadings.

---

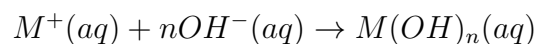
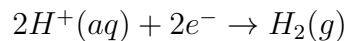
## Part B: Corrosion-fatigue

Environment Assisted Cracking (EAC) was first reported by [Haigh \(1917\)](#), followed by [Mc Adam \(1926\)](#), who used the term *Corrosion fatigue* for the first time. The combined action of environment and mechanical loads can lead to Stress Corrosion Cracking (SCC). Corrosion fatigue is considered as a particular case of SCC where the load is cyclic.

### 1.4 Electrochemical aspects

Aqueous corrosion is the electrochemical degradation of the materials with continuous dissolution (oxidation) of the metal surface in contact with the environment (electrolyte), resulting in a potential difference,  $\Delta E$ , between the metal (negative) and the electrolyte (positive). This oxidation process is accompanied by the simultaneous reduction of metals cations ( $M^+$ ) or hydrogen ( $H_2$ ) or dissolved oxygen ( $O_2$ ) in the electrolyte, acting as cathode. Corrosion is thus a consequence of a redox reaction. In aqueous environment, it can be represented by the following redox reactions:

- *Anodic Reaction.*  $M \rightarrow M^{n+}(aq) + ne^-$
- *Water Hydrolysis.*  $H_2O \rightleftharpoons H^+(aq) + OH^-(aq)$
- *Cathodic Reactions.*  $O_2(g) + 2H_2O + 4e^- \rightarrow 4OH^-(aq)$



Cathodic reactions determine the rate of corrosion i.e. the more acidic the medium is (more  $H^+$  ions), the higher is the corrosion rate. These reactions are charge-transfer processes dependent on the *interfacial potential* corresponding to what is called the electrode potential of metals ( $E_{M/M^{n+}}$ ).

### 1.5 Polarization

The electrode reactions (anodic or cathodic) are reversible at their equilibrium potential. The anodic reaction occurs above the equilibrium potential, while the cathodic reaction occurs below the equilibrium potential. A metal electrode corroding in an aqueous so-

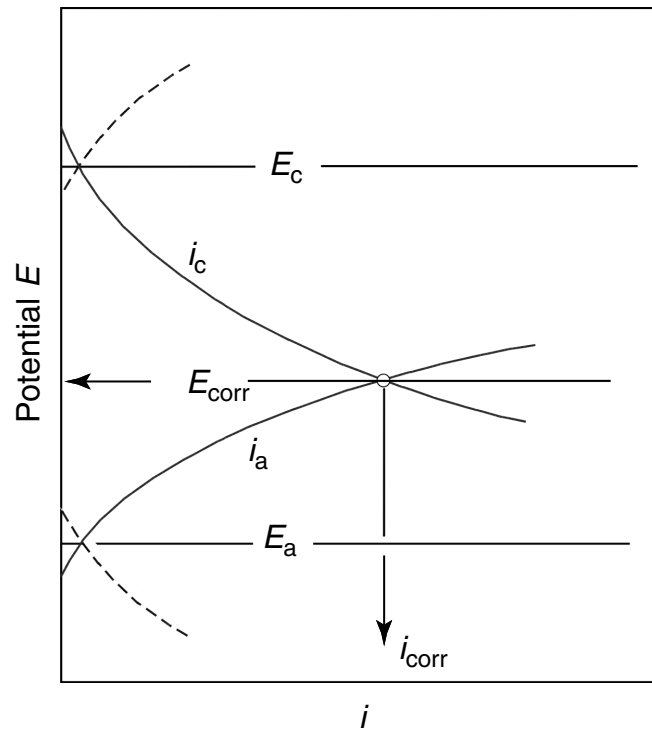


**Figure 1.16:** Schematic polarization curve of metallic corrosion. Subscript ‘a’ stands for anode, ‘c’ for cathode and ‘corr’ for corrosion. ‘i’ is current, ‘E’ is equilibrium potential.

lution has an electrode potential called corrosion potential ( $E_{corr}$ ), at which the anodic current (+) is equal to the cathodic current (–) (figure 1.16). A deviation of electrode potential from the corrosion potential due to flow of current is called polarization. In general, two types of polarization techniques are used:

- Anodic polarization
- Cathodic polarization

### 1.5.1 Anodic polarization

A displacement of electrode potential in the positive direction making electrode more anodic is called anodic polarization or anodic protection. A schematic anodic polarization curve is illustrated in figure 1.17. It starts from A, which is the corrosion potential ( $E_{corr}$ ) at which there is not net current. As potential increases, the current increases until B, which is the critical current density. The potential corresponding to B is called the Flade potential or passivation potential. Region AB is the active region in which metal oxidation is dominant. A further increase in potential leads to a sudden drop in current

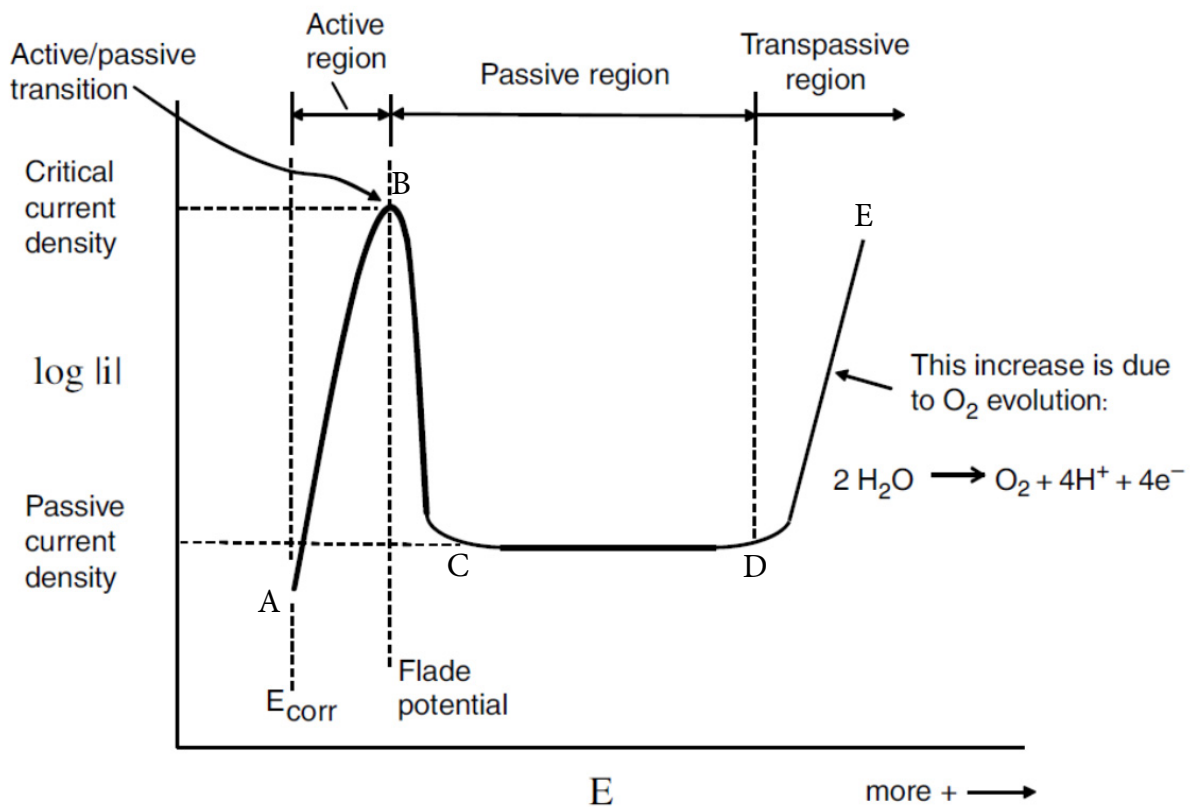
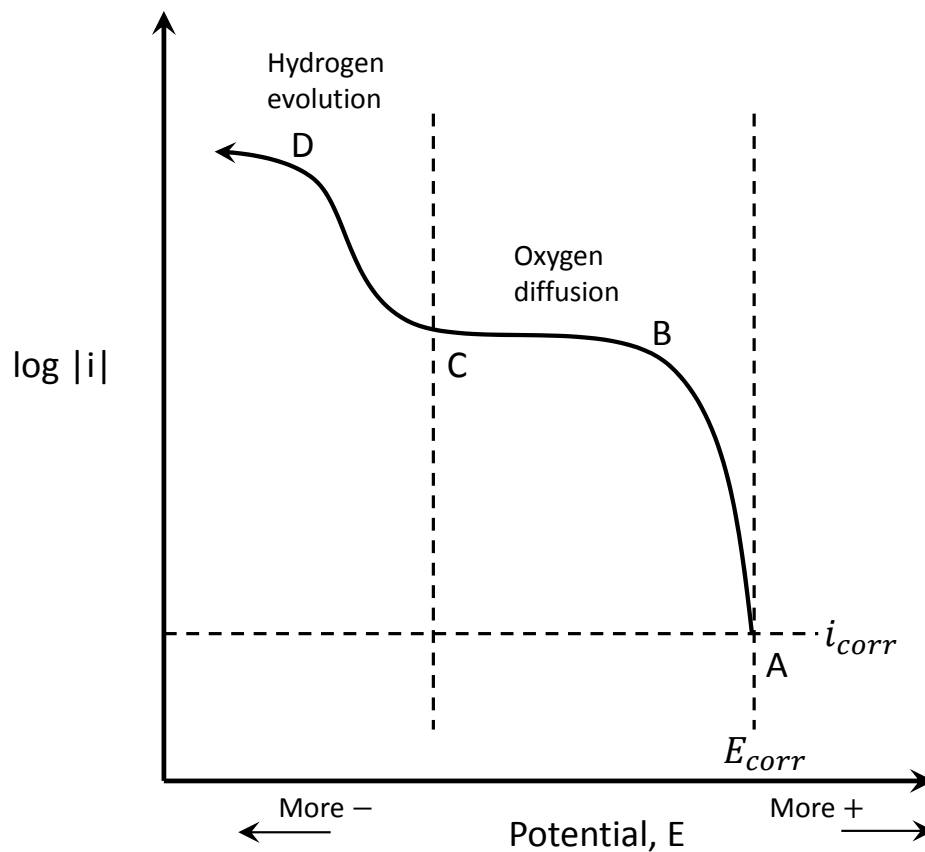


**Figure 1.17:** A schematic of Anodic Polarization curve, [McCafferty \(2010\)](#).

until it reaches the passive current density (order of few  $\mu\text{Acm}^{-2}$ ). Region CD is named as “passive region”, in which a passive oxide layer forms on the metal surface and protects it from further corrosion. For transition elements (Fe, Cr, Ni etc.) and their alloys, the thickness of this layer can reach a few hundreds ångström (Å). A sufficient increase in potential leads to the transpassive region (region DE). The sudden increase in current can be, depending upon the alloy/environment combination, due to pitting (localized breakdown of passive film) or evolution of oxygen through an electrolysis of the aqueous media.

## 1.5.2 Cathodic polarization

A displacement of the electrode potential in the negative direction making it more cathodic, is called cathodic polarization or cathodic protection. A schematic cathodic polarization curve is illustrated in figure 1.18. It starts from A and ends at D in negative direction of potential. Open circuit potential is located at point A. A decrease in potential increases the current until B. Depending upon the pH and dissolved oxygen content,

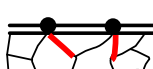
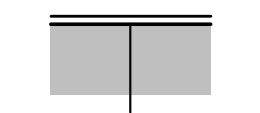
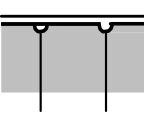
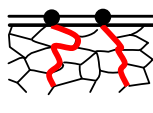


**Figure 1.18:** A schematic of Cathodic Polarization curve.

region BC may represent the reduction of oxygen (as described in section 1.4). Since the reaction rate is controlled by oxygen diffusion, it cannot increase indefinitely. Instead, the current reaches a limiting value, which is a function of the oxygen concentration and its diffusivity. For sufficiently negative potentials, another cathodic reaction comes into picture as illustrated by region CD. This reaction is due to the reduction of other species, typically an evolution of hydrogen ( $H_2$ ) from water reduction. As the potential increases, this reaction becomes dominant. The ingress of hydrogen into the metal is known to enhance fatigue crack growth by the mechanism called “hydrogen embrittlement”.

## 1.6 Damage mechanisms

In general, an active environment reacts with the metal surface and initiates damage. [Schneider \(1983\)](#) represented a schematic of corrosion fatigue damage process depending upon the initial state of the surface, figure 1.19. Damage involves the following stages:

| Initial state      | Active  | Passive   | Passive  | Passive   |
|--------------------|---|---|--|---|
| Initial state      |  |  |  |  |
| Crack Nucleation   |  |  |  |  |
| Intermediate stage |  |  |  |  |
| Crack Initiation   |  |  |  |  |
| Crack Propagation  |  |  |  |  |

**Figure 1.19:** Schematic of modes of corrosion fatigue damage, [Schneider \(1983\)](#).

- *Environmental Attack.* Localized corrosion reaction (oxidation of metal surface) leading to formation of pits which serve as crack nucleation sites.
- *Crack Initiation.* Initiation of cracks from surface pits or localized corrosion on susceptible slip bands or grain boundary precipitates (Inter-granular or Trans-granular SCC).
- *Crack Propagation.* Propagation of cracks assisted by environment through dissolution based mechanisms, or adsorption based mechanisms, or “hydrogen embrittlement”.
- *Sudden Fracture.* Unstable propagation leading to final fracture.

### 1.6.1 Crack initiation

Depending upon the initial state of the surface, different initiation mechanisms can occur. It is known that slip bands, twins, grain boundaries and constituent particles are classical sites. For active metal surfaces, it can occur from localized dissolution of metal (pitting), dealloying or intergranular corrosion (associated with anodic grain boundary precipitates)

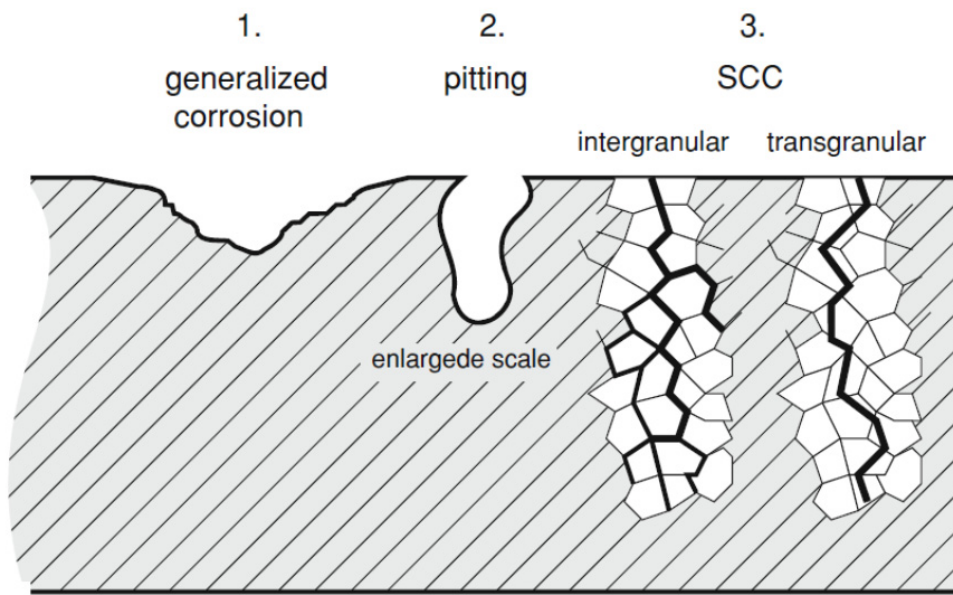


**Figure 1.20:** Schematic of modes of corrosion fatigue crack initiation on active metal surface, [Milella \(2013\)](#).

as illustrated in figure 1.20. For passive interface, it is the cleavage of passive film followed by active surface initiation. It is also possible that crack initiates as in air (discussed in part A of this chapter), without any influence of corrosion because the frequency of loading or the threshold for SCC could be high.

## Persistent slip bands

The persistent slip bands (PSBs) have been observed to react with the corrosive medium. The presence of mobile dislocations enhances the electrochemical reactions. Consequently, the PSBs are anodic compared to the undeformed material and are preferentially dissolved, which enhances local plastic deformation, and thus contributes to crack initiation. Corrosive environment has been shown to increase the number of PSBs and reduce their inter-spacing distribution ([Gangloff and Duquette, 1987](#)) which can affect crack initiation.

## Grain boundary precipitation

Cracks have also been observed to initiate from precipitates at grain boundaries, making it susceptible to inter-granular SCC ([Strauss et al., 1930](#)). This phenomenon is also known

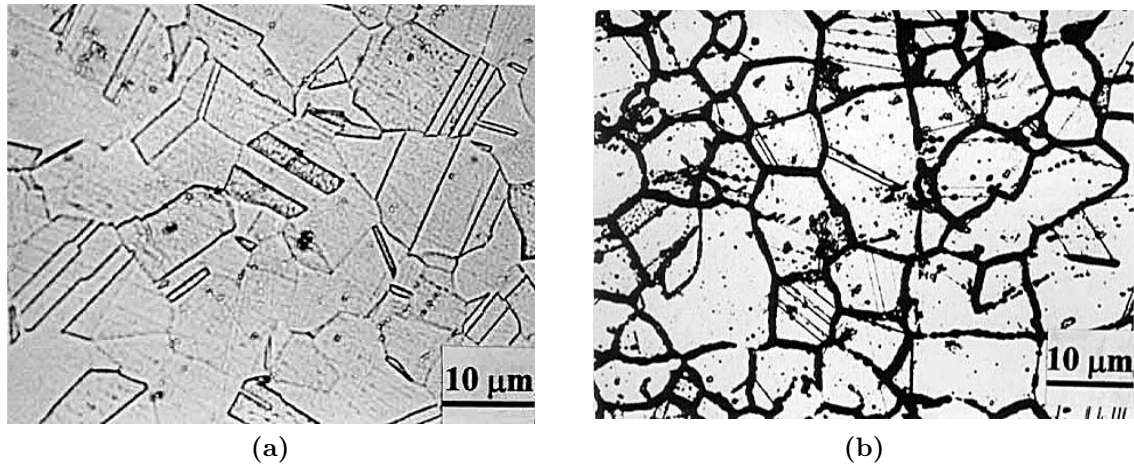


**Figure 1.21:** (a) Unsensitized 304 Austenitic stainless steel (b) Sensitized 304 Austenitic stainless steel after etching.<sup>a</sup>

<sup>a</sup>source: <http://www.corrosionclinic.com/types of corrosion/intergranular corrosion cracking.htm>

as *Sensitization* of materials. A typical example is offered by 304 austenitic stainless steel as illustrated in figure 1.21. The precipitation of chromium carbides consumes the alloying element from a narrow band along the grain boundary and this makes an anodic zone (illustrated by dark lines). The chromium-depleted zone becomes a preferential paths for corrosion attack or crack propagation leading to inter-granular corrosion.

## Passivity breakdown

Crack initiation for passive surfaces takes place by breakdown of passive film. Various mechanisms exist in literature to explain this phenomenon, of which the most popular and commonly observed mechanisms are:

- Film-breaking mechanism.
- Adsorption mechanism.

The film-breaking mechanism proposed by [Vetter and Strehblow \(1970\)](#) involves rupture of film giving direct access of the anions to the unprotected metal surface, figure 1.22(a). Stresses induced within the film by tensile load leads to the formation of slip bands intersecting the film and slowly damaging it. Stresses can also be induced by a change in electrode potential, resulting in sudden release of metal cations into the electrolyte (even in absence of aggressive ions).

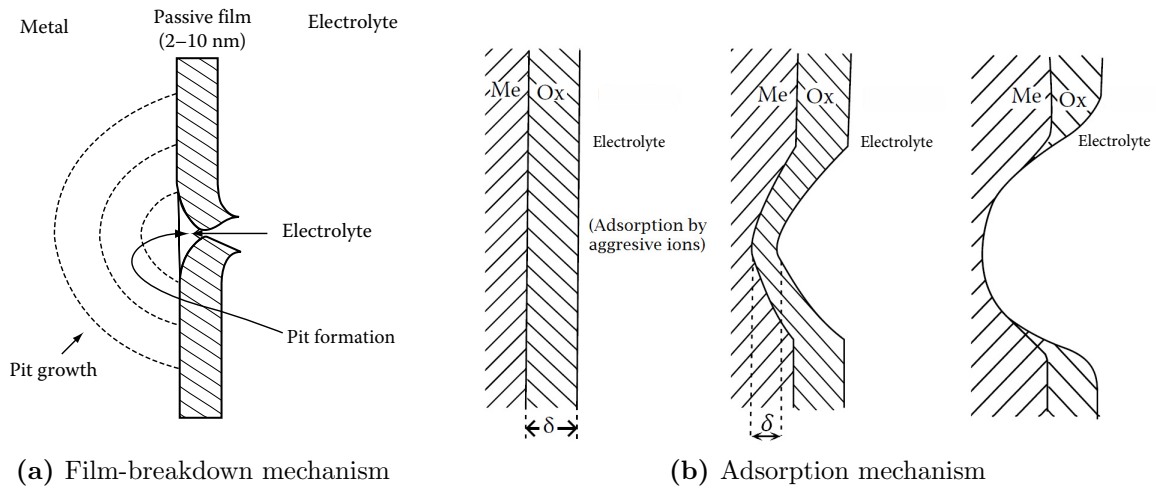


**Figure 1.22:** Schematic of passivity-breakdown mechanisms.

The adsorption mechanism proposed by [Kolotyркин \(1964\)](#) involves the adsorption of aggressive anions onto the oxide surface and subsequent dissolution of metal cations in electrolyte, figure 1.22(b). Exposure of oxide film to aggressive ions, especially the halides ( $X^-$ ) as chloride or fluoride, results in the formation of soluble metal complexes. This leads to thinning of the passive layer and finally, its removal, resulting in enhanced localized dissolution.

Both types of passivity breakdown mechanisms are followed by formation of pits which is the most commonly observed phenomenon for crack initiation in corrosion fatigue.

## Corrosion pitting

Corrosion pitting is an important phenomenon of crack initiation in corrosion fatigue involving nucleation of pits, their growth, pit to short crack transition, growth of short cracks in and around the pits and finally, crack growth by coalescence of small cracks. This mechanism was first proposed by [Mc Adam \(1926\)](#). For a metal electrode, there exist a critical potential below which not pitting occurs called the pitting potential ( $E_p$ ), point D in figure 1.17. This potential depends upon the concentration of aggressive ions in electrolyte.

The chloride ions have special importance in pitting corrosion because they are ubiquitous and common contaminants in various electrolyte systems and they can reduce the  $E_p$  significantly. Being a strong base with high diffusivity, chloride ions have tendency to

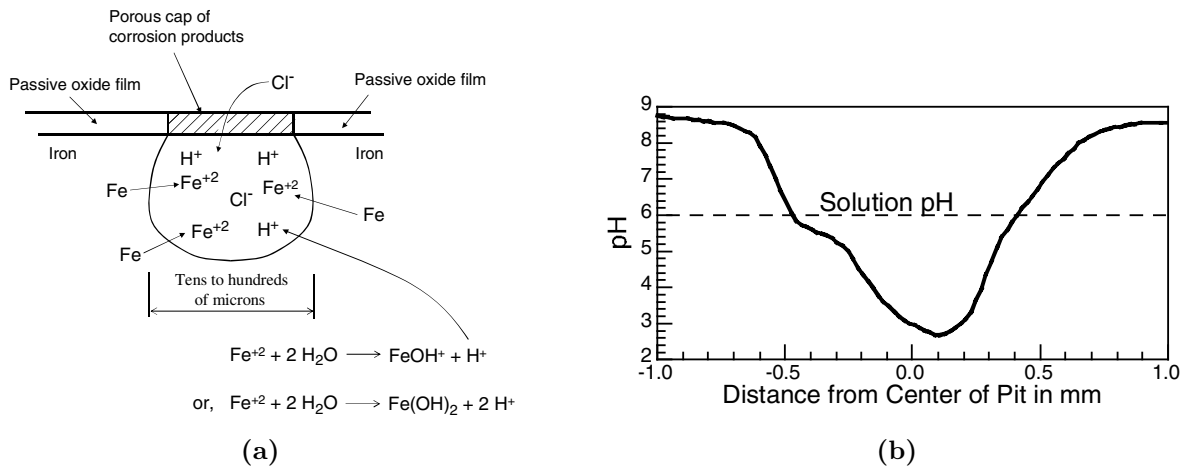


**Figure 1.23:** (a) Development mechanism for corrosion pits, [Rosenfeld \(1974\)](#) (b) Variation of pH across the pit on iron in dilute chloride solution, [Butler et al. \(1972\)](#).

dissolve metal surface and nucleate pits. Corrosion pits almost always initiate at some chemical or physical heterogeneity on the metal surface, such as inclusions, second phase particles, flaws, mechanical damage or dislocation ([Wang et al., 2003](#)). A micro-pit of only a few microns can form very quickly after immersion and then grow.

A schematic view of pit growth is illustrated in figure 1.23(a) ([Rosenfeld, 1974](#)). Nucleation of pits increases the current density because of the confinement of current to a small volume inside the pit, while nearby film remains unattacked. The hydrolysis of metal cations confined inside the pit, increases the local pH ([Butler et al., 1972](#)). The variation of pH across the pit for iron in dilute chloride solution is shown in figure 1.23(b). The local increase in acidity inside the pit forces the aggressive anions ( $Cl^-$ ) from the electrolyte to migrate into the pit so as to maintain neutrality of the solution. These aggressive ions are responsible for the dissolution of metal, forming metal cations. Hence, the process of metal hydrolysis repeats, making the pit grow.

The growth of pit is a time dependent process and its growth law can be expressed as:  $c \propto t^b$ , where ‘c’ is the pit size, ‘t’ is time and ‘b’ is constant depending upon material and environment. The pit grows until it reaches a critical size and then a transition occurs: “pit-to-crack” during which short crack initiates in and around the pit, due to the local stress concentration factor. After this transition, a fracture mechanics approach is often used assuming the pit as a short crack ([Kondo, 1989](#); [Zhang et al., 2013](#); [Haddad et al., 1979](#); [Schönbauer et al., 2015](#)).

For the “pit-to-crack-growth” transition to occur, two conditions have to be satisfied: (1)

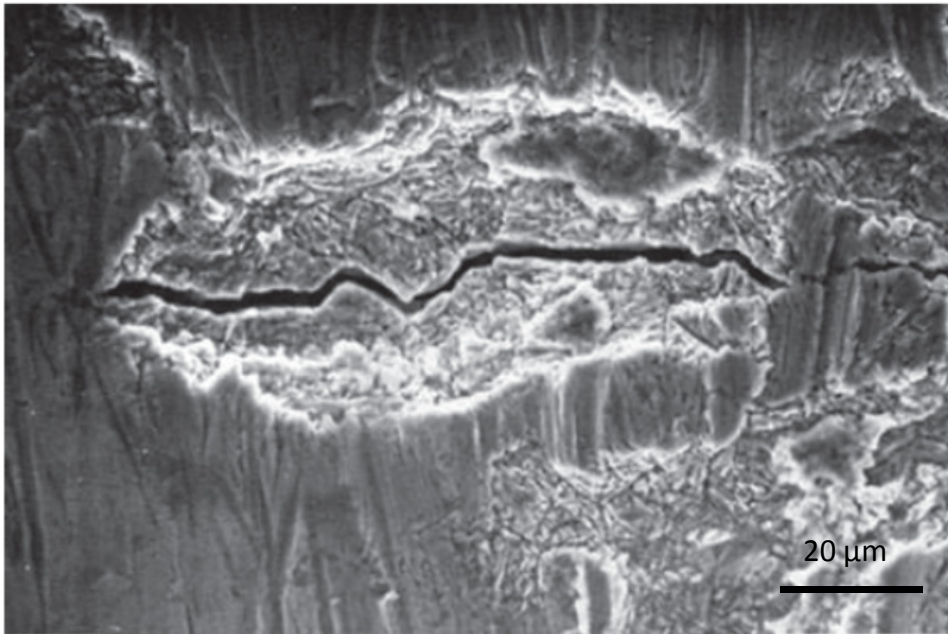


**Figure 1.24:** A typical example of crack initiating from corrosion pit, Lynch (2012).

considering the pit as a semi-elliptical crack, the stress intensity factor has to be greater than the threshold value and (2) the fatigue crack growth rate should exceed the pit growth rate. A typical example of crack initiation from a pit is shown in figure 1.24.

## 1.6.2 Crack growth

A finite threshold stress intensity factor for stress-corrosion crack propagation under sustained load exists, denoted as  $K_{I,sc}$ . It depends upon the material, the corrosive medium, pH and temperature.

A typical growth kinetics for SCC is illustrated in figure 1.25(a) with three different regimes. In regime I,  $da/dt$  sharply increases with  $K_I$  and is controlled by the creation of fresh, unpassivated metallic surfaces. In regime II,  $da/dt$  is controlled by movement of ions towards the crack tip and is independent of  $K_I$ . In regime III,  $K_I$  gets closer to the fracture toughness,  $K_{I,c}$  and the crack growth rate increases rapidly due to mechanically induced ductile or brittle fracture.

Under cyclic loading, depending upon the relative values of  $K_{I,sc}$  and  $\Delta K_{I,threshold}$ , the whole crack growth kinetics curve is shifted upward (figure 1.25(b)) or just the part for which  $K_{I,max} > K_{I,sc}$  (figure 1.25(c)).

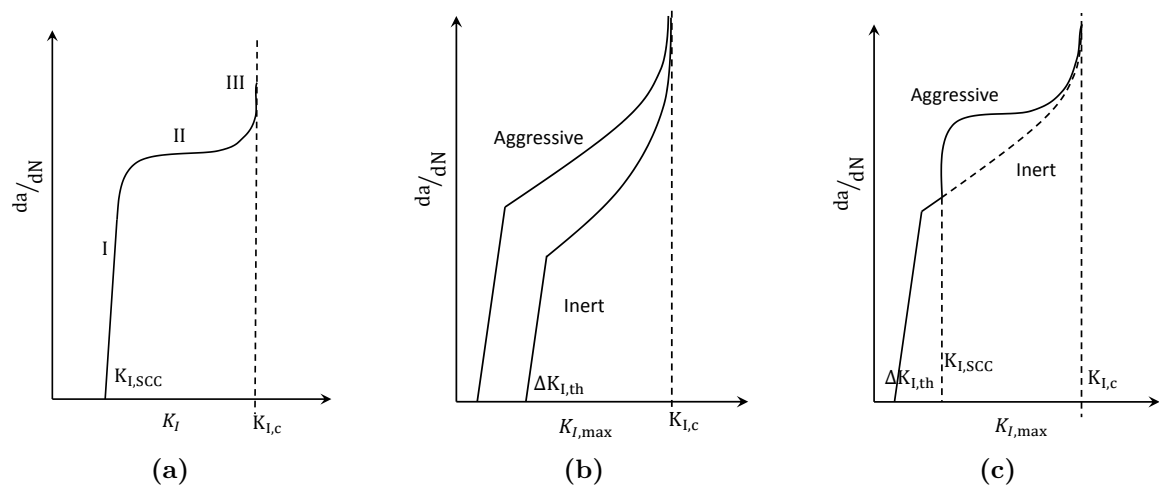


**Figure 1.25:** A typical crack growth kinetics for (a) Stress corrosion cracking (b) True corrosion fatigue (c) Stress corrosion fatigue, modified from (Austen et al., 1976).

## 1.7 Parameters influencing corrosion-fatigue

Various parameters have been known to affect the fatigue life and therefore, the crack growth rate in corrosion by enhancing one mechanism or the other, which are discussed below.

### 1.7.1 Effect of frequency

Corrosion is a time-dependent process, so the frequency of fatigue tests is an important parameter. Any possible mechanism, dissolution-based or hydrogen-based, depends upon the exposure time of crack surface to the environment. Therefore, a dependency of fatigue crack growth rate (FCGR) and fatigue lives on the frequency is generally expected. The detrimental effect of a corrosive medium is significantly more important at lower frequencies.

Various studies have shown that the decrease in frequency increases the crack growth rate in corrosive environment (Dawson and Pelloux, 1974; Vosikovski, 1975; Barsom and Rolfe, 1977; Krishnan, 1997; Berge et al., 2009; Knop et al., 2010). This is attributed to the fact that at lower frequencies, the crack remains open for a longer duration of time, thereby, allowing more time for corrosion action.

However, for martensitic steels in de-mineralized water at 288°C, an increase in FCGR with decreasing frequency is found only until 0.1 Hz (Van Der Sluys and Emanuelson,

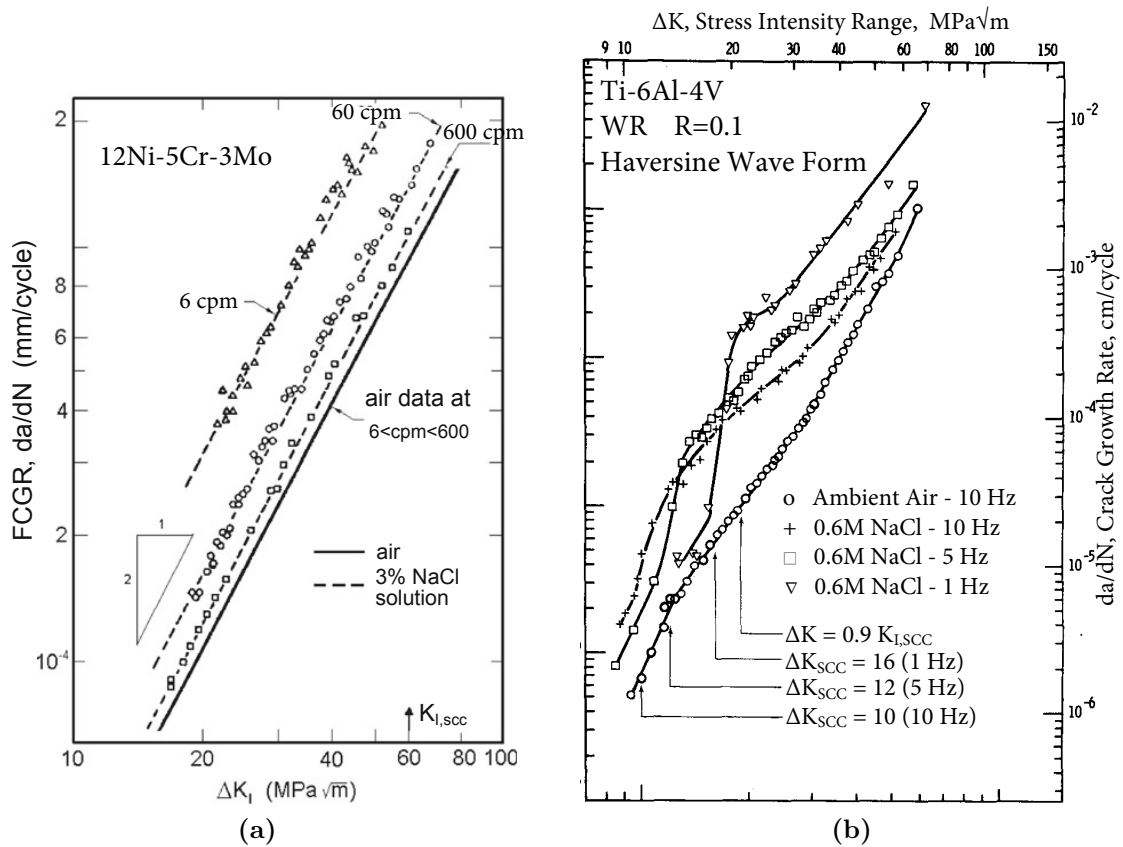


**Figure 1.26:** Effect of frequency (a) on FCGR of 12Ni-5Cr-3Mo steel, Barsom and Rolfe (1977) (b) on FCGR of Ti-6Al-4V in aqueous NaCl solution, Dawson and Pelloux (1974).

1986; Cullen, 1987). This is because at too low frequencies, enough time is provided to material to passivize, blocking any further environmental effect.

A typical example of effect of frequency on behavior of fatigue crack growth rate is shown in figure 1.26(a). The growth kinetics of NiCrMo steel in 3% NaCl solution shows a significant reduction in threshold and an increase in crack growth rate at low frequency (6 cpm = 0.1 Hz) but this effect nearly vanishes at 600 cpm (= 10 Hz). Frequency has also been found to affect the threshold value for crack growth in opposite way, in Ti alloy loaded in 3% NaCl solution, as illustrated in figure 1.26(b): the threshold value for FCGR ( $\Delta K_{th}$ ) increases with decrease in frequency (from 10 Hz to 1 Hz).

Besides, a change in frequency is not always felt instantaneously in terms of crack growth rate as illustrated in figure 1.27(a). A decrease in frequency is felt almost instantaneously through corresponding increase in crack growth rate while an increase in frequency takes some time for crack growth to decrease.

In-spite of the fact that the depreciation of fatigue lives due to corrosive environment tends

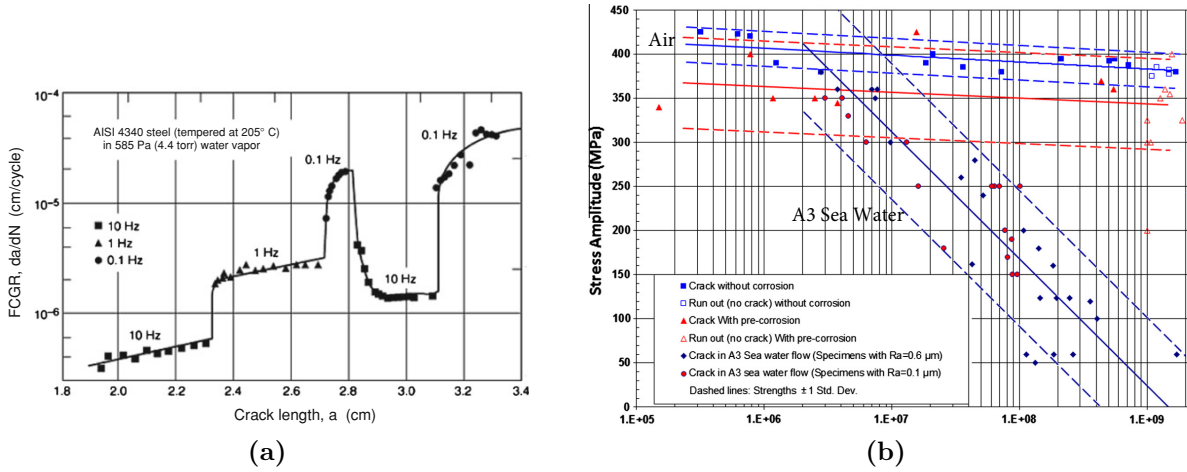


**Figure 1.27:** (a) Response of FCGR from changes in load frequency in 4340 steel in water vapours at 4.4 torr, [Achilles and Bulloch \(1986\)](#) (b) SN curves of the R5 martensitic steel under fully reversed tension at 20 kHz, [Pérez-Mora et al. \(2015\)](#).

to vanish at higher frequencies, some studies have shown the existence of a depreciation in fatigue lives at higher frequencies too ([Cruz and Ericsson, 1998](#); [Pérez-Mora et al., 2015](#); [Pfennig et al., 2013](#)). A drop in fatigue lives of martensitic steel in A3 standard synthetic sea water with 24.53% NaCl solution at 20kHz frequency is illustrated in figure 1.27(b).

### 1.7.2 Effect of the R ratio

The influence of the stress ratio ( $R = \sigma_{\min}/\sigma_{\max}$ ) on fatigue crack growth is often more important than in air, and the detrimental effect of a corrosive environment on fatigue lives is often enhanced by high R ratios ([Jones and Blackie, 1989](#); [Bucci, 1970](#); [Sivaprasad et al., 2006](#)) (figure 1.28(a)). In corrosive environment, an increase in mean stress promotes SCC that would not have appeared at low R ratios ([Banford et al., 1977](#)).

Figure 1.28(b) shows the superposition of fatigue and corrosion fatigue for a sinusoidal loading with a time period T.  $\Delta t$  corresponds to the time for which  $K_I > K_{I,SCC}$ . An estimate of crack growth can be made using this superposition as:

$$\frac{da}{dt} = \frac{\Delta a}{T} = \frac{\Delta a}{\Delta t} + f \frac{da}{dN}_{\text{fatigue}} = \frac{1}{\Delta t} \int_t^{t+\Delta t} \frac{da}{dt}(K_I) dt + f \frac{da}{dN}_{\text{fatigue}} \quad (1.18)$$

With an increase in R ratio, the mean stress goes up which increase the time for which  $K_I > K_{I,SCC}$  i.e.  $\Delta t$ , which should increase the crack growth rate.

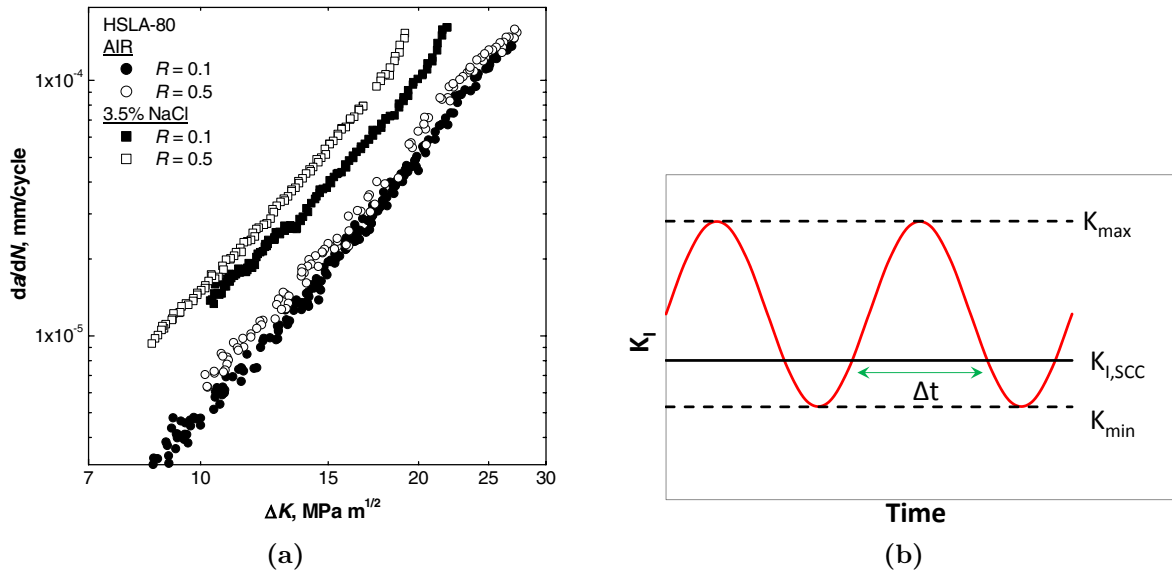


**Figure 1.28:** (a) Effect of R ratio on fatigue crack growth rate of HSLA-80 steel in air and in 3.5% NaCl solution (Sivaprasad et al., 2006) (b) An example of a sinusoidal loading depicting the superposition of fatigue and corrosion fatigue.

### 1.7.3 Effect of electrode potential

The effect of cathodic electrode potential on fatigue life has been studied widely. Uhlig and Cook (1969) found that for stainless steel in  $MgCl_2$  solution, the cathodic polarization results in increase in time to failure, with a critical potential below which no SCC occurs (figure 1.29(a)). The phenomenon has been explained on the basis of absorption and desorption of aggressive  $Cl^-$  ions above and below the critical potential. But later on, it

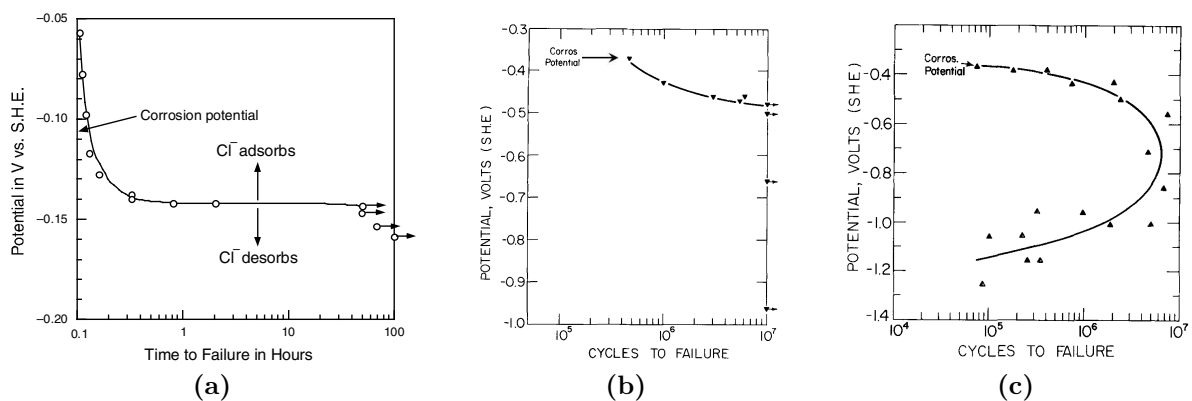


**Figure 1.29:** Effect of electrode potential on corrosion fatigue (a) 304 Stainless steel in  $MgCl_2$  (Uhlig and Cook, 1969) and AISI 4140 steel in 3% NaCl solution (b)  $R_c = 20$  (c)  $R_c = 52$  (Uhlig and Lee, 1972).  $R_c$  is Rockwell Hardness.

was found that this behavior is dependent on the hardness of the metal. For mild steel or low strength steel, a critical potential has been observed (figure 1.29(b)), while for high strength steels the fatigue life increases with cathodic polarization up to a certain level above which it starts decreasing again as illustrated in figure 1.29(c) (Uhlig and Lee, 1972; Genel et al., 2002). This phenomenon can be explained by the evolution of hydrogen on metal surface at high cathodic potential, resulting in hydrogen embrittlement.

### 1.7.4 Effect of pH and $\text{Cl}^-$ ions

In general, more acidic the medium is, higher is the corrosion rate (Maruyama et al., 2011). The evolution of fatigue life of carbon steel in 3% NaCl with different pH is illustrated in figure 1.30(a). The fatigue life decreases with decrease in pH. The phenomenon is explained by the presence of a stable passive layer on metal surface in alkaline medium, which hinders the interaction between metal surface and environment. For crack propagation, global pH may not be very significant since a local development of acidity near the crack tip has been observed (Butler et al., 1972).

$\text{Cl}^-$  ions, being aggressive in nature, are one of the important species from corrosion fatigue point of view. An increase in its concentration leads to significant depreciation in fatigue life as illustrated in figure 1.30(b) (Sedriks, 1979; Ebara, 2010). The concentration

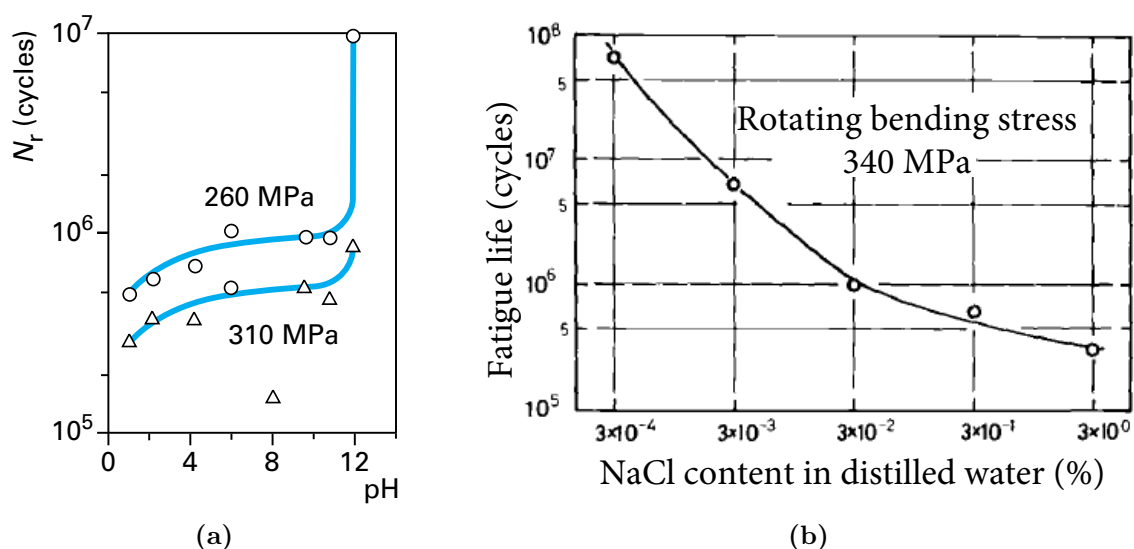


**Figure 1.30:** (a) Effect of pH on fatigue life of steels under aerated 3% NaCl solution (Duquette and Uhlig, 1969) (b) Effect of  $\text{Cl}^-$  on fatigue life of 13% Cr steel in NaCl environment (Ebara et al., 1978).

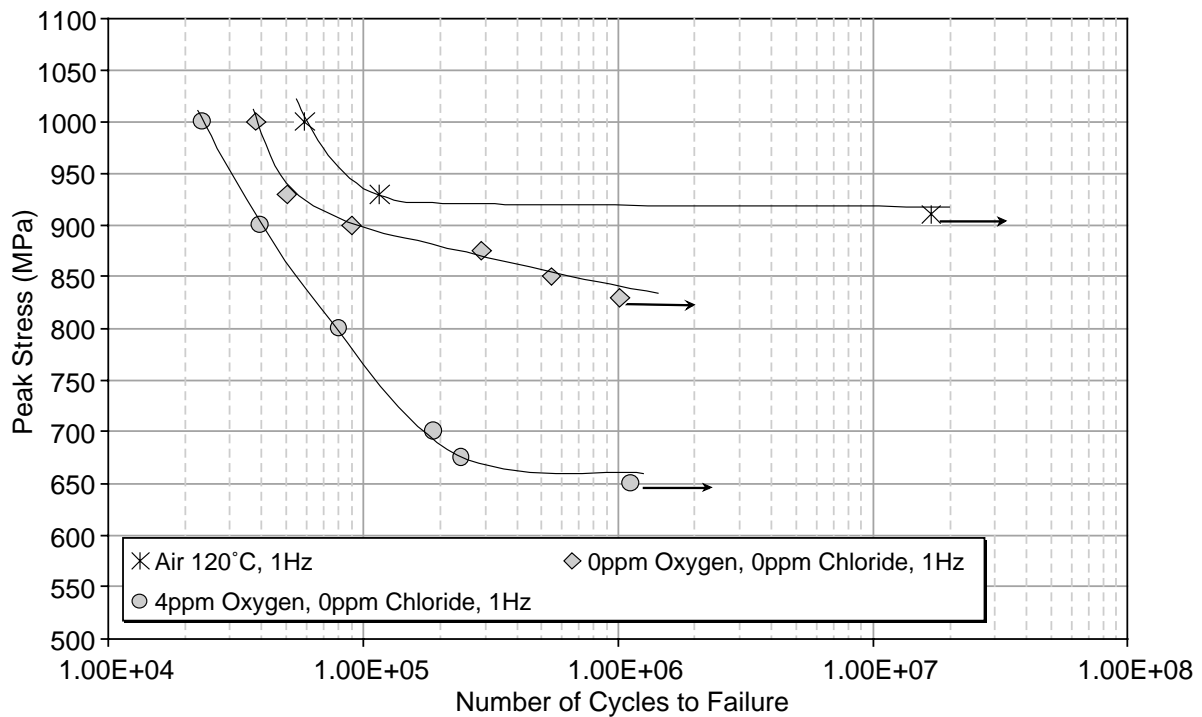


**Figure 1.31:** Effect of oxygen content on fatigue life of 12% Cr steel in de-ionised water, Perkins and Bache (2005).

of  $\text{Cl}^-$  ions accelerates crack propagation by dissolution or adsorption-based mechanisms.

### 1.7.5 Effect of dissolved $\text{O}_2$

An increase in concentration of  $\text{O}_2$  in the electrolyte enhances the SCC and thereby reduces the fatigue life as illustrated in figure 1.31 (Uhlig and Lee, 1972; Perkins and Bache, 2005; Schönbauer and Stanzl-Tschegg, 2013). The evolution of oxygen enhances the rate of cathodic reduction reactions, thereby producing more hydroxyl ( $\text{OH}^-$ ) ions. These ions are aggressive and increase the crack propagation rate by a dissolution-based mechanism. It often results in a local increase in pH because of production of  $\text{H}^+$  ions, which further enhances the dissolution process. Higher oxygen content has been found to lead to transgranular crack initiation (Perkins and Bache, 2005).

### 1.7.6 Effect of hydrogen

Many materials have been shown to exhibit cracking associated with a diffusion of hydrogen into the metal lattice resulting in a loss of ductility. This phenomenon has been

named as *Hydrogen embrittlement*, even though this term does not always reflect the real micromechanisms. Damaging effects of hydrogen was first reported by Johnson (1874-75) and since then, efforts have been made to understand this phenomenon.

Attempts have been by some researchers to model hydrogen-induced crack growth in finite elements (Krom et al., 1997; Bjerken and Ståhle, 2008; Olden et al., 2012). Two most popular hydrogen induced damaged mechanisms are:

*Hydrogen-enhanced decohesion mechanism.* Pfeil (1926) was probably the first one to demonstrate the decohesion phenomenon due to diffusion of hydrogen. A simple schematic for hydrogen cracking based on its diffusion is illustrated in figure 1.32. Hydrogen diffuses into the region with high hydrostatic stress ahead of crack tip. The accumulation of hydrogen nucleates micro-cracks because of local weakening of inter-atomic bonds and the process repeats, leading to discontinuous cracking in preference to slip. The small atomic size of hydrogen facilitates its solubility and diffusion in materials. Lufrano et al. (1996) proposed a thermodynamic formulation for hydrogen diffusion flux ( $J_H$ ) as a function of hydrostatic stress:

$$J_H = -\frac{DC}{RT} \nabla \mu \quad (1.19)$$

$$\mu = \mu_0 + RT \log_e C - \frac{\sigma_{kk} \bar{V}_H}{3} \quad (1.20)$$

$$C(\sigma) = C_0 \exp \left[ \frac{\sigma_{kk} \bar{V}_H}{RT} \right] \quad (1.21)$$

$\sigma_{kk}$  is the trace of stress tensor,  $\mu$  is the chemical potential of hydrogen in metal,  $\bar{V}_H$  is partial molar volume of hydrogen,  $C$  is the equilibrium concentration,  $R$  is gas constant,  $D$  is diffusivity and  $T$  is temperature. This type of mechanism mainly requires

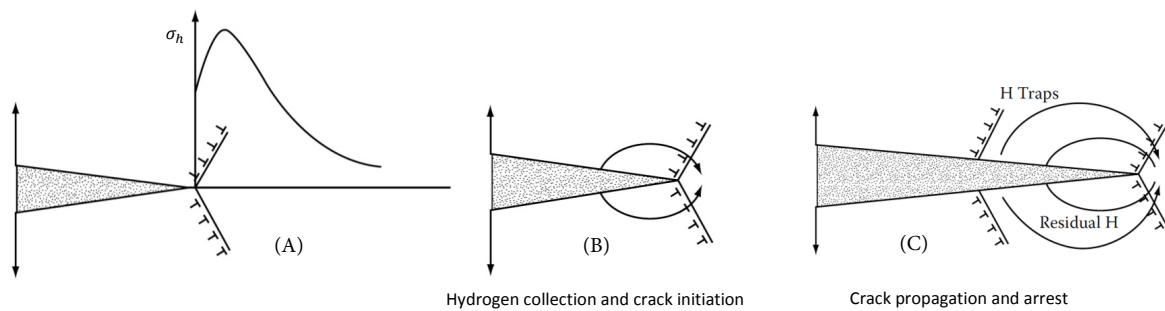


**Figure 1.32:** Schematic illustration of Hydrogen Assisted Cracking, Magnin (1996).

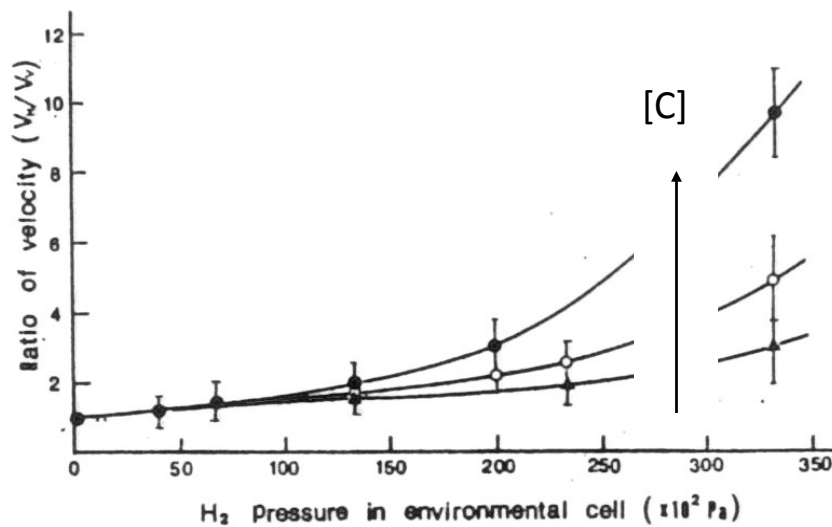


**Figure 1.33:** Direct TEM measurements of the influence of hydrogen on dislocation velocity ratio in a carbon steel (Birnbaum et al., 2000). [C] is the carbon content.

high hydrostatic stresses ahead of crack tip which facilitates hydrogen diffusion.

*Hydrogen-enhanced localized plasticity.* This mechanism was first proposed by Beachem (1972) and based on the assumption that solute hydrogen atoms facilitates dislocations movement. The localized hydrogen concentration near crack tips, due to hydrostatic stresses, leads to localized plastic deformation and crack grows by localized coalescence of micro-voids. The process is localized plastic failure rather than embrittlement, thereby softening the material in front of the crack allowing ductile fracture. Birnbaum et al. (2000) observed with a TEM the effect of hydrogen on dislocation velocities in a stretched thin foil of carbon steel with different carbon (C) content, as shown in figure 1.33. The introduction of hydrogen enhanced the dislocations mobility and the increase in mobility rose with the increase in carbon content.

## 1.8 Effect of biaxial tension in corrosive medium

Nearly all the corrosion-fatigue studies that have been discussed so far, were done under uniaxial loading and only handful of corrosion fatigue investigation has been carried out to the author's best knowledge (Misak et al., 2013, 2014; Perel et al., 2015). These studies investigated the effect of cyclic biaxial tension ( $B = 0, 1$  and  $1.5$ ) on the crack growth rate in 2024-T3, 7075-T6 and 5083-H116 aluminum alloys in salt water in high-cycle fatigue

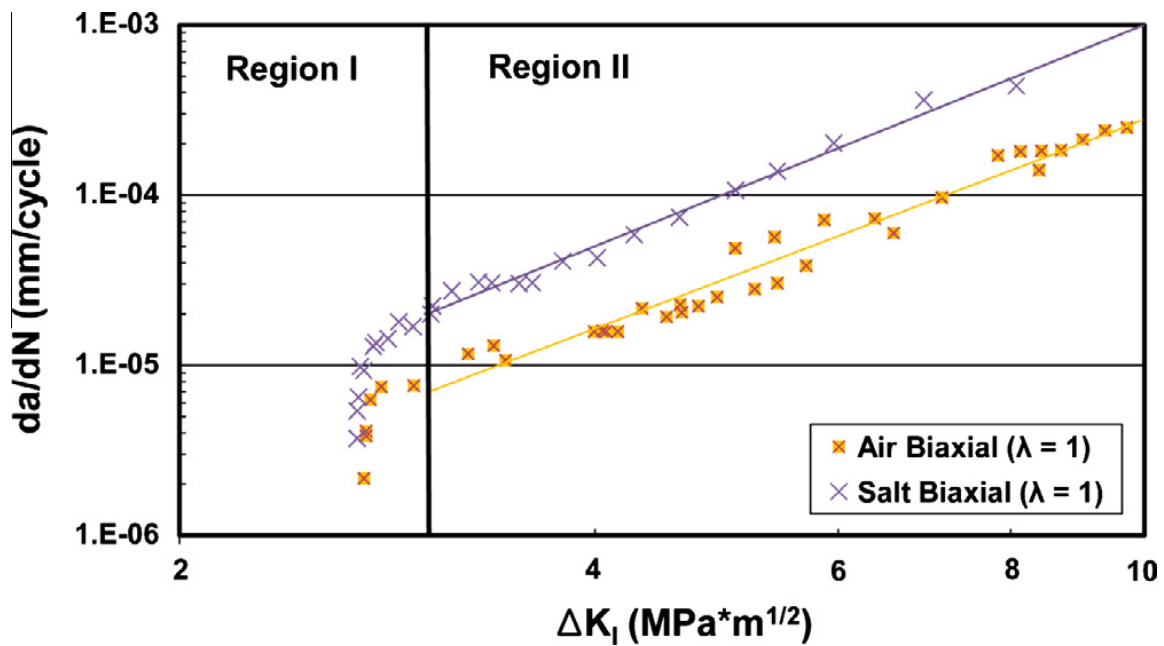


**Figure 1.34:** Effect of equibiaxial tension on crack growth rate in 7075-T6 aluminum alloys, in air and in salt water (Misak et al., 2013).

regime.

An enhanced detrimental effect of equibiaxial tension was observed in the Paris regime for 7075-T6 alloy but nearly no effect in the near threshold regime (figure 1.34) while for 2024-T3 alloy, a detrimental effect of load biaxiality was observed in the near threshold regime only (Misak et al., 2013, 2014). Perel et al. (2015) also reported a detrimental effect of load biaxiality on crack growth rates in 5083-H116 aluminum alloy.

The influence of load biaxiality on corrosion fatigue crack growth seems thus very dependent on the material and has not been investigated in steels so far and it could be different. One of the objectives of this thesis is to investigate these effects in steels.

---

## Part C: Synthesis and open questions

There are different crack initiation mechanisms in fatigue and crack initiation is considered to be the most significant part of the fatigue life in high cycle fatigue regime. But, there are still some questions about this fact when crack initiation is internal, partly because of the lack of data on crack growth in vacuum.

Most of the multiaxial fatigue studies were done in uniaxial or in tension-torsion loadings. Thus, the effects of biaxial tension are not totally clear. Few recent studies have shown that the existing multiaxial fatigue criteria are not suitable under biaxial tension ([Koutiri et al., 2013](#)).

An extensive literature review has shown that biaxial tension loading can have depreciating ([Bonnand et al., 2011](#); [Joshi and Shewchuk, 1970](#); [Vansovich et al., 2015](#); [Clàudio et al., 2014](#)), beneficial ([Bellett et al., 2010](#); [Doquet and De Greef, 2012](#); [Kane and Doquet, 2006](#); [Lee and Taylor, 2011](#)) or neutral effect ([Marquis and Karjalainen-Roikonen, 2001](#); [Leevers et al., 1976](#); [Kitagawa et al., 1978](#); [Misak et al., 2014](#)) on the fatigue life and the fatigue crack growth (depending upon R ratio and loading amplitude) leading to no general perception. The effect of cyclic biaxial tension on fatigue life and damage mechanisms thus deserves an investigation.

In corrosive environment, various parameters like the frequency, R ratio, pH, dissolved O<sub>2</sub>, Cl<sup>-</sup>, electrode potential etc. have been observed to affect the fatigue life and FCGR. Most of the studies in corrosive media have been done under uniaxial loading except few ([Misak et al., 2013, 2014](#); [Perel et al., 2015](#)). These studies indicated different effects of biaxial-tension in salt water for different aluminum alloys in high-cycle fatigue regime, leading to no general idea. As a result, there is a need to explore this area.

# Chapter 2

## Material characterization

Clip connectors are made up of F22 low alloy steel whose microstructural and mechanical characterization are described in this chapter. The composition of this steel, according to ASTM A 182, is shown in table 2.1.

The ring rolling process is used to manufacture the clip connector, which is then roughly machined to the delivery dimensions. After that, it is heat-treated, which includes austenitization between 940°C and 970°C, followed by water-quenching (this producing a martensitic structure) and finally tempering at around 625°C (this leading to precipitation-induced hardening). At last, the parts are machined to the final dimensions of the clip connector.

### 2.1 Microstructural characterization

Small cubical samples (10 mm in edge size) were cut from the same areas of a clip connector (figure 2.1) as the fatigue specimens were cut, for microstructural characterizations using optical or scanning electron microscopy as well as Electron Back Scattering Diffraction (EBSD) analysis. The observations reported below refer to two different faces

| C             | Mn            | P            | S            | Si         | Cu          | Ni          | Cr          | Mo            | Al          | V           | Nb          |
|---------------|---------------|--------------|--------------|------------|-------------|-------------|-------------|---------------|-------------|-------------|-------------|
| 0.10-<br>0.15 | 0.50-<br>0.60 | Max<br>0.015 | Max<br>0.015 | Max<br>0.4 | Max<br>0.35 | Max<br>0.50 | 2.0-<br>2.5 | 0.90-<br>1.10 | Max<br>0.04 | Max<br>0.05 | Max<br>0.01 |

**Table 2.1:** Nominal composition of F22 steel (weight %), ASTM A 182 standard

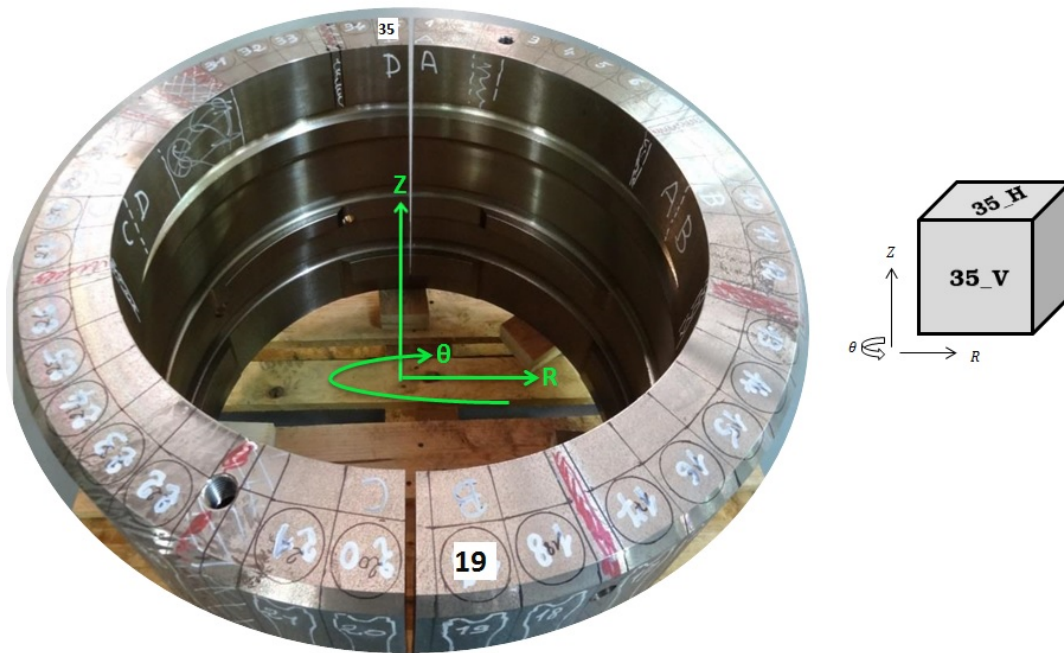


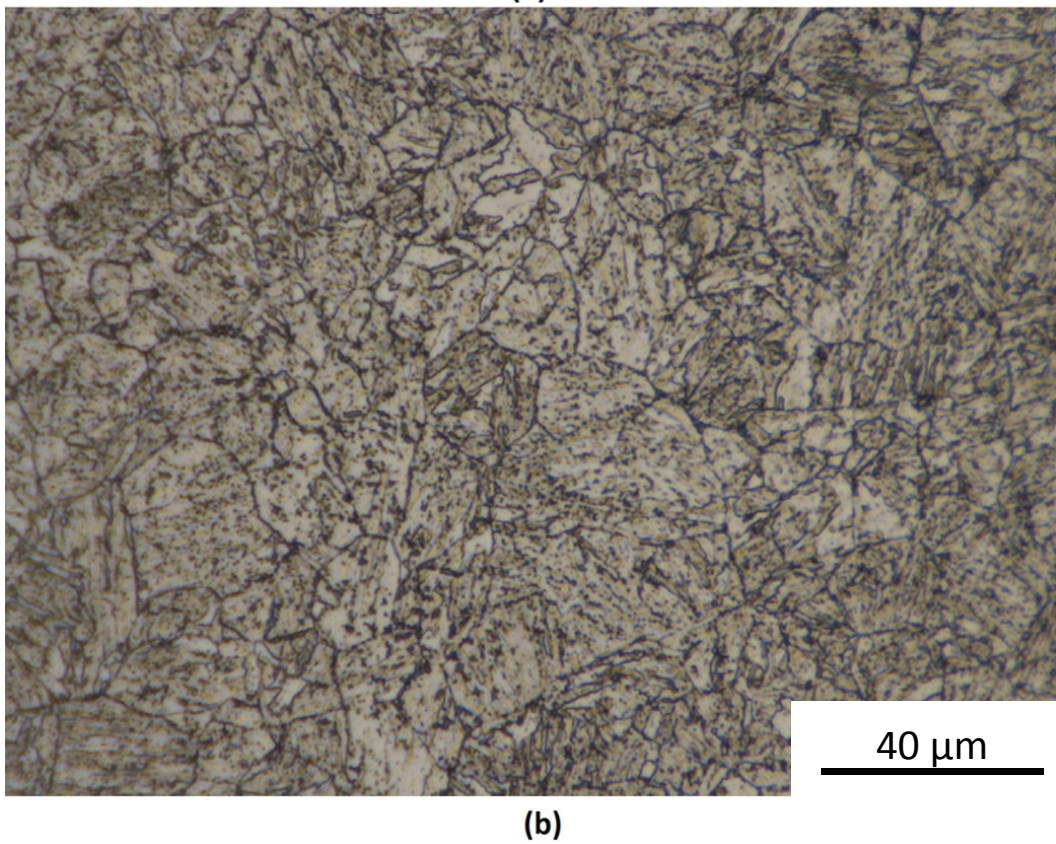
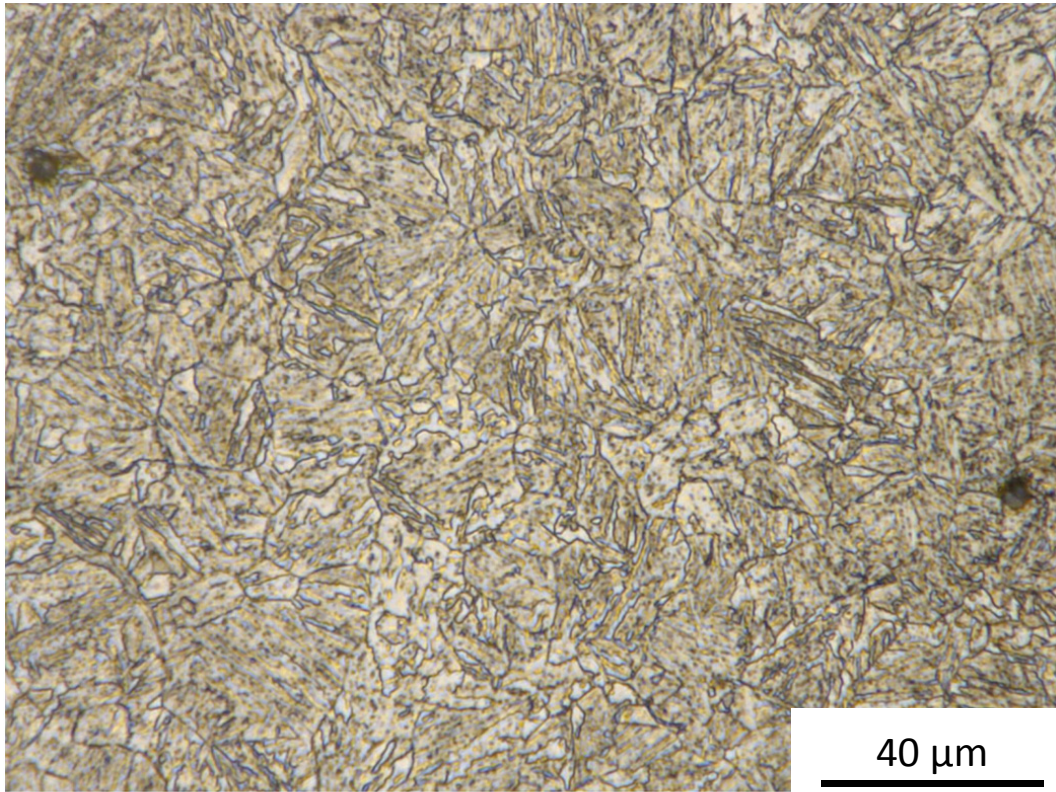
**Figure 2.1:** Sample location

(normal and parallel to the longitudinal axis of the connector) of a sample cut at a position marked as “35” in figure 2.1.

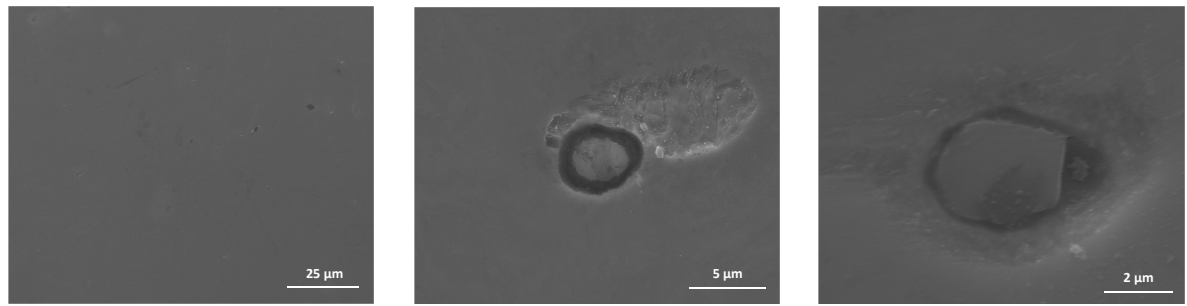
The specimens were polished down to  $3\ \mu\text{m}$  surface roughness and etched using 5% Nital solution (5% nitric acid [ $\text{HNO}_3$ ] in Ethanol [ $\text{C}_2\text{H}_5\text{OH}$ ]) for 10 seconds. The microstructural observations has been done using a KEYENCE digital optical microscope using Z500 objective lens

Figure 2.2 shows the microstructure on two surfaces, normal (35\_H in figure 2.1) and parallel (35\_V in figure 2.1) to the longitudinal axis. No significant differences in microstructure could be observed with samples cut from different positions. The microstructure is very complex with a wide variety in grain sizes. The features inside the more or less polygonal former austenite grains look like remnants of a lamellar martensite microstructure after aging. In order to estimate the grain size, the line intercepts method was adopted. The average grain size on the two surfaces and along two mutually orthogonal directions is shown in table 2.2. Former austenite grains are more or less equiaxed, with an average size of  $7.1\ \mu\text{m}$ . Inclusions with an average size of  $4.5\ \mu\text{m}$  are present.

Chemical analyses of these inclusions were done, using an Energy Dispersive Spectrum [EDS] device in the SEM, and the results are compared to the chemical composition of the matrix in figure 2.3. The spectrum of the matrix gave a global composition in



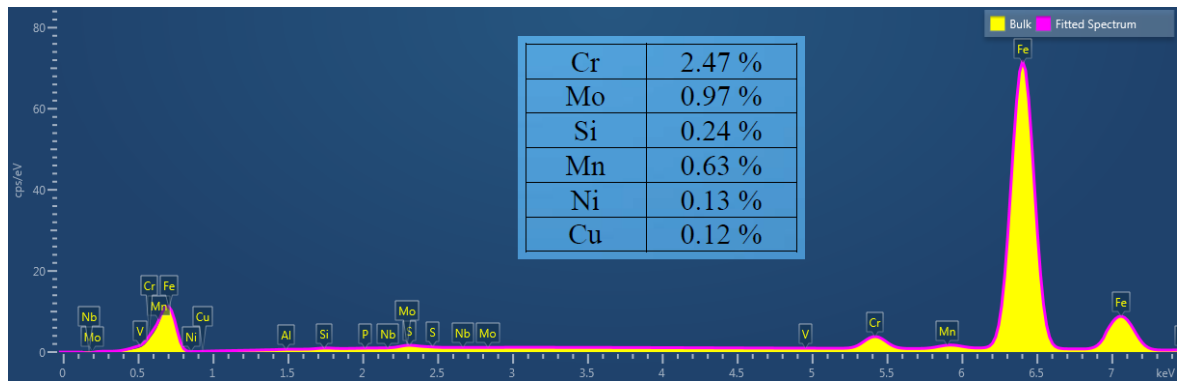
**Figure 2.2:** Optical Micrographs: (a) Normal to longitudinal axis (35\_H) (b) Parallel to longitudinal axis (35\_V)



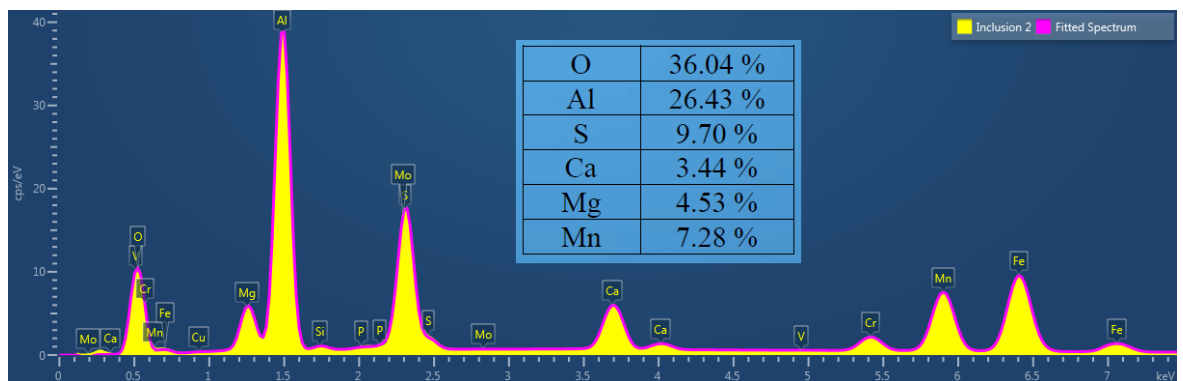
(a)

(b)

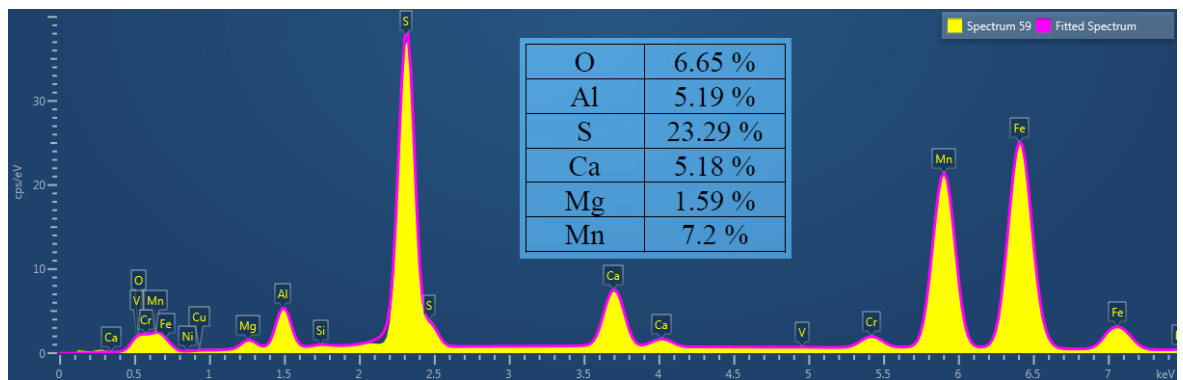
(c)



(d)



(e)



(f)

**Figure 2.3:** EDS analyses(a),(b),(c) are electron image of Bulk, type 1 inclusion and type 2 inclusion respectively and (d),(e),(f) are their respective spectrums

agreement with the ASTM standard provided in table 2.1. Two types of inclusions were found. In the first type, aluminum, calcium and magnesium contents along with oxygen were high. These metallic oxides are believed to come from the refractory furnace used for steel manufacturing. In the second type of inclusion, mostly sulphur and manganese were high. These are probably manganese sulphide particles.

Texture analysis was done using the Electron Back Scattering Diffraction technique (EBSD) (Reimer (1998); Engler and Randle (2010)). The specimen was tilted at a high angle (70°) relative to the incident electron beam and back-scattered electrons for which the Bragg condition was satisfied form diffraction patterns called Kikuchi lines, each related to a particular set of lattice planes. Knowing the crystalline structure (BCC in the present case) and the lattice parameter, the HKL software automatically deduces from these patterns the orientation of the analyzed volume relative to the macroscopic reference axes in the form of three Euler angles.

A vibratory polisher (VibroMet) and a OP-A acidic alumina suspension, (50 ml in 150 ml of water) acting as a lubricant as well as an etchant was used for 3-4 hrs to prepare specimens for EBSD analysis. The parameters chosen for EBSD mappings are shown in table 2.3. Keeping in mind the complexity of the microstructure and the small grain size, a small pitch was chosen. A  $130 \mu\text{m} \times 130 \mu\text{m}$  area (representing approximately 340 grains) in a plane normal to the connector axis (35\_H) as well as a  $100 \mu\text{m} \times 100 \mu\text{m}$  area (representing approximately 200 grains) in a plane parallel to the connector axis(35\_V) have been analyzed.

Figure 2.4 shows the band contrast and the inverse pole figures maps obtained as a result of EBSD analysis. The diffraction band contrast makes the microstructure more visible than optical microscopy. The grains do not exhibit preferential elongation in any particular direction. Pole figures (figure 2.5) represent the intensity of each orientation

| Position | $\theta$ - direction | R/Z - direction   |
|----------|----------------------|-------------------|
| 35_H     | $6.5 \mu\text{m}$    | $7.2 \mu\text{m}$ |
| 35_V     | $7.2 \mu\text{m}$    | $7.7 \mu\text{m}$ |

**Table 2.2:** Mean intercept grain size on two surfaces and along two orthogonal directions

| HV    | Spot Size | WD    | Tilt | Pitch               | Exposure |
|-------|-----------|-------|------|---------------------|----------|
| 20 kV | 4         | 17 mm | 70°  | $0.137 \mu\text{m}$ | 48.7 ms  |

**Table 2.3:** Parameters used for EBSD mappings

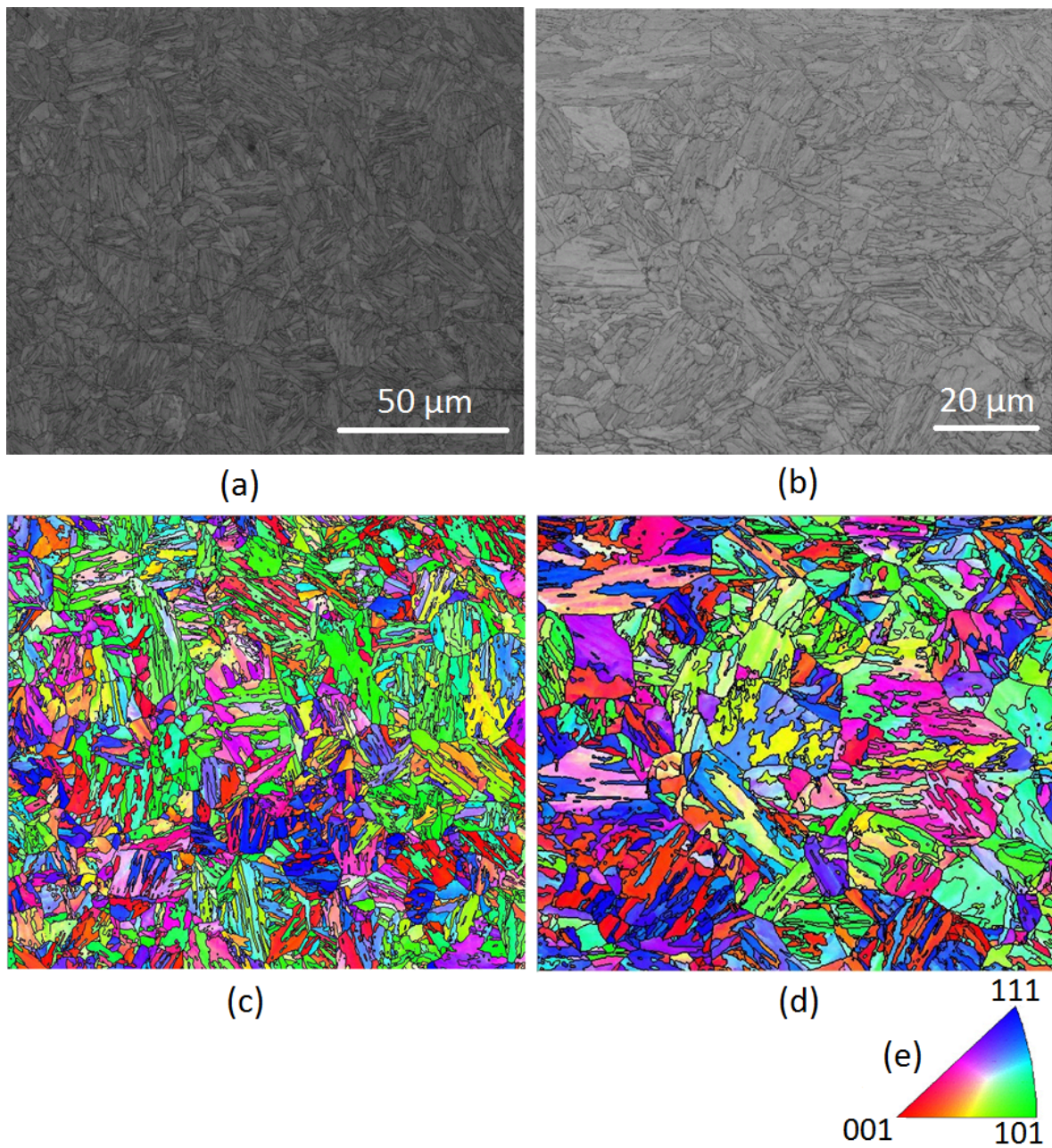


**Figure 2.4:** Band contrast image (a) normal to connector axis (35\_H) (b) Parallel to connector axis (35\_V). Inverse pole figures for surface (c) normal to connector axis (35\_H)(d) Parallel to connector axis (35\_V) (e) Color code.

in the texture relative to that of a textureless material. The maximum relative intensity is 3.48. The crystallographic texture is thus weak.

However, many special Coincidence Site Lattice (CSL) grain boundaries were present. The relation between the number of lattice points in the unit cell of a CSL and the number of lattice points in a unit cell of the generating lattice is called  $\Sigma$  (Sigma); it is

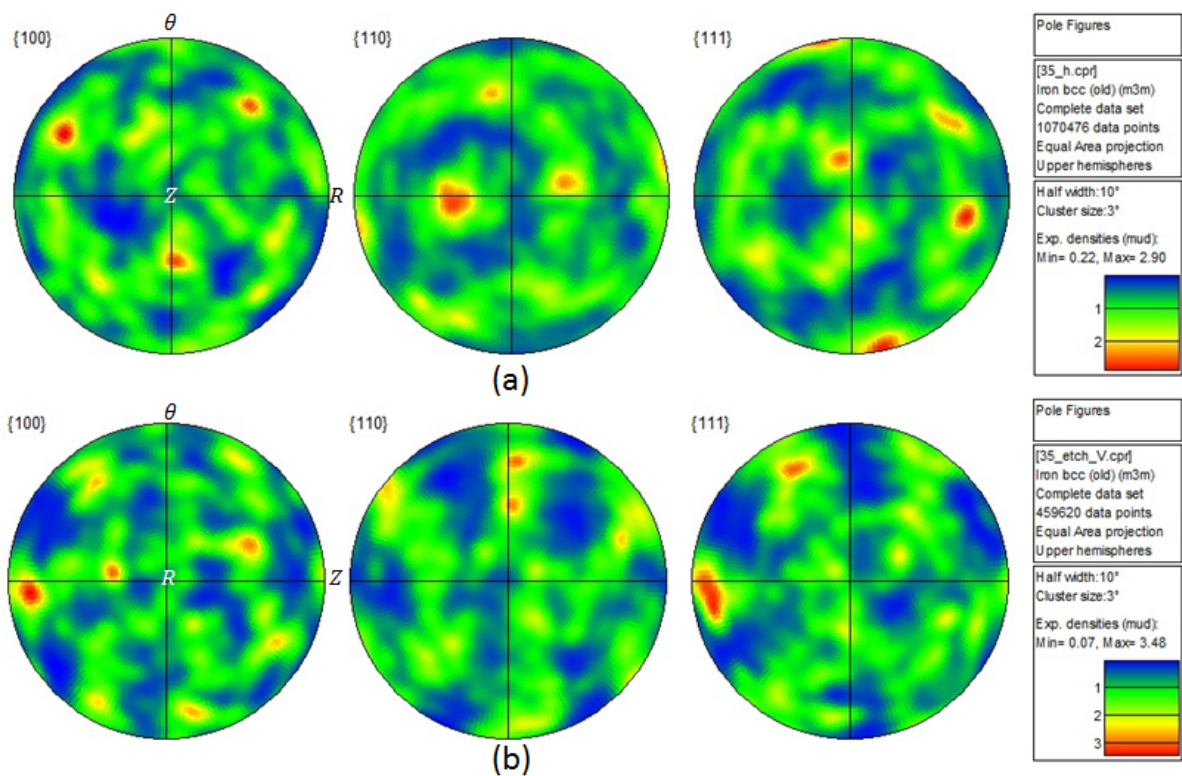


**Figure 2.5:** Pole figures obtained from EBSD mappings (a)normal to connector axis (35\_H)(b) Parallel to connector axis (35\_V)

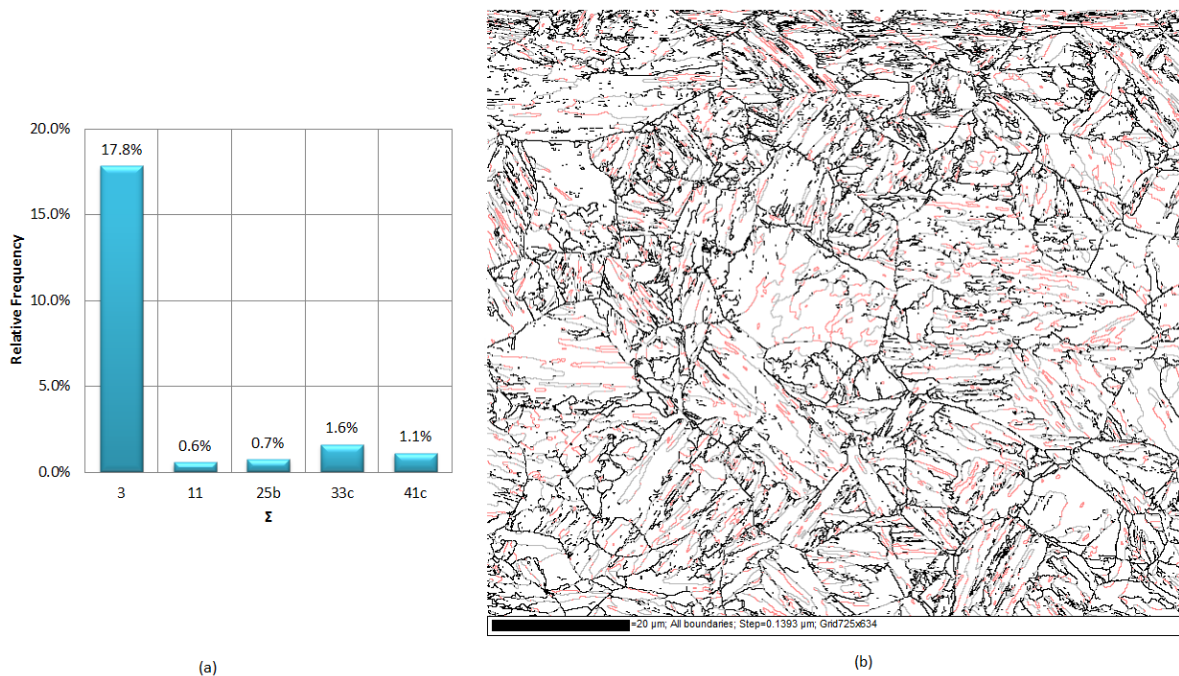


**Figure 2.6:** (a) Statistics of different  $\Sigma$  CSL boundaries (b) CSL boundaries in microstructure

the unit cell volume of the CSL in units of the unit cell volume of the elementary cells of the crystals. The relative percentage of CSL with high  $\Sigma$  values (random high energy boundaries) is lower as compared to those with low  $\Sigma$  values, figure 2.6(a). Lots of twin boundaries,  $\Sigma 3$  (18% average), have been observed. In figure 2.6(b), red lines represent  $\Sigma 3$  boundaries and grey lines represent rest of CSL boundaries with black lines as random grain boundaries.

## 2.2 Mechanical characterization

Cylindrical specimens with a gage length of 16 mm and a diameter of 8 mm were cut from the clip connector and were used to characterize the tensile and cyclic behaviour of the material. An extensometer with a full range of  $\pm 15\%$  was used. The tensile properties of F22 alloy steel identified by uniaxial test (figure 2.7) at constant strain rate,  $\dot{\epsilon} = 10^{-3}$ , are shown in table 2.4.  $E$  and  $\sigma_u$  are the Young's modulus and the ultimate tensile strength respectively.  $\nu$  is the poisson's ratio,  $\sigma_{y,0.2\%}$  is the conventional yield strength at 0.2 % offset strain,  $\sigma_p$  is the proportional limit,  $\epsilon_{neck}$  is the necking strain or uniform elongation and HV is the Vickers hardness.

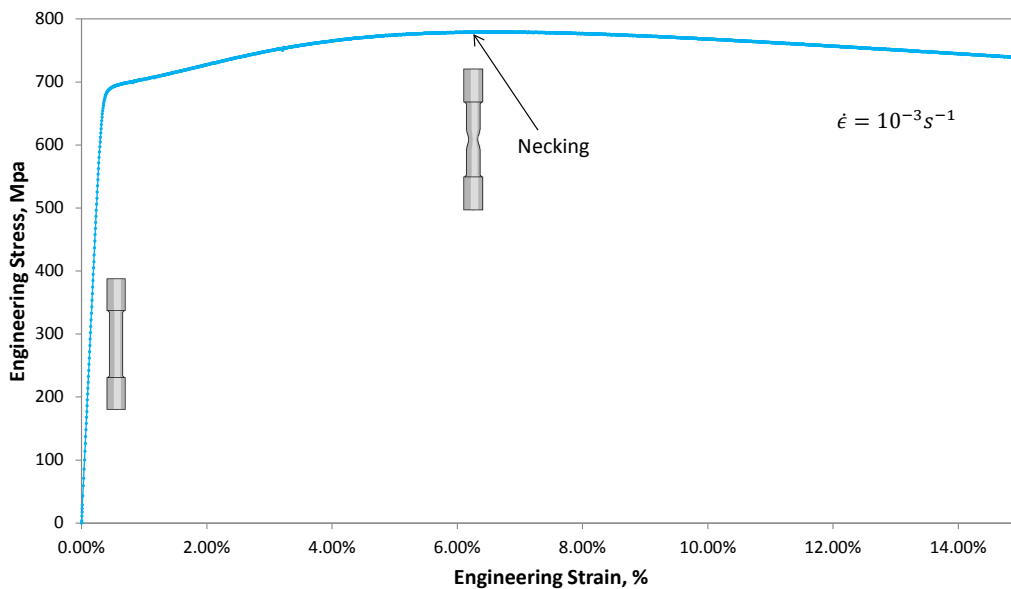


**Figure 2.7:** Engineering stress-strain curve.

| $E$ (GPa) | $\nu$ | $\sigma_p$ (MPa) | $\sigma_{y,0.2\%}$ (Mpa) | $\sigma_u$ (Mpa) | $\epsilon_{neck}$ | HV  |
|-----------|-------|------------------|--------------------------|------------------|-------------------|-----|
| 207.4     | 0.27  | 600              | 694                      | 780              | 6.7%              | 267 |

**Table 2.4:** Mechanical properties of F22 alloy steel

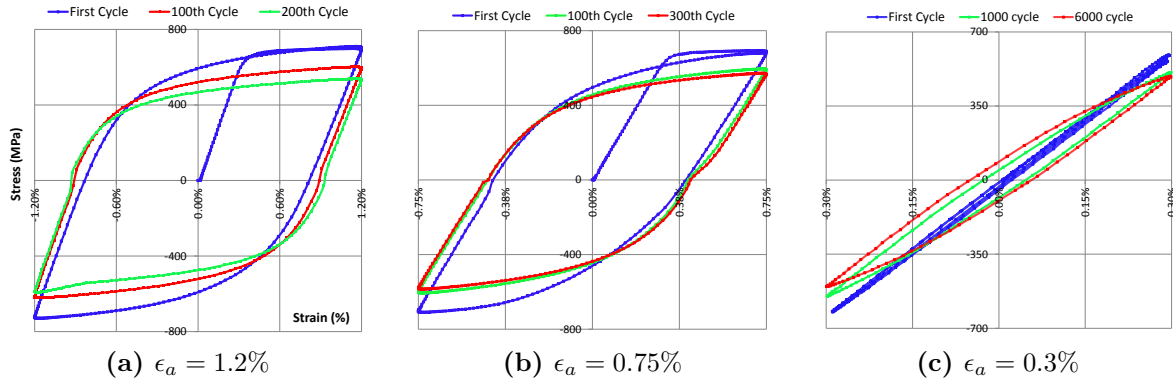


**Figure 2.8:** Stress strain loops for low-cycle fatigue tests.

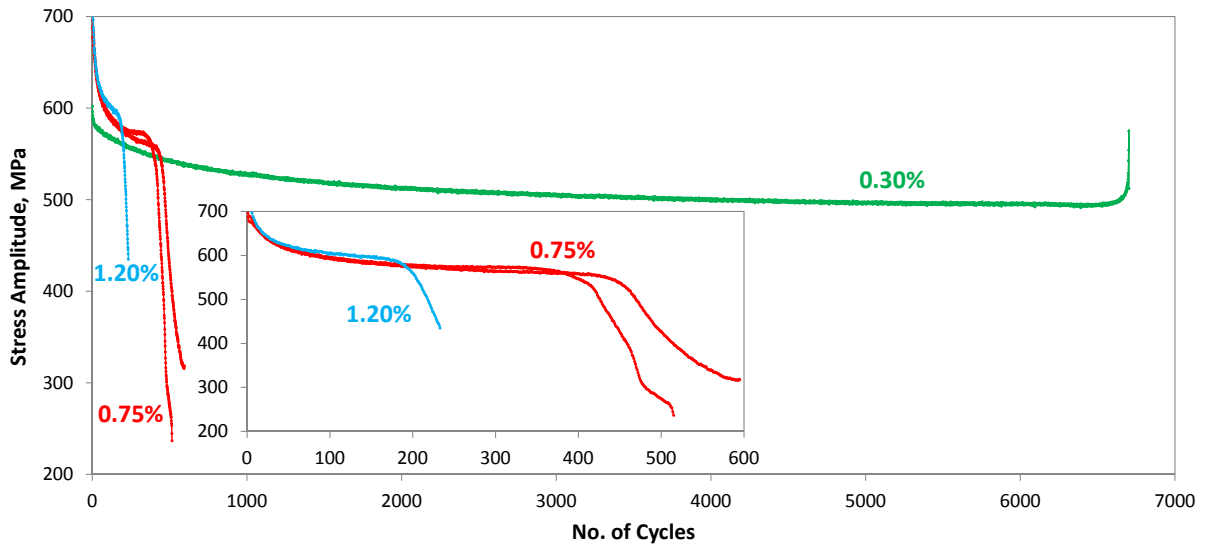


**Figure 2.9:** Evolution of Stress amplitude during low-cycle fatigue tests.

In order to model the cyclic behaviour of the material for numerical simulations on clip connectors, it was necessary to identify its constitutive equations. For that purpose, four fully reversed strain controlled tests ( $R_\epsilon = -1$ ) at constant amplitudes of  $\pm 0.3\%$ ,  $\pm 0.75\%$  (two tests) and  $\pm 1.2\%$  were run using sinusoidal wave form. A strain rate of  $\dot{\epsilon} = 10^{-3} \text{ s}^{-1}$  was chosen for all tests. In order to maintain the same strain rate at different strain amplitudes ( $\Delta\epsilon/2$ ), different loading frequencies ( $f$ ) were thus chosen so that:

$$\dot{\epsilon} = 2\Delta\epsilon f = 10^{-3} \text{ s}^{-1}$$

The stress strain loops for different strain amplitudes are shown in figure 2.8. A progressive increase in the plastic strain range was observed. At  $\pm 0.3\%$ , there was very small or no macroscopic plastic strain during the first cycle but the stress strain loop began to

---

open up as the number of cycles went on, figure 2.8(c). For the two higher strain ranges, plasticity occurred during the first ramp of loading with very limited hardening (that is very near to a perfectly plastic behavior) but during subsequent cycles, hardening became non zero. Figure 2.9 shows the variation of stress amplitude with the number of cycles. It first decreased (depicting cyclic softening of the material) and then, remained constant for most part of the fatigue life until crack growth became unstable.

There are different ways to model cyclic behavior of material, using two types of hardening variables:

- Isotropic Hardening (R)
- Kinematic Hardening (X)

Isotropic hardening accounts for a change in size of the elastic domain while kinematic hardening accounts for the displacement of the elastic domain i.e. Bauschinger effect. There are various mathematical laws in literature to model these hardening but most commonly used are the models proposed by [Voce \(1948\)](#) for isotropic hardening and by [Armstrong and Frederic \(1966\)](#) for kinematic hardening.

Isotropic Hardening:

$$R = R_0 + Q(1 - e^{-b\epsilon_p}) \quad (2.1)$$

Kinematic hardening:

$$\delta X = C\delta\epsilon_p - \gamma X\delta p \quad (2.2)$$

where  $R_0$ ,  $Q$ ,  $b$ ,  $C$  and  $\gamma$  are material constants and  $\epsilon_p$  and  $p$  are the plastic strain and accumulated plastic strain. The constant  $R_0$  represents the yield stress of the material.  $Q > 0$  denotes hardening and  $Q < 0$  denotes softening. Parameter  $b$  accounts for the rate of hardening or softening. The accumulated plastic strain is defined as:

$$\delta p = \sqrt{\frac{2}{3}\dot{\epsilon}_p : \dot{\epsilon}_p}$$

where ‘:’ represents the double inner product. For monotonic tension,  $|\dot{p}| = |\dot{\epsilon}_p|$  or  $\delta p = \delta\epsilon_p$ , which simplifies the expression of kinematic hardening to:

$$\delta X = (C - \gamma X)\delta\epsilon_p \quad (2.3)$$

| $R_0$ , MPa | $Q$ , MPa | $b$ | $C_1$ , GPa | $\gamma_1$ | $C_2$ , GPa | $\gamma_2$ |
|-------------|-----------|-----|-------------|------------|-------------|------------|
| 343.6       | -130.7    | 2.0 | 350.8       | 1140.6     | 12.5        | 32.1       |

**Table 2.5:** Coefficients of constitutive equation (one isotropic and two kinematic hardening).

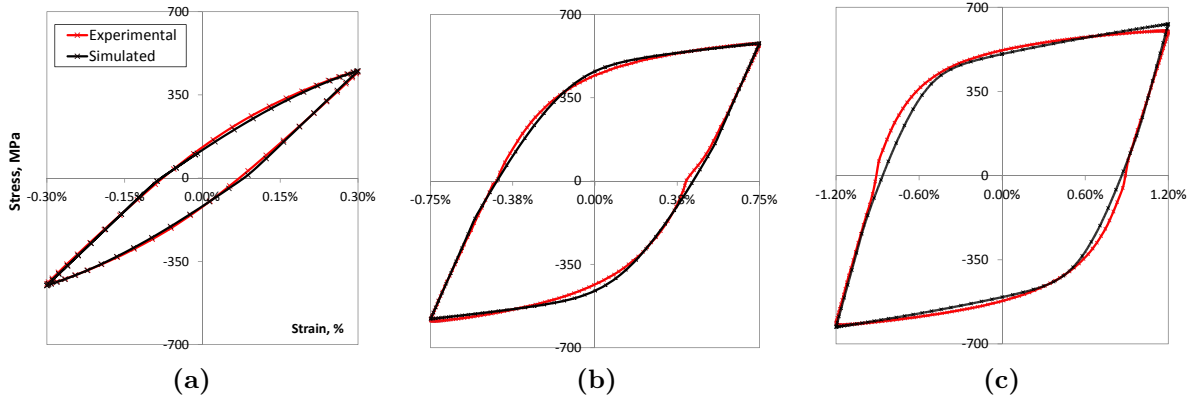


**Figure 2.10:** Stabilized stress-strain loops comparison for low-cycle fatigue tests (Strain amplitudes (a)  $\pm 0.30\%$  (b)  $\pm 0.75\%$  (c)  $\pm 1.20\%$ ) at respective half life.

which can be integrated to:

$$X = \frac{C}{\gamma}(1 - \exp(-\gamma\epsilon_p)) \quad (2.4)$$

$C/\gamma$  is the saturated value of kinematic hardening. The yield criterion, in which Von Mises criterion can be used if the plastic behavior is isotropic, can be written as:

$$f(\sigma - X) - R = 0 \quad (2.5)$$

Von Mises:

$$f(\sigma - X) = \sqrt{\frac{3}{2}(\sigma - X)^D : (\sigma - X)^D}$$

where the superscript ‘D’ denotes the deviatoric part of the stress tensor. Sometimes more than one kinematic or isotropic hardening parameters may be required to model the material behavior. The constants defined in equation 2.1 and in equation 2.3 have to be identified using experimental stress strain loops. The Z-set code, ZéBulon, was used with Levenberg optimization technique (Levenberg (1944); Moré (1977)) in order to optimize the variables. In present work, one isotropic hardening variable and two kinematic hardening variables were used. The coefficients of constitutive equations so obtained after optimization are tabulated in table 2.5. Figure 2.10 shows the comparison of quasi-static experimental and simulated stress-strain loop at half life. This constitutive

| Stress at half life (MPa)              | $\pm 0.30\%$ | $\pm 0.75\%$ | $\pm 1.20\%$ |
|--|--------------|--------------|--------------|
| Experimental ( $\sigma_{\text{exp}}$ ) | 504          | 574          | 567          |
| Predicted ( $\sigma_{\text{sim}}$ )    | 451          | 578          | 578          |
| Error (%)                              | -10.5%       | +0.7%        | +1.9%        |

**Table 2.6:** Predicted and measured stress amplitude at mid lives for LCF tests using 1 isotropic and 2 kinematic hardening variables.

| $\Delta\epsilon/2$ (%) | $R_\epsilon$ | $\dot{\epsilon}$ | $f$ (Hz) | $N_f$ |
|------------------------|--------------|------------------|----------|-------|
| 0.30                   | -1           | $10^{-3}$        | 0.0833   | 6701  |
| 0.75                   | -1           | $10^{-3}$        | 0.0333   | 515   |
| 1.20                   | -1           | $10^{-3}$        | 0.0208   | 233   |

**Table 2.7:** Low cycle fatigue tests data.  $N_f$  is the number of cycles to failure.

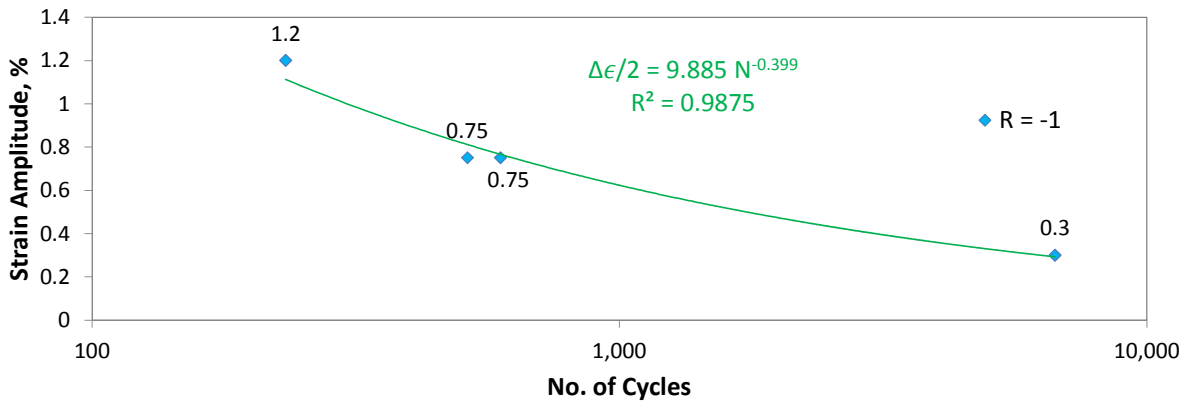


**Figure 2.11:** Coffin-Manson Curve.

equation was used to do finite element analyses of clip connectors. For high-cycle fatigue life prediction, the most important parameter is the steady state stress range (stress range at half life). So, large number of cycles under different strain amplitudes i.e.  $\pm 0.30\%$ ,  $\pm 0.75\%$  &  $\pm 1.20\%$  were simulated, and a comparison of measured and predicted steady state stress amplitudes is shown in table 2.6. The stress range is underestimated by 10.5% for the test with the lowest strain amplitude,  $\pm 0.30\%$ , while for the two higher strain ranges, the error is within acceptable limits.

These strain-controlled fatigue tests were continued until fracture and the corresponding fatigue lives are reported in table 2.7 in which the stress amplitudes correspond to the values measured at mid-life. The Coffin-Manson curve is shown in figure 2.11 and follows

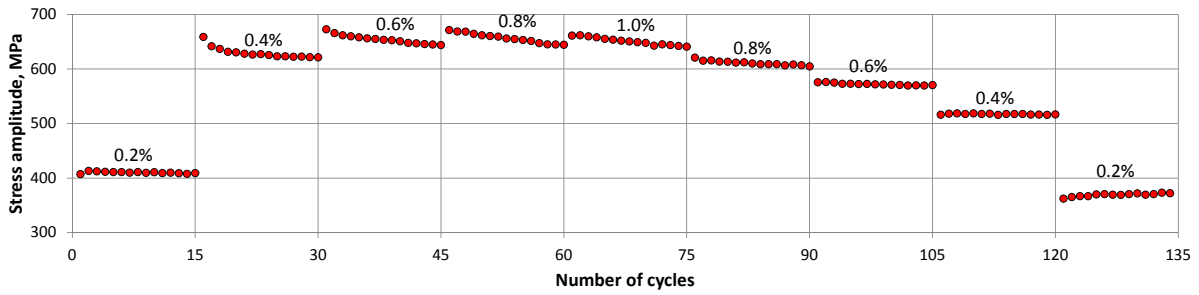


**Figure 2.12:** Evolution of stress amplitude for variable amplitude test.

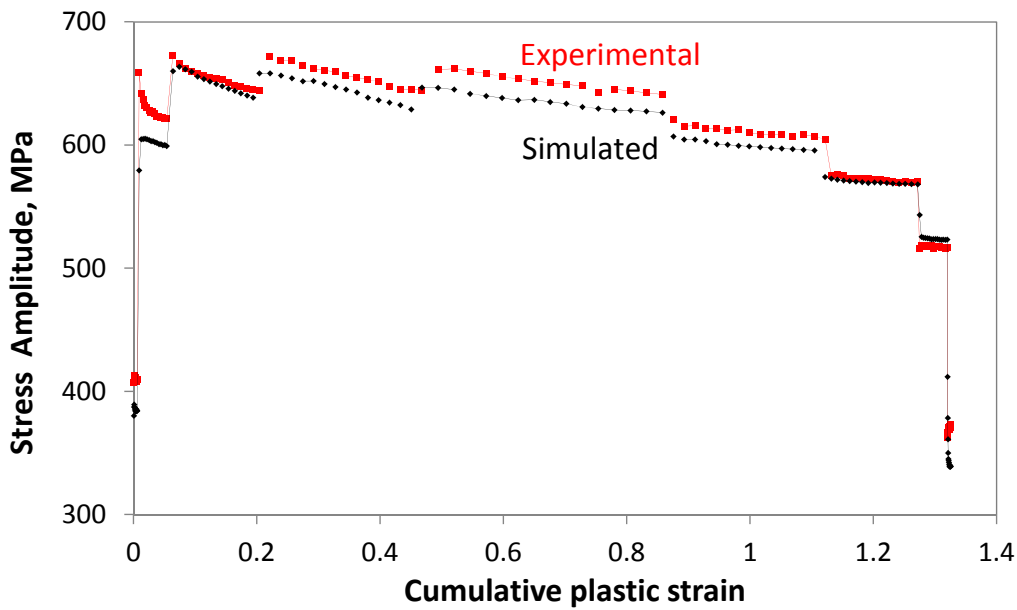


**Figure 2.13:** Experimental and simulated stress amplitude against cumulative plastic strain.

a trendline given by:

$$\frac{\Delta\epsilon}{2}(\%) = 9.885 N_f^{-0.399}$$

A variable amplitude test was done at constant strain rate ( $\dot{\epsilon} = 10^{-3} \text{ s}^{-1}$ ) in order to detect a potential memory effect in the material. The loading consists of 15 cycles at each strain amplitude in the order:  $\pm 0.2\%$ ,  $\pm 0.4\%$ ,  $\pm 0.6\%$ ,  $\pm 0.8\%$ ,  $\pm 1.0\%$ ,  $\pm 0.8\%$ ,  $\pm 0.6\%$ ,  $\pm 0.4\%$  and  $\pm 0.2\%$ . Figure 2.12 shows the evolution of stress range during the whole test. A comparison was made between the experiment and simulated stress amplitude plotted against cumulative plastic strain, figure 2.13. The constitutive equation, without any extra variable, predicted the experimental results quite nicely. Hence, it can be concluded that the material exhibits no memory effect and can be suitably modeled using the constitutive equations identified earlier.



# Chapter 3

## Finite element analysis of clip connector

A Finite Element (FE) analysis of the stress and strain state in clip connector has been performed in ABAQUS using the elastic-plastic constitutive equations identified in previous chapter.

The Clip Riser<sup>TM</sup> assembly model consisting of the lock ring plus the female part and male part is shown in figure 3.1(a). Because of an axial symmetry, only 1/8<sup>th</sup> part was modeled to reduce the computation time. An independent model of lock ring is shown in figure 3.1(b). Because of lack of symmetry in the arrangement of lugs in lock ring and female member as well, a model was created in different sections. The mesh was generated manually using 3D modified quadratic tetrahedral elements of type C3D10M with 4 integration points, figure 3.1(c). This type of element is robust for large deformation and contact problems. The mesh was refined in the regions where the lock ring is in contact with the male and female parts of the assembly to ensure good convergence and accuracy of computations.

The load is transmitted to the lock ring through the contacts at lugs. There are two types of algorithm available in ABAQUS for modeling contacts: general contacts and contact pairs. In present case, the general contact algorithm (node to surface) was used since it is less complicated and faster.

Numerical simulations were performed under two different cyclic loading conditions, provided by IFPEN: Connected mode (where the riser tubes are in tension and fixed at both top and bottom) and disconnected mode (where the riser tubes are hanging from top

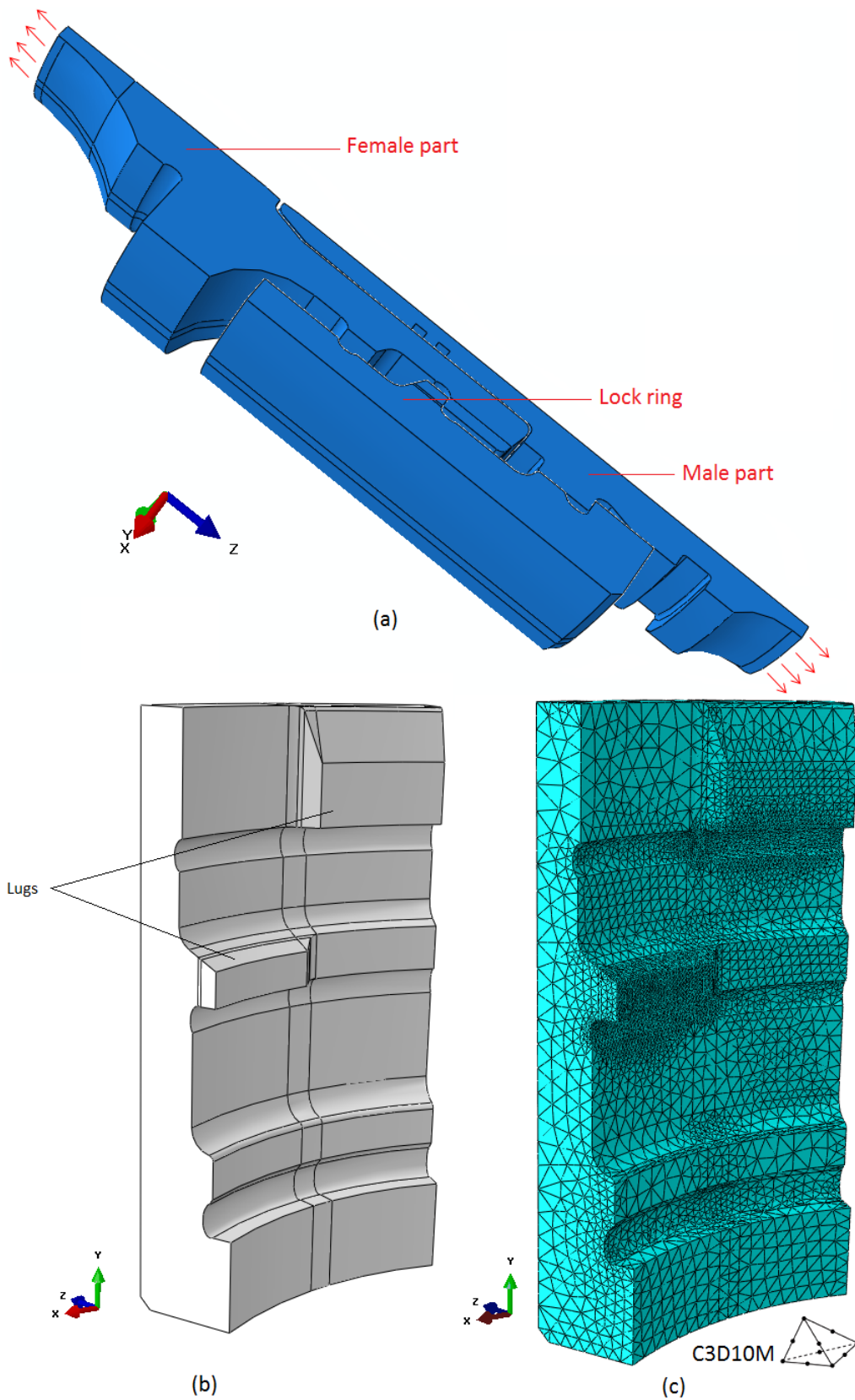


**Figure 3.1:** (a) Clip connector model in ABAQUS software (b) Lock ring model (c) Corresponding meshed model using tetrahedral element type C3D10M.

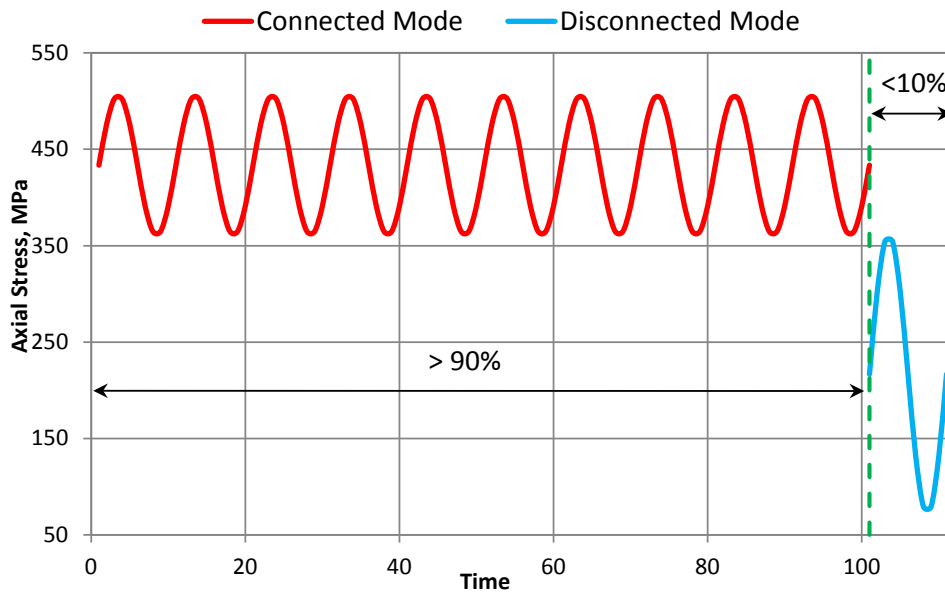


**Figure 3.2:** Loading stress cycle for different loading conditions depicting the difference in duration of connected mode and disconnected mode during working time.

platform). The maximum and minimum values of the tensile loads in the connected and disconnected mode are:

**Connected Mode:**

Minimum Tensile Load: 2500 kips (11120.5 kN)

Maximum Tensile Load: 3500 kips (15568.8 kN)

**Disconnected Mode:**

Minimum Tensile Load: 500 kips (2224.1 kN)

Maximum Tensile Load: 2500 kips (11120.5 kN)

Although the Clip-Riser™ assembly most of the time remains in connected mode under working condition (> 90% of service life), but the time spent in disconnected mode (< 10% of service life) might induce more fatigue damage since the stress amplitude is almost doubled, figure 3.2. Abaqus simulations were performed for both situations. The Von Mises stress contours in lock ring as obtained in connected mode after 50 loading cycles at maximum stress is shown in figure 3.3. The contacts at lugs are in crossed way so that contact occurs only at a point in the edge of the lug, thus leading to very high contact stresses at that point which drop very quickly upon cycling, as shown in figure 3.4(a).

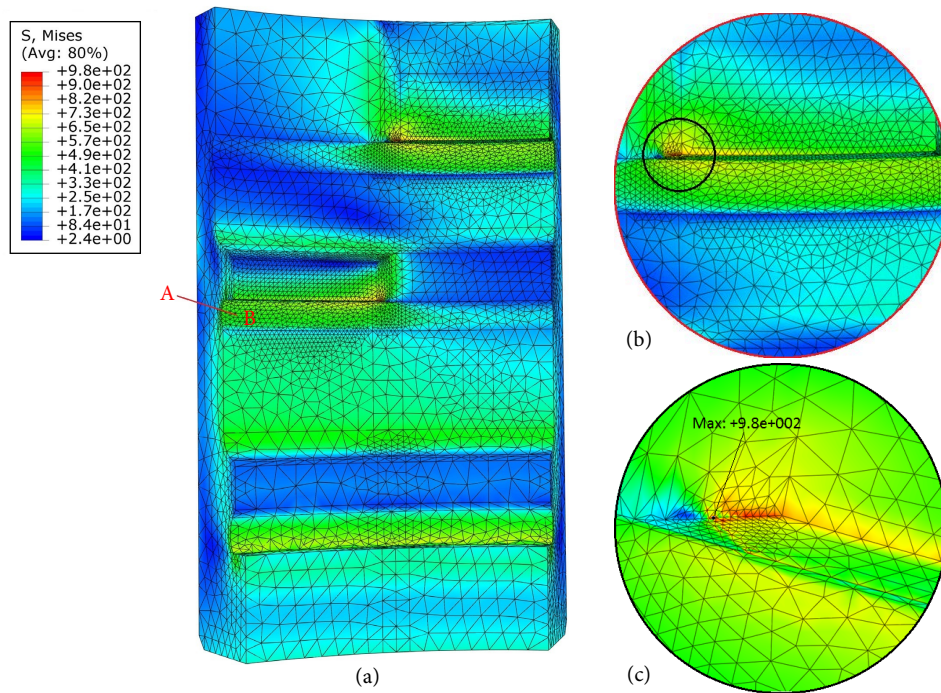


**Figure 3.3:** Stress contours in lock ring in connected mode after 50 cycles (a) overview (b) zoomed in lugs region where stress gradient exist (c) zoomed in contact region where maximum stress exist.

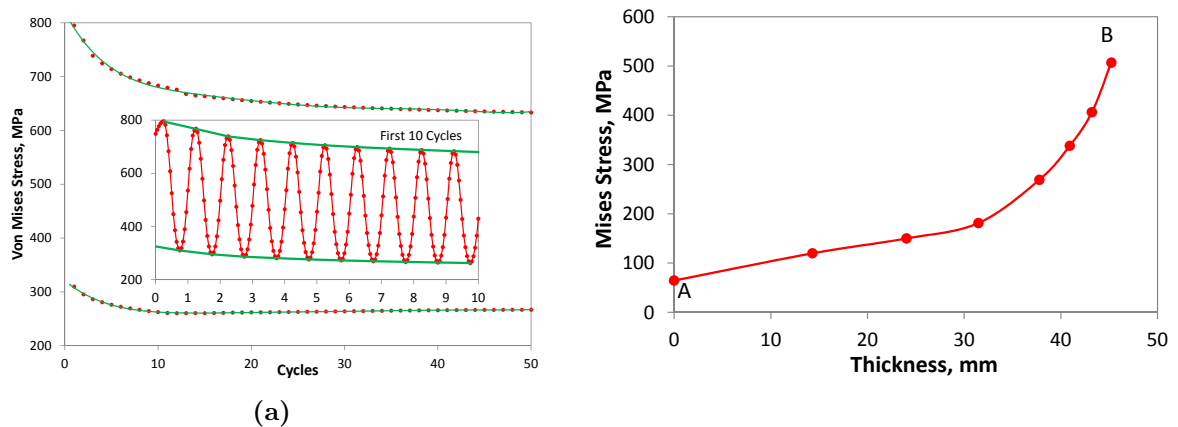


**Figure 3.4:** (a) Von-Mises stress evolution at contact element during 50 cycles and (b) Stress gradient along section line A-B (marked in figure 3.3) in connected mode after 50 cycles.

The high compressive principal stress at the contact node leads to a high Von Mises stress, while in the area below the lugs, Von Mises stress is lower but the principal stresses are positive. A very sharp stress gradient exists along the thickness of the lock ring, as shown in figure 3.4(b).

Another important parameter to be analyzed for design of clip connector is the plastic

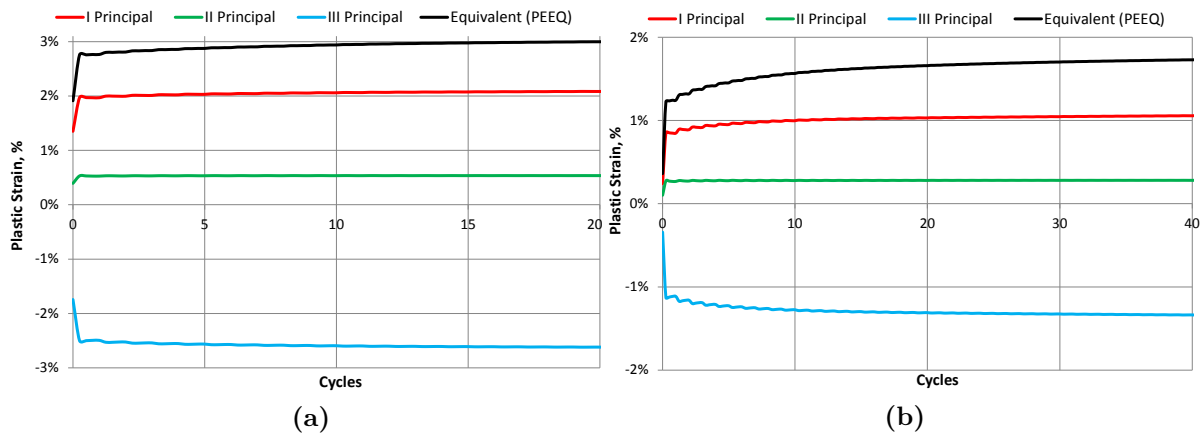


**Figure 3.5:** Evolution of principal and equivalent plastic strains at centroid of contact element after 50 cycles at maximum stress (a) Connected Mode (b) Disconnected Mode.

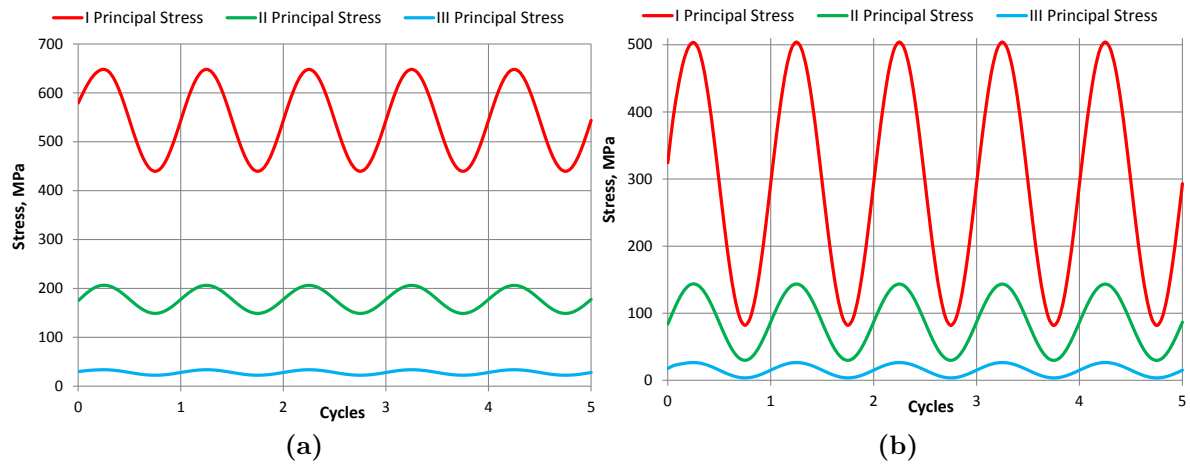


**Figure 3.6:** Variation of the three principal stresses at same element under (a) Connected Mode (b) Disconnected Mode (observe amplification of amplitude).

strain. Figure 3.5 shows the evolution of plastic strains at centroid of the contact element (where Von Mises stress is maximum) under connected mode and disconnected mode after 50 cycles at maximum stress. The plastic strain accumulates for the first few cycles and then saturates very quickly.

The regions below the lugs are critical because of the presence of positive principal stresses. The variation in the principal stresses computed at a randomly chosen node in this critical area of the lock ring (region below the lugs) in connected and disconnected modes are shown in figure 3.6(a) and figure 3.6(b), respectively. Although the far-field loading is uniaxial, locally, due to geometry effects, the loading is more or less an in-phase biaxial tension with different mean stresses.

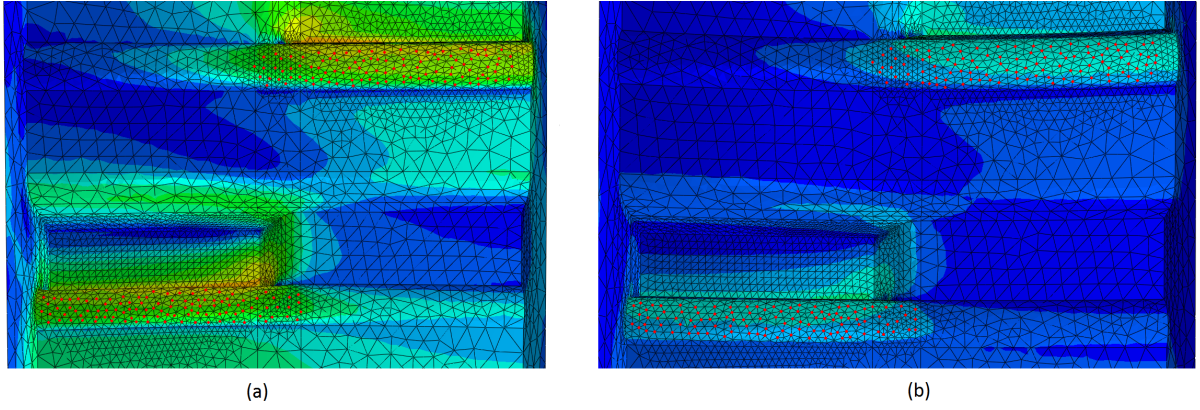


**Figure 3.7:** Location of selection of nodes (red dots) in (a) Connected Mode (b) Disconnected Mode.

Mathematically, the local stress state at any element in the region below the lugs can be written as:

$$\begin{aligned}
 \sigma_I &= \sigma_{I,\text{mean}} + \sigma_{I,a} \text{Sin } \omega t \\
 \sigma_{II} &= \sigma_{II,\text{mean}} + \sigma_{II,a} \text{Sin } \omega t \\
 \sigma_{III} &\approx 0
 \end{aligned} \tag{3.1}$$

$\sigma_I$ ,  $\sigma_{II}$  and  $\sigma_{III}$  are the three principal stresses in numerically decreasing order, and the subscripts ‘mean’ and ‘a’ are their corresponding mean and amplitude values.

In order to study the statistics of biaxiality ratio and mean stress in the critical area, a random set of approximately 200 nodes was chosen for both type of loading conditions, figure 3.7. The biaxiality ratio at each node was defined as:

$$B = \frac{\sigma_{II,a}}{\sigma_{I,a}}$$

where  $\sigma_{a,I}$  and  $\sigma_{a,II}$  are as defined in equation 3.1. The R ratio has been defined independently for each principal stress as:

$$R_I = \frac{\sigma_{I,\text{min}}}{\sigma_{I,\text{max}}} \quad \text{and} \quad R_{II} = \frac{\sigma_{II,\text{min}}}{\sigma_{II,\text{max}}}$$

The statistical distributions of the biaxiality ratio (B) and the two R ratios ( $R_I$  and  $R_{II}$ ) at these nodes under the connected mode and the disconnected mode respectively, are shown in figure 3.8.

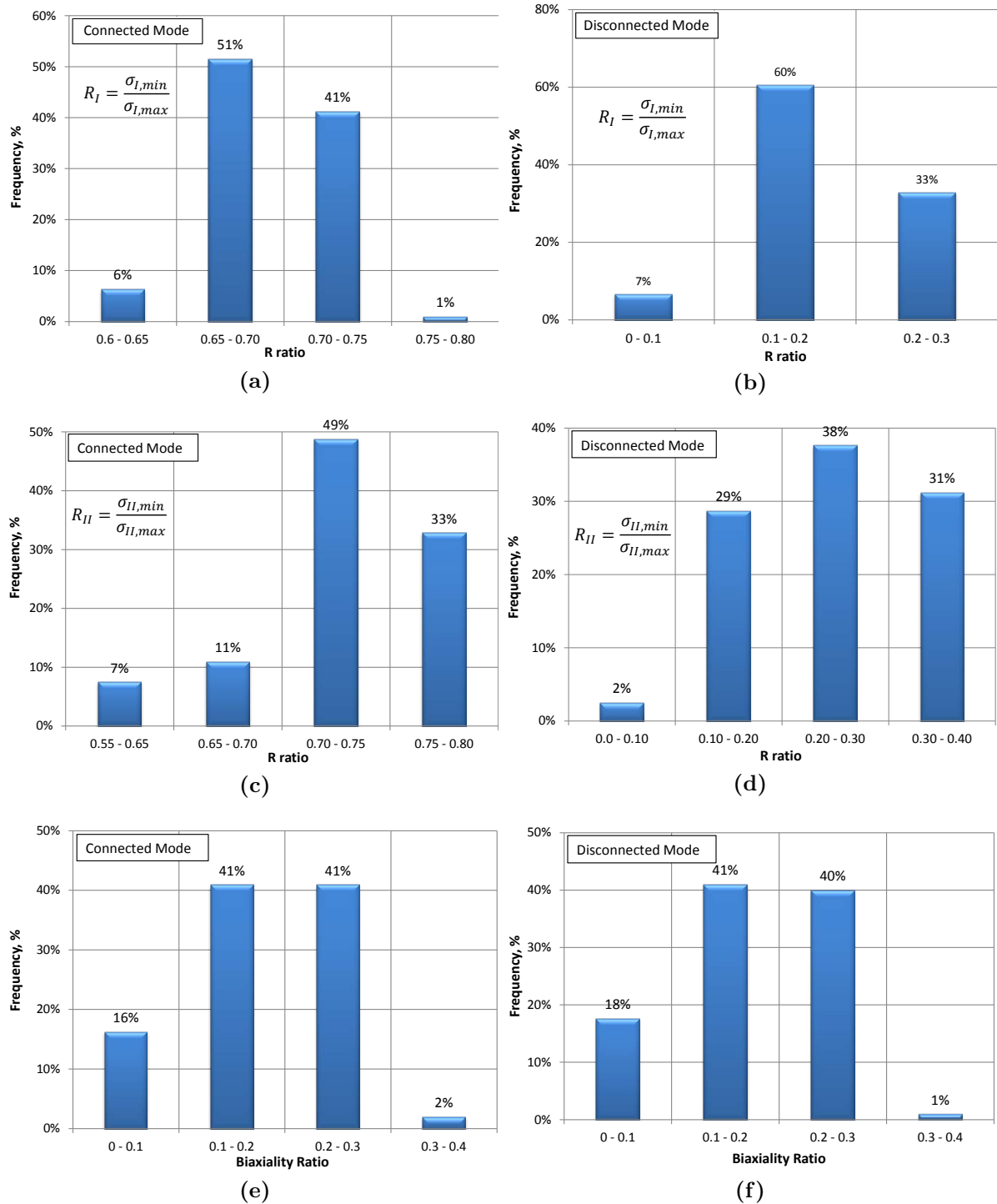


**Figure 3.8:** Statistical distribution of parameters at randomly selected 200 nodes: R ratio for Maximum principal stress in (a) and (b), R ratio for mid principal stress in (c) and (d), and for biaxiality ratio in (e) and (f).

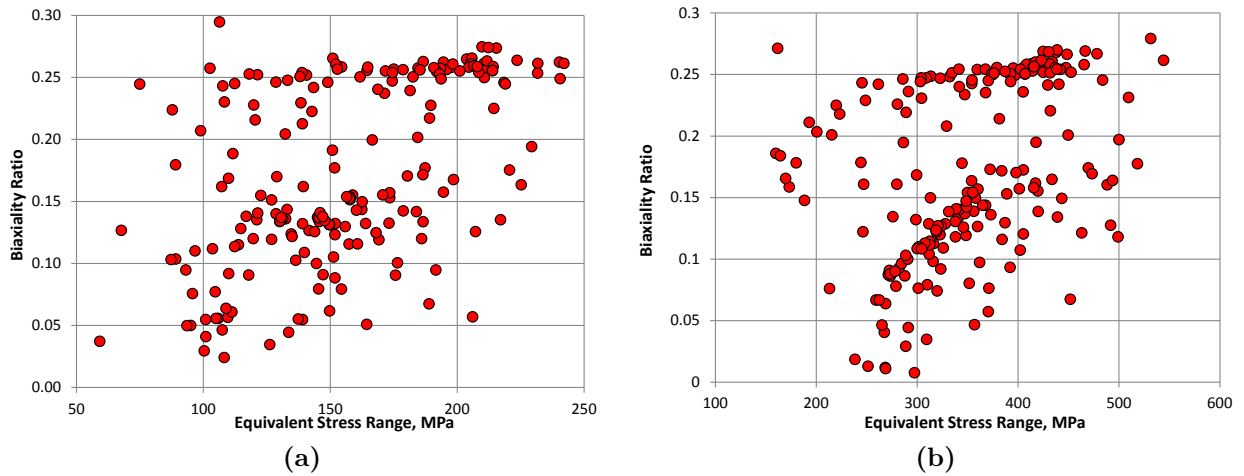


**Figure 3.9:** Variation of biaxiality with the corresponding Von-mises equivalent stress range at each node in (a) Connected Mode (b) Disconnected Mode.

In the connected mode, the far field R ratio was 0.7 while in the disconnected mode it was 0.2. It can be seen that at most of the points, the R ratio is almost equal to applied one, for both principal stresses. Many points exist with a biaxiality ratio between 0.1 and 0.3 (82% for connected mode and 81% for disconnected mode).

In order to precise the effect of biaxiality, the distribution of load biaxiality was plotted against the corresponding Von-mises equivalent stress range for the two types of loadings, as shown in figure 3.9. The most critical points could be the ones with a high biaxiality ratio and a high Von-mises equivalent stress range values.

Hence, the fatigue behavior of this material was investigated by performing experiments under in-phase biaxial tension loading (combined tension and internal pressure tests) in this range of biaxiality ratio and the mean stress (R ratio).

# Chapter 4

## Influence of the mean stress

Uniaxial load-controlled high-cycle fatigue tests at different R ratios ( $\sigma_{\min}/\sigma_{\max}$ ): -1, -0.5, 0, 0.25, 0.5, 0.6 & 0.7 were performed in air to study the fatigue lives and the mean stress effects. As will be shown below, important modifications in the damage mechanisms were found with change in mean stress.

### 4.1 Experimental procedures

Uniaxial tension fatigue tests were performed using a hydraulic machine with maximum load capacity of  $\pm 100$  kN. Three kinds of cylindrical specimens were used: 8 mm dia & 16 mm gage length with a surface roughness of  $R_a \leq 0.4 \mu\text{m}$  for tests at low mean stresses and 7 & 6 mm dia, 15 & 14 mm gage length with  $R_a = 0.2 \mu\text{m}$  for tests at high mean stresses, figure 4.1. The diameter of specimens was reduced at high mean stresses so as to avoid crack initiation in threaded region. These specimens were cut along the longitudinal direction from the same area of the clip connector as the samples used to characterize the microstructure.

An extensometer with a gage length of 10 mm and a range of  $\pm 15\%$  was used, figure 4.2. In order to avoid fretting-induced crack initiation, small clots of glue were put between the specimen surface and extensometer knives. Sinus loading was applied with a fixed frequency of 10 Hz.

Load-controlled high-cycle fatigue tests were performed at different R ratios ( $R = \sigma_{\min}/\sigma_{\max} = -1, -0.5, 0, 0.25, 0.5, 0.6, 0.7$ )

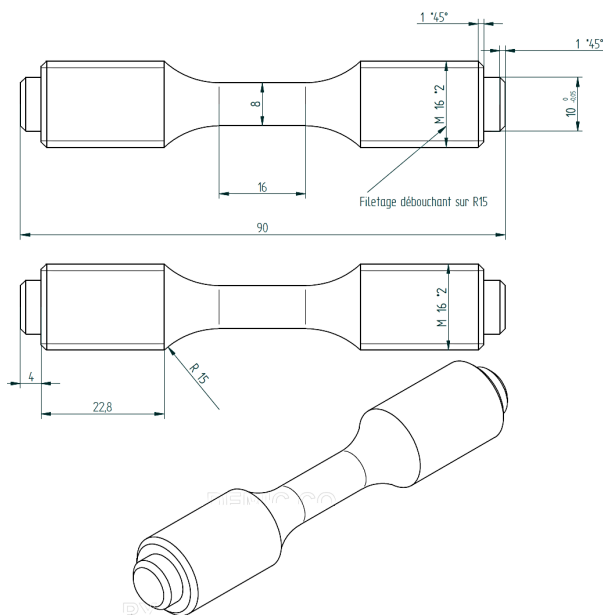


Figure 4.1: Cylindrical specimen.

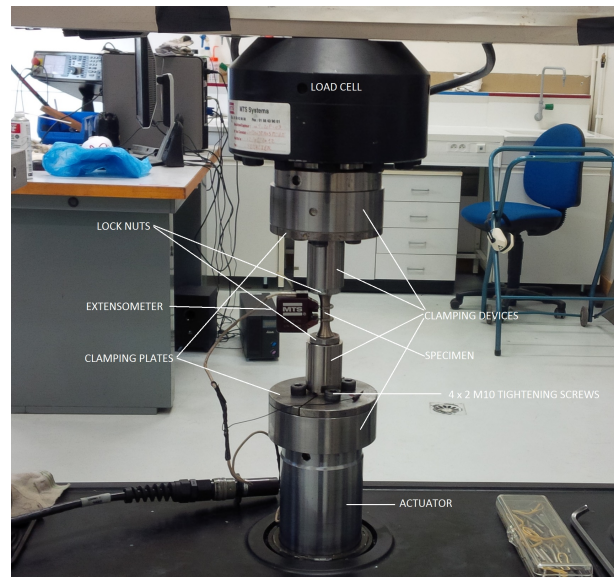


Figure 4.2: Experimental device.

## 4.2 Experimental results

### 4.2.1 Fatigue lives

The resulting fatigue lives are reported in table 4.1 and plotted as Whöler curves (S-N curves) to illustrate the effect of mean stress on fatigue life, figure 4.3. For  $R \leq 0.25$ , tests were stopped at 3,000,000 cycles and the corresponding stress amplitude was defined as the endurance limit for that R ratio. For  $R > 0.5$ , tests were run until 10,000,000 cycles and no fatigue failure could be observed. The endurance limit as well as slope of the curves tends to drop with increasing R ratio. Horizontal arrows denote the corresponding run-out tests.

In some tests, cracks were found to initiate from defects (internal and surface) in the material, as discussed in section 4.2.2.

Another representation of fatigue test data is the Goodman plot (Amplitude-mean stress plane) shown in figure 4.4. The Goodman plot can be divided into three domains: safe domain, fatigue failure and ductile failure respectively. Ductile failure occurs when the amplitude or the mean stress crosses the line:  $\sigma_a + \sigma_m = \sigma_u$ . Fatigue data has been

| Test No. | Dia, mm | $R_a$ , $\mu\text{m}$ | $\sigma_a$ , MPa | $\sigma_{\text{max}}$ , MPa | R    | Cycles to failure, $N_f$ | Initiation Type             |
|----------|---------|-----------------------|------------------|-----------------------------|------|--------------------------|-----------------------------|
| 8        | 8       | < 0.4                 | 435              | 435                         | -1   | 193,620                  | Surface without defect      |
| 7        | 8       | < 0.4                 | 410              | 410                         | -1   | 367,166                  | Surface without defect      |
| 9        | 8       | < 0.4                 | 385              | 385                         | -1   | 1,137,624                | Surface without defect      |
| 20       | 8       | < 0.4                 | 370              | 370                         | -1   | 521,343                  | Surface without defect      |
| 40       | 6       | 0.2                   | 370              | 370                         | -1   | > 3,000,000              | -                           |
| 21       | 8       | < 0.4                 | 365              | 365                         | -1   | > 3,000,000              | -                           |
| 15       | 8       | < 0.4                 | 390              | 520                         | -0.5 | 322,888                  | Surface without defect      |
| 19       | 8       | < 0.4                 | 378              | 502                         | -0.5 | 390,914                  | Surface without defect      |
| 14       | 8       | < 0.4                 | 375              | 500                         | -0.5 | 182,856                  | Surface without defect      |
| 18       | 8       | < 0.4                 | 365              | 485                         | -0.5 | 741,938                  | Internal Pore with fish-eye |
| 16       | 8       | < 0.4                 | 360              | 479                         | -0.5 | 2,207,630                | Internal Pore with fish-eye |
| 21       | 8       | < 0.4                 | 350              | 466                         | -0.5 | > 3,000,000              | -                           |
| 11       | 8       | < 0.4                 | 322              | 644                         | 0    | 21,064                   | Surface without defect      |
| 13       | 8       | < 0.4                 | 318.5            | 637                         | 0    | 153,518                  | Surface without defect      |
| 39-2     | 6       | 0.2                   | 317              | 634                         | 0    | 575,063                  | Surface without defect      |
| 10       | 8       | < 0.4                 | 315              | 630                         | 0    | 833,695                  | Surface without defect      |
| 22       | 8       | < 0.4                 | 310              | 620                         | 0    | 198,067                  | Surface without defect      |
| 39-1     | 6       | 0.2                   | 305              | 610                         | 0    | > 3,000,000              | -                           |
| 23       | 8       | < 0.4                 | 300              | 600                         | 0    | > 3,000,000              | -                           |
| 29       | 7       | 0.2                   | 273              | 729                         | 0.25 | 228,359                  | Surface without defect      |
| 30       | 7       | 0.2                   | 270              | 721                         | 0.25 | 160,277                  | Internal Inhomogeneity      |
| 29       | 7       | 0.2                   | 265              | 708                         | 0.25 | > 3,000,000              | -                           |
| 26       | 7       | 0.2                   | 260              | 694                         | 0.25 | 1,704,174                | Internal Pore               |
| 23       | 8       | < 0.4                 | 260              | 694                         | 0.25 | 373,933                  | Internal Inhomogeneity      |
| 24       | 7       | 0.2                   | 255              | 681                         | 0.25 | 300,333                  | Internal Inhomogeneity      |
| 26       | 7       | 0.2                   | 250              | 668                         | 0.25 | > 3,000,000              | -                           |
| 25       | 7       | 0.2                   | 250              | 668                         | 0.25 | 339,602                  | Surface Pore                |
| 26       | 7       | 0.2                   | 245              | 654                         | 0.25 | > 3,000,000              | -                           |
| 26       | 7       | 0.2                   | 240              | 641                         | 0.25 | > 3,000,000              | -                           |
| 37       | 6       | 0.2                   | 193              | 772                         | 0.5  | 163,919                  | Machining mark              |
| 33       | 6       | 0.2                   | 190              | 760                         | 0.5  | 459,584                  | Machining mark              |
| 38       | 6       | 0.2                   | 190              | 760                         | 0.5  | 279,630                  | Machining mark              |
| 36-2     | 6       | 0.2                   | 187              | 748                         | 0.5  | > 3,000,000              | -                           |
| 34       | 6       | 0.2                   | 185              | 740                         | 0.5  | 1,166,933                | Surface Pore                |
| 35       | 6       | 0.2                   | 180              | 720                         | 0.5  | 1,462,890                | Surface Pore                |
| 36-1     | 6       | 0.2                   | 175              | 700                         | 0.5  | > 10,000,000             | -                           |
| 36-4     | 6       | 0.2                   | 154              | 770                         | 0.6  | > 10,000,000             | -                           |
| 36-3     | 6       | 0.2                   | 148              | 740                         | 0.6  | > 10,000,000             | -                           |
| 31-3     | 6       | 0.2                   | 116.5            | 777                         | 0.7  | > 10,000,000             | -                           |
| 32       | 6       | 0.2                   | 115.5            | 770                         | 0.7  | > 10,000,000             | -                           |
| 31-2     | 6       | 0.2                   | 115              | 767                         | 0.7  | > 10,000,000             | -                           |
| 31-1     | 6       | 0.2                   | 112.5            | 750                         | 0.7  | > 10,000,000             | -                           |

**Table 4.1:** Test data obtained from high-cycle fatigue tests in air at 10 Hz.  $\sigma_a$  is the applied stress amplitude and  $R_a$  is the measure of surface roughness.

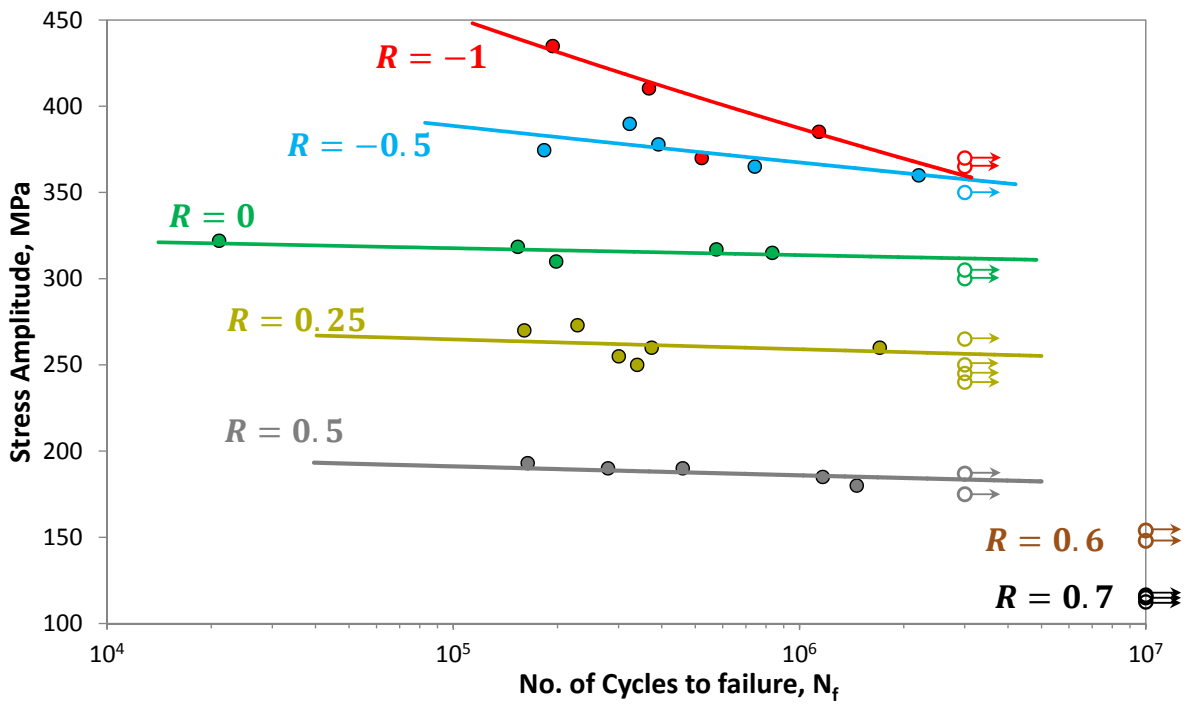


Figure 4.3: Whöler curve for high-cycle fatigue tests at different R ratios.

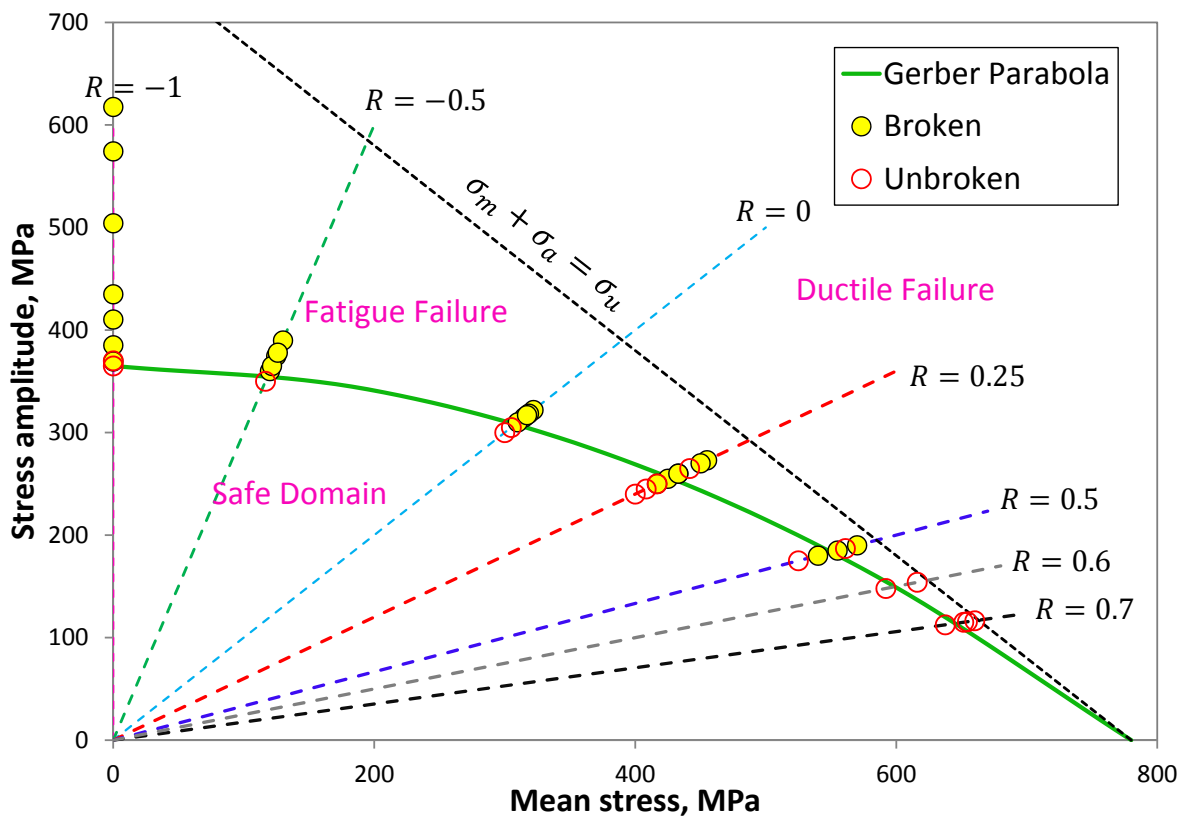


Figure 4.4: Goodman diagram for high-cycle fatigue tests at different R ratios.

---

compared with Gerber's parabola (Gerber, 1874):

$$\sigma_{a,R} = \sigma_{-1} \left( 1 - \left( \frac{\sigma_m}{\sigma_u} \right)^2 \right) \quad (4.1)$$

$\sigma_{a,R}$  denotes the amplitude corresponding to endurance limit at given mean stress,  $\sigma_m$ .  $\sigma_u$  and  $\sigma_{-1}$  denotes ultimate tensile stress and the fatigue strength (at  $3 \times 10^6$  cycles) under fully reversed push-pull test ( $R = -1$ ). Gerber's parabola is found to provide an accurate prediction of the endurance limit at different R ratios.

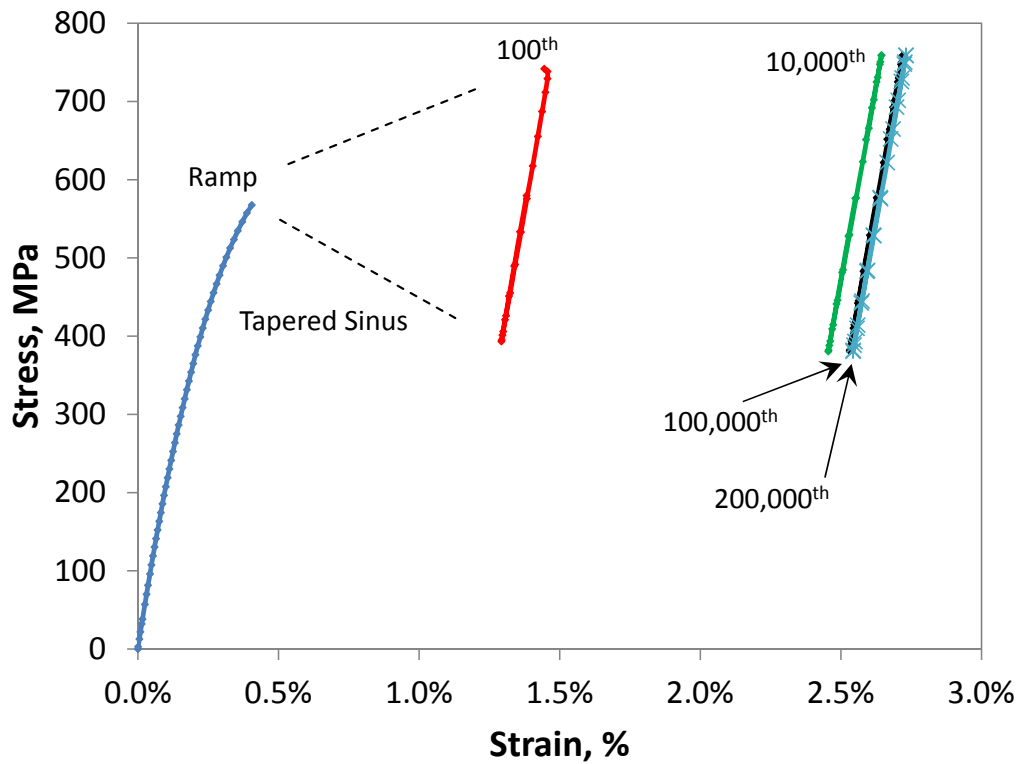
At high mean stresses, although no macroscopic plasticity was observed beyond the first ramp, but the ratcheting did occur. Figure 4.5 shows the measured engineering stress-strain loops for two high R ratios: one for which fatigue failure occurred at 459,584 cycles (for  $R = 0.5$ ) and one for which there was no fatigue failure (for  $R = 0.7$ ). Shakedown was always achieved, well before the fatigue fracture with up to 3% accumulated strain which did not induce significant difference between the engineering stresses and the true stresses. That is why, engineering stresses were used in the whole manuscript.

## 4.2.2 Damage mechanisms

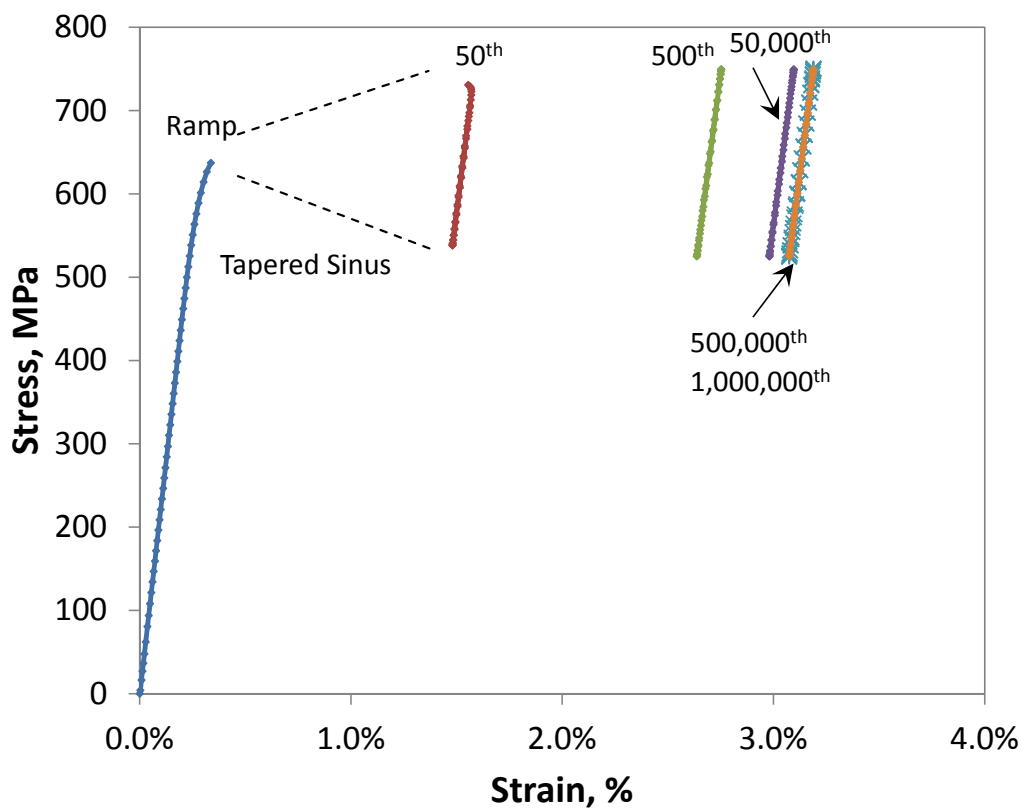
To study the crack initiation and propagation mechanisms under different mean stress levels, the fracture surfaces of broken specimens were analyzed using a Keyence digital optical Microscope in addition to the Scanning Electron Microscope (SEM).

The analysis of fracture surfaces revealed the presence of four types of fatigue crack initiation mechanisms in this steel:

- Surface crack initiation merely due to local plasticity.
- Surface crack initiation from surface-cutting defects.
- Internal crack initiation from pores.
- Internal crack initiation from chemical in-homogeneity.



(a)  $R = 0.5$ ,  $\sigma_a = 190$  MPa,  $\sigma_{\max} = 760$  MPa and  $N_f = 459,584$  cycles



(b)  $R = 0.7$ ,  $\sigma_a = 112.5$  MPa,  $\sigma_{\max} = 750$  MPa and  $N_f > 3,000,000$  cycles.

**Figure 4.5:** Measured engineering stress-strain loops.

---

## Surface crack initiation without defects

All the fatigue failures at  $R = -1$  and  $R = 0$  and most of the fatigue failures at  $R = -0.5$  initiated from the surface of the specimen without any responsible defect, figure 4.6a. Such surface initiation could be due to the stress concentration at intrusions and extrusions generated on the surface as discussed in literature review or from machining marks. However the latter mechanism seems less probable since the specimens had a good surface finish with  $R_a = 0.4$  or  $0.2 \mu\text{m}$ .

The fracture surfaces were often mated, especially when  $R < 0$ . When it was not the case, striations typical of mode I fatigue crack growth could be observed, as shown in figure 4.6b.

To investigate further the surface crack initiation and propagation mechanism, longitudinal sections of the broken specimens were observed carefully under SEM after mechanical polishing and chemical etching (with a 5% Nital solution).

Several secondary micro-cracks were observed in the specimens submitted to low-cycle fatigue. Most of these cracks followed a crystallographic zig-zag path as shown in figure 4.7(a). The cracks were often deflected by grain boundaries or martensite laths inside the grains and sometimes followed the grain boundaries.

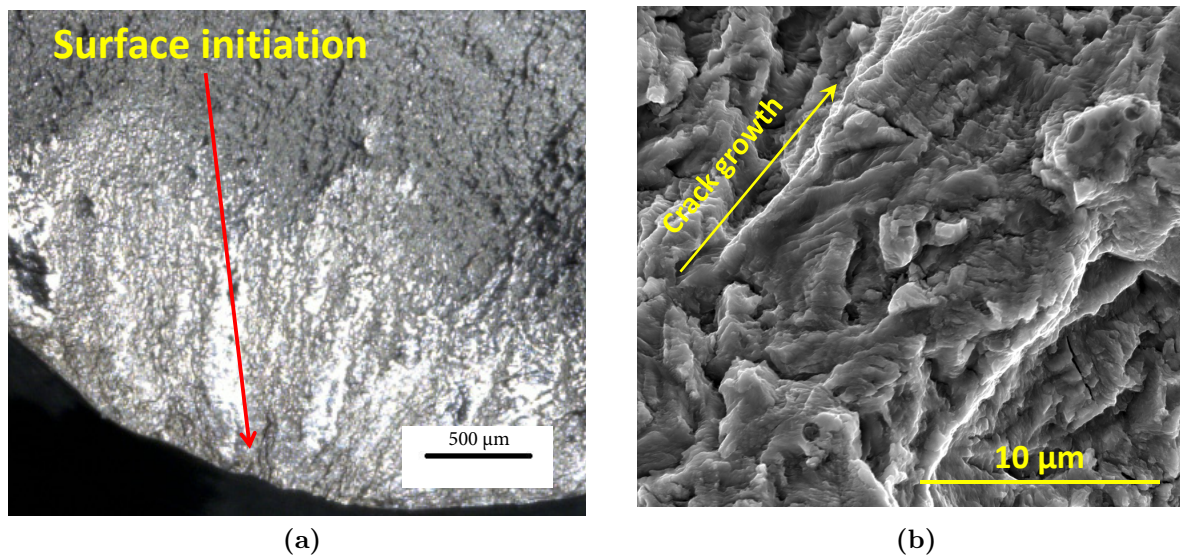


**Figure 4.6:** (a) Fracture surface showing surface crack initiation at  $R = -1$ ,  $\sigma_a = 385 \text{ MPa}$ ,  $N_f = 1,137,624$  cycles. (b) Striations observed on a fracture surface under SEM at  $R = 0.25$ ,  $\sigma_a = 260 \text{ MPa}$ ,  $N_f = 373,933$  cycles.

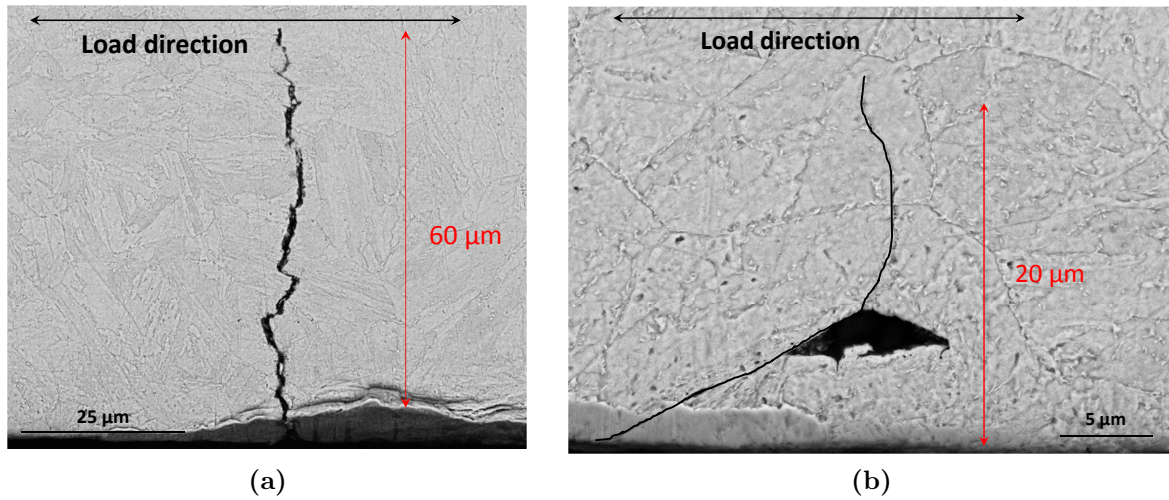


**Figure 4.7:** Longitudinal section under SEM at  $R = -1$ ,  $\epsilon_a = 0.3\%$ ,  $N_f = 6,701$  (a) Crystallographic crack propagation (b) A microcrack with clear stage I within a single grain.

For few cracks, a clear distinction could be made between the stage I and stage II of propagation as shown in figure 4.7(b). The crack has been overlaid with dashed line so as to give a better visualization. The crack initiated in stage I and then got deflected, perhaps by an inclusion or defect, and then continued to propagate in stage II. In terms of size, the stage I of crack propagation is very short and the transition from stage I to stage II occurs within the first grain.

## Crack initiation from surface or internal pores

Internal crack initiation from defects became more and more frequent as the R ratio was increased. Internal initiation is generally observed in very high-cycle fatigue regime ( $> 10^7$  cycles), but in the present study it was found to exist for relatively low fatigue lives in order of  $10^5$  to  $10^6$  cycles.

In some cases, crack initiated from a pore located very near to the specimen's surface as shown in figure 4.8, while in some others, the crack initiated from a defect located further from the surface, leading to the formation of “Fish eye” pattern, figure 4.9. The 3D topographic analysis of the fracture surface around the initiation site revealed that the crack initiates along a maximum shear plane at an angle of  $42^\circ - 43^\circ$  with respect to the loading axis, as shown in figure 4.10(a). But as the crack grew, it became normal to the loading axis. As in case of surface crack initiation, a stage I to stage II transition seems to occur.

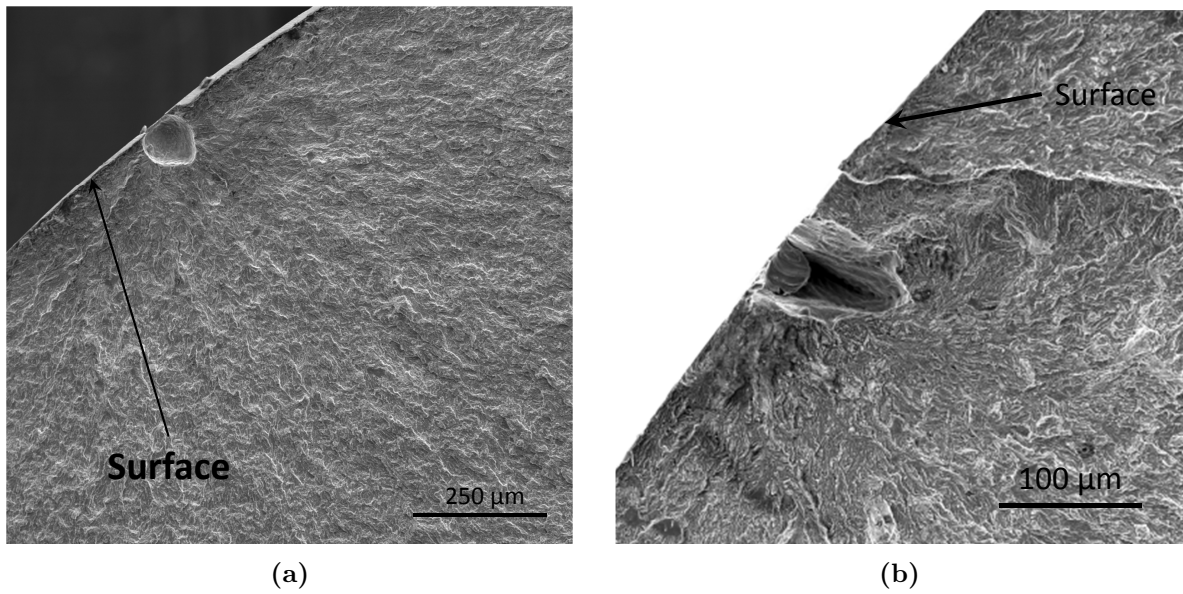


**Figure 4.8:** SEM observation of a fracture surface showing (a) sub-surface crack initiation from a pore at  $R = 0.25$  (b) initiation from a surface Pore at  $R = 0.5$ .

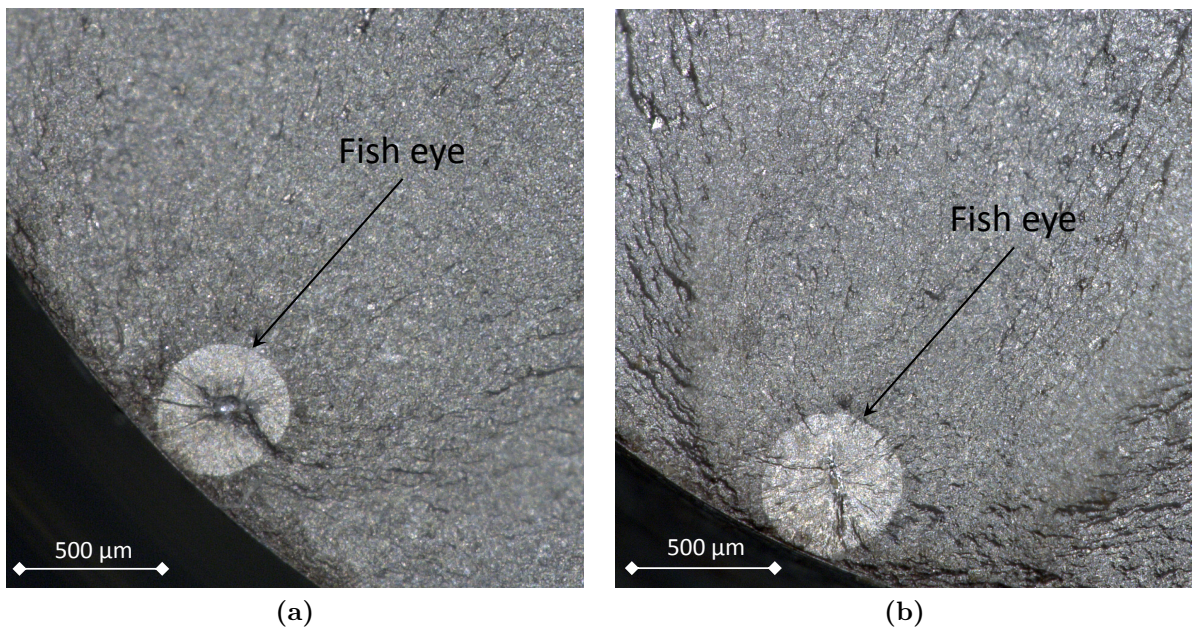


**Figure 4.9:** Fracture surfaces under optical microscopy with “Fish eye” (a)  $R = -0.5$ ,  $\sigma_a = 360$  MPa,  $N_f = 2,207,630$  (b)  $R = -0.5$ ,  $\sigma_a = 365$  MPa,  $N_f = 741,938$ .

Under the optical microscope, the fish eye area appears brighter as compared to the rest of the fracture surface because it corresponds to crack development without any interaction with moist air and thus without any oxidation of the crack face until the crack reaches the surface. The crack propagates first “in vacuum” and then in air and hence both

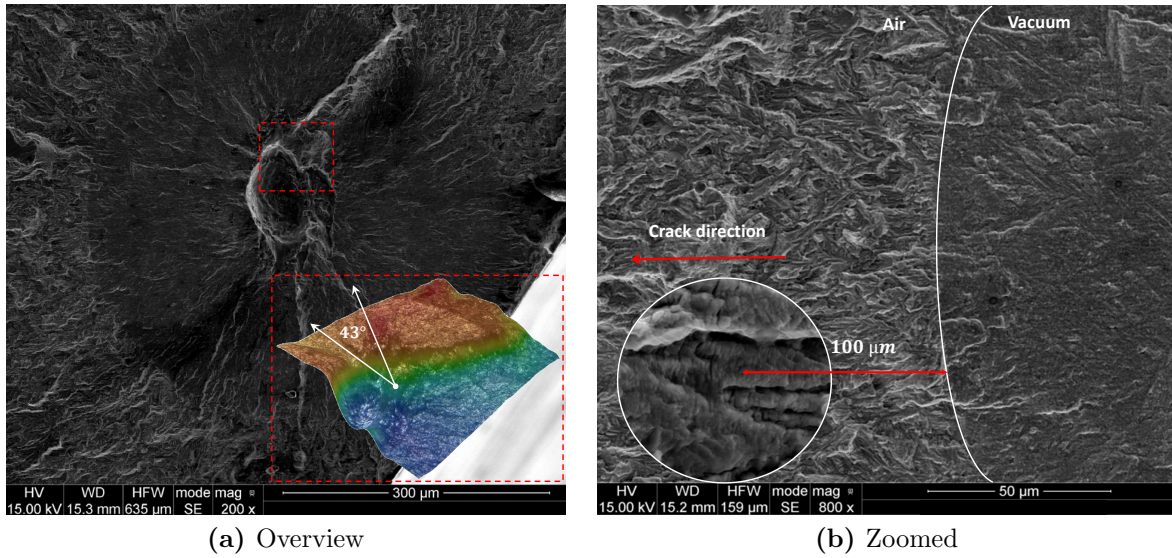


**Figure 4.10:** Fracture surface under SEM showing a clear difference in aspect of roughness, striations between crack growth in air and in vacuum at  $R = -0.5$ ,  $\sigma_a = 360$  MPa,  $N_f = 2, 207, 630$

the growth kinetics and the mechanism, are different. SEM observations revealed the different aspects of the regions corresponding to crack growth under vacuum and in air, shown in figure 4.10. The frontier separating the two regions is shown by the white line. The region within the fish eye appeared to be much smoother as compared to that in air. No striations were found in this region but as soon as the crack propagated in air, striations could be observed easily. This is in accordance with the results available in the literature (McEvily and Gonzalez Velazquez, 1992). The shape of the fish eye is circular, following the contours of iso-stress intensity factor. SEM observations did not show the presence of any Optically Dark Area (ODA) or any Fine Granular Area (FGA), which is in consistent with the observations made by Li et al. (2014) according to which they were observed only for very high fatigue lives and tend to disappear when the R ratio increases (Nakamura et al., 2010).

A few detailed observations of fracture surface in and around the fish-eye were done after platinum deposit and Focus Ion Beam (FIB) sectioning, using a FEI Helios 660 dual-beam microscope. 5 to 10 μm deep, 20 to 100 μm wide sections normal to the fracture surface were cut in a specimen broken after 1.7 million cycles at  $R = 0.25$  at various distances from the internal crack initiation site (figure 4.11). The sections cut 128 μm and 186 μm away from the initiation site (figure 4.11(c) and (d)) are located inside the fish-eye, while the section cut 600 μm away (figure 4.11(a,b)) is outside. While a rough crack profile (peak roughness value,  $R_p \approx 4$  μm) with many tiny secondary cracks could

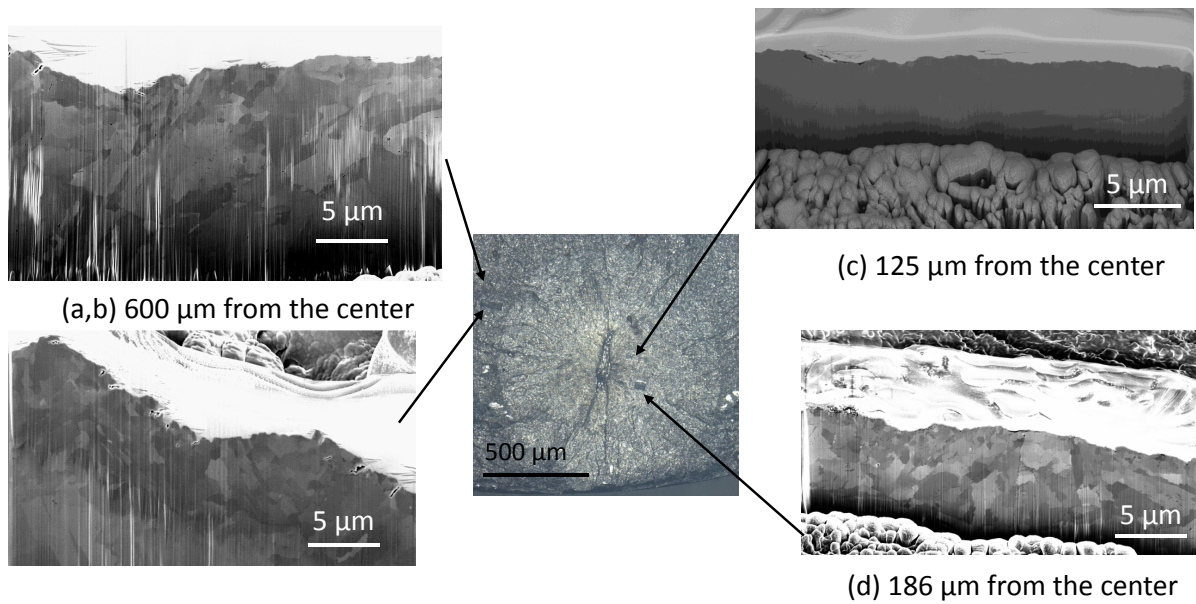
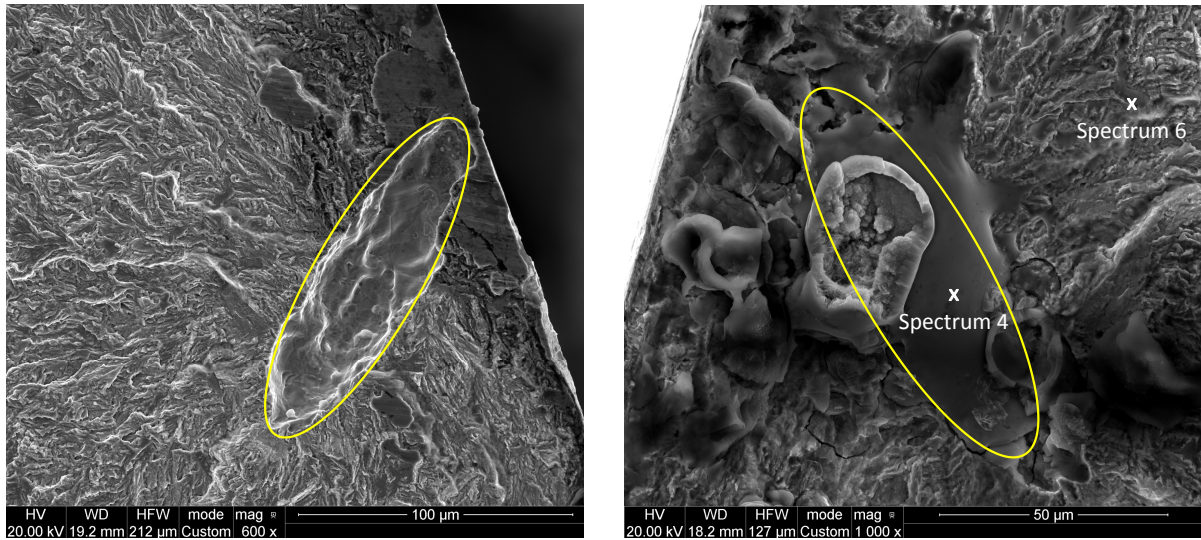


**Figure 4.11:** SEM images of cross sections made with a FIB after platinum coating at various distances from a fish-eye center on the fracture surface of a specimen broken after 1,704,174 cycles at  $R = 0.25$ .

be observed outside the fish-eye, a much smoother crack profile appeared inside the fish eye ( $R_p \approx 0.6$  and  $1 \mu\text{m}$  at  $128 \mu\text{m}$  and  $186 \mu\text{m}$  from the center, respectively) without secondary cracks. No modification of the mean grain size was observed below the fish eye surface.

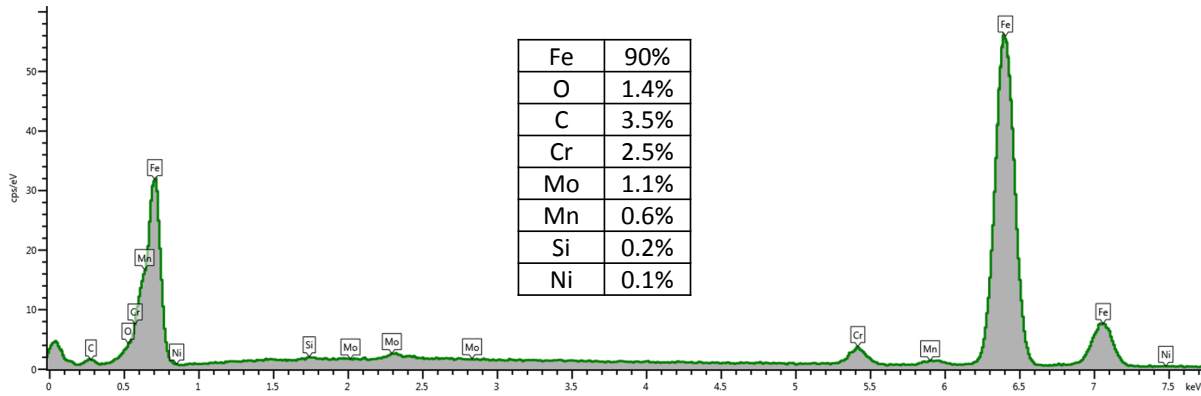
## Crack initiation from internal chemical in-homogeneity

In some specimens, cracks had also been found to initiate from material inhomogeneity. SEM images of both fracture surfaces of a specimen in which the crack initiated from an in-homogeneous area are shown in figure 4.12. There was a crater on one of the fracture surfaces while on the other one there was no such crater, rather some irregular accumulation of non-homogeneous material. Chemical analysis was performed using the Energy Dispersive Spectrum (EDS) device available in the SEM at two places indicated in figure 4.12(a,b) and the corresponding spectra obtained in these locations are shown in figure 4.12(c,d). In the non-homogeneous part (spectrum 4), the oxygen and carbon contents were higher than in the matrix (spectrum 6). The chromium and molybdenum contents were also slightly higher than the average. EDS technique has its limitation in quantification of carbon because it is a light element. Hence, the values for carbon content are not reliable but there is no doubt that the carbon content is not uniform in this area.

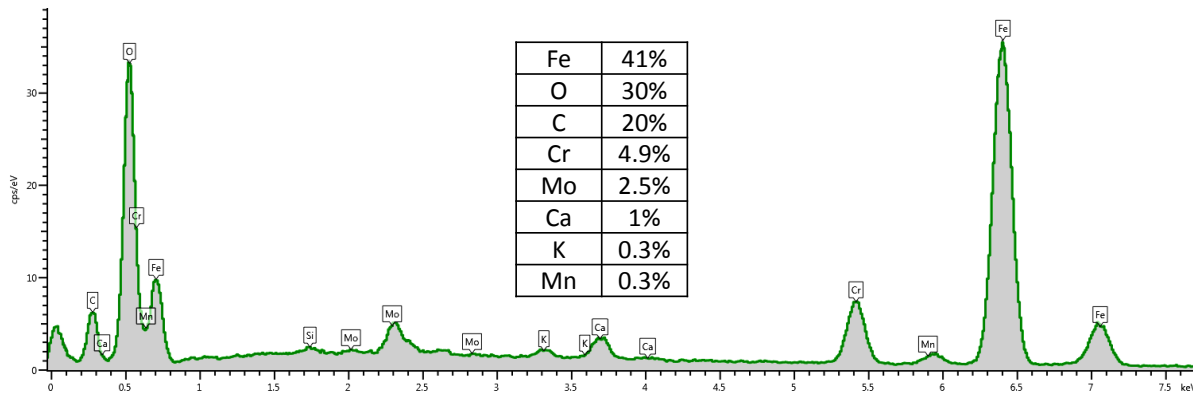


(a)

(b)



(c) Spectrum 6



(d) Spectrum 4

**Figure 4.12:** SEM image of Fracture surfaces (two halves (a) and (b)) and areas chosen for chemical analysis of specimen at  $R = 0.25$ ,  $\sigma_a = 270$  MPa,  $N_f = 160, 277$  and EDS analysis at two locations on the fracture surface (c) Matrix composition, Spectrum 6 (d) Inhomogeneity, Spectrum 4.

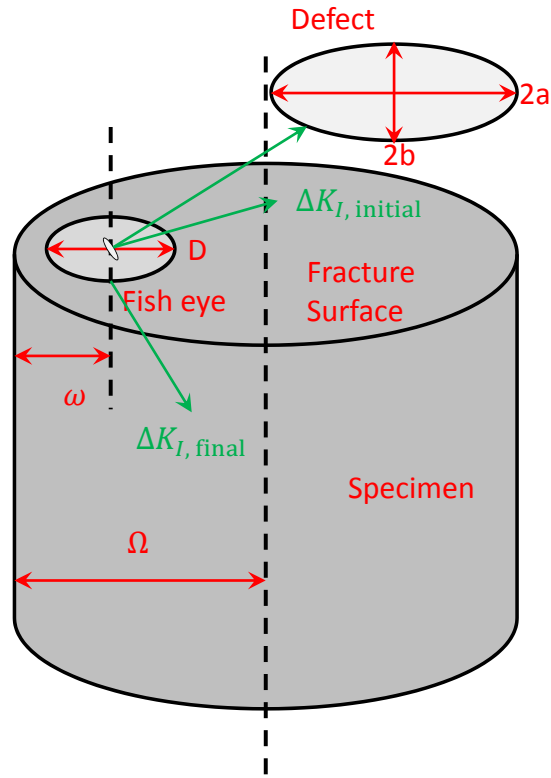


**Figure 4.13:** Parameters used to define location of fish eyes with respect to surface.

This oxygen and carbon rich matter behaves like an inclusion with different chemical composition and thus different mechanical properties than the matrix. De-bonding of this heterogeneous part from the matrix initiated a crack leaving a crater on one of the fracture surfaces.

To characterize the location of the defects, an eccentricity parameter,  $e$ , has been defined as:

$$e = \frac{\Omega - \omega}{\Omega} \quad (4.2)$$

where  $\Omega$  is radius of the cylinder and  $\omega$  is the distance from the center of the fish eye to the surface as described in figure 4.13. Eccentricity will be 0 for a defect located at the center of the specimen and close to 1 when it is located near to surface. The size and location of the defects responsible for internal initiation are tabulated in table 4.2. The diameter of the fish eye is represented by  $D$  and the major ( $2a$ ) and minor ( $2b$ ) axes of the defects are indicated, assuming an elliptical shape.

When  $e$  is close to 1, no fish eye exist and  $\Delta K$  is not reported. All the defects responsible for internal crack initiation were found near the surface (between  $165 \mu\text{m}$  and  $600 \mu\text{m}$  from the surface) and not randomly distributed on the fracture surface as expected for

| Test No. | R    | $\sigma_a$ | Size of defect    |                   | D<br>$\mu\text{m}$ | $\omega$<br>$\mu\text{m}$ | e    |
|----------|------|------------|-------------------|-------------------|--------------------|---------------------------|------|
|          |      | MPa        | 2a, $\mu\text{m}$ | 2b, $\mu\text{m}$ |                    |                           |      |
| 16       | -0.5 | 360        | 135               | 66                | 471                | 277                       | 0.93 |
| 18       | -0.5 | 365        | 199               | 66                | 660                | 330                       | 0.92 |
| 23-1     | 0    | 300        | 120               | 60                | 139                | 165                       | 0.96 |
| 26-1     | 0.25 | 250        | 304               | 50                | 500                | 514                       | 0.85 |
| 25       | 0.25 | 250        | 95                | 95                | -                  | 95                        | 0.97 |
| 24       | 0.25 | 255        | 127               | 65                | -                  | 104                       | 0.97 |
| 26-2     | 0.25 | 260        | 304               | 50                | 1028               | 514                       | 0.85 |
| 23-2     | 0.25 | 260        | 120               | 60                | 355                | 165                       | 0.96 |
| 30       | 0.25 | 270        | 120               | 40                | -                  | 60                        | 0.98 |

**Table 4.2:** Size and position of the defects giving rise to internal crack initiation. Specimens marked (1,2) survived 3 million cycles and reloaded. In that case, D corresponds to the crack diameter at the corresponding beach mark on the fracture surface

tensile fatigue tests, which are supposed to produce a uniform stress field, provided any misalignment and bending stresses are avoided. The absence of such artifacts was verified. This suggests that machining-induced residual stresses, more or less redistributed by plastic flow during the first half cycle at high R ratio, were present in the specimens and might played a role in the competition between surface and internal crack initiation.

### 4.2.3 Residual stress analyses

In order to clarify this question, XRD analyses of surface residual stresses were performed at LAMPA Angers, using a PROTO iXRD diffractometer (Achouri et al., 2014) equipped with a Cr anode (figure 4.14). For this anode material, the penetration depth (63% of absorption) of X-rays in steel is about 5  $\mu\text{m}$ . The peak positions associated with  $\{2\ 1\ 1\}$  planes were measured with two scintillation detectors with a  $2\theta$  range of  $18.5^\circ$  each. For each analysis, the irradiated zone was delimited with a circular collimator (0.5 mm diameter). Residual stresses were estimated from peak positions using the  $\text{Sin}^2\psi$  method (Noyan and Cohen, 1987). The X-ray elastic constants ( $s_1 = -1.28 \times 10^{-6} \text{ MPa}^{-1}$  and  $\frac{1}{2}s_2 = 5.83 \times 10^{-6} \text{ MPa}^{-1}$ ) identified for  $\alpha$ -ferrite were used to compute the residual stress state. A preliminary calibration of the device and of the post-treatment parameters done on F22 steel powder (without residual stresses) had shown that the positions of the diffraction peaks are consistent with these elastic constants.

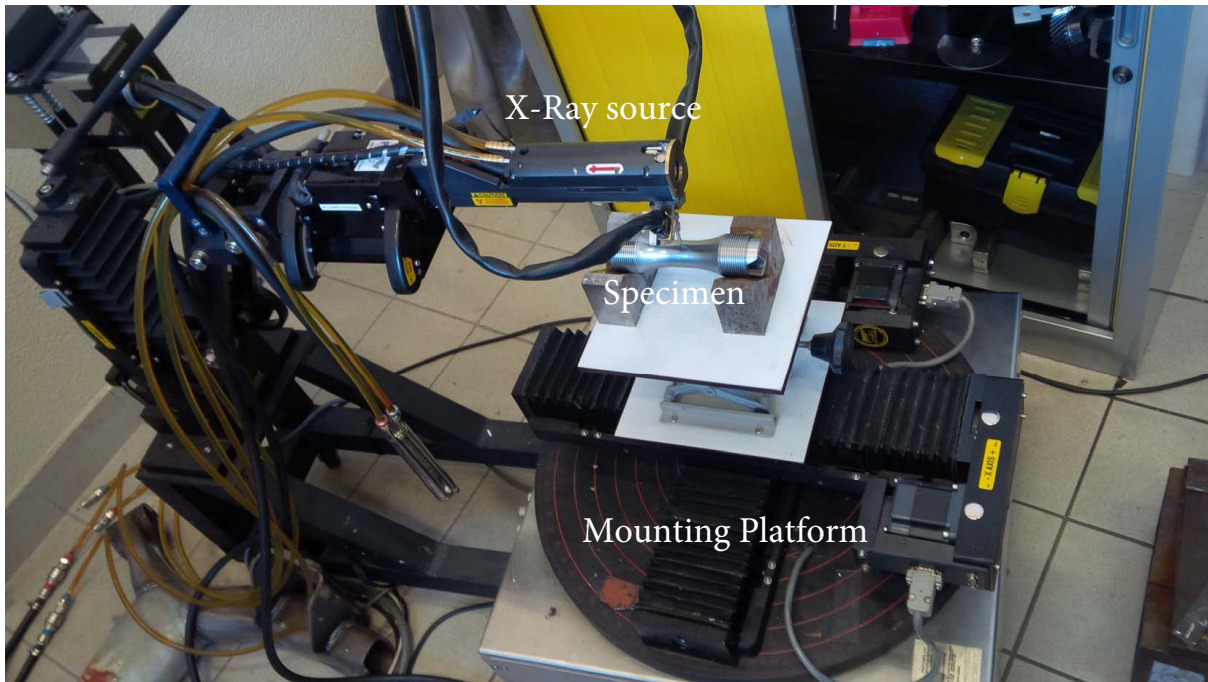


**Figure 4.14:** PROTO iXRD diffractometer used to perform residual stress analyses.

| Specimen (Position) | Residual stress (MPa) |                 |
|---------------------|-----------------------|-----------------|
|                     | Axial                 | Circumferential |
| 1 (a)               | $-400 \pm 8$          | $-288 \pm 9$    |
| 1 (b)               | $-376 \pm 10$         | $-345 \pm 12$   |
| 1 (c)               | $-382 \pm 9$          | $-304 \pm 9$    |
| 2 (a)               | $-407 \pm 5$          | $-329 \pm 11$   |
| 2 (b)               | $-388 \pm 8$          | $-239 \pm 14$   |
| 2 (c)               | $-361 \pm 12$         | $-208 \pm 14$   |

**Table 4.3:** Measured surface residual stresses on virgin specimens 1 and 2.

For virgin specimens, the analyses were done for three equally-spaced surface points along the periphery, at mid-height of the gage length (denoted by a,b and c in table 4.3) and revealed the presence of significant biaxial compressive residual stresses, scattered between  $-338$  MPa and  $-407$  MPa in the axial direction and between  $-208$  and  $-345$  MPa in the circumferential direction.

To estimate the in-depth distribution of longitudinal residual stresses, successive material removal operations to a depth of  $150 \mu\text{m}$  were performed using an electrochemical polishing technique with a solution of salted water. An in-depth profile of residual stresses

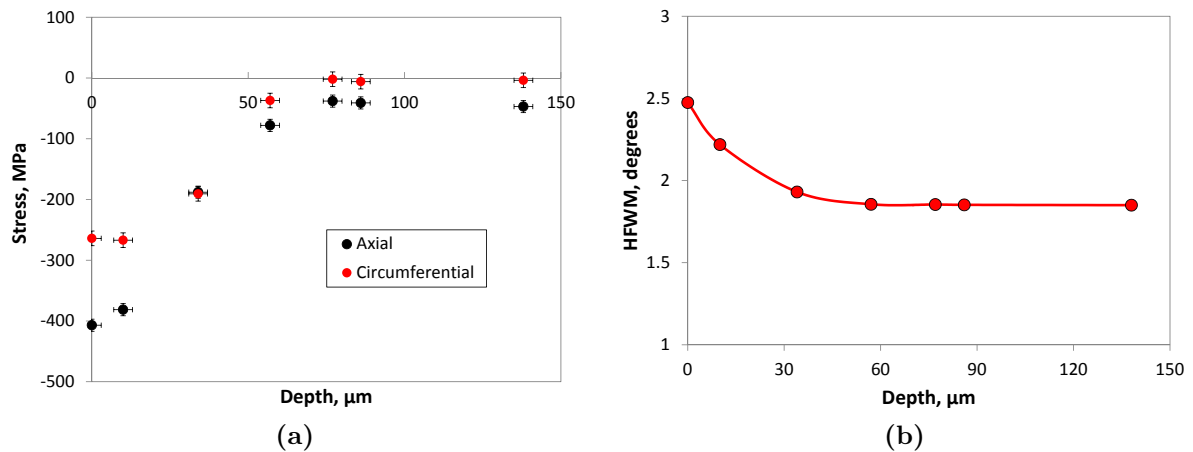


**Figure 4.15:** (a) In-depth profile of initial surface residual stresses and (b) its corresponding profile of Full-width at Half maximum (FWHM) of the X-ray diffraction peaks measured in a virgin cylindrical specimen.

is plotted in figure 4.15(a). No correction of the calculated stresses, to take into account their redistribution due to material removal, was attempted. Therefore, this is not the exact distribution of residual stresses which should satisfy self-equilibrium conditions and thus exhibit an internal tensile peak. The profile of full-width at half maximum (FWHM) (figure 4.15(b)) suggests that the depth affected by residual stresses is less than 60  $\mu\text{m}$ , which is smaller than the depth of all internal crack initiating defects.

As mentioned above, limited “ratcheting”, without any detectable cyclic plasticity, was observed and suspected to correspond to a relaxation of residual stresses. Thus, this potential relaxation was examined by measuring the residual stresses on the tested specimens, as far as possible ( $> 6 \text{ mm}$ ) from the fracture surface. Based on the superposition of the loading cycle with the maximum axial and circumferential residual stresses found in virgin specimens ( $-407$  and  $-329 \text{ MPa}$ , respectively), the minimum and maximum Von-Mises equivalent stresses ( $\sigma_{\text{Mises}}$ ) over a cycle were computed and compared with the proportional limit ( $\sigma_p = 600 \text{ MPa}$ ): If either the min or max equivalent stress exceeded the proportional limit, the residual stresses were expected to relax. The provisions made with this simple criterion are compared with the residual stresses ( $\sigma_r$ ) estimated after the fatigue tests for various R ratios and amplitudes (see table 4.4). In spite of a larger scatter in the measurements than on virgin materials, the following trends were found:

- For  $R = -1$ , the residual stresses were expected to relax, but compressive residual stresses exceeding 200 MPa were observed along the axial direction.
- For  $R = -0.5, 0$  and  $0.25$ , relaxation was neither expected nor observed.

| $R_\sigma$ | $\sigma_{applied}$ |     | $\sigma_{Mises}$ with |     | Relaxation<br>Expected | $\sigma_r$ after |              |
|------------|--------------------|-----|-----------------------|-----|------------------------|------------------|--------------|
|            | MPa                |     | $\sigma_r$ , MPa      |     |                        | fatigue, MPa     |              |
|            | Min                | Max | Min                   | Max |                        | Axial            | Tangential   |
| -1         | -385               | 385 | 318                   | 690 | Yes                    | -209 to -238     | -211 to -244 |
| -1         | -365               | 365 | 311                   | 675 | Yes                    | -215 to -304     | -180 to -185 |
| -0.5       | -240               | 480 | 370                   | 560 | No                     | -397 to -417     | -247 to -281 |
| -0.5       | -243               | 487 | 375                   | 563 | No                     | -262 to -350     | -256 to -285 |
| 0          | 0                  | 637 | 374                   | 486 | No                     | -252 to -368     | -244 to -248 |
| 0          | 0                  | 620 | 374                   | 473 | No                     | -31 to -480      | -197 to -229 |
| 0.25       | 170                | 680 | 294                   | 522 | No                     | -137 to -300     | -236 to -251 |
| 0.5        | 386                | 772 | 319                   | 601 | Yes                    | 45 to 74         | -113 to -176 |
| 0.5        | 360                | 720 | 308                   | 556 | No                     | 11 to -181       | -118 to -312 |
| 0.7        | 539                | 770 | 411                   | 600 | Yes                    | -6 to -26        | -12 to -32   |

**Table 4.4:** Surface residual stresses ( $\sigma_r$ ) measured after fatigue tests far away from the fracture surface ( $> 6$  mm).

- For  $R = 0.5$ , stress relaxation was expected only for the highest stress range but it seems to be partially relaxed only.
- For  $R = 0.7$ , relaxation was expected and indeed observed.

## 4.3 Discussion

### 4.3.1 Crack initiation

Surprisingly, the significant surface compressive residual stresses that partially or totally persisted after the tests did not inhibit surface crack initiation at  $R = -1$ ,  $-0.5$  or  $0$ . In addition, when internal crack initiation occurred, the depth of the responsible defects were higher than that of the tensile peak of longitudinal residual stresses, which according to figure 4.15(b) is less than  $60 \mu\text{m}$ . Thus, the transitions from a majority of cyclic plasticity-induced surface crack initiation for  $R = -1$ ,  $-0.5$  and  $0$  to a majority of internal crack initiation from a defect at  $R = 0.25$  and then to defect-induced surface crack initiation for  $R = 0.5$  do not seem to be controlled by residual stresses and their relaxation.

---

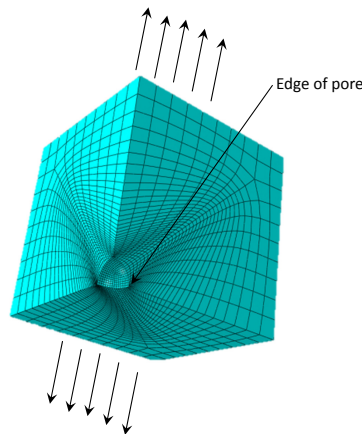
The potential role played by the changes in specimen's geometry in these transitions must be examined. For a uniform distribution of defects, the larger the gage volume, higher is the probability to find a large internal defect inside. In the 7 mm diameter specimens used for the tests at  $R = 0.25$ , the gage volume and thus this probability were smaller than in the 8 mm diameter specimens used for the tests at lower R ratio by a factor of 0.72. In spite of this, the proportion of internal crack initiation (83%) was higher than in the previous cases. This effect, although it is based on a limited number of tests, thus suggests a mechanical effect of the higher R ratio and of the associated decrease in stress range.

For the tests ran at  $R = 0.5$  and above, with diameter of 6 mm, the gage surface-to-volume ratio was increased by a factor of 1.17 compared to the specimens tested at  $R = 0.25$ . This should increase the probability for a large defect to be located on the surface rather than in the volume in the same proportion. Such a moderate effect cannot explain a change from 83% internal cracks at  $R = 0.25$  to 100% defect-initiated surface cracks at  $R = 0.5$ .

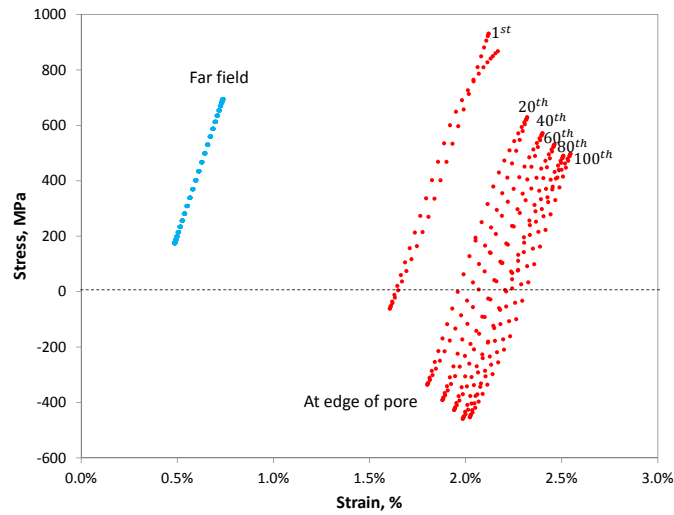
Alternative explanations for this transition have been suggested below by a compared analysis of the stress and strain fields around an internal or surface-cutting inclusion and fracture mechanics arguments.

The analytical solution of [Goodier \(1933\)](#) for the stress field around a spherical pore in an infinite elastic medium, yields a stress concentration factor  $K_t$  of 2.04 under uniaxial tension. For the stress amplitudes corresponding to the endurance limit at  $R \geq 0$ , this is sufficient to induce monotonic plastic flow ( $2.04\sigma_{max} > \sigma_p$ ) around a pore, and in some cases, cyclic plastic flow and ratcheting ( $2.04\Delta\sigma > 2\sigma_{yc}$ , where  $\sigma_{yc}$  denotes the cyclic yield stress, substantially lower than  $\sigma_p$  in this steel, see table 2.4).

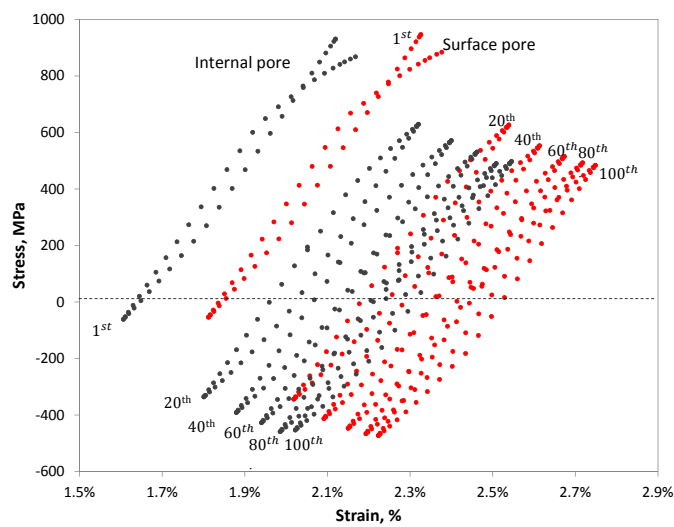
To analyze the stress and strain fields around an internal pore, a 3D finite element unit cell model containing  $1/8^{th}$  of a spherical pore was developed using quadratic hexahedron type elements (C3D20R) (figure 4.16(a)). Symmetric boundary conditions were applied on the faces adjoining the pore. Elastic-plastic simulations were run for 100 cycles of the loadings leading to internal crack initiation. The constitutive equations identified earlier, were used. For the example at  $\Delta\sigma = 520$  MPa and  $R = 0.25$ , the equivalent plastic strain at the edge of pore reached 1.8% at the first peak load and ratcheting up to 2.5% strain was observed. After 100 cycles, the steady-state normal strain range was 0.5% and the local R ratio was close to  $-1$ , which is quite different from the far field stress ratio of 0.25, as illustrated in figure 4.16(b),.



(a) FE Model with  $1/8^{th}$  pore



(b) Stress-strain loops for internal pore



(c) Stress-strain loops for internal and surface pore

**Figure 4.16:** A 3D Meshed unit cell model and normal stress-strain loops at the edge of a spherical surface and internal pore for  $\Delta\sigma = 520$  MPa,  $R = 0.25$ .

---

Similar elastic-plastic F.E. computations were run for a surface-cutting pore. For that purpose, the same mesh was used, but a symmetry condition was removed, to represent the free surface. Due to a plane stress condition, the plastic strains reach higher values at the pore edges than for an internal pore under the same far field loading. At the first peak load, the equivalent plastic strain at the edge of a surface pore is 2.0% as compared to 1.8% for an internal pore and after ratcheting during 100 cycles, it reaches 2.7% instead of 2.5% (figure 4.16(c)). However, the steady-state normal strain amplitude is same in both cases, i.e. 0.3%.

Even though the HCF tests were stress-controlled at a given R ratio, the F.E. computations clearly show that close to a pore, the local loading conditions are quite different and closer to strain-controlled low-cycle fatigue. That is why fatigue data collected in such conditions are considered to provide a reasonable baseline. Based on these fatigue data, the strain amplitude computed close to a pore should lead to crack initiation after a few thousand push-pull cycles only, in air. The lack of moist air and the sharp strain gradient on the one hand, and the higher stress triaxiality around an internal pore, on the other hand, certainly make fatigue crack initiation kinetics different from those in push-pull in air, but considering the above mentioned peak strain and amplitude, it seems quite improbable that crack initiation from internal pores controls the fatigue lives at  $R = 0.25$ .

Internal chemical heterogeneities produce smaller stress concentrations than internal pores of similar shape and size (Goodier, 1933). However, the data-points for failures initiated from the former or from the latter do not segregate on the Wöhler plot. This supports the idea that crack initiation constitutes a small fraction of the fatigue lives at  $R = 0.25$ . For the VHCF regime, there is a consensus about the predominance of the crack initiation stage from internal defects over the crack growth stage, such a conclusion does not seem to hold here.

Simulations were also run at  $R = 0.5$  for  $\Delta\sigma = 360$  MPa for a surface and internal pore respectively. At first peak load, an equivalent plastic strain of 3.9% (and 3.6% resp.) was found at the edge of the pore with ratcheting up to 4.1% (and 3.9% resp.) within 100 cycles. The normal strain amplitude at the 100<sup>th</sup> cycle was 0.2% in both cases, and the local R ratio  $-0.5$  (and  $-0.4$  resp.). These local conditions would probably be sufficient for early internal initiation from a pore at this R ratio as well.

Similar simulations ran for an internal pore at  $R = 0.6$  and the highest stress amplitude (154 MPa) used in the experiments yielded an equivalent plastic strain of 4% on the edge of pore at first peak load but no ratchetting, due to the absence of cyclic plasticity.

---

So, for  $R \geq 0.6$ , fatigue crack initiation seems improbable, in spite of the local stress concentration provided by a surface or internal pore (and even more, a surface or internal inhomogeneity). Anyway, should a crack initiate, it would probably be unable to grow, as discussed in the next section.

### 4.3.2 Crack growth

#### Mechanisms

The reduced roughness and the absence of striations on the fracture surfaces within the fish-eye are consistent with the literature on fatigue crack growth in vacuum (Stewart, 1980; McEvily and Gonzalez Velazquez, 1992). The latter attribute the absence of striations in stainless steels fatigued in vacuum to the diffuse crack tip plasticity observed in this environment. The relatively large blunting of the tip resulting from such plastic flow would reduce the crack growth rate. By contrast, Hydrogen-Enhanced-Localized-Plasticity (HELP) (Beachem, 1972; Birnbaum and Sofronis, 1994; Lynch, 2011) in moist air would induce coarse, localized crack tip plasticity, producing clear striations and leading to faster crack growth.

Note that all the defects responsible for internal crack initiation were found near the surface and that the border of each fish-eye was tangent to the free surface (as visible in figure 4.9). The frontier of the fish-eye thus corresponds to a sudden ingress of the outside air into the crack.

The presence of intergranular facets on fatigue fracture surfaces formed at low crack growth rates in Ni-Cr-Mo-V and Cr-Mo steels has often been reported as a clear sign of combined temper and hydrogen embrittlement (Stewart, 1980; Islam et al., 2005; Ritchie, 1977; Hénaff et al., 1992; Liaw et al., 1983). Islam et al. (2005) have shown that a preliminary segregation of impurities during the heat treatment is necessary for this phenomenon, but that hydrogen released by a reaction of water vapor with the metal is also necessary and that the latter readily occurs in air at room-temperature and low crack growth rate.

In the present study, the absence of any intergranular or inter-lamellar facet or secondary crack within the fish-eye areas but their presence just outside the fish-eyes (figure 4.17) is consistent with this conclusion. It is also consistent with the lower roughness within the fish-eye than outside, since Liaw et al. (1983) underlined that the presence of such

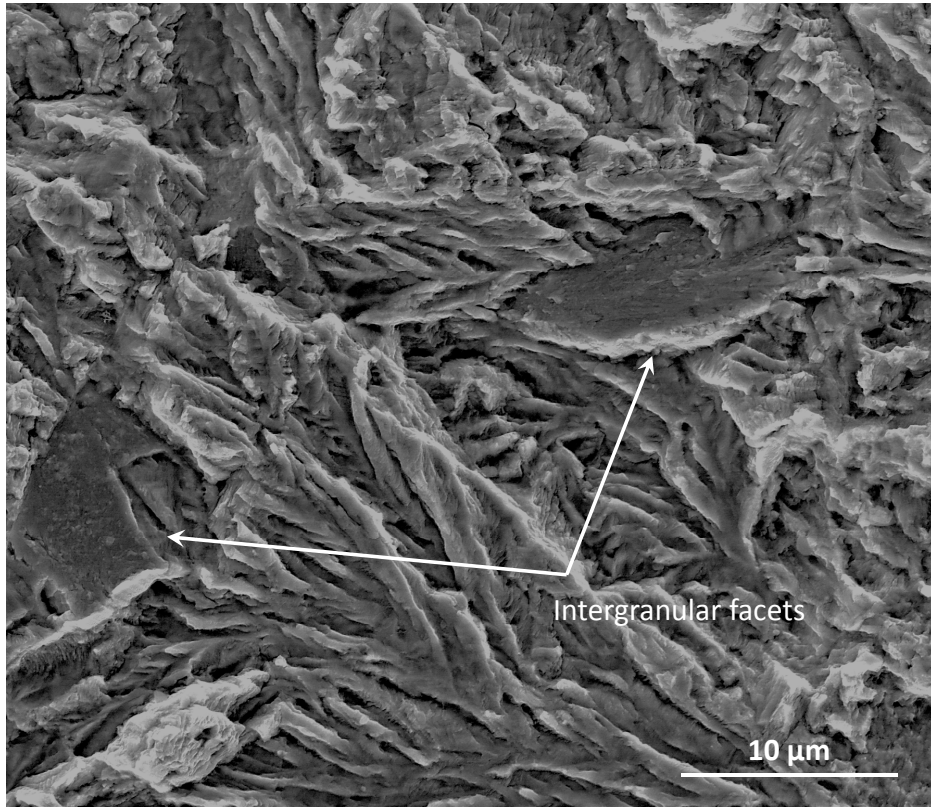


**Figure 4.17:** Presence of Intergranular facets outside the fish-eye for  $R = -0.5$ ,  $\sigma_a = 360$  MPa and  $N_f = 2,207,630$  cycles

facets increases with the roughness.

The SEM observations of twisted and mated facets near the border of a fish eye (figure 4.10(a)) and the FIB sections (figure 4.11) suggest a slight increase in roughness as the crack grows further from an internal defect with increasing  $\Delta K$ . However, roughness-induced crack closure effects (RICC) are certainly less important during crack growth inside the fish-eyes than outside. In addition, oxide-induced crack closure as well as plasticity-induced crack closure (PICC) is absent inside fish-eye. The latter can be expected because of the low  $\Delta K$ , plane strain/stress state for internal cracks and short crack lengths (although much larger than the former austenite grain size of  $7 \mu\text{m}$ , so that LEFM can reasonably be used). To check that assumption, an axisymmetric FE model of penny shaped crack with a radius typical of that found for internal cracks was developed, with sufficient mesh refinement ahead of the crack tip (less than  $1/10^{\text{th}}$  of the reversed cyclic plastic zone size). Elastic-plastic simulations with periodic node release were run for similar cyclic loadings and R ratios, as those leading to internal cracking in the experiments (without taking into account the residual stresses). The closure level was evaluated at the second node behind the crack tip and no plasticity-induced closure

---

was observed.

In summary, in the present study, internal cracks not only seem to grow with very few, if any, closure effects, but also without any assistance from moist air.

## Threshold and kinetics

The cracks grown from internal defects were considered as elliptical, their major/minor semi-axes: ‘a’ and ‘b’, were measured and the stress intensity factor was computed as (Murakami et al., 1994):

$$\Delta K_{I,max} = \frac{\Delta\sigma\sqrt{\pi b}}{E(k)} \quad (4.3)$$
$$E(k) = \int_0^{\frac{\pi}{2}} (1 - k^2 \sin^2 \phi)^{1/2} d\phi$$
$$k^2 = 1 - \left(\frac{b}{a}\right)^2$$

The maximum value for an elliptical crack occurs at the end point of the minor axis, “b”. The stress intensity factor range is calculated by taking into account only the tensile part of the stress. Both the initial and final  $\Delta K_I$  (considering the defect as a crack in the former case and at the border of the fish eye in the latter) have been calculated and are reported in table 4.5.

The  $\Delta K_I$  values computed with the approximate expression from Murakami (2002) (equation 4.4) were less than 8% different from those computed with equation 4.3.

$$\Delta K_I = \beta\sigma_{max}\sqrt{\pi\sqrt{area}} \quad (4.4)$$

where “area” denotes the area of the defect projected on the plane normal to the tensile stress,  $\beta = 0.5$  for an internal defect and  $\beta = 0.65$  for a surface defect.

The initial  $\Delta K_I$  is almost constant for all defects observed and lies between 3.8 and 4.4  $\text{MPa}\sqrt{m}$  (see the bar superimposed on figure 4.18(a) and the comparison with threshold data in air from Suresh et al. (1981) and Liaw et al. (1983) is shown in figure 4.18(b)). In particular, the values found for the two specimens broken at  $R = -0.5$  are close to

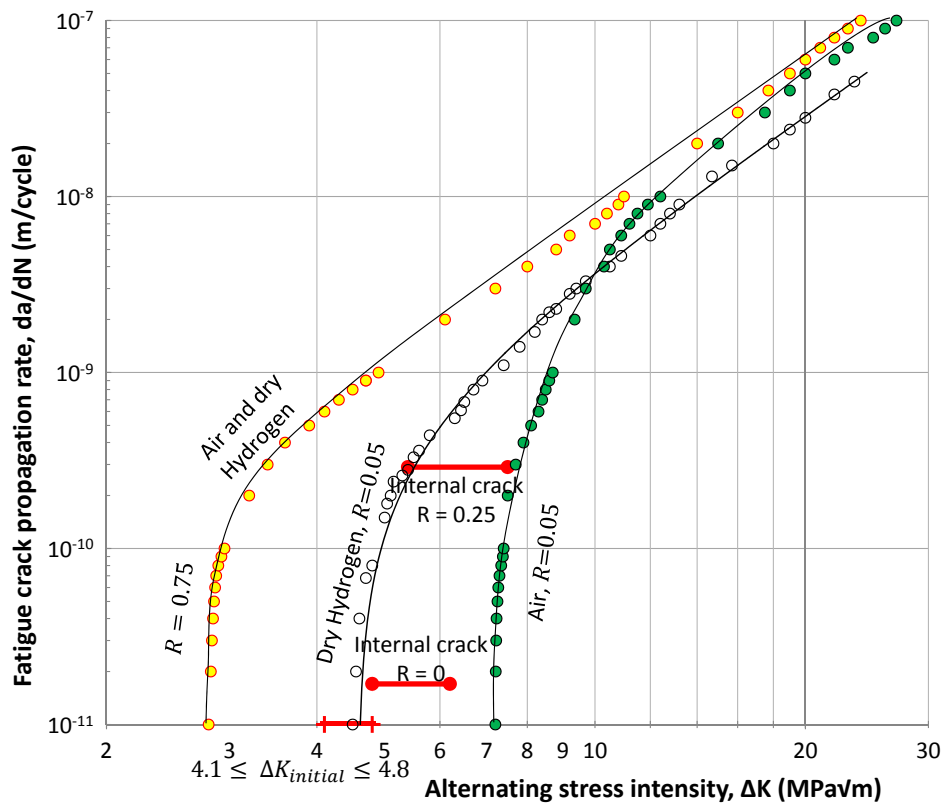
| Test | R    | $\Delta\sigma$<br>MPa | Size of defect    |                   | $\Delta K_{I,max}$ (MPa $\sqrt{m}$ ) |       | $N_f$       | $N_{fish}$ |
|------|------|-----------------------|-------------------|-------------------|--------------------------------------|-------|-------------|------------|
|      |      |                       | 2a, $\mu\text{m}$ | 2b, $\mu\text{m}$ | Initial                              | Final |             |            |
| 16   | -0.5 | 480                   | 135               | 66                | 4.1                                  | 8.3   | 2,207,630   | 160,000    |
| 18   | -0.5 | 487                   | 199               | 66                | 4.4                                  | 10.0  | 741,938     | 150,000    |
| 23-1 | 0    | 600                   | 120               | 60                | 4.8                                  | 6.2   | > 3,000,000 | 50,000     |
| 26-1 | 0.25 | 500                   | 304               | 50                | 4.3                                  | 8.9   | > 3,000,000 | 110,000    |
| 25   | 0.25 | 500                   | 95                | 95                | 3.9                                  | -     | 339,602     | -          |
| 24   | 0.25 | 510                   | 127               | 65                | 4.2                                  | -     | 300,333     | -          |
| 26-2 | 0.25 | 520                   | 304               | 50                | 9.2                                  | 13.3  | 1,704,174   | 40,000     |
| 23-2 | 0.25 | 520                   | 120               | 60                | 5.4                                  | 7.5   | 373,933     | 70,000     |
| 30   | 0.25 | 540                   | 120               | 40                | 3.8                                  | -     | 160,277     | -          |

**Table 4.5:** Initial and final Stress intensity factor range and estimated number of cycles for crack propagation within the fish eye ( $N_{fish}$ ). Specimens marked (1,2) survived 3 million cycles and were reloaded. In that case, crack growth from the last beach mark was considered.

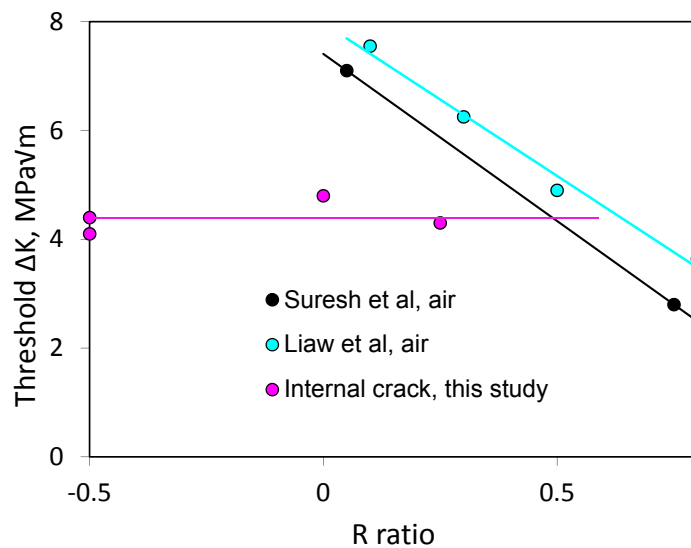
the specimens broken at  $R = 0.25$ . This is consistent with the idea of [Stewart \(1980\)](#) and [Vasudevan et al. \(2005\)](#), that the threshold  $\Delta K$  for crack growth in vacuum is much less dependent on the R ratio than in air, although both studies, contrary to the present one, considered only positive R ratios.

[Suresh et al. \(1981\)](#) investigated fatigue crack growth kinetics and thresholds on a similar 2.25%Cr-1%Mo steel in air, dry helium and dry hydrogen for  $R = 0.05$  and 0.75 (figure 4.18(a)). They obtained  $\Delta K_{threshold} = 7.1$  MPa $\sqrt{m}$  at  $R = 0.05$  in air. In a reducing atmosphere (dry H<sub>2</sub>), which nearly suppressed oxide-induced closure, the threshold at  $R = 0.05$  dropped to 4.5 MPa $\sqrt{m}$ . The initial  $\Delta K_I$  values for the crack grown from internal defects are even below this threshold. This seems logical since these internal cracks, which grow in vacuum, are not only free from oxide-induced closure but they are also short and rather smooth cracks and undergo very limited plasticity and roughness-induced closure.

Anyway, based on the threshold of 7.1 MPa $\sqrt{m}$  that [Suresh et al. \(1981\)](#) obtained in air at  $R = 0.05$ , and the usually accepted idea that vacuum makes crack growth slower and the threshold higher, the internal cracks found here at  $R = -0.5$  should not propagate. The fact that these cracks actually grew at such a low  $\Delta K$  in spite of a lower R ratio suggests either that the reduction in crack closure compensates (or even overcompensates) the lack of environmental assistance to crack growth or that some moist air trapped in the



(a)



(b)

**Figure 4.18:** (a) Crack growth kinetics in 2.25Cr-1Mo steel at various R ratios in air and dry Hydrogen (Re-plotted from [Suresh et al. \(1981\)](#)) with some data (red bars) from present study superimposed. (b) Comparison of threshold  $\Delta K$  values issued from [Liaw et al. \(1983\)](#), [Suresh et al. \(1981\)](#) and the present study.

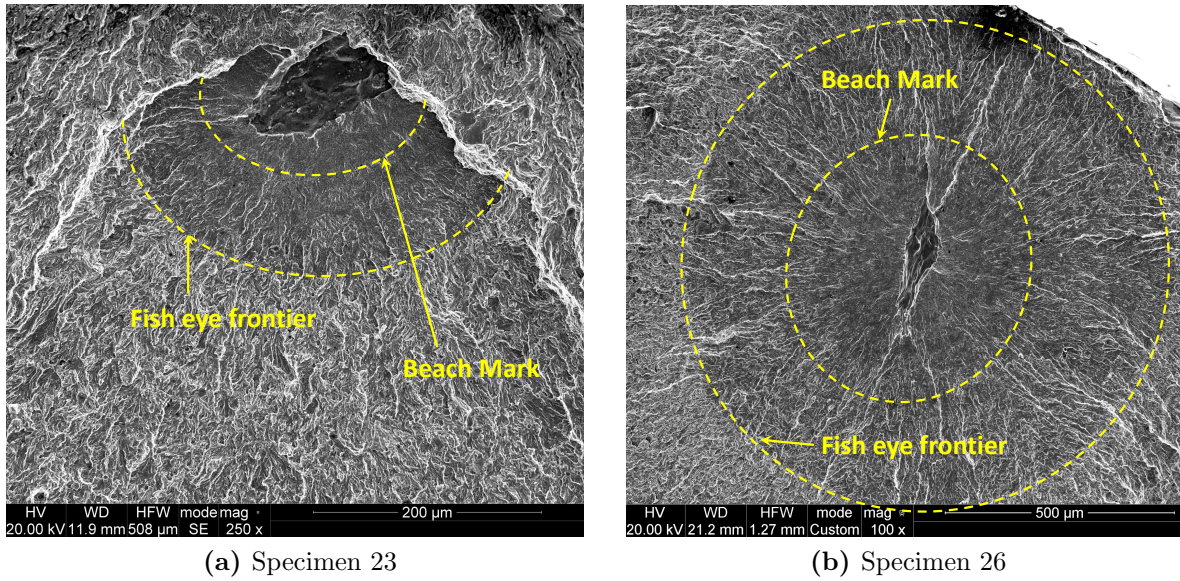


**Figure 4.19:** Beach marks observed in fish eye for specimens 23 and 26 respectively.

pore assists incipient crack growth. However, no crystallographic, intergranular or inter-lamellar area, expected in case of environment-assisted crack growth was observed around the defects, but a smooth featureless surface, so that the first explanation is preferred.

An attempt to use the crack growth kinetics measured by Suresh et al. (1981) in air or reducing atmosphere at  $R = 0.75$ , which probably corresponds to an intrinsic, closure-free crack growth kinetics to evaluate the number of cycles spent in internal crack growth from the defect to the border of fish-eye is made. The curve was thus digitized and integrated stepwise (see appendix Appendix A). The result, denoted by  $N_{\text{fish}}$  is reported in table 4.5. It can be seen that  $N_{\text{fish}}$  does not constitute a negligible fraction of the measured fatigue lives: it reaches 39% for specimen 18.

However, the real growth rates of internal cracks growing without any assistance of moist air is probably significantly lower than suggested by these crack growth data obtained in air.

Beach marks observed on the fracture surface within the fish eye of two specimens (23 and 26) submitted successively to different loading amplitudes provide some information on crack growth kinetics that support this assumption. Specimen 23 survived 3 million cycles at  $\sigma_a = 300$  MPa,  $R = 0$  and was then reloaded at  $\sigma_a = 260$  MPa,  $R = 0.25$ . It failed after only 373,933 cycles. Figure 4.19a shows that a beach mark separates the areas corresponding to those two loading blocks. From the position of the beach mark, it can be deduced that under the second loading, it took 373,933 cycles for the crack to

---

grow by 87  $\mu\text{m}$ . The average crack growth rate is thus  $2.9 \times 10^{-10}$  m/cycle while  $\Delta K$  increased from 5.6 to 7.5  $\text{MPa}\sqrt{\text{m}}$  so that the mean  $\Delta K$  is 6.55  $\text{MPa}\sqrt{\text{m}}$ . Specimen 26 survived 3 million cycles at  $\sigma_a = 240$  MPa,  $\sigma_a = 245$  MPa and  $\sigma_a = 250$  MPa and finally failed after 1,704,174 cycles at  $\sigma_a = 260$  MPa. Figure 4.19b shows that a beach mark separates the areas corresponding to the third and fourth loading blocks. The position of this beach mark gives an average crack growth rate of  $1.5 \times 10^{-10}$  m/cycle for a mean  $\Delta K$  of 11.6  $\text{MPa}\sqrt{\text{m}}$ . These data, corresponding to internal crack growth at  $R = 0$  and  $R = 0.25$ , are superimposed on the kinetics curves re-plotted from Suresh et al. (1981) (figure 4.18(a)) and appears to be on the left side of the kinetics curve obtained in air at  $R = 0.05$ .

For a better analysis of internal crack growth, crack growth kinetics collected in vacuum would thus be more pertinent which is currently not in scope of present thesis.

For  $R = 0.5$ ,  $\Delta K$  was found to be 3.7 to 3.9  $\text{MPa}\sqrt{\text{m}}$  for surface defects as shown in figure 4.8(b). No threshold data is available for crack growth in air at that R ratio in the paper by Suresh et al. (1981), but according to the extensive  $\Delta K_{threshold}$  versus R database gathered by Bulloch (1991) for steels with a tempered martensite microstructure, these values are still compatible with crack growth and thus fatigue failure, as observed. Comparatively, according to equation 4.4,  $\Delta K_I$  for a crack initiated from an internal defect of similar size would be between 2.85 and 3  $\text{MPa}\sqrt{\text{m}}$ , which is clearly below the scatter-band of threshold  $\Delta K$  values reported by Bulloch (1991) for this R ratio in air, and also well below the smallest  $\Delta K$  computed for any of the internal cracks observed (see figure 4.18). This explains why at  $R = 0.5$ , only cracks initiated from surface defects were observed.

By contrast, the  $\Delta K$  computed for the cyclic loading conditions used at  $R = 0.6$  or  $0.7$ , assuming the presence of the most critical observed defect in a specimen (which is 199  $\mu\text{m}$  by 66  $\mu\text{m}$  wide), comes out to be around 2  $\text{MPa}\sqrt{\text{m}}$ . Comparing it with the 2.8  $\text{MPa}\sqrt{\text{m}}$  threshold measured, in the absence of closure by Suresh et al. (1981) at  $R = 0.75$  in air and dry  $H_2$ , it seems that such defects would not propagate. This explains why specimens at very high R ratio did not fail from defects by fatigue within  $10^7$  cycles only.

## 4.4 Concluding remarks

A decrease in the slope of Wöhler curves and an increased scatter in fatigue lives were observed when the R ratio rose. Similar effects have been reported in literature (see for example fig. 6.29 in Murakami (2002)). It can be suggested that for  $R < 0$  and

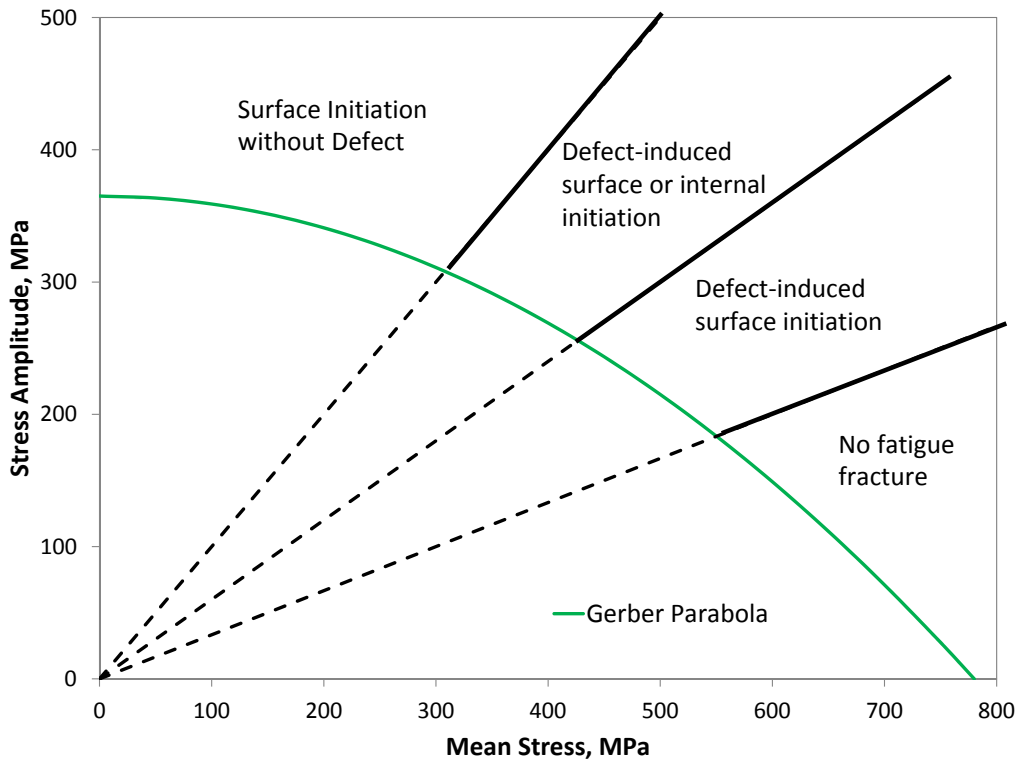


**Figure 4.20:** A tentative map of the mechanisms of fatigue failure depending upon the mean stress or R-ratio at 3 million cycles.

thus relatively high stress ranges, that allow the threshold  $\Delta K$  for crack growth to be surpassed easily for very small cracks, the crack growth rates and thus the fatigue lives vary significantly with the loading range. By contrast, for higher R ratios and thus smaller stress ranges, the fatigue lives become more and more dependent on the presence of defects large enough to allow the threshold  $\Delta K$  to be reached. The scatter in fatigue lives increases and the slope of Wöhler curves decreases, which makes the safe fatigue design of structures tricky. It might be reasonable to consider R-ratio dependent safety factors but [Murakami \(2002\)](#) advised not to use such (more or less arbitrary) safety factors in design, rather a lower bound for the endurance limit issued from a statistical analysis of defects size distribution. Although, such an approach is more rational and based on fracture mechanics, it is however not clear if it would capture the R-ratio dependence of the scatter in fatigue lives.

Finally, a tentative map of the mechanisms that control the fatigue strength at 3 million

---

cycles depending on the mean stress or R ratio is shown in figure 4.20. For low mean stresses, surface crack initiation merely due to cyclic plasticity predominates, but when the mean stress rises and the amplitude decreases, the stress concentration provided by a defect becomes necessary for crack initiation. At intermediate R ratios and amplitudes, cracks are able to grow from surface or internal defects, but as the R ratio is further increased (to 0.5 in the present case) and the amplitude decreased, only the cracks grown in air from surface defects which, according to equation 4.4, undergo a higher  $\Delta K$  than those from internal defects of similar size can cause failure. For even higher R ratios, the amplitude becomes too small to allow any crack to grow, be it in air or in vacuum.

Note that this map would change if a larger number of cycles was chosen to define the endurance limit: the defect-controlled fracture domain would probably extend to lower mean stresses/R ratios. The map, which is plotted for uniaxial loading, would probably change for biaxial loading, because the stress concentration around a defect depends on the far-field stress state [Goodier \(1933\)](#). For example, the  $K_t$  around an internal spherical pore is 1.36 under equibiaxial tension instead of 2.04 in uniaxial tension. The defect-controlled fracture domain is then expected to shrink.



# Chapter 5

## Effect of biaxial tension in air

Combined cyclic tension and internal pressure tests with various proportions of each loading were run to investigate the effect of positive stress biaxiality on fatigue lives and damage mechanisms.

The ability of various fatigue criteria to capture the effects of mean stress and biaxiality was then evaluated. For that purpose, the endurance limit of the material in reversed torsion was also determined. The endurance limits predicted by existing criteria appeared inconsistent with the experimental data, so that a new criterion had to be formulated.

### 5.1 Experimental procedures

Tubular specimens (figure 5.1a) with 25 mm outer diameter, thickness  $e = 1$  mm and  $R_a = 0.2 \mu\text{m}$  internal/external surface roughness were used for load/pressure-controlled, in-phase tension and internal oil pressure tests run at 10 Hz with  $R = 0.25$  on a triaxial testing machine ( $\pm 100$  kN,  $\pm 600$  Nm, 1500 bars).

In an infinite tube of inner/outer radius  $R_1$  and  $R_2$  an internal pressure  $P$  induces at a point of radius  $r$ , a tangential stress ( $\sigma_{\theta\theta}$ ) is given by:

$$\sigma_{\theta\theta}(r) = \frac{P R_1^2}{R_2^2 - R_1^2} + \frac{P R_1^2 R_2^2}{R_2^2 - R_1^2} \frac{1}{r^2} \quad (5.1)$$

which is maximum on the inner surface. The ratio of the inner to outer tangential stress

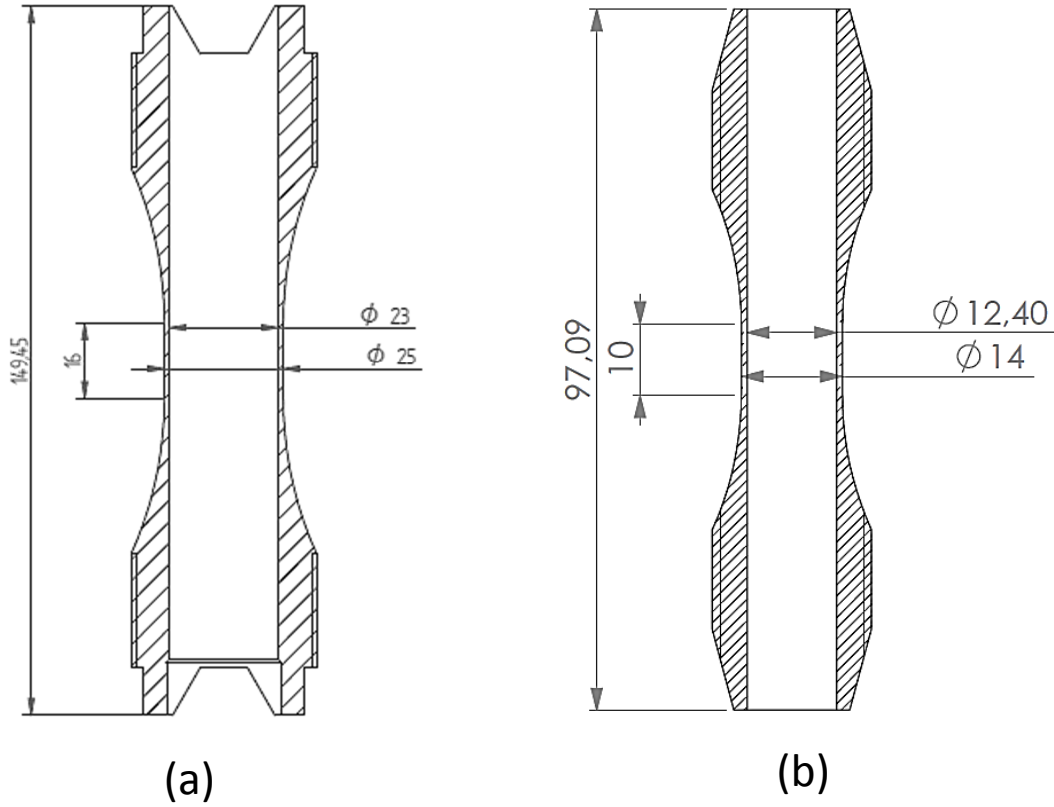


**Figure 5.1:** Geometry of specimens used for a) Biaxial tension and b) Torsion fatigue tests.

is thus:

$$\frac{\sigma_{\theta\theta,\max}}{\sigma_{\theta\theta,\min}} = 0.5 \left[ 1 + \left( \frac{R_2}{R_1} \right)^2 \right] \quad (5.2)$$

For the present geometry, this ratio is equal to 1.08. As it will be shown below, it explains a preference for crack initiation on the inner surface for equibiaxial loading. However, this weak hoop stress gradient was ignored to chose the axial load range  $\Delta F$  and pressure range  $\Delta P$ , so as to get the desired biaxiality ratio (B), defined as:

$$B = \frac{\Delta\sigma_{\theta\theta}}{\Delta\sigma_{zz}} = \frac{\frac{\Delta PR_m}{e}}{\frac{\Delta F}{S} + \frac{\Delta PR_m}{2e}} \quad (5.3)$$

where  $R_m$  is the mean radius and S is the cross section of the tubes. Strain gage rosettes were used to check the consistency of expected and measured stress states in the gage length within the elastic regime and to determine Poissons ratio,  $\nu$ , and Youngs moduli  $E_z$  and  $E_\theta$  along the longitudinal and transverse directions. Less than 3% difference was

---

found between  $E_z$  (214 GPa) and  $E_\theta$  (220 GPa).

The tests were performed at various biaxiality ratios (0, 0.25, 0.5 and 1) and run until a through crack with oil leakage was formed, or until specimen ran out at  $3 \cdot 10^6$  cycles. Where more than 1 specimen ran out, the endurance limit was assumed to be the maximum stress amplitude below which none failed.

Tubular specimens (figure 5.1b) with 14 mm outer diameter, 0.8 mm thickness, 16 mm gage length, and  $R_a = 0.2 \mu\text{m}$  internal/external surface roughness were used for torque-controlled reversed torsion tests run at 10 Hz, on the same testing machine until the complete separation of the specimens. Where more than 1 specimen ran out after  $3 \cdot 10^6$  cycles, the endurance limit was assumed to be the maximum stress amplitude below which none failed.

Scanning Electron Microscopy (SEM) was used for fractographic observations, in order to investigate the damage mechanisms. A digital optical microscope was used to perform topographic measurements along the crack paths.

## 5.2 Experimental results

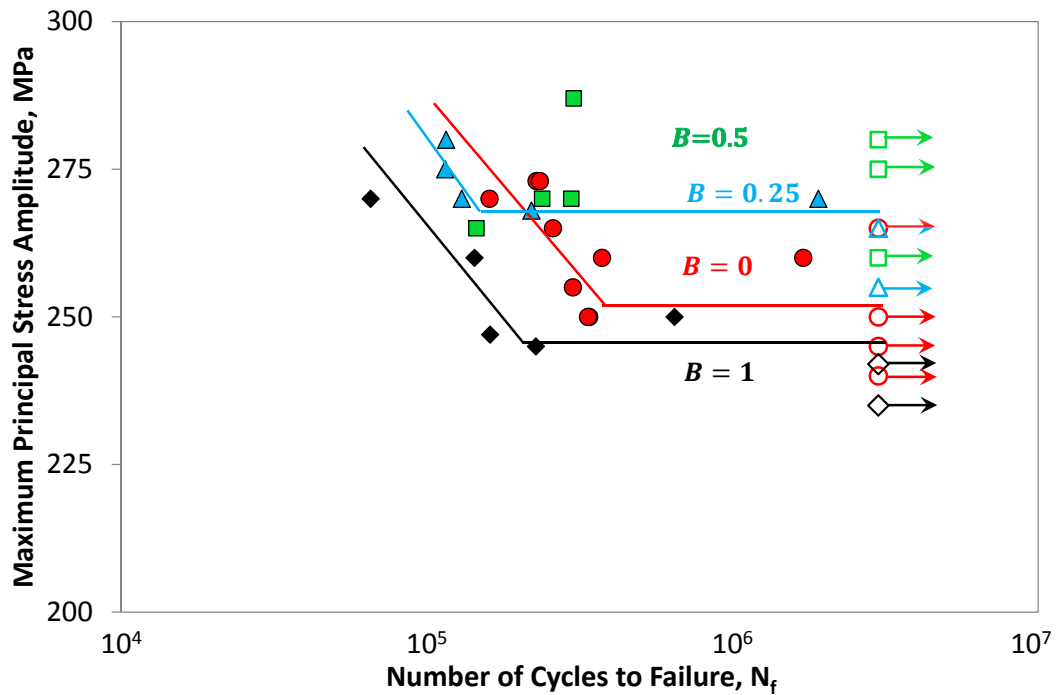
### 5.2.1 Cyclic biaxial tension

Biaxial tension fatigue results are reported in table 5.1. Figure 5.2a compares the evolutions of fatigue lives with the amplitude of the maximum principal stress, for different biaxiality ratios,  $B$ , including those obtained previously on cylindrical specimens for  $B = 0$ . A few uniaxial fatigue tests on tubular specimens at  $R = 0.25$  have shown no significant difference in lives with cylindrical specimens.

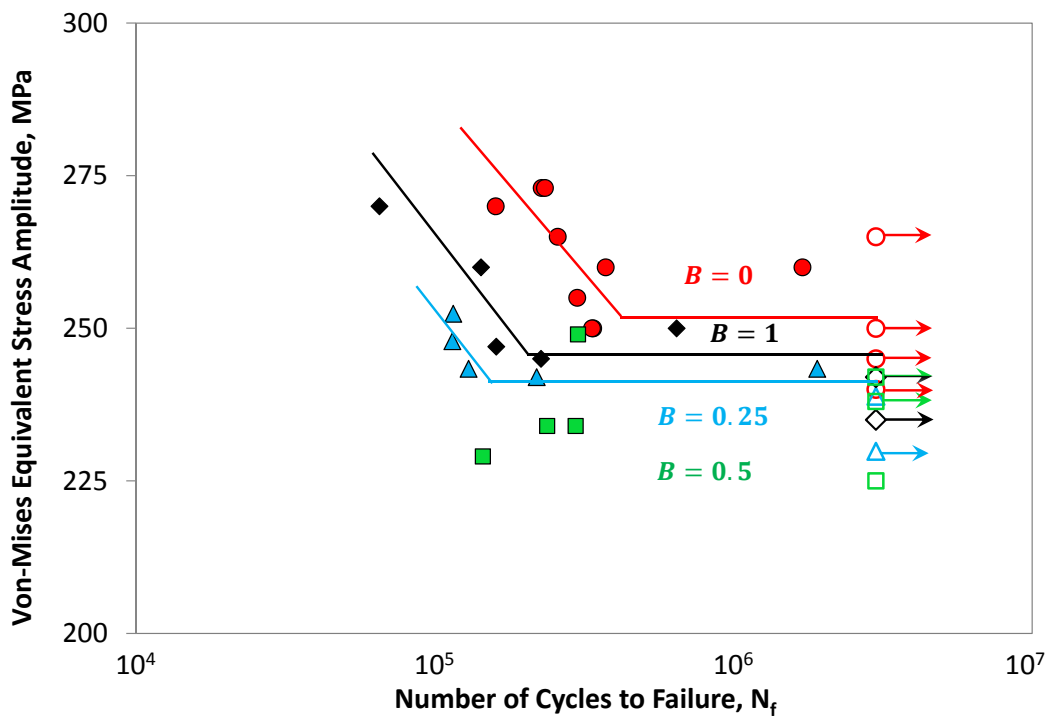
In spite of a large scatter, the asymptote of the Wöhler curve for  $B = 0.25$  seems to lie above that for  $B = 0$ , suggesting a beneficial effect of that specific stress biaxiality, while the contrary seems to hold for  $B = 1$ . The scatter in fatigue lives for  $B = 0.5$  does not allow a firm conclusion, but most fatigue data points for this biaxiality lie above the uniaxial Wöhler curve, and even above the curve for  $B = 0.25$ , suggesting a more pronounced beneficial effect. This trend is consistent with results from [Bellett et al. \(2010\)](#) who reported a beneficial effect of biaxial tension for  $B = 0.45$  on the fatigue life of two aluminum alloys.

| $\sigma_{zz,a}$ , MPa | B    | Cycles to failure, $N_f$ | Initiation type              | Crack orientation |
|-----------------------|------|--------------------------|------------------------------|-------------------|
| 273                   | 0    | 234,213                  | Inner surface Pore           | Transverse        |
| 265                   | 0    | 258,366                  | Outer surface Inhomogeneity  | Transverse        |
| 250                   | 0    | 336,596                  | Outer surface Pore           | Transverse        |
| 280                   | 0.25 | 115,531                  | Outer surface                | Transverse        |
| 275                   | 0.25 | 114,701                  | Inner surface                | Transverse        |
| 270                   | 0.25 | 129,972                  | Inner surface Inhomogeneity  | Transverse        |
| 270                   | 0.25 | 1,908,883                | Inner surface                | Transverse        |
| 268                   | 0.25 | 219,697                  | Inner surface without defect | Transverse        |
| 265                   | 0.25 | > 3,000,000              | -                            | -                 |
| 255                   | 0.25 | > 3,000,000              | -                            | -                 |
| 287                   | 0.5  | 302,091                  | Outer surface Inhomogeneity  | Transverse        |
| 280                   | 0.5  | > 3,000,000              | -                            | -                 |
| 275                   | 0.5  | > 3,000,000              | -                            | -                 |
| 270                   | 0.5  | 238,224                  | Outer surface Inhomogeneity  | Transverse        |
| 270                   | 0.5  | 296,839                  | Outer surface Inhomogeneity  | Transverse        |
| 265                   | 0.5  | 145,221                  | Outer surface Pore           | Transverse        |
| 260                   | 0.5  | > 3,000,000              | -                            | -                 |
| 270                   | 1    | 65,424                   | Inner surface                | Longitudinal      |
| 260                   | 1    | 143,084                  | Inner surface                | Longitudinal      |
| 250                   | 1    | 645,832                  | Outer surface                | Longitudinal      |
| 247                   | 1    | 160,916                  | Outer surface                | Longitudinal      |
| 245                   | 1    | 227,250                  | Inner surface Pore           | Transverse        |
| 242                   | 1    | > 3,000,000              | -                            | -                 |
| 235                   | 1    | > 3,000,000              | -                            | -                 |

**Table 5.1:** Biaxial cyclic tension data at  $R = 0.25$ ,  $\sigma_{zz,a}$  is the applied axial stress amplitude and B is the biaxiality ratio.



(a)



(b)

**Figure 5.2:** Whöler curves for  $R = 0.25$  and various load biaxiality ratios,  $B$  (equation 5.3). (a) in terms of first principal stress amplitude and b) in terms of Von Mises stress amplitude. For  $B = 0$ , data obtained previously on cylindrical specimens have been added.

---

Note that in plane stress, Von-Mises equivalent stress range ( $\Delta\sigma_{eq}$ ) is a non-linear function of load biaxiality, B:

$$\Delta\sigma_{eq} = \Delta\sigma_{zz}\sqrt{1 - B + B^2} \quad (5.4)$$

It decreases from  $\Delta\sigma_{zz}$  for  $B = 0$ , to  $0.90\Delta\sigma_{zz}$  for  $B = 0.25$  and down to a minimum value of  $0.87\Delta\sigma_{zz}$  for  $B = 0.5$ , before going up again, to  $\Delta\sigma_{zz}$ , for  $B = 1$ .

The seemingly beneficial effect of load biaxiality for  $B = 0.25$  or  $0.5$  could thus be expected to rationalize when the equivalent stress is used to correlate the fatigue lives. But this is not the case, as shown in figure 5.2b, on which the data-points for  $B = 0.25$  and  $0.5$ , now all lie well below the uniaxial Wöhler curve. By contrast, the relative positions of the uniaxial and equibiaxial Wöhler curves do not change when Von Mises equivalent stress is used instead of the first principal stress. Figure 5.2a and Figure 5.2b both suggest a slight depreciating effect of equibiaxial loading on fatigue lives. Clearly, for all biaxiality ratios, life predictions based on uniaxial fatigue data and Von Mises equivalent stress amplitudes would be non-conservative.

All biaxial fatigue failures initiated from the surface, and in many cases, due to a surface-cutting defect. The orientation of the crack (longitudinal or transverse) and its origin (internal/external surface of the tube) are reported for each test in table 5.1. For predominant axial loading ( $B = 0.25$  or  $0.5$ ), transverse cracks initiated either from the inner or the outer surface of the tubes, while for equibiaxial tension, longitudinal or transverse cracks initiated, and the latter most often from the inner surface of the tubes. This is probably due to the slight gradient in hoop stress, 8% higher on the internal surface than on the external one.

For the cases where the crack initiated from the inner diameter of the tubes ( $B = 1$  only), the gradient in hoop stress (higher on inner diameter) was taken into account and the fatigue data was replotted as shown in figure 5.3. But the conclusion (slight detrimental effect of equibiaxial tension) remained unchanged.

Fractographic observations revealed the presence of a many intergranular facets among areas of transgranular crack growth (figure 5.4a). To evaluate the surface fraction of intergranular facets along the crack path, through the depth, high resolution SEM images were captured with a magnification of 400. The line fraction of intergranular facets intercepted by a  $50 \mu\text{m}$ -long radial segment (so that  $\Delta K_I$  does not change significantly over this segment) was measured at various depths and plotted against  $\Delta K_I$  (figure 5.4b).

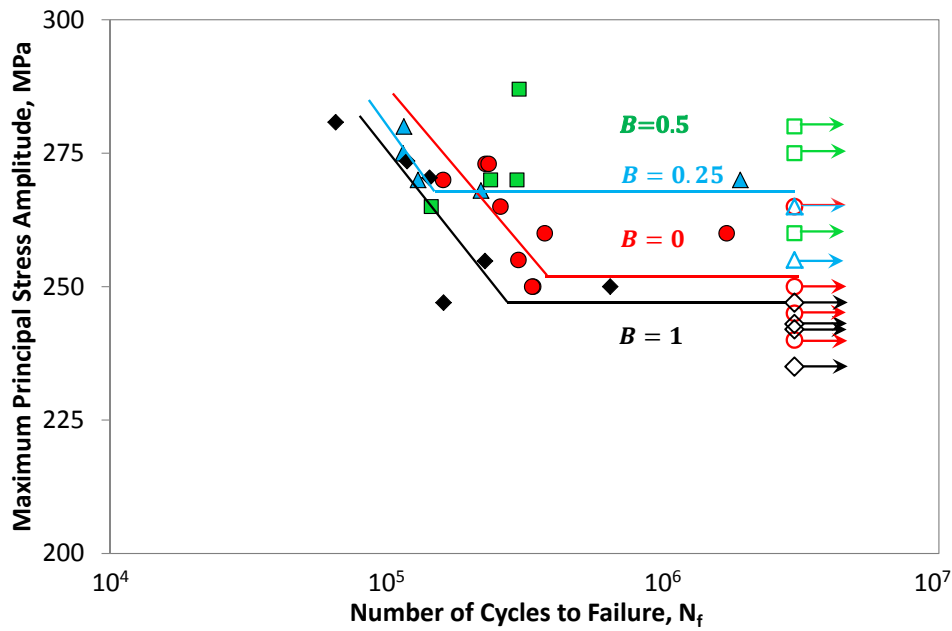
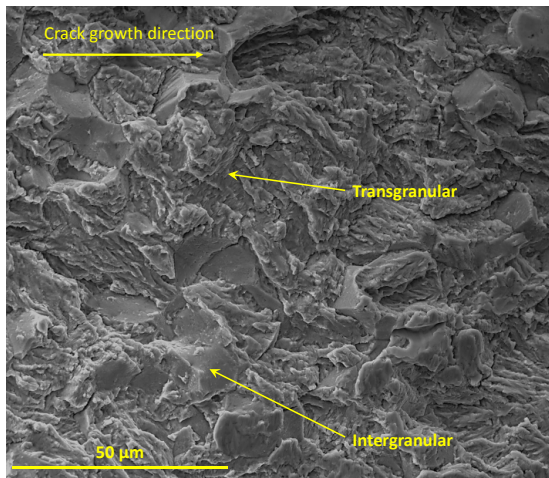
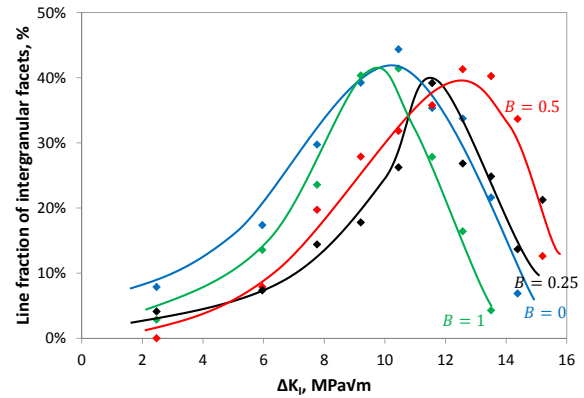


**Figure 5.3:** Modified Whöler curves including the gradient in hoop stress for data points where crack initiated from inner surface.



(a)



(b)

**Figure 5.4:** (a) Fracture surface with intergranular facets after biaxial tension fatigue at  $R = 0.25$ ,  $B = 1$  and  $\Delta\sigma_{zz}/2 = 275$  MPa. (b) Measured line fraction of intergranular facets as a function of  $\Delta K_I$ , for the same axial stress amplitude (270 MPa) and various stress biaxiality ratios,  $B$ .

$\Delta K_I$  was computed with Newman and Rajus equation for a surface crack in a plate of finite thickness loaded in tension (Newman and Raju, 1984), assuming that the crack is semi-circular. The latter assumption is supported by fractographic observations. According to Linear Elastic Fracture Mechanics, a secondary stress parallel to a crack (T

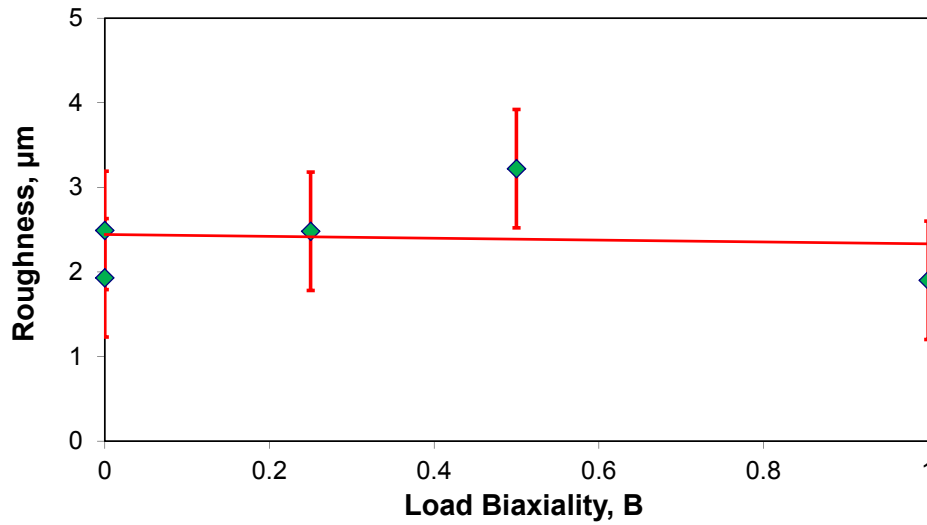


**Figure 5.5:** Peak roughness values for various load biaxialities at same stress amplitude (270 MPa).

stress) does not modify the stress intensity factor. Newman and Raju's equation are thus equally valid for uniaxial or biaxial tension. For the small cracks considered here (less than 600  $\mu\text{m}$  deep and 1.2 mm long), the error committed on  $\Delta K_I$  by considering a plate instead of a tube is limited. For all stress states, the surface fraction of intergranular facets first rises with  $\Delta K_I$ , reaches a peak value of 40 – 45% which does not seem to vary with the load biaxiality ratio, and then decreases. The curves however seem to be shifted and the value of  $\Delta K_I$  corresponding to the maximum fraction of facets is around 10  $\text{MPa}\sqrt{\text{m}}$  for  $B = 0$  and  $B = 1$ , 12  $\text{MPa}\sqrt{\text{m}}$  for  $B = 0.25$ , and 13  $\text{MPa}\sqrt{\text{m}}$  for  $B = 0.5$ .

A digital optical microscope was used to measure and compare the roughness of fracture surfaces, but no significant difference in peak roughness values along the crack path, from the initiation site to the other surface of the tube, was found between specimens tested at the same axial stress amplitude (270 MPa), but different load biaxiality ratios (figure 5.5).

## 5.2.2 Reversed torsion

The results of the fully reversed torsion tests are summarized in table 5.2 and the corresponding Wöhler curve is plotted on figure 5.6. Out of nine tests, seven gave rise to transverse, shear-mode failure, and two specimens did not fail until 3 million cycles. These data allowed an estimation of the endurance limit for torsion  $\tau_{-1}$  at 250 MPa, which was used to calibrate a few fatigue criteria, as discussed below. The fracture sur-

| $\tau_a$ , MPa | Cycles to failure, $N_f$ | Crack orientation |
|----------------|--------------------------|-------------------|
| 300            | 15,290                   | Transverse        |
| 285            | 43,946                   | Transverse        |
| 260            | 107,141                  | Transverse        |
| 255            | 174,550                  | Transverse        |
| 252            | 201,773                  | Transverse        |
| 250            | 181,415                  | Transverse        |
| 250            | > 3,000,000              | -                 |
| 245            | 114,677                  | Transverse        |
| 220            | > 3,000,000              | -                 |

**Table 5.2:** Fully-reversed torsion data at 10 Hz,  $\tau_a$  is the applied shear stress amplitude.

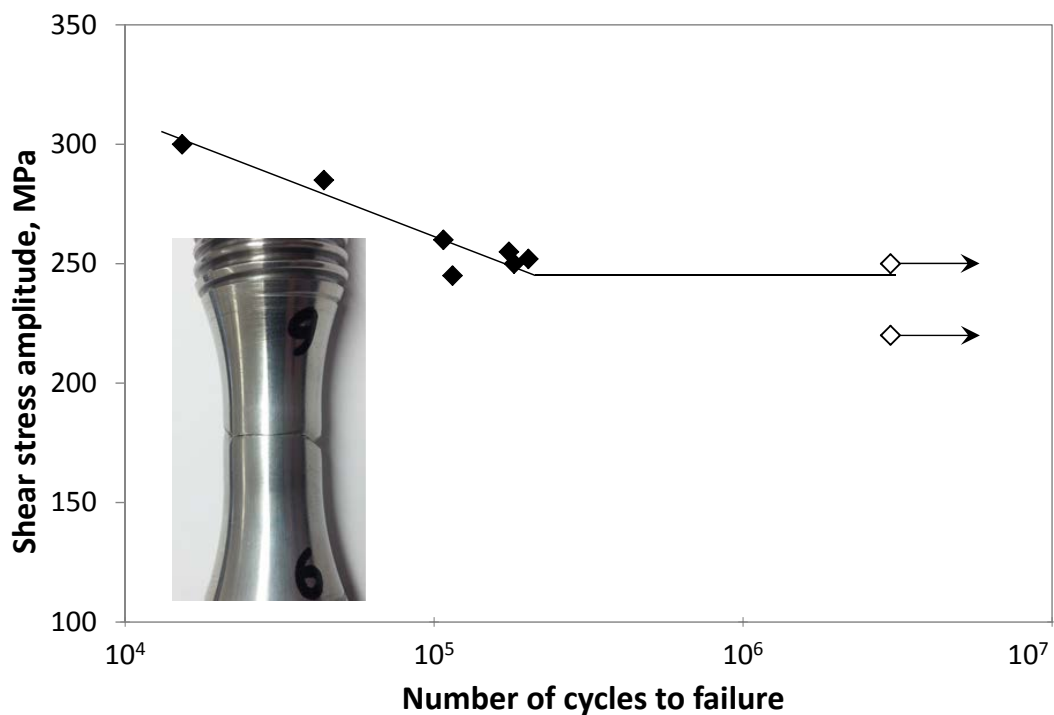


**Figure 5.6:** Whöler curve for fully reversed torsion.

faces were severely worn and so, was very difficult to analyze them under SEM or optical microscope.

---

## 5.3 Discussion

### 5.3.1 Crack initiation

In the high-cycle fatigue regime investigated here, crack initiation, controlled by microscale plasticity, would certainly constitute a large fraction of the fatigue lives for a defect-free material. Since plasticity is related to the equivalent stress, biaxial tension with  $B = 0.25$  ( $\Delta\sigma_{eq} = 0.90\Delta\sigma_{zz}$ ) and  $B = 0.5$  ( $\Delta\sigma_{eq} = 0.87\Delta\sigma_{zz}$ ) could be expected to delay crack initiation, compared to uniaxial and equibiaxial loadings with the same  $\Delta\sigma_{zz}$ .

However, the present steel contains metallurgical defects (pores and chemically inhomogeneous areas, as detailed in previous chapter) and were found responsible for many crack initiations (see table 5.1 and figure 5.7). A finite element model (figure 5.8) was thus used to compute the stress concentration factor,  $K_t$ , near a surface semi-spherical pore in a unit cell with quadratic hexahedron elements, loaded in biaxial tension. The computed values of  $K_t$  decrease as load biaxiality increases:  $K_t = 2.04$  for  $B = 0$ , 1.90 for  $B = 0.25$ , 1.81 for  $B = 0.5$ , and 1.64 for  $B = 1$ . Due to this reduction in stress concentration, biaxial tension should thus reduce fatigue strength as compared to uniaxial tension, and the reduction should increase with increasing biaxiality ratio.

On the other hand, for  $B = 1$ , a “pseudo size effect” might partly explain the detrimental effect observed for this particular biaxiality. In high cycle fatigue, life is to a large extent, controlled by the number of cycles needed for microcracks to cross the first grain boundaries that they encounter, which depends on the relative misorientations of the grains (Zhang and Edwards, 1992). Fatigue crack initiation thus depends on the presence in the first principal plane, on each side of a grain favourably oriented for cyclic plasticity and crack nucleation, of moderately misoriented grains. Under equibiaxial tension, all planes are equi-probable for crack initiation, so that the probability to find an easy path for crack propagation should be higher.

In summary, for a given axial stress range, crack initiation either from a defect or from the surface, should be postponed for  $B = 0.25$  and even more, so for  $B = 0.5$ , compared to  $B = 0$ . For  $B = 1$ , even though crack initiation from surface-cutting defects should be slightly more difficult than under uniaxial loading, the crack initiation from slip bands should not be affected, and the chance that one of the initiated microcracks propagates instead of being arrested at a grain boundary should be higher.

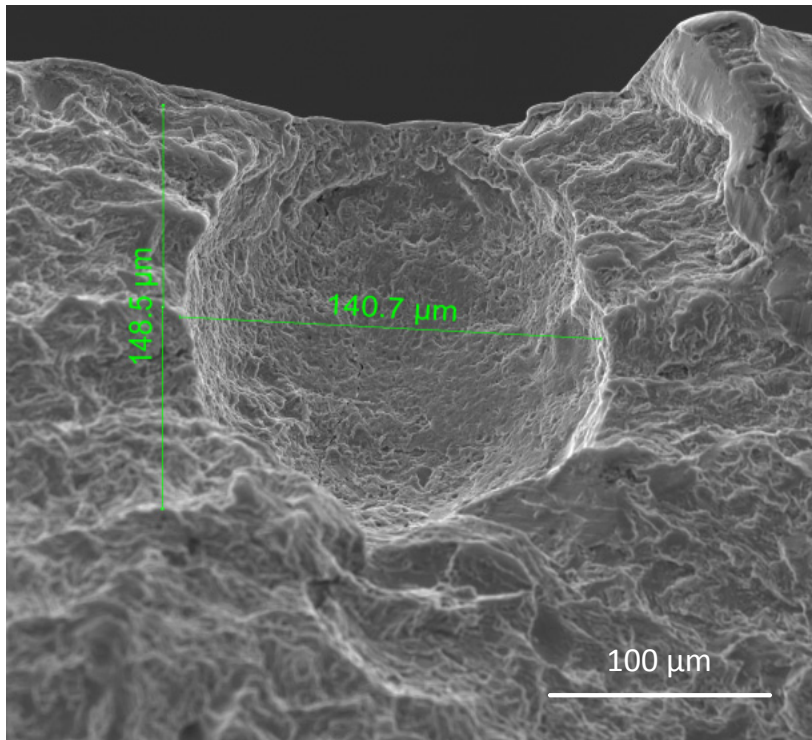


**Figure 5.7:** SEM image of crack initiation from surface defect,  $B = 1$ ,  $\sigma_a = 245$  MPa and  $N_f = 227, 250$  cycles.

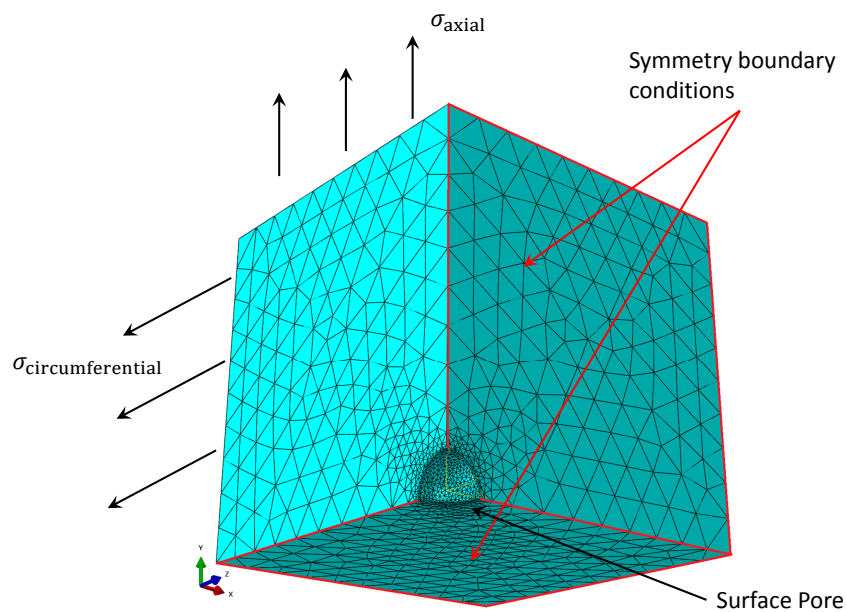


**Figure 5.8:** Finite element model and boundary conditions used to evaluate the stress concentration at a surface pore in biaxial tension.

---

### 5.3.2 Crack growth

The presence of intergranular facets on fatigue fracture surfaces in Ni-Cr-Mo-V and Cr-Mo steels loaded in air has often been reported as a clear sign of combined temper and hydrogen embrittlement (Hénaff et al., 1992; Ritchie, 1977; Islam et al., 2005; Stewart, 1980). Islam et al. (2005) have shown that a preliminary segregation of impurities during the heat treatment is necessary for this phenomenon, but that hydrogen released by a reaction of water vapor with the metal at the crack tip is also necessary.

Similar evolutions of the density of intergranular facets with  $\Delta K$  as those obtained here, have been reported in the literature, for uniaxial fatigue (Zhu and Xuan, 2009; Irving and Kurzfeld, 1978; Cooke et al., 1975). Some authors considered that the peak density of intergranular facets occurs at the  $\Delta K$  value for which the reversed plastic zone size is equal to the prior austenite grain size. Below this  $\Delta K$ , Stage I-like crystallographic fatigue crack growth would favour hydrogen transport towards the grain boundaries by the dislocations emitted at the crack tip, contrary to the more diffuse crack tip plasticity observed above this transition value. In the present case, assuming a plane strain state at the deepest point of a surface crack, the cyclic plastic zone size in uniaxial fatigue would be approximately:

$$CPZ = \frac{1}{3\pi} \left( \frac{\Delta K}{2\sigma_y} \right)^2 \quad (5.5)$$

For  $\Delta K = 10 \text{ MPa}\sqrt{\text{m}}$  and  $\sigma_y = 600 \text{ MPa}$ , equation 5.5 yields  $6.7 \text{ }\mu\text{m}$ , which is close to the former austenite grain size. A tensile stress parallel to a crack, like that generated here on transverse cracks by internal pressure, can reduce the plastic zone size, for a given  $\Delta K$  (Brown and Miller, 1985). However, elastic-plastic finite element computations have shown that in the present case, the influence of load biaxiality on the plastic zone size is limited and cannot explain the shift in the curves observed for  $B = 0.25$  and  $B = 0.5$ . In addition, an explanation based on a modification of the plastic zone size would not be consistent with the absence of shift in the curve for  $B = 1$ .

Some other authors (Irving and Kurzfeld, 1978; Hénaff et al., 1992) consider that the surface fraction of intergranular facets is controlled by the crack growth velocity  $\frac{da}{dt} = f \frac{da}{dN}$ , where  $f$  is the loading frequency. If the crack growth velocity is too high, hydrogen bulk diffusion to the grain boundary becomes too slow, and if it is too low, the rate of hydrogen production at the crack tip is reduced. According to Irving and Kurzfeld (1978), the peak surface fraction of intergranular facets occurs at the crack velocity for which the hydrogen

---

concentration achieved by diffusion at the point of maximum hydrostatic tension ahead of the crack tip is maximum.

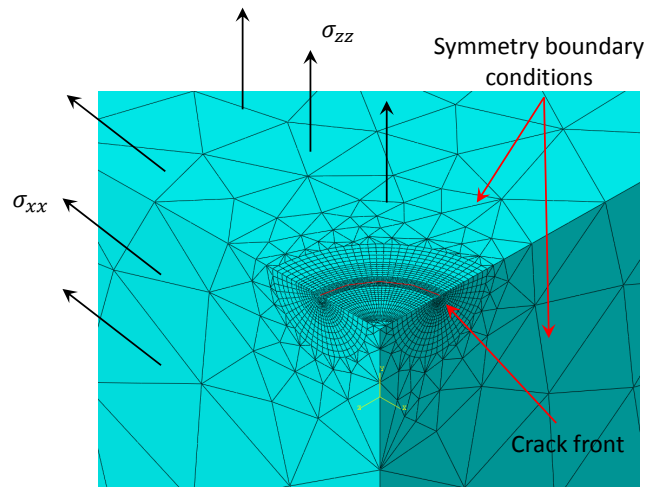
Following this interpretation, the shift of the curves corresponding to  $B = 0.25$  and  $B = 0.5$  towards higher values of  $\Delta K$ , compared to  $B = 0$ , in figure 5.4b, would suggest that a higher  $\Delta K$  is needed to achieve a given crack growth rate, in other words: crack deceleration, while the absence of shift for  $B = 1$  would suggest an absence of effect on the crack growth rate. The reason for such effects is not clear.

Hydrogen atoms in a metal are attracted towards areas of high hydrostatic tension, according to the relation provided by [Oriani and Josephic \(1974\)](#).

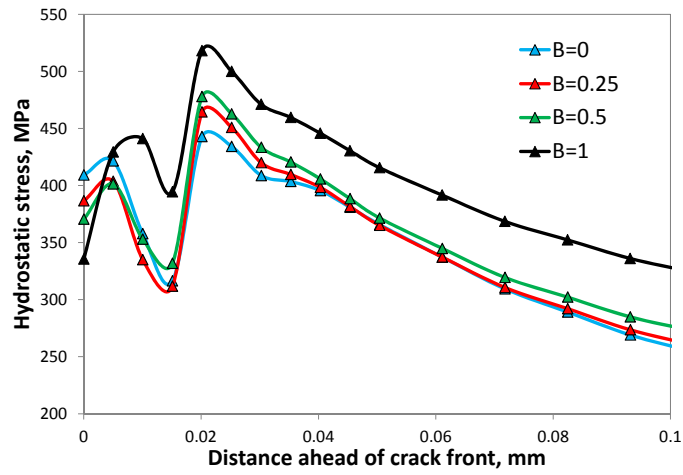
$$C(\sigma) = C_0 \exp \left[ \frac{\sigma_{kk} \bar{V}_H}{RT} \right] \quad (5.6)$$

where  $C(\sigma)$  is the equilibrium concentration of hydrogen in stressed metal,  $C_0$  is the equilibrium concentration in the stress-free metal,  $\sigma_{kk}$  is the hydrostatic stress,  $T$  is temperature,  $\bar{V}_H$  is the molar volume of hydrogen in the metal and  $R$  is the gas constant. Following this idea, [Ritchie \(1977\)](#) introduced hydrostatic tension into equations evaluating the reduction of the threshold  $\Delta K$  and the acceleration of crack growth in the near-threshold regime by H-embrittlement of the grain boundaries.

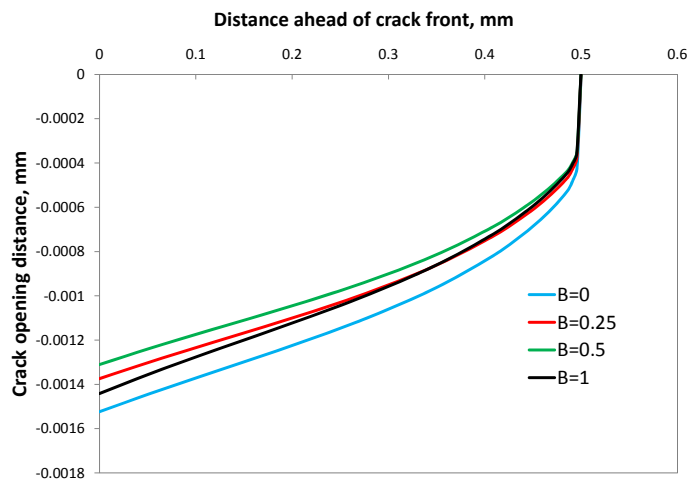
In order to estimate the effect of cyclic biaxial tension on hydrostatic tension ahead of the deepest point of a surface crack, a 3D finite element model of a 500  $\mu\text{m}$  deep semi-circular crack in a 10 mm ( $\Delta K \approx 10$  MPa, corresponding to peak of fraction of intergranular facets) thick plate was developed using quadratic hexahedron type elements (C3D20R) (figure 5.9a). An appropriate mesh refinement was adopted ahead of the crack front (less than  $1/10^{\text{th}}$  of the reversed cyclic plastic zone size). For symmetry reasons, only 1/2 of the plate was considered. 10 cycles of combined opening stress  $\sigma_{zz}$  and tensile stress parallel to the free surface  $\sigma_{xx} = B\sigma_{zz}$  were applied at  $R = 0.25$  for  $B = 0, 0.25, 0.5$  and 1, so as to have same  $\Delta K$  for which intergranular facets were maximum ( $\sim 10$  MPa $\sqrt{\text{m}}$ ). The comparison of the hydrostatic tension profiles ahead of the deepest point at  $K_{\text{max}}$  is shown in figure 5.9b. Compared to uniaxial loading ( $B = 0$ ), biaxial tension increases the hydrostatic tension, but this increase is not very large. A comparison of the crack opening displacement profiles behind the deepest point is shown in figure 5.9c. Compared to uniaxial tension, biaxial tension reduces crack tip blunting. A localized slip band allowing hydrogen transport by the dislocations to the grain boundary is more likely to form at a sharp crack tip than at a blunt tip.



(a) FE model and boundary conditions



(b) Profile of hydrostatic stress ahead of crack front



(c) Crack opening profile

**Figure 5.9:** FE model and results for a semi-elliptical crack in plate for different biaxialities.

---

Contrary to [Marquis and Karjalainen-Roikonen \(2001\)](#) or [Kane and Doquet \(2006\)](#) who reported an increased crack roughness under equibiaxial tension, the present study did not reveal any significant variation in crack roughness with the biaxiality ratio (figure 5.5). As a consequence, no effect of biaxial tension on asperity-induced closure seems to exist in this material. According to the computations done by [Kane and Doquet \(2006\)](#), the effects on plasticity-induced closure should be very limited as well.

In summary, the improvement of fatigue lives observed for  $B = 0.25$  and  $0.5$  is probably due to a retardation of crack initiation and maybe also be due to a reduction of the crack growth rate, while for  $B = 1$ , the “pseudo size-effect” mentioned above might be responsible for a slight reduction in fatigue resistance of the material.

## 5.4 Fatigue criterion

Three popular HCF strength criteria, calibrated using the fatigue strength (at  $3 \times 10^6$  cycles) measured in fully reversed torsion ( $\tau_{-1} = 250$  MPa) and in push-pull at  $R = -1$  ( $\sigma_{-1} = 365$  MPa), have been tested against the data obtained from the uniaxial fatigue tests and the biaxial fatigue tests.

In Findley’s criterion ([Findley, 1959](#)) the damage function is a linear combination of the maximum shear stress amplitude ( $\tau_a$ ) and peak normal stress ( $\sigma_{N,\max}$ ) acting on the critical plane, which is the plane maximizing the damage function:

$$\tau_a + k\sigma_{N,\max} \leq \tau_{-1} \quad (5.7)$$

where  $k$  is a material parameter. As shown in figure 5.10, it is too conservative for high  $R$  ratios and positive biaxialities.

Matake’s criterion ([Matake, 1977](#)) uses the same damage function but the definition of critical plane is different: it is the plane of maximum shear stress amplitude. As shown in figure 5.11, it is better for biaxial tension, but non-conservative under uniaxial fatigue at  $R = 0.5$ .

Dang-Van’s criterion ([Dang Van, 1973](#)) is given by:

$$aT_a + b\sigma_{h,\max} \leq \sigma_{-1} \quad (5.8)$$

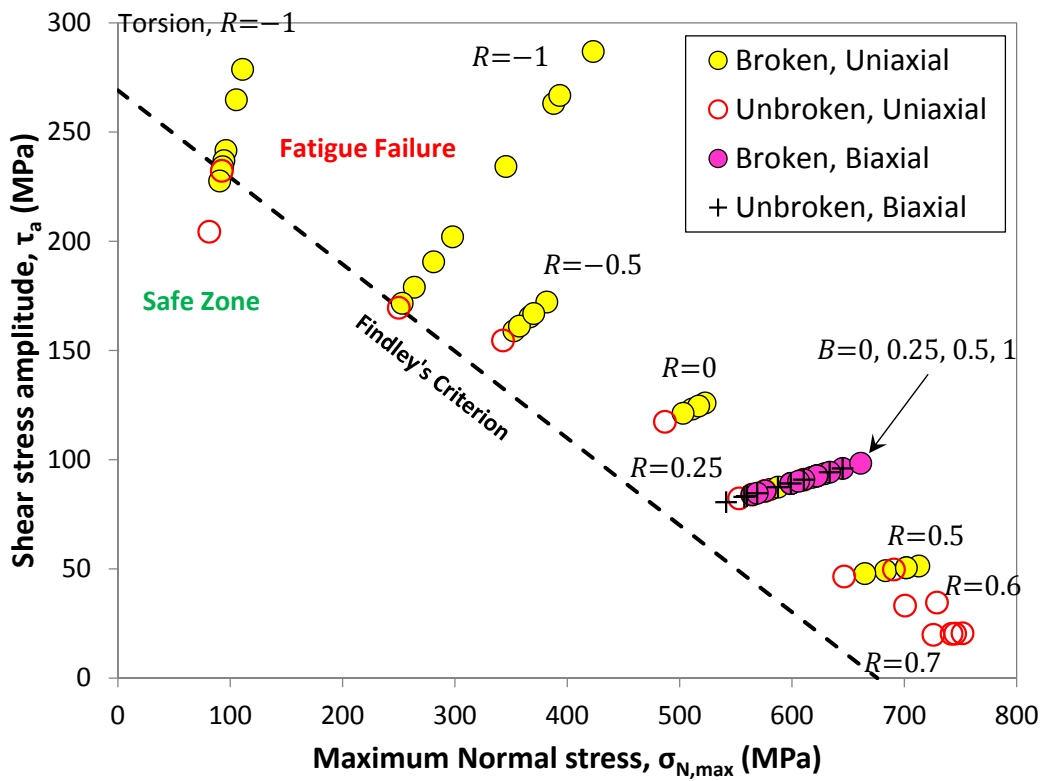


Figure 5.10: Existing fatigue data plotted against Findley's criterion.

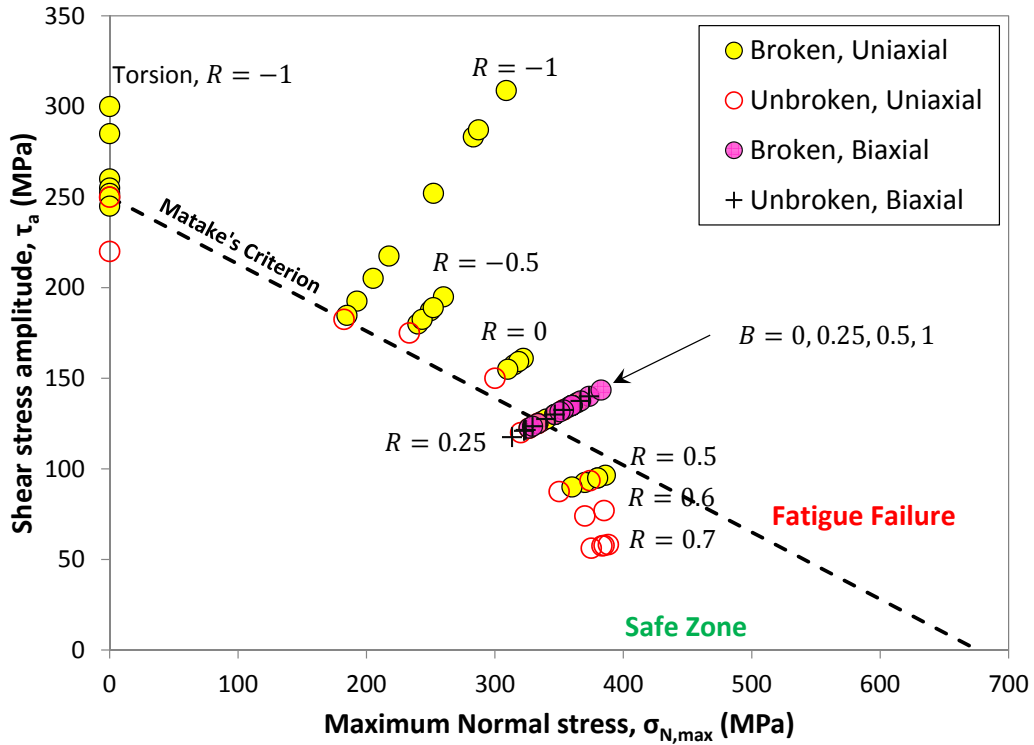
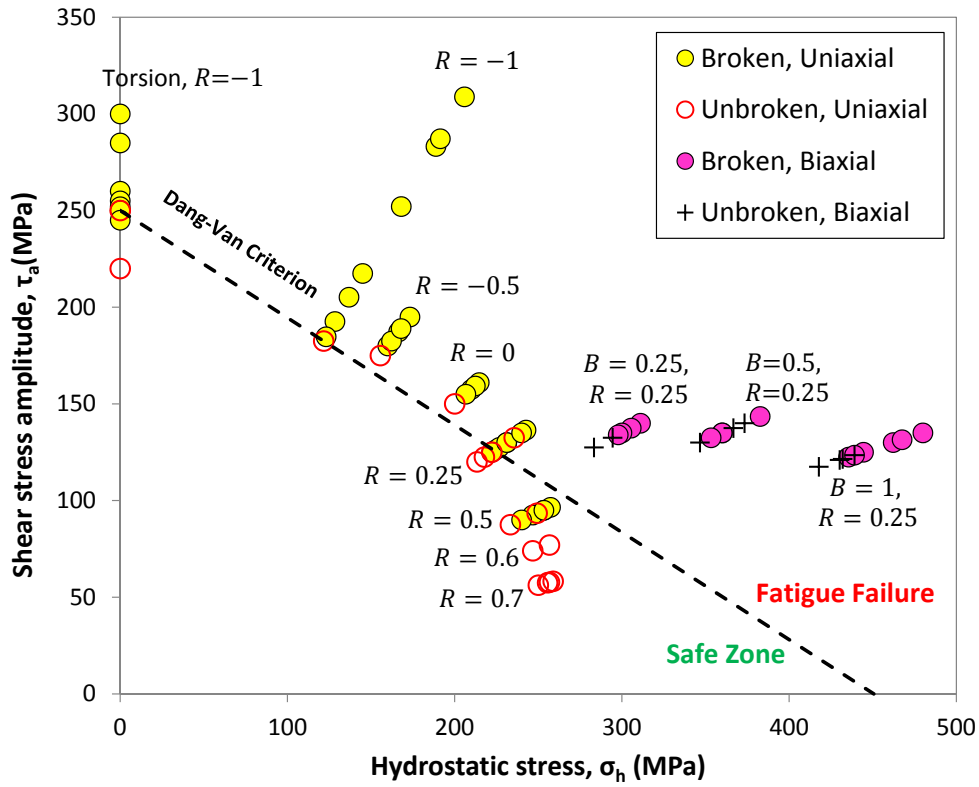


Figure 5.11: Existing fatigue data plotted against Mataka's criterion.



**Figure 5.12:** Existing fatigue data plotted against Dang-Van's criterion.

where  $a$  and  $b$  are material constants,  $T_a$  is the mesoscopic shear stress amplitude,  $\sigma_{h,max}$  is the maximum hydrostatic stress and  $\sigma_{-1}$  is the fatigue limit in push-pull. As shown in figure 5.12, it is non conservative under uniaxial fatigue at  $R = 0.5$  and too much conservative for biaxial tension (especially for equibiaxial,  $B = 1$ ). The hydrostatic tension term does not discriminate the effect of a mean stress normal to the crack plane from that of a second tensile stress, parallel to the crack. [Koutiri et al. \(2013\)](#) reached a similar conclusion. More generally, criteria that predict a linear effect of the mean normal or hydrostatic stress, are not consistent with the fact that uniaxial data follow a non-linear evolution, described by Gerber's parabola, already shown previously.

An alternative criterion, respecting this non-linear dependency, is thus proposed as:

$$\frac{\sigma_{\text{eff},a}}{1 - (\sigma_{I,m}/\sigma_u)^2} \leq \sigma_{-1} \quad (5.9)$$

where the effective stress amplitude,  $\sigma_{\text{eff},a}$  is defined as:

$$\sigma_{\text{eff},a} = \sigma_{I,a} \left( \frac{\sigma_{eq,a}}{\sigma_{I,a}} \right)^x \left( \frac{\text{Tr}(\sigma_a)}{\sigma_{eq,a}} \right)^y \quad (5.10)$$

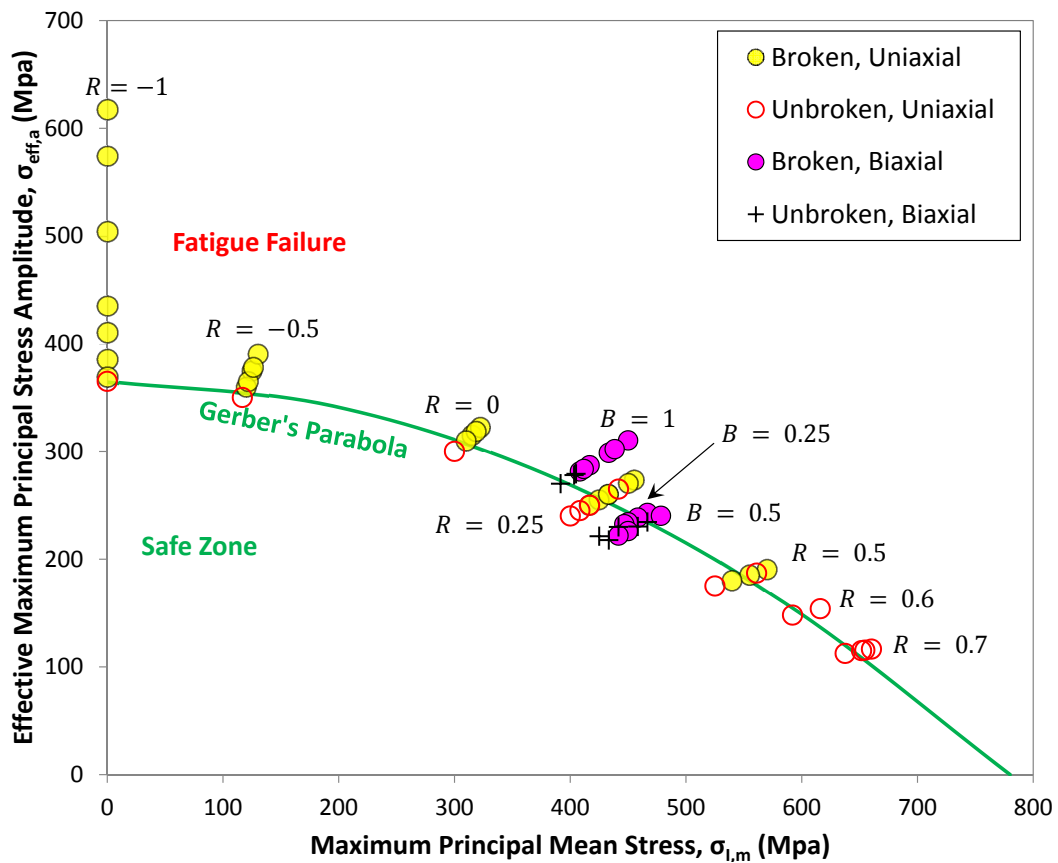


**Figure 5.13:** Existing fatigue data plotted against the proposed criterion.

$\sigma_{I,m}$  and  $\sigma_{I,a}$  are the mean value and amplitude of the first principal stress, respectively,  $\sigma_{eq,a}$  is the amplitude of Von-Mises equivalent stress,  $\sigma_u$  is the ultimate tensile stress, and  $x$  and  $y$  are material parameters.  $\text{Tr}(\sigma_a)$  is the trace of the tensor of stress amplitudes. Note that this term is not modified by the presence of a mean stress, whose non-linear effect is already taken into account in equation 5.9. It is modified only by the presence of a secondary or tertiary cyclic loading. This criterion, which coincides with the Gerber's parabola under uniaxial loading, can discriminate the distinct effects of a mean stress and positive load biaxiality.

For the present steel,  $x = 2$  and  $y = 1/5$  were found suitable to rationalize both the uniaxial and biaxial tension data (figure 5.13). Data from the torsion tests were not used to fit the criterion, because the latter correspond to shear-mode fracture while the present criterion focuses on opening mode fracture.

An alternative way to compare these criteria could be in terms of error in the prediction of endurance limits at various R ratios and biaxiality ratios. The error index has been

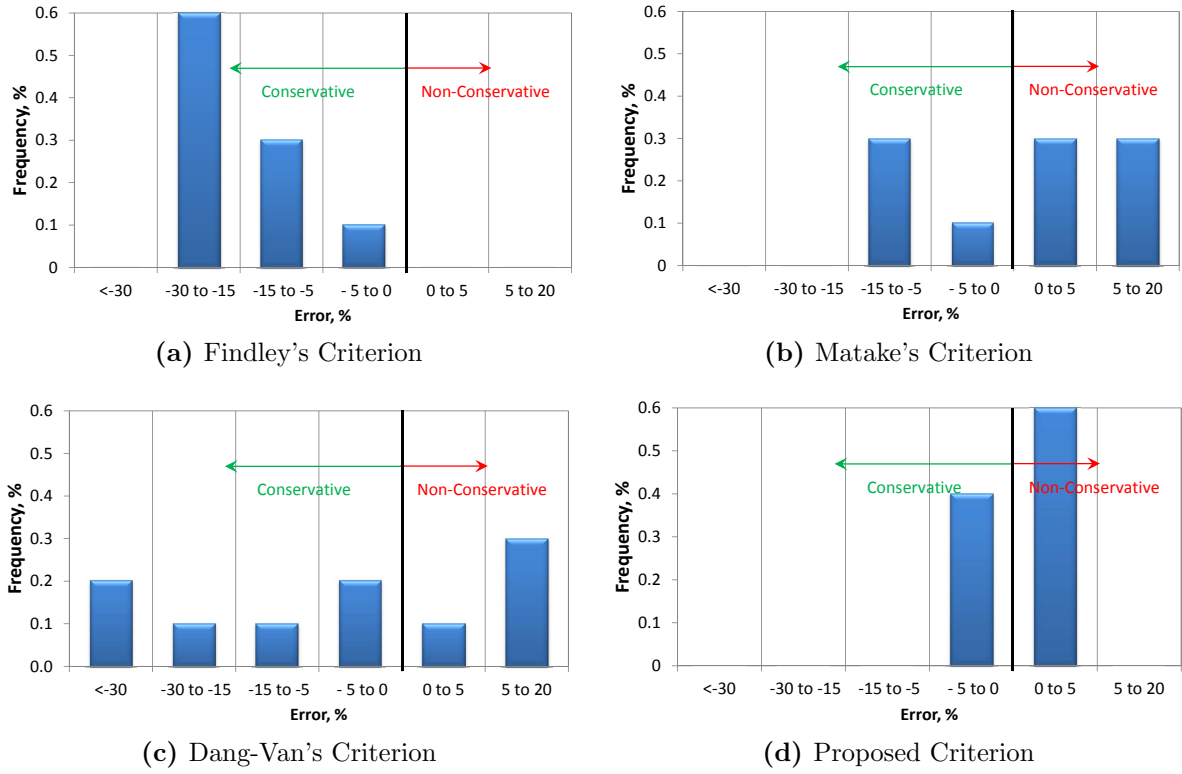


**Figure 5.14:** Histogram of the errors in the estimate of endurance limits by different criteria.

defined as:

$$\text{Error, } I = \frac{\sigma_{\text{Predicted}} - \sigma_{\text{Actual}}}{\sigma_{\text{Predicted}}} \quad (5.11)$$

Where  $\sigma_{\text{Predicted}}$  and  $\sigma_{\text{Actual}}$  are the predicted and actual values of the endurance limit. The error (I%) is evaluated for these criteria and the histograms so obtained are shown in figure 5.14. It can be seen that the range of error for Findley's criterion is from  $-30\%$  to  $0\%$ , for Mataka's criterion, it is from  $-15\%$  to  $20\%$  and for Dang-van's criterion, it lies between  $< -30\%$  and  $20\%$ . The errors in prediction of endurance limits are widely scattered for these criteria. For the proposed criterion, the error (I) lies between  $-5\%$  to  $5\%$ , which seems to be more accurate than the rest of the criteria.



# Chapter 6

## Corrosion-fatigue

Combined cyclic tension and internal pressure tests with various proportions of each loading were run to determine the effect of biaxial tension on fatigue lives of this steel in salt water. Only a handful of studies have been done to investigate the effect of biaxial tension in salt water and these studies have shown different effect of load biaxiality on crack growth rates in different aluminum alloys (Misak et al., 2013, 2014; Perel et al., 2015). However, the behavior of steels could be different from aluminum alloys, so one of the objectives in this part is to investigate the behavior of this steel under uniaxial and biaxial tension in salt water.

Two types of test conditions were used: 1) free corrosion and 2) cathodic potential. The latter was meant to enhance hydrogen ingress in the metal and to study the corresponding effect on fatigue damage mechanisms and fatigue lives.

### 6.1 Experimental procedures

The experimental setup for corrosion-fatigue tests is shown in figure 6.1. The tubular specimen was surrounded by a transparent reservoir filled with a 35 g/l NaCl solution in distilled water, which was circulated by a peristaltic pump to a 5 litre reservoir. This volume corresponds approximately to 100 mL of solution per cm<sup>2</sup> of exposed specimen. To avoid any leakage of the solution, a silicone polymer joint was made at the junction between the specimen and the reservoir. An aeration pump was used to continuously bubble air into the reservoir, so as to keep it saturated with oxygen. A mean temperature of 22°C ± 3°C and a mean pH of 7.2 ± 0.5 existed in the solution throughout the test. The

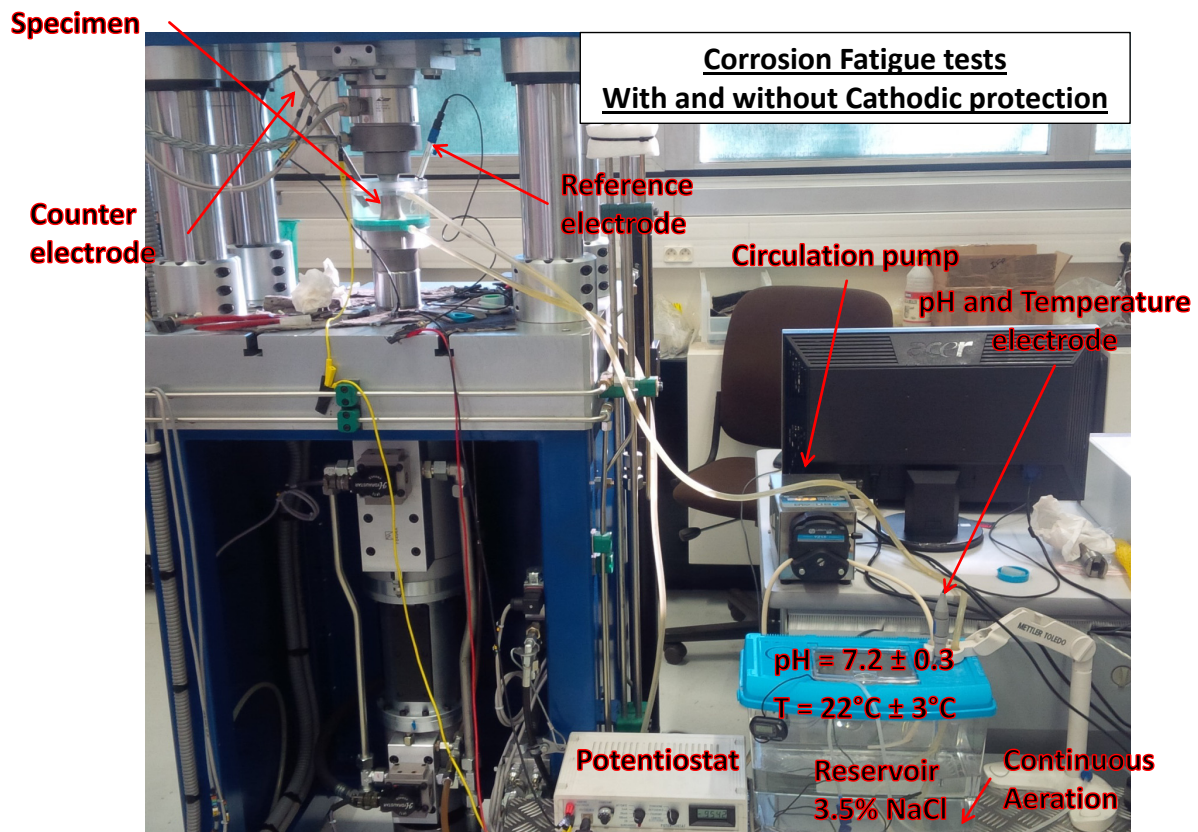


**Figure 6.1:** Experimental setup for corrosion fatigue tests.

solution was renewed after each test. To keep the reasonable testing times for fatigue lives between  $10^5$  and  $2 \times 10^6$  cycles, a frequency of 4 Hz was chosen to evaluate the behavior of this steel in salt water.

Two series of tests were run in salt water: 1) without cathodic protection i.e. free corrosion, for  $B = 0$  and  $B = 1$  and 2) with cathodic protection for  $B = 0, 0.25$  and  $1$ . An R ratio of 0.25 was fixed for both types of tests.

In order to apply cathodic potential, a potentiostat was used along with a reference electrode (Ag/AgCl electrode filled with saturated KCl solution) and a counter electrode (Platinum electrode). A constant potential of  $-950$  mV/ref was applied to the specimen using this potentiostat, which was sufficiently negative for such steel to provide cathodic protection (i.e. reduces the corrosion rate). However, this potential also enhances the rate of the electrochemical reduction of water, with the risk of hydrogen ingress into the steel, and a potential impact on fatigue behavior. The tests were run until complete separation of the specimen (for  $B = 0$ ) or until oil leakage (for  $B = 1$  and  $0.25$ ) or until  $2 \times 10^6$  cycles for ran-out specimens.

---

## 6.2 Experimental results and discussion

### 6.2.1 Free corrosion

#### Fatigue lives

The results of uniaxial and equibiaxial corrosion-fatigue tests are reported in table 6.1. Figure 6.2 compares the evolutions of fatigue lives with the amplitude of the maximum principal stress, for  $B = 0$  and 1 in air and in salt water.

The fatigue lives get dramatically reduced in salt water for both biaxialities, and the endurance limit is vanished. While in air, equibiaxial loading was slightly detrimental,

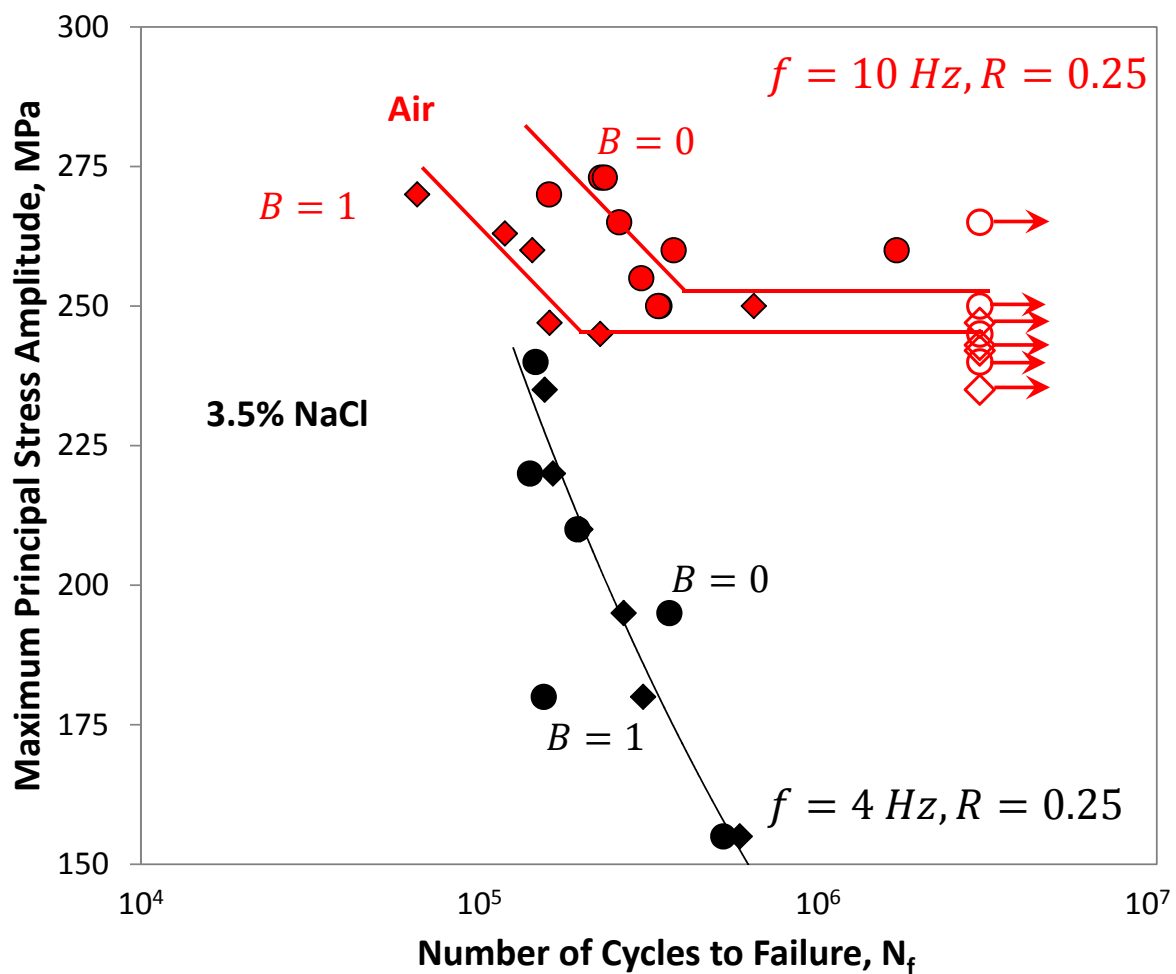


**Figure 6.2:** Whöler curve for uniaxial ( $B = 0$ ) and biaxial tension ( $B = 1$ ) in air and in salt water. Circular symbols are for uniaxial tension and squares ones are for equibiaxial tension.

| $\sigma_{zz,a}$ , MPa | B | Cycles to failure, $N_f$ | Location      | Crack orientation                              |
|-----------------------|---|--------------------------|---------------|--|
| 240                   | 0 | 146,333                  | Outer surface | Transverse                                     |
| 220                   | 0 | 140,797                  | Outer surface | Transverse                                     |
| 210                   | 0 | 194,558                  | Outer surface | Transverse                                     |
| 195                   | 0 | 363,411                  | Outer surface | Transverse                                     |
| 180                   | 0 | 154,735                  | Outer surface | Transverse                                     |
| 155                   | 0 | 524,377                  | Outer surface | Transverse                                     |
| 235                   | 1 | 155,831                  | Outer surface | Longitudinal                                   |
| 220                   | 1 | 164,753                  | Outer surface | Inclined crack 15° with longitudinal direction |
| 210                   | 1 | 198,505                  | Outer surface | Longitudinal                                   |
| 195                   | 1 | 266,320                  | Outer surface | Inclined crack 69° with longitudinal direction |
| 180                   | 1 | 304,076                  | Outer surface | Inclined crack 80° with longitudinal direction |
| 155                   | 1 | 586,777                  | Outer surface | Inclined crack 58° with longitudinal direction |

**Table 6.1:** Corrosion fatigue data under uniaxial ( $B = 0$ ) and equibiaxial tension ( $B = 1$ ) at  $R = 0.25$ , in free corrosive environment.  $\sigma_{zz,a}$  is the applied axial stress amplitude and B is the biaxiality ratio.

especially in the low cycle fatigue regime, in salt water, no significant difference between  $B = 0$  and 1 can be observed.

## Corrosion weight loss and surface pitting

The specimens were weighted before and after the fatigue tests and their weight loss was plotted against the duration of the test (figure 6.3a). A similar increase in weight loss with the exposure time was found for uniaxial and biaxial fatigue.

However, this parameter does not reflect the localized character of corrosion, since the specimens were in fact covered with micro-pits. 3D optical imaging of micro-pits (figure 6.3b) was done to measure their widths and depths and an average of 10 measurements was taken for each specimen. Their average aspect ratio (ratio of depth to surface radius) was found to be 0.33 in uniaxial tension and 0.31 in biaxial tension. Images of the

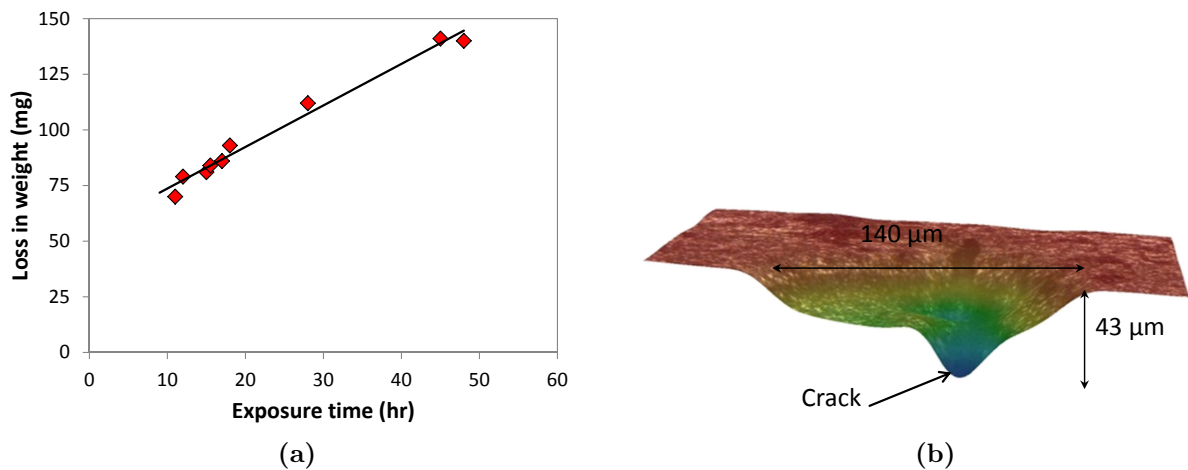


**Figure 6.3:** (a) Weight loss of the specimens as a function of exposure time during the fatigue tests. (b) 3D topographic image of a typical micro-pit.

specimens submitted to uniaxial and biaxial tension with same axial stress amplitude (155 MPa) were taken at the same magnification, and the number of pits on a surface of  $2000 \times 2000 \mu\text{m}^2$  was counted. The density of pits was approximately  $2.7/\text{mm}^2$  in uniaxial tension, and  $3.1/\text{mm}^2$  in biaxial tension. Thus, biaxial tension does not seem to influence much the aspect ratio and density of pits, as compared to uniaxial tension.

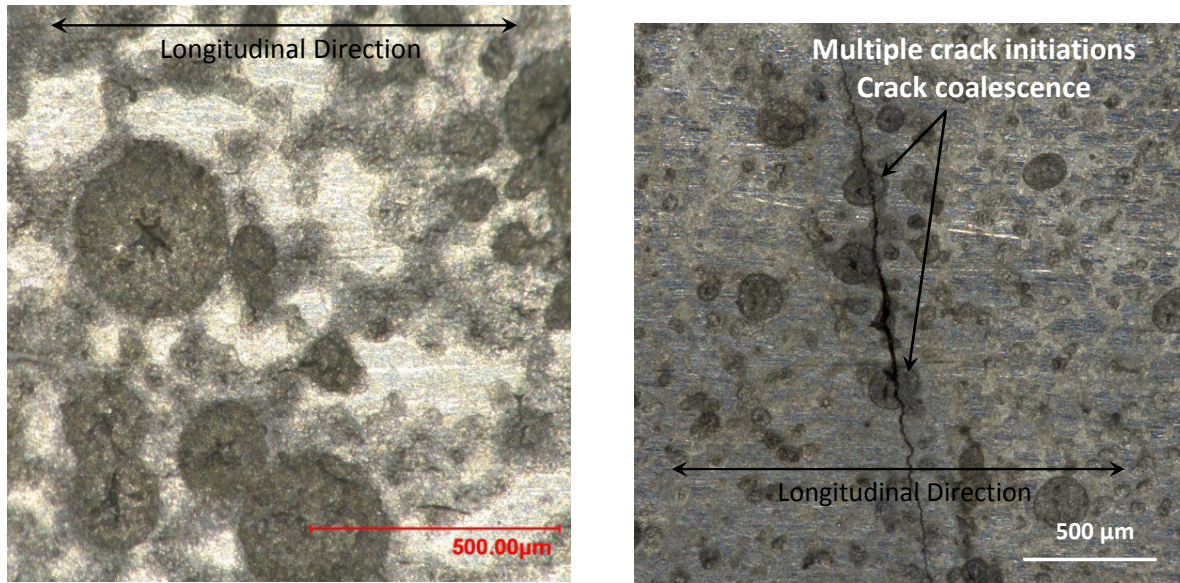
## Crack initiation

All fatigue failures in salt water initiated from the outer surface, in contact with the corrosive solution, most often from the bottom of a pit, as shown in figure 6.3b and figure 6.4a.

Remember that in air, a majority of cracks in equibiaxial tension had been found to initiate from the inner diameter of the tubes, which was attributed to the slight gradient in hoop stress, 8% higher on the inner diameter than on the outer diameter. In salt water, the stress concentration provided by the pits was thus high enough to overcome this gradient effect, so that cracks initiated from the outer surface.

An additional difference with fatigue in air was the multiplicity of crack initiations, due to the high density of pits. In some cases, merging of small cracks into a large crack was observed (figure 6.4b). This suggests that salt water in free corrosion makes crack initiation very easy and very fast.

Under uniaxial tension, all the microcracks were perpendicular to the loading direction.



(a)  $B = 0, R = 0.25$

(b)  $B = 1, R = 0.25$

**Figure 6.4:** (a) Corrosion pits formed during corrosion fatigue tests. (b) An example of merging of cracks initiating from micro-pits.

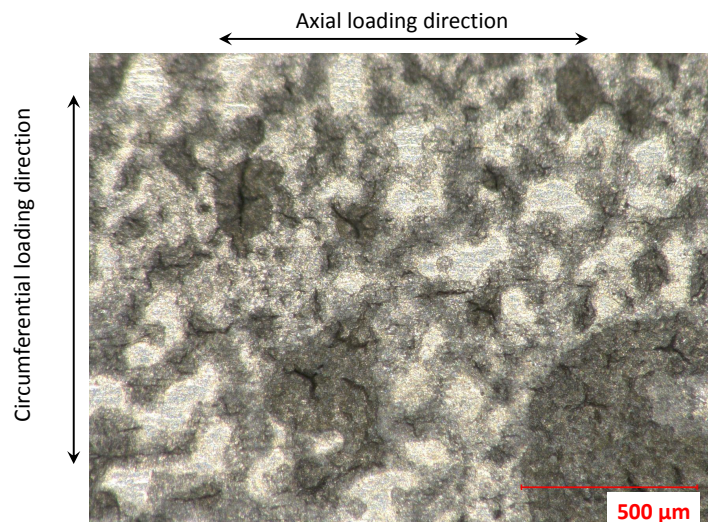


**Figure 6.5:** Randomly oriented micro-cracks under equibiaxial tension.

By contrast, in equibiaxial tension, the orientations of the cracks were random, unlike in air, where only transverse and longitudinal cracks were found. This random orientation of the cracks, illustrated on figure 6.5, confirms the absence of any anisotropy in the specimens.

The surface diameter of pits initiating major cracks, lied between 100 and 1000  $\mu\text{m}$ . No definite correlation with the stress level could be found.

---

## Crack growth

The fracture surfaces were covered with corrosion products, potentially responsible for crack closure effects. A solution of 3.5 mg of hexamethylene tetramine in 500 mL of hydrochloric acid on a cotton stick was thus used to clean the corroded fracture surfaces before observations.

For uniaxial loading, the fracture surfaces exhibit crystallographic patterns evoking transgranular brittle decohesion (figure 6.6), with a very limited proportion of intergranular facets, while for equibiaxial loading, transgranular cleavage-like areas were also present, but the frequency of intergranular facets was much higher. Many micro-pits could be observed on the broken grain boundaries, near the initiation site, but their frequency decreases in depth, and near the inner surface, the grain boundaries look smooth (figure 6.7). It cannot be due to an attack by the cleansing solution, otherwise the distribution of pits would be homogeneous. These micro-pits on the fracture surface might be formed by salt water in the same way as on the outer surface, and the reason for their disappearance near the inner surface is probably the reduced exposure time compared to the outer surface.

Even though the crack growth mechanisms for uniaxial and biaxial tension in salt water

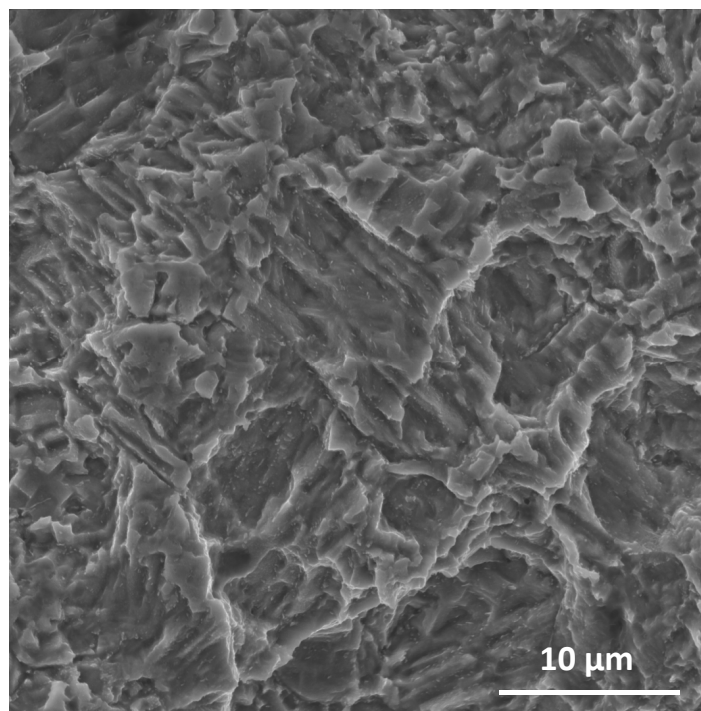
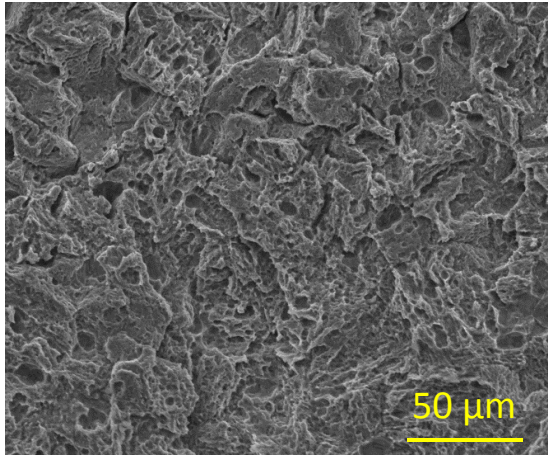
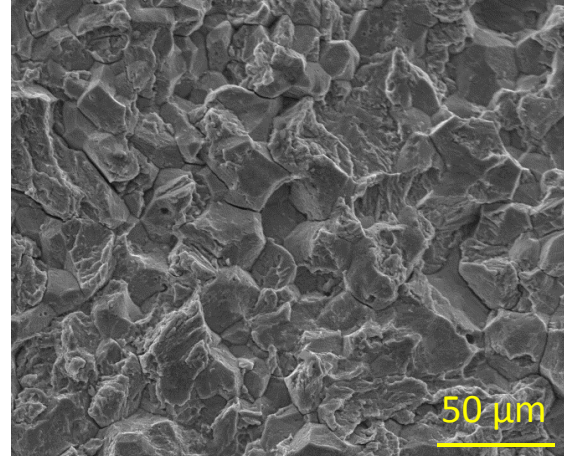


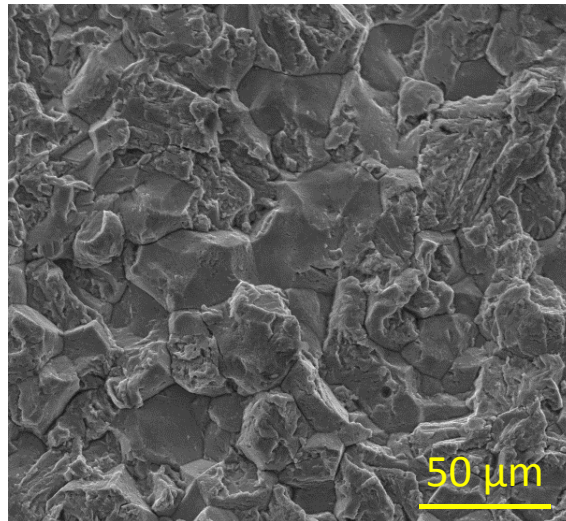
**Figure 6.6:** SEM image of the fracture surface in uniaxial tension in salt water with axial stress amplitude of 155 MPa.



(a) Near initiation



(b) At mid-thickness



(c) Near End

**Figure 6.7:** SEM images of the fracture surface showing micro-pits and mixed intergranular and brittle type surface and their distribution at different depths of the crack growth, in equibiaxial tension in salt water with axial stress amplitude of 210 MPa ( $N_f = 198,505$  cycles).

seem relatively different, the fatigue lives fall within the same scatter band. It suggests either that crack initiation from pits, which does not seem to be influenced by load biaxiality, constituted the major part of the fatigue lives, for the stress range investigated, so that a change in crack growth mechanisms and kinetics would have a limited impact, or that the change from transgranular to intergranular decohesion did not make a significant difference in terms of crack growth rate. The first explanation seems quite inconsistent with the high density of microcracks formed in salt water. The second explanation however is consistent with the literature: [Irving and Kurzfeld \(1978\)](#) wrote: “The addition

of up to 35% intergranular fracture does not produce detectable enhancement of crack growth rates”. Hénaff et al. (1992) wrote “the crack growth rates are not affected by variations of the rate of intergranular cracking”.

## 6.2.2 With cathodic potential

### Fatigue lives

The results of the tests run at  $B = 0, 0.25$  and  $1$  in salt water with a cathodic potential of  $-950$  mV/ref are reported in table 6.2. A small number of tests were done at each biaxiality ratio because of a limitation in the number of specimens.

Figure 6.8 shows the evolution of fatigue lives with the maximum principal stress amplitudes for the three biaxiality ratios in comparison with the data obtained in air. Contrary to what happened in free corrosion, when cathodic potential was applied the fatigue lives remain unaltered as compared to those in air.

### Crack initiation

Figure 6.9 compares the surface conditions of the specimen as seen under optical microscope after the fatigue tests in free corrosion and with cathodic potential. The latter merely suppressed surface pitting and the formation of corrosion deposits.

| $\sigma_{zz,a}$ , MPa | B    | Cycles to failure, $N_f$ | Location      | Crack orientation |
|-----------------------|------|--------------------------|---------------|-------------------|
| 270                   | 0    | 165,675                  | Outer surface | Transverse        |
| 262                   | 0    | 187,877                  | Outer surface | Transverse        |
| 250                   | 0    | > 3,000,000              | -             | -                 |
| 278                   | 0.25 | 81,012                   | Outer surface | Transverse        |
| 270                   | 0.25 | 603,263                  | Inner surface | Transverse        |
| 260                   | 0.25 | > 3,000,000              | -             | -                 |
| 265                   | 1    | 145,296                  | Inner surface | Transverse        |
| 244                   | 1    | 455,176                  | Outer surface | Longitudinal      |

**Table 6.2:** Corrosion fatigue data for different load biaxialities ( $B = 0, 0.25, 1$ ) at  $R = 0.25$ , with cathodic potential.  $\sigma_{zz,a}$  is the applied axial stress amplitude and B is the biaxiality ratio.

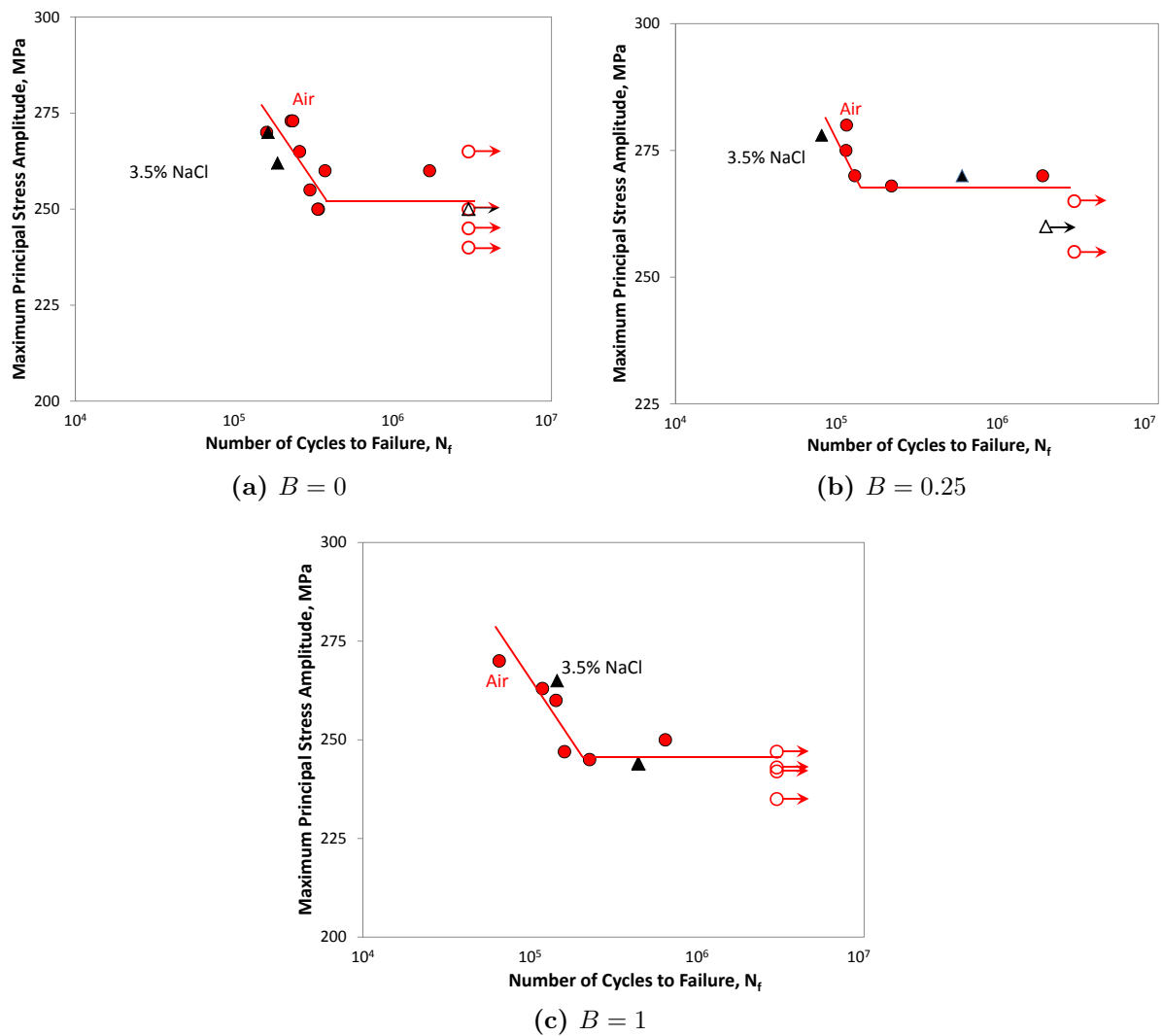


**Figure 6.8:** Whöler curves for fatigue data in air and in salt water with cathodic potential for different load biaxialities ( $B = 0, 0.25$  and  $1$ ). Hollow symbols represent the ran-out specimens.

In the absence of pits, failures initiated from the outer surface or even, in some of the specimens tested at  $B = 1$ , from the inner surface, exactly like in air. For  $B = 0$  and  $0.25$ , cracks initiated in a transverse direction, while for  $B = 1$  cracks initiated in longitudinal or transverse directions.

## Crack growth

In that case, fractographic observations could be performed directly, without any cleansing treatment. While for the tests run in air, the fraction of intergranular facets was found to depend on  $\Delta K$ , but never to exceed 45% (see figure 5.4b in chapter 5), for all the tests

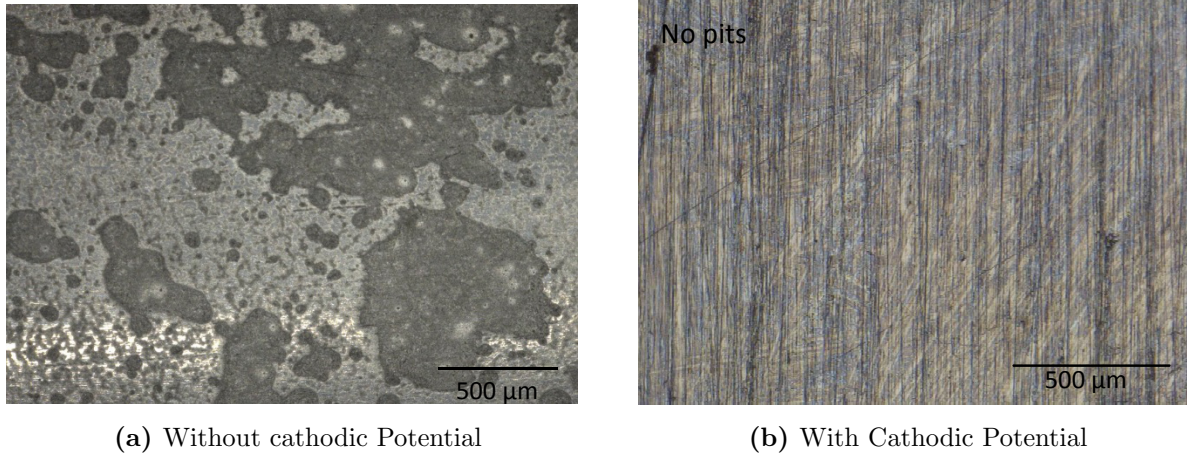


**Figure 6.9:** Comparison of surface condition after fatigue tests in salt water.

run with cathodic potential, the fracture surfaces were nearly fully intergranular along the whole crack path, for all biaxialities. A comparison of fracture surfaces in air and in salt water at same load biaxiality ( $B = 0.25$ ) and nearly same axial stress amplitude ( $\sigma_{zz,a} = 275$  MPa and 278 MPa) is shown in figure 6.10. This enhancement of intergranular fracture provides evidence for an enhancement of hydrogen-induced embrittlement.

Again, the absence of associated reduction in fatigue lives suggests either that crack initiation constituted the major part of the fatigue lives, and was not affected by hydrogen effects, or that the material already underwent such a substantial hydrogen-induced em-

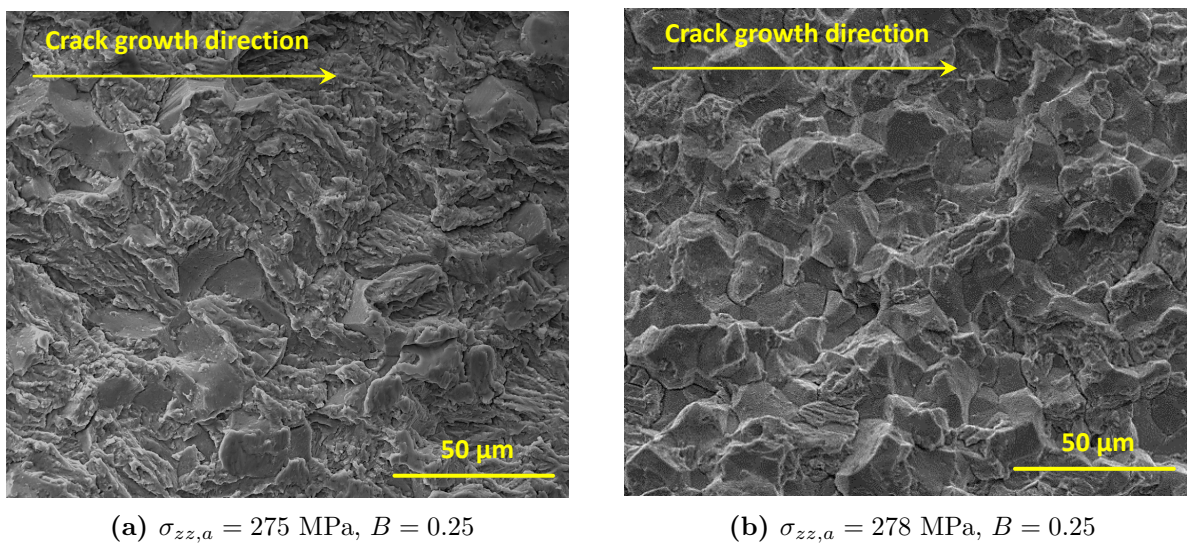


**Figure 6.10:** A typical SEM image of fracture surface (a) in air and (b) in salt water with cathodic protection, at nearly same  $\Delta K$  and same magnification.

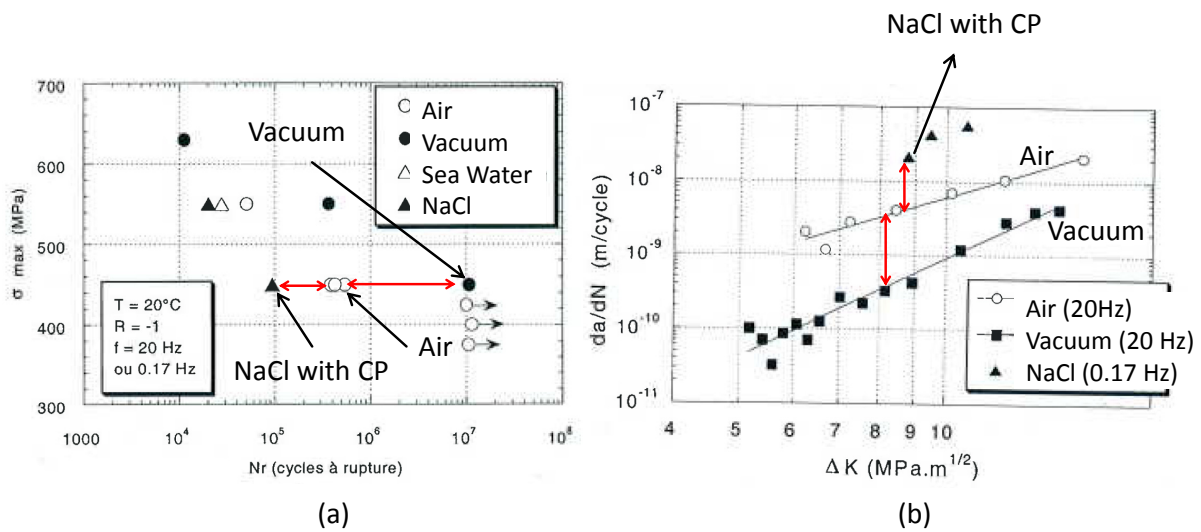


**Figure 6.11:** Effect of environment on (a) fatigue lives and (b) crack growth in superalloy SE702 steel (modified from Huneau et al. (2000)).

brittleness in air that the enhancement of this effect by cathodic protection only had a marginal impact in terms of crack growth rate. The first explanation is much more probable than it was for free corrosion. However, the second explanation is supported by the drastic change in aspect of the fracture surface when an internal crack, initiated from a defect and growing in vacuum finally meets the free surface (figure 4.9 and figure 4.10 in chapter 4) and the presence of up to 45% intergranular facets. It is also supported by the work of Huneau et al. (2000) on a martensitic steel tested in fatigue in vacuum, air, salt water and natural sea water with a cathodic potential of  $-1050\text{ mV/ECS}$ . As can be seen on figure 6.11, a large drop in fatigue lives and increase in crack growth rate were observed when the tests were run in air instead of vacuum. The further drop in life and increase in crack growth rate when the tests are run in salt water are comparatively smaller. Note that if these tests had been run at a cathodic potential of  $-950\text{ mV/ref}$  as in the present study, the hydrogen flux would have been much less, and the detrimental effects even less.

Finally, considering the enhancement in fraction of intergranular facets as observed with cathodic protection under uniaxial tension, it seems logical that an already saturated hydrogen-induced embrittlement phenomenon is not further enhanced by biaxial tension.

# Conclusions

The clip connectors used to join the riser tubes for offshore oil drilling undergo variable amplitude cyclic loading due to sea waves. 90% of the service life is spent in the “connected mode” with a high mean stress ( $R = 0.7$ ) and 10% in the “disconnected mode” with a lower mean stress ( $R = 0.2$ ).

Elastic-plastic finite element computations on a FE model of a Clip-Riser<sup>TM</sup> assembly revealed in-phase biaxial tension in its critical areas, along with high mean stresses. Both the mean stress effect and the biaxiality effect are thus needed to be addressed, for a proper design of these structures. However, most of the multiaxial fatigue criteria are based on tension-torsion fatigue data and do not discriminate the influence of biaxial tension from that of a mean stress.

The influence of mean stress and that of load biaxiality on the fatigue lives and damage mechanisms of 2.5%Cr-1%Mo steel constituting the clip connectors were thus investigated separately.

To investigate the mean stress effect, push-pull fatigue tests were run with various R ratios ( $\sigma_{\min}/\sigma_{\max}$ ) ranging from -1 to 0.7. The fatigue lives, as well as the slope of the S-N curves were found to decrease with increasing R, and the endurance limit (defined as fatigue strength at  $3 \times 10^6$  cycles) to follow Gerber’s parabola.

At low R ratio and thus relatively high stress ranges, fatigue cracks were found to initiate from the surface, merely due to local cyclic plasticity, while for high R ratios, and thus low stress ranges, cracks initiated due to stress concentrations induced by internal or surface-cutting defects (pores or carbon and oxygen segregation areas), sometimes forming “fish-eye” patterns on the fracture surface. At very high R ratio ( $R \geq 0.6$ ), no fatigue failures could be observed, within  $10^7$  cycles. In spite of significant residual stresses within a thin surface layer, their R-ratio and amplitude-dependent relaxation did not seem to control the crack initiation sites. The transition in crack initiation mode associated with an increase in mean stress and correlative decrease in amplitude was thus attributed to stress concentration effects.

---

Internal cracks were found to propagate for a low  $\Delta K$ , compared to the threshold values reported in the literature for crack growth in air, and this  $\Delta K$  seemed not to depend on the R ratio. This was attributed to a quasi absence of crack closure, which might, to some extent, compensate the lack of assistance to crack growth provided by moist air.

To investigate the effect of positive stress biaxiality, combined cyclic tension and internal pressure tests with various stress biaxiality ratios ( $B = 0, 0.25, 0.5$  and  $1$ ) were run on tubular specimens, at a fixed R ratio ( $0.25$ ). The evolution of the fatigue lives as a function of the maximum principal stress amplitude showed a beneficial effect for moderate stress biaxiality ( $B = 0.25$  and  $0.5$ ) while equibiaxial tension had a slightly detrimental effect.

The stress concentration around defects was shown to decrease with load biaxiality. In addition, for  $B = 0.25$  and  $0.5$ , the Von-Mises equivalent stress range is reduced, compared to uniaxial loading, this probably leading to a retardation of crack initiation consistent with the beneficial effect observed at those biaxialities.

Intergranular facets due to temper-induced segregation of impurities and hydrogen-induced embrittlement were observed on the fracture surfaces. The evolutions of their surface fraction with  $\Delta K$  and load biaxiality suggested a possible reduction in crack growth rate at moderate biaxialities, but the detrimental effect of equibiaxial tension could not be explained in terms of crack growth rate based on these data.

The tentative explanation proposed for the latter is a “pseudo size effect” i.e. a higher probability that micro-cracks propagate instead of being arrested at a grain boundary, when there are two equivalent principal planes.

Several popular fatigue criteria failed to describe all fatigue data. Endurance criteria that include a linear mean stress term or hydrostatic tension term fail to predict the variations of the endurance limit of this material with the R ratio and biaxiality ratio. Thus, a new fatigue criterion based on Gerber’s parabola was proposed. It captured the evolution of the endurance limit under the combined effects of a positive mean stress and positive biaxiality.

In spite of protective coatings, clip connectors might be in contact with sea water. A part of the study was thus devoted to the influence of salt water on the fatigue behavior of the steel. The purpose was to determine if the effect of salt water on fatigue lives was influenced by load biaxiality, particularly in conditions leading to hydrogen release.

For that purpose, combined cyclic tension and internal pressure tests with various proportions of each loading were run in a  $35$  g/l NaCl solution, in free corrosion and with

---

–950 mV/ref cathodic protection. The latter was meant to enhance hydrogen release in the solution.

In free corrosion, salt water strongly reduced the fatigue lives and suppressed the endurance limit for  $B = 0$  as well as for  $B = 1$ . This was due to the formation of corrosion pits. Biaxial tension did not seem to influence much the aspect ratio and the density of pits, as compared to uniaxial tension, but increased the frequency of intergranular facets on the fracture surfaces. The fatigue lives for uniaxial and biaxial tension however fell within the same scatter band, suggesting that the biaxiality-induced change in crack growth mechanisms did not make any significant difference in terms of crack growth rate.

This observation should not be generalized to other materials, as results in the literature (Misak et al., 2013, 2014; Perel et al., 2015) indicate different effects of biaxial-tension in salt water for different aluminum alloys.

Cathodic protection suppressed surface pitting and cancelled the detrimental effect of salt water for all biaxialities, in spite of a clear enhancement of H-induced embrittlement of the grain boundaries. The fracture surfaces were nearly fully intergranular along the whole crack path, for all biaxialities, while in air, the fraction of intergranular facets was  $\Delta K$ -dependent and never exceeded 45%. The absence of reduction in fatigue lives suggests either that crack initiation constitutes the major part of the fatigue lives, or that the material already undergoes such a substantial hydrogen-induced embrittlement in air that the enhancement of this effect in salt water with cathodic protection has a marginal impact.

The absence of enhancement of hydrogen effects by biaxial tension observed in this medium strength, temper-embrittled steel should not be extrapolated to other materials, especially high purity, high strength steels, nor to thicker structures, in which hydrostatic stress might reach higher values and also, because of existence of its gradient in such structures.



# Perspectives

Assumptions regarding the relative proportions of crack initiation and propagation stages in fatigue lives had to be made for the interpretation of the test results in air or salt water. To check the validity of these assumptions, plastic replicas of the surface of the specimen could be made periodically during interrupted tests and observed with the SEM. This would be possible for the tests run in air and in salt water with cathodic protection, when no corrosion products layer is formed on the surface. It would allow the detection and monitoring of microcracks, provided they do not initiate on the internal surface. In free corrosion, replication might perturbate the corrosion process and should thus be avoided. However, direct observations with a travelling microscope would be possible, to monitor the evolution of pit size and shape and would allow a better understanding of the pit-to-crack transition.

A fracture mechanics approach was attempted to analyze fatigue fracture from defects, and might also be used for fracture initiated from corrosion pits. However, it was based on crack growth kinetics and thresholds from the literature, mainly measured in air. A characterization of fatigue crack growth kinetics and thresholds in air, vacuum and salt water, with or without cathodic protection, depending on load biaxiality, would be useful.

Sharp gradients in stress and biaxiality ratio were found along the thickness of the clip connector. Cracks might thus initiate at the critical point, but become unable to grow, so that the application of the proposed endurance criterion for safe life design would be too conservative. To deal with this problem, two approaches could be envisaged.

- Use the proposed criterion, and in case it predicts fatigue failure at the critical point, use fracture mechanics to predict crack growth or crack arrest, assuming that the appropriate threshold  $\Delta K$  has been determined, as suggested above.
- Include gradient effects in a non-local criterion, which might keep the form proposed here, but introduce some averaging of stresses over a critical distance or volume related to some material length scale. Specific experiments on notched specimens would be necessary to calibrate and validate this type of criterion.

---

Constant amplitude fatigue loadings with various R ratios were investigated here, but the actual loading conditions on clip connectors are random variable amplitude. Very few studies investigated variable amplitude multiaxial fatigue, and mainly for combined tension and torsion ([Marciniak et al., 2008](#); [Shamsaei et al., 2011](#); [Kim et al., 1999](#)). Variable amplitude in biaxial-tension loading is still an open question.

It might be possible to estimate the crack initiation life from constant amplitude data, using the classical rainflow cycle counting method and Miner's linear damage cumulation method. For crack growth under variable amplitude biaxial tension, the model developed by [Hamam et al. \(2007\)](#) which takes into account the T stress (and thus biaxiality) could probably be used, after a preliminary calibration, based on crack growth kinetics data.

# Appendices



## Appendix A

### Algorithm for stepwise integration of Paris equation for internal cracks

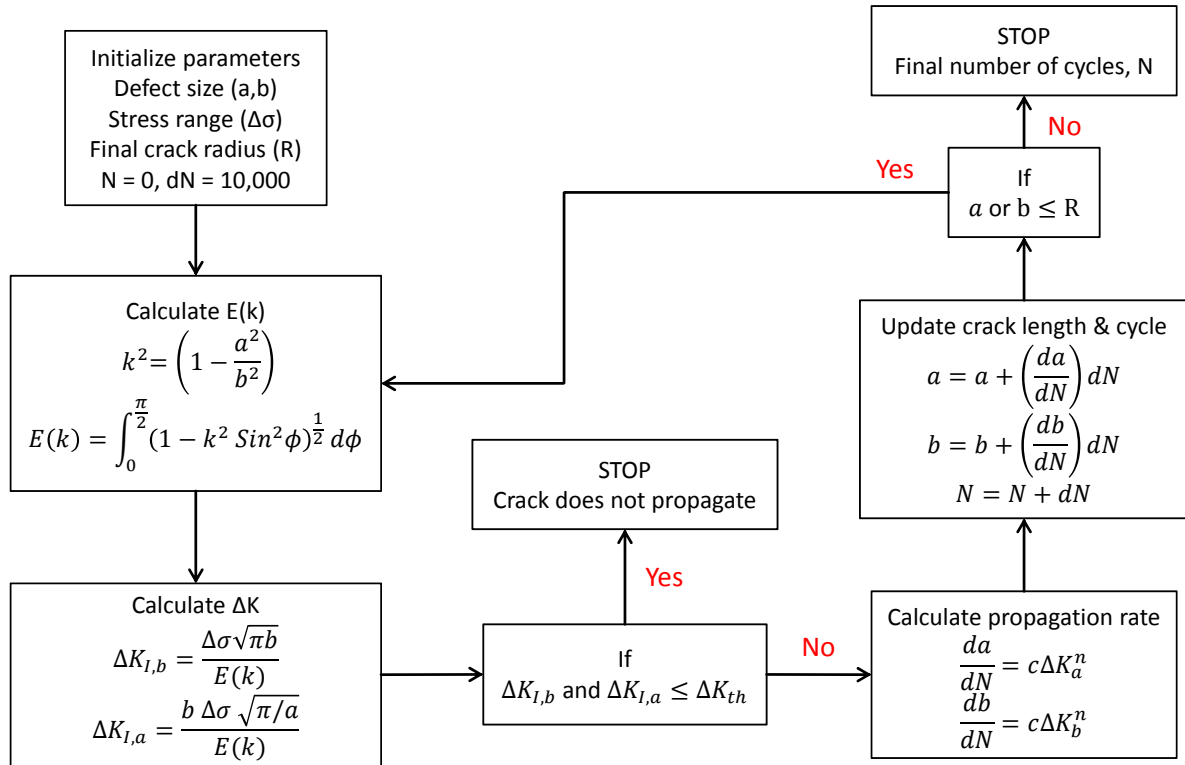


**Figure A.1:** Flowchart depicting the algorithm for stepwise integration of crack growth kinetics for an internal elliptical crack



# Appendix B

## Murakami's $\sqrt{area}$ model

The SIF range for the defects that give rise to internal initiation, can be approximated using Murakami's  $\sqrt{area}$  model for internal cracks (Murakami, 2002) as:

$$\Delta K_{I,max} = 0.5 \sigma_{max} \sqrt{\pi \sqrt{Area}} \quad (\text{B.1})$$

The comparison of the exact SIF range computed with equation 4.3 with the approximate value given by equation B.1 is shown in table B.1.

| Test No. | $\sigma_{max}$ | Size of defect    |                   | $\sqrt{Area}$ | $\Delta K_{I,max}$ , MPa $\sqrt{m}$ |             |
|----------|----------------|-------------------|-------------------|---------------|-------------------------------------|-------------|
|          | MPa            | 2a, $\mu\text{m}$ | 2b, $\mu\text{m}$ | $\mu\text{m}$ | Exact                               | Approximate |
| 18       | 487            | 199               | 66                | 101.6         | 4.4                                 | 4.3         |
| 16       | 480            | 135               | 66                | 83.6          | 4.1                                 | 3.9         |
| 30       | 720            | 120               | 40                | 61.4          | 5.1                                 | 5.0         |
| 23       | 693            | 120               | 60                | 75.2          | 5.5                                 | 5.3         |
| 26       | 693            | 304               | 50                | 109.3         | 5.9                                 | 6.4         |
| 24       | 680            | 127               | 65                | 80.5          | 5.6                                 | 5.4         |
| 25       | 667            | 95                | 95                | 84.2          | 5.2                                 | 5.4         |

**Table B.1:** Initial stress intensity factor for internal cracks growth from defects.

An extreme value statistics for defects has also been performed using the procedure described in Murakami (2002). The cumulative probability plot so obtained is shown in figure B.1.

In order to perform this analysis, the data has to be arranged in increasing order of

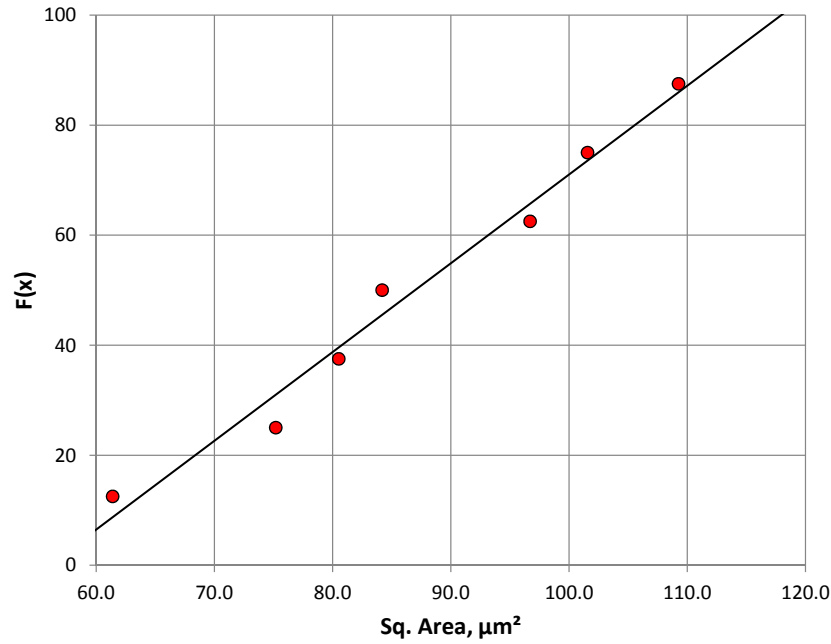


**Figure B.1:** Extreme value statistics plot.

$\sqrt{Area_{max}}$ . For calculation of  $\sqrt{Area_{max}}$  it is assumed that for a particular specimen, the size of the defect from which the crack has initiated, is the maximum size in the specimen. Then a function  $F(x)$  is defined as  $(i * 100 / (N + 1)) \%$ , where “N” is the total number of specimens ( $N = 7$  for present case) and “i” is the value of the current specimen. This function when plotted against the respective  $\sqrt{Area_{max}}$ , gives a straight line. With help of this chart, one can calculate the maximum size of the defect that can exist in certain volume or number of specimens using the relation  $T = 1 / (1 - F(x))$ . For 100 specimens ( $T = 100$ ), the maximum size of defect comes out to be  $117.4 \mu\text{m}$ .

# REFERENCES

- Achilles, R. and Bulloch, J. (1986), The Influence of Frequency, Waveform and Environment on the fatigue crack growth behaviour of SA 508 RPV steel, *in* ‘Proceedings of the Second IAEA Specialists Meeting on Subcritical Crack Growth, NUREG/CP 0067’, Vol. 1, pp. 379–422.
- Achouri, M., Gildemyn, E., Germain, G., Dal Santo, P. and Potiron, A. (2014), ‘Influence of the edge rounding process on the behaviour of blanked parts: Numerical predictions with experimental correlation’, *International Journal of Advanced Manufacturing Technology* **71**, 1019–1032.
- Armstrong, P. and Frederic, C. (1966), ‘A Mathematical Representation of the Multiaxial Baushinger Effect’, *Technical Report RD/B/N731 CEGB* .
- Austen, I., Walker, E. and May, M. (1976), ‘Factors affecting the rate of growth of cracks by corrosion-fatigue. Technical Report STF-6210/KE/18/802’.
- Banford, W., Moon, D. and Ceschini, L. (1977), Crack growth rate testing in reactor pressure vessel steels., *in* ‘Fifth Water Reactor Safety Information Meeting Gaithersburg MD’.
- Barsom, J. and Rolfe, S. (1977), *Fracture and Fatigue Control in Structures. Application of Fracture Mechanics*, Englewood Cliffs, N.J : Prentice-Hall.
- Bathias, C. and Pineau, A. (2010), *Fatigue of Materials and Structures: Fundamentals*, ISTE Ltd and John Wiley & Sons, Inc.
- Beachem, C. (1972), ‘A new model for hydrogen assisted cracking (hydrogen embrittlement).’, *Metallurgical Transactions A* **3**, 437–451.
- Bellett, D., Morel, F., Morel, A. and Lebrun, J.-L. (2010), ‘A Biaxial fatigue specimen for uniaxial loading’, *Strain: An International Journal for Experimental Mechanics* **47** (3), 227–240.
- Berge, S., Langhelle, N. and Eggen, T. (2009), ‘Environmental effects on fatigue strength

---

of armour wire for flexible risers', *International Conference on Ocean, offshore and arctic engineering, OMAE2009-80262, ASME* .

Bertolino, G., Doquet, V. and Sauzay, M. (2005), 'Modelling of the scatter in short fatigue cracks growth kinetics in relation with the polycrystalline microstructure', *International Journal of Fatigue* **27** (5), 471480.

Birnbaum, H. K., Robertson, I. M. and Sofronis, P. (2000), *Multiscale Phenomena in Plasticity: From Experiments to Phenomenology, Modelling and Materials Engineering*, Springer Netherlands, Dordrecht, chapter Hydrogen Effects on Plasticity, pp. 367–381.

Birnbaum, H. and Sofronis, P. (1994), 'Hydrogen-enhanced localized plasticity-a mechanism for hydrogen-related fracture', *Materials Science and Engineering: A* **176**, 191–202.

Bjerkén, C. and Ståhle, P. (2008), 'Simulation of corrosion fatigue crack growth under mixed-mode loading', *Engineering Fracture Mechanics* **75** (3), 440–451.

Bonnand, V., Chaboche, J., Gomez, P., Kanouté, P. and Pacou, D. (2011), 'Investigation of multiaxial fatigue in the context of turboengine disc applications', *International Journal of Fatigue* **33**, 1006–1016.

Brown, M. and Miller, K. (1973), 'A theory for fatigue failure under multi-axial stress-strain conditions', *Proceedings of the Institution of Mechanical Engineers* **187**, 745–55.

Brown, M. W. and Miller, K. J. (1979), 'Initiation and growth of cracks in biaxial fatigue', *Fatigue & Fracture of Engineering Materials and Structures* **1**(2), 231–246.

Brown, M. W. and Miller, K. J. (1985), 'Mode I fatigue crack growth under biaxial stress at room and elevated temperature', *American society for testing and materials, Philadelphia* pp. 135–152.

Bucci, R. (1970), Environment enhanced fatigue and stress corrosion cracking of a titanium alloy plus a simple model for the assessment of environmental influence on fatigue behavior, PhD thesis, Lehigh University, Bethlehem.

Bulloch, J. (1991), 'The influence of mean stress or R ratio on the fatigue crack threshold characteristics of steels-A review', *International Journal of Pressure Vessels and Piping* **47** (3), 263–292.

Butler, G., Stretton, P. and Beynon, J. (1972), 'Initiation and Growth of Pits on High-

- 
- Purity Iron and its Alloys with Chromium and Copper in Neutral Chloride Solutions’, *Corrosion Engineering, Science and Technology* **7** (4), 168–173.
- Clàudio, R., Reis, L. and Freitas, M. (2014), ‘Biaxial high-cycle fatigue life assessment of ductile aluminium cruciform specimens’, *Theoretical and Applied Fracture Mechanics* **73**, 82 – 90.
- Cooke, R., Irving, P., Booth, G. and Beevers, C. (1975), ‘The slow fatigue crack growth and threshold behaviour of a medium carbon alloy steel in air and vacuum’, *Engineering Fracture Mechanics* **7**, 69–77.
- Cotterell, B. and Rice, J. (1980), ‘Slightly curved or kinked cracks’, *International Journal of Fracture* **16** (2), 155–169.
- Crossland, B. (1956), ‘Effect of large hydrostatic pressure on the torsional fatigue strength of an alloy steel’, *Proceedings of the International Conference on Fatigue of Metals*, Institution of Mechanical Engineers, London, pp. 138–149.
- Cruz, P. D. I. and Ericsson, T. (1998), ‘Influence of sea water on the fatigue strength and notch sensitivity of a plasma nitrided B-Mn steel’, *Materials Science and Engineering* **A247**, 204–213.
- Cullen, W. (1987), Fatigue crack growth rates in pressure vessel and piping steels in LWR environment, Technical report, USNRC Report NUREG/CR-4724.
- Dang Van, K. (1973), ‘Sur la résistance a la fatigue des métaux’, *These de Doctorat es Sciences, Sci. Techniq. l’Armement*, 47 pp. 647–722.
- Dawson, D. and Pelloux, R. (1974), ‘Corrosion Fatigue Crack Growth of Titanium Alloys in Aqueous Environments’, *Metallurgical Transactions A* **5**, 723–731.
- Désamais, N., Félix-Henry, A., Taravel-Condat, C. and Drouës, A. (2007), ‘Use of High Strength Steel Wires for Flexible Pipe in Low Sour Service Conditions: Impact on Deep Water Applications’, *International Offshore and Polar Engineering Conference*, ISBN 978-1-880653-68-5 .
- Dietmann, H., Bhonghibhat, T. and Schmid, A. (1989), ‘Multiaxial fatigue behavior of steels under In-Phase and Out of phase loading including different wave forms and frequencies’, *Third International conference on Biaxial/Multiaxial Fatigue*, University STUTTGART **2**, 61.1–61.17.

- 
- Donnel, L. (1974), ‘Stress concentration factors’, *Wiley, New York* p. 223.
- Doquet, V. and De Greef, V. (2012), ‘Dwell fatigue of a titanium alloy at room temperature under uniaxial or biaxial tension’, *International Journal of Fatigue* **38**, 118–129.
- Doudard, C., Poncelet, M., Calloch, S., Boue, C., Hild, F. and Galtier, A. (2007), ‘Determination of an {HCF} criterion by thermal measurements under biaxial cyclic loading’, *International Journal of Fatigue* **29**(4), 748 – 757.
- Duckworth, W. and Ineson, E. (1963), ‘The effects of Externally introduced Alumina Particles on the fatigue life of En24 Steel, Clean steel’, *Iron and Steel Institute Special Report* **77**, 87–103.
- Duquette, D. and Uhlig, H. (1969), ‘The critical reaction rate for corrosion fatigue of 0.18% Carbon steel and the effect of pH’, *Transactions ASM* **62**, 839.
- Ebara, R. (2010), ‘Corrosion fatigue crack initiation behavior of stainless steels’, *Procedia Engineering* **2**(1), 1297–1306.
- Ebara, R., Kai, T. and Inoue, K. (1978), ‘Corrosion fatigue behavior of 13Cr stainless steel in sodium-chloride aqueous solution and steam environment’, *Corrosion-fatigue Technology, ASTM, STP 642* pp. 155–166.
- Elber, W. (1970), ‘Fatigue crack closure under cyclic tension’, *Engineering Fracture Mechanics* **2**, 37–45.
- Elber, W. (1971), ‘Damage Tolerance in Aircraft Structures’, *American Society for Testing and Materials, STP 486* pp. 230–242.
- Ellyin, F. (1989), ‘Cyclic strain energy density as a criterion for multiaxial failure fatigue’, *Biaxial and multiaxial fatigue (Edited by M.W. Brown and K.J. Miller), Mechanical Engineering publications* pp. 571–583.
- Engler, O. and Randle, V. (2010), *Introduction to Texture Analysis*, CRC Press, Taylor & Francis Group.
- Fatemi, A. and Socie, D. (1988), ‘A critical plane to multiaxial fatigue damage including out-of-phase loading’, *Fatigue & Fracture of Engineering Materials & Structures* **11** (3), 149–65.
- Findley, W. N. (1959), ‘A theory for the effect of mean stress on fatigue of metals under combined torsion and axial load or bending’, *Transactions of the ASME Series B*

---

81, 301–306.

Forsyth, P. (1972), ‘Fatigue behaviour and its dependence on microstructure’, *15eme Colloque de mtallurgie de Saclay, France* pp. 1–25.

Furuya, Y. (2008), ‘Specimen size effects on gigacycle fatigue properties of high-strength steel under ultrasonic fatigue testing’, *Scripta Materialia* **58**, 1014–1017.

Gangloff, R. and Duquette, D. (1987), *Chemistry and Physics of Fracture*, Martinus Nijhoff.

Genel, K., Demirkol, M. and Ürgen, M. (2002), ‘Effect of cathodic polarisation on corrosion fatigue behaviour of ion nitrated AISI 4140 steel’, *International Journal of Fatigue* **24**, 537–543.

Gerber, W. (1874), ‘Calculation of allowable stresses in iron structures’, *Z. Bayer Archit. Ing. Ver.* **6 (6)**, 101–110.

Glinka, G., Shen, G. and Plumtree, A. (1995), ‘A multiaxial fatigue strain energy density parameter related to the critical plane.’, *Fatigue & Fracture of Engineering Materials & Structures* **18**, 37–46.

Gonçalves, C., Araújo, J. and Mamiya, E. (2005), ‘Multiaxial fatigue: a stress based criterion for hard metals’, *International Journal of Fatigue* **27(2)**, 177–187.

Goodier, J. (1933), ‘Concentration of Stress Around Spherical and Cylindrical Inclusions and Flaws’, *Trans. ASME* **55 (7)**, 39.

Goodman, J. (1899), ‘Mechanics Applied to Engineering’, (*first ed.*) Longmans, Green and Co., London .

Gough, H., Pollard, H. and Clenshaw, W. (1951), ‘Some experiments on the resistance of metals to fatigue under combined stresses’, *Aeronautical Research Council Reports, R and M 2522*, London: HMSO, .

Guesnon, J., Gaillard, C. and Richard, F. (2002), ‘Ultra Deep Water Drilling Riser Design and Relative Technology’, *Oil & Gas Science and Technology* **57**, 39–57.

Haddad, M., Topper, T. and K.N., S. (1979), ‘Prediction of non propagating cracks’, *Engineering Fracture Mechanics* **11**, 573–584.

Haigh, B. (1917), ‘Experiments on the Fatigue of Brasses’, *Journal of the Institute of*

---

*Metals* **18**, 55–86.

- Hamam, R., Pommier, S. and Bumbieler, F. (2007), ‘Variable amplitude fatigue crack growth, experimental results and modeling’, *International Journal of Fatigue* **29**, 1634–1646.
- Havard, D. G. and Topper, T. H. (1969), ‘Low cycle biaxial fatigue of AISI 1018 steel’, *Ont. Hydro Res. Q.* **21** (2), 1–12.
- Hénaff, G., Petit, J. and Bouchet, B. (1992), ‘Environmental influence on the near-threshold fatigue crack propagation behaviour of a high strength steel’, *International Journal of Fatigue* **14** (4), 211–218.
- Hoshida, T., Tanaka, K. and Yamada, A. (1981), ‘Stress-ratio effect of fatigue crack propagation in biaxial stress field’, *Fatigue of Engineering Materials and structures* **4** (4), 355–366.
- Huneau, B., Mendez, J. and Choqueuse, D. (2000), ‘Influence de l’environnement sur le comportement en fatigue d’un acier à haute limite d’élasticité’, *19èmes journées de printemps de la SF2M : Fatigue et Environnement, Paris* .
- Irving, P. and Kurzfeld, A. (1978), ‘Measurements of intergranular failure produced during fatigue crack growth in quenched and tempered steels’, *Metal Science* **12** (11), 495–502.
- Islam, M., Bowen, P. and Knott, J. (2005), ‘Intergranular fracture on fatigue fracture surface of 2.25Cr-1Mo steel at room temperature’, *Journal of Materials Engineering and Performance* **14** (1), 28–36.
- Itoh, T., Fukumoto, K., Hagi, H., Itoh, A. and Saitoh, D. (2013), ‘Low Cycle Fatigue Damage of Mod.9Cr-1Mo Steel under Non-Proportional Multiaxial Loading’, *Procedia Engineering* **55**, 457–462.
- Jacquelin, B., Hourlier, F. and Pineau, A. (1983), ‘Crack Initiation Under Low-Cycle Multiaxial Fatigue in Type 316L Stainless Steel’, *Journal of Pressure Vessel Technology* **105** (2), 138–143.
- Johnson, W. (1874-75), ‘On the remarkable changes produced in iron and steel by the action of hydrogen and acids.’, *Proc. Royal Society of London* **23**, 168–180.
- Jones, W. and Blackie, A. (1989), ‘Effect of stress ratio on the cyclic tension corrosion

- 
- fatigue life of notched steel BS970:976M33 in sea water with cathodic protection', *International Journal of Fatigue* **11 (6)**, 417–422.
- Joshi, S. R. and Shewchuk, J. (1970), 'Fatigue-crack Propagation in a Biaxial-stress Field', *Experimental Mechanics* pp. 529–33.
- Journet, B., Lefrancois, A. and Pineau, A. (1989), 'A crack closure study to predict the threshold behaviour of small cracks', *Fatigue & Fracture of Engineering Materials & Structures* **12 (3)**, 237–246.
- Kamaya, M. and Tsuji, T. (2014), 'Evaluation of equi-biaxial fatigue of stainless steel by the pressurized disc fatigue test', *International Journal of Fatigue* **61**, 107–115.
- Kandil, F., Brown, M. and Miller, K. (1982), 'Biaxial low cycle fatigue fracture of 316 stainless steel at elevated temperatures', *The Metal Society, London* **280**, 203–10.
- Kane, A. and Doquet, V. (2006), 'Surface crack and cracks networks in biaxial fatigue', *Engineering Fracture Mechanics* **73(2)**, 233–251.
- Kaufman, R. P. and Topper, T. (2003), 'The influence of static mean stresses applied normal to the maximum shear planes in multiaxial fatigue', *Biaxial and Multiaxial Fatigue and Fracture, (Edited by A. Carpinteri, M. de Freitas and A. Spagnoli), Elsevier andESIS* pp. 123–143.
- Kenmengen, B., Yidal-Salle, E., Robert, J. and Bahuaud, J. (1996), 'On a new multiaxial fatigue criterion based on a selective integration approach', *Proc of the Sixth International Fatigue Congress, Fatigue* **2**, 1013–1018.
- Kim, K., Park, J. and Lee, J. (1999), 'Multiaxial fatigue under variable amplitude loads', *Journal of Engineering Materials and Technology: Trans ASME* **21**, 286–293.
- Kitagawa, H., Yuki, Y., Togo, K. and Sumita, Y. (1978), 'Fracture mechanics study of fatigue crack growth in high-strength steel sheet under in-plane biaxial loading', *Preprint of JSME Fall Meeting* **780 (13)**, 155–162.
- Knop, M., Heath, J., Sterjovski, Z. and Lynch, S. P. (2010), 'Effects of cycle frequency on corrosion-fatigue crack growth in cathodically protected high-strength steels', *Procedia Engineering* **2(1)**, 1243–1252.
- Kolotyrkin, Y. (1964), *Corrosion* **19:261t**.
- Kondo, Y. (1989), 'Prediction of fatigue crack initiation life based on pit growth', *Cor-*

---

rosion **45** (1), 7–11.

- Koutiri, I., Bellett, D., Morel, F., Augustins, L. and Adrien, J. (2013), ‘High cycle fatigue damage mechanisms in cast aluminium subject to complex loads’, *International Journal of Fatigue* **47**, 44–57.
- Krishnan, K. (1997), ‘Mechanism of corrosion fatigue in super duplex stainless steel in 3.5 percent NaCl solution’, *International Journal of Fracture* **88**, 205–213.
- Krom, A., Bakker, A. and Koers, R. (1997), ‘Modeling hydrogen-induced cracking in steel using a coupled diffusion stress finite element analysis’, *International Journal of Pressure Vessels and Piping* **72**, 139–147.
- Lagoda, T., Macha, E. and Beçdkowski, W. (1999), ‘A critical plane approach based on energy concepts: application to biaxial random tension-compression high-cycle fatigue regime’, *International Journal of Fatigue* **21**, 431–443.
- Laird, C. (1967), ‘The influence of Metallurgical Structure on the Mechanisms of Fatigue Crack Propagation’, *Fatigue Crack Propagation, ASTM STP 415* p. 131.
- Lankford, J. (1985), ‘Influence of microstructure on the growth of small fatigue cracks’, *Fatigue & Fracture of Engineering Materials and Structures* **8** (2), 161–175.
- Lee, E. and Taylor, R. (2011), ‘Fatigue behavior of aluminum alloys under biaxial loading’, *Engineering Fracture Mechanics* **78**(8), 1555 – 1564.
- Leevers, P., Radon, J. and Culver, L. (1976), ‘Crack growth in plastic panels under biaxial stress’, *Polyrnccx.* **17**, 627–632.
- Levenberg, K. (1944), ‘A method for the solution of certain non-linear problems in least squares’, *Quarterly of Applied Mathematics* **2**, 164–168.
- Li, W., Sakai, T., Wakita, M. and Mimura, S. (2012), ‘Effect of surface finishing and loading condition on competing failure mode of clean spring steel in very high cycle fatigue regime’, *Materials Science and Engineering* **552**, 301–309.
- Li, W., Yuan, H., Sun, Z. and Zhang, Z. (2014), ‘Surface vs. interior failure behaviors in a structural steel under gigacycle fatigue: Failure analysis and life prediction’, *International Journal of Fatigue* **64**, 42–53.
- Liaw, P., Saxena, A., Swaminathan, V. and Shih, T. (1983), ‘Effect of load ratio and temperature on the near-threshold fatigue crack propagation behaviour in a CrMoV

- 
- steel', *Metallurgical and Materials Transactions A* **14**, 1631–1640.
- Lin, G. and Fine, M. (1982), 'Effect of grain size and cold work on the near threshold fatigue crack propagation rate and crack closure in iron', *Scripta Metallurgica* **16** (11), 1249–1254.
- Liu, J. and Zenner, H. (1993), 'Berechnung der Dauerschwingfestigkeit bei mehrachsiger Beanspruchung', *Mat.-wiss. u. Werkstofftech* **24**, 240–249.
- Liu, Y. and Mahadevan, S. (2005), 'Multiaxial high-cycle fatigue criterion and life prediction for metals', *International Journal of Fatigue* **27**(7), 790–800.
- Lufrano, J., Sofronis, P. and Birnbaum, H. (1996), 'Modeling of hydrogen transport and elastically accommodated hydride formation near a crack tip', *Journal of the Mechanics and Physics of Solids* **44** (2), 179–205.
- Lynch, S. (2011), 2 - Hydrogen embrittlement (HE) phenomena and mechanisms, in V. Raja and T. Shoji, eds, 'Stress Corrosion Cracking', Woodhead Publishing Series in Metals and Surface Engineering, Woodhead Publishing, pp. 90 – 130.
- Lynch, S. (2012), 'Mechanistic and fractographic aspects of stress corrosion cracking', *Corrosion Reviews* **30**, 63–104.
- Magnin, T. (1996), Advances in corrosion-deformation interactions, in 'Zurich-Uetikon, Switzerland, Trans Tech Publications'.
- Makinde, A., Thibodeau, L. and Neale, K. (1992), 'Development of an apparatus for biaxial testing using cruciform specimens', *Experimental Mechanics* **32** (2), 138–144.
- Marciniak, Z., Rozumek, D. and Macha, E. (2008), 'Fatigue lives of 18G2A and 10HNAP steels under variable amplitude and random non-proportional bending with torsion loading', *International Journal of Fatigue* **30**, 800–813.
- Marin, J. (1956), 'Interpretation of Fatigue Strength for combined stresses', *Proceedings of the International Conference on Fatigue of Metals*, Institution of Mechanical Engineers, London pp. 184–194.
- Marquis, G. and Karjalainen-Roikonen, P. (2001), 'Long-life multiaxial fatigue of SG cast iron', *Proc. 6th International Conference on Biaxial/Multiaxial loading and Fracture* pp. 151–159.
- Maruyama, N., Mori, D., Hiromoto, S., Kanazawa, K. and Nakamura, M. (2011), 'Fa-

- 
- tigue strength of 316L-type stainless steel in simulated body fluids', *Corrosion Science* **53**(6), 2222–2227.
- Matake, T. (1977), 'An explanation of fatigue limit under combined stress', *Bull JSME* **20**, 257–263.
- Mc Adam, D. (1926), 'Stress-Strain-Cycle Relationship and Corrosion-Fatigue of Metals', *Proceedings - American Society for Testing Materials* **26**, 224–280.
- McCafferty, E. (2010), *Introduction to Corrosion Science*, Springer.
- McClung, R. (1989), 'Closure and Growth of mode I cracks in biaxial fatigue', *Fatigue of Engineering Materials and structures* **12** (5), 447–460.
- McDiarmid, D. (1994), 'A shear stress based critical-plane criterion of multiaxial fatigue failure for design and life prediction', *Fatigue & Fracture of Engineering Materials & Structures* **17**, 1475–1484.
- McEvily, A. and Gonzalez Velazquez, J. (1992), 'Fatigue Crack Tip Deformation Processes as Influenced by the Environment', *Metallurgical Transactions A* **23**, 2211–2221.
- Milella, P. (2013), *Fatigue and Corrosion in Metals*, Springer.
- Misak, H., Perel, V., Sabelkin, V. and Mall, S. (2013), 'Corrosion fatigue crack growth behavior of 7075-T6 under biaxial tension-tension cyclic loading condition', *Engineering Fracture Mechanics* **106**, 38–48.
- Misak, H., Perel, V., Sabelkin, V. and Mall, S. (2014), 'Biaxial tension fatigue crack growth behavior of 2024-T3 under ambient air and salt water environments', *Engineering Fracture Mechanics* **118**, 83–97.
- Moré, J. (1977), 'The levenberg-marquardt algorithm: Implementation and theory', In *G.A. Watson, editor, Numerical Analysis Proceedings, Lecture Notes in Mathematics, Springer Verlag, Berlin, Germany* pp. 105–116.
- Murakami, Y. (2002), *Metal Fatigue: Effects of small defects and nonmetallic inclusions*, Elsevier Science.
- Murakami, Y., Hasebe, M., Itoh, Y., Kishimoto, K., Miyata, H., Miyazaki, N., Terada, H., Tohgo, K., Yuuki, R. and Kobayashi, A. (1994), 'Stress Intensity Factor Handbook', *Experimental Techniques* **18** (1), 46.

- 
- Murakami, Y., Nomoto, T. and Ueda, T. (2000a), ‘On the mechanism of fatigue failure in the super long life regime ( $N > 10^7$ ) cycles. Part 1: influence of hydrogen trapped by inclusions’, *Fatigue & Fracture of Engineering Materials & Structures* **23**, 893–902.
- Murakami, Y., Nomoto, T. and Ueda, T. (2000b), ‘On the mechanism of fatigue failure in the super long life regime ( $N > 10^7$ ) cycles. Part II: a fractographic investigation’, *Fatigue & Fracture of Engineering Materials & Structures* **23** (11), 903–910.
- Naito, T., Ueda, H. and Kikuchi, M. (1984), ‘Fatigue behavior of carburized steel with internal oxides and nonmartensitic microstructure near the surface’, *Metallurgical Transactions A* **15**(7), 1431–1436.
- Nakamura, T., Oguma, H. and Shinohara, Y. (2010), ‘The effect of vacuum-like environment inside sub-surface fatigue crack on the formation of ODA fracture surface in high strength steel’, *Procedia Engineering* **2**, 2121–2129.
- Newman, J. and Raju, I. (1984), Stress-intensity factor equations for cracks in three-dimensional finite bodies subjected to tension and bending loads, Technical report, NASA Technical Memorandum 85793.  
**URL:** <http://ntrs.nasa.gov/archive/nasa/casi.ntrs.nasa.gov/19840015857.pdf>
- Noyan, I. and Cohen, J. B. (1987), *Residual stress - measurement by diffraction and interpretation*.
- Ochi, Y., Matsamura, T., Masaki, K. and Yoshida, S. (2002), ‘High-cycle rotating bending fatigue property in very long-life regime of high strength steels.’, *Fatigue & Fracture of Engineering Materials & Structures* **25**, 823–830.
- Ogawa, T., Stanzl-Tschegg, S. and Schönbauer, B. (2014), ‘A fracture mechanics approach to interior fatigue crack growth in the very high cycle regime’, *Engineering Fracture Mechanics* **115**, 241–254.
- Olden, V., Alvaro, A. and Akselsen, O. (2012), ‘Hydrogen diffusion and hydrogen influenced critical stress intensity in an API X70 pipeline steel welded joint - Experiments and FE simulations’, *International Journal of Hydrogen Energy* **37**, 11474–11486.
- Oriani, R. and Josephic, P. (1974), ‘Equilibrium aspects of hydrogen-induced cracking of steels’, *Acta Metallurgica* **22**, 1065–1074.
- Pan, W.-F., Hung, C.-Y. and Chen, L.-L. (1999), ‘Fatigue life estimation under multiaxial loadings’, *International Journal of Fatigue* **21**, 3–10.

- 
- Papadopoulos, I. (1995), ‘A high-cycle fatigue criterion applied in biaxial and triaxial out-of-phase stress conditions’, *Fatigue & Fracture of Engineering Materials and Structures* pp. 18–79.
- Papadopoulos, I., Davoli, P., Gorla, C., Filippini, M. and Bernasconi, A. (1997), ‘A comparative study of multiaxial high-cycle fatigue criteria for metals’, *International Journal of Fatigue* **19**, 219–235.
- Papuga, J. and Ruzika, M. (2008), ‘Two new multiaxial criteria for high cycle fatigue computation’, *International Journal of Fatigue* **30**(1), 58–66.
- Pearson, S. (1975), ‘Initiation of fatigue cracks in commercial aluminum alloy and the subsequent propagation of very short cracks’, *Engineering Fracture Mechanics* **7**, 235–247.
- Perel, V. Y., Misak, H. E., Mall, S. and Jain, V. K. (2015), ‘Biaxial Fatigue Crack Growth Behavior in Aluminum Alloy 5083-H116 Under Ambient Laboratory and Saltwater Environments’, *Journal of Materials Engineering and Performance* **24**(4), 1565–1572.
- Pérez-Mora, R., Palin-Luc, T., Bathias, C. and Paris, P. C. (2015), ‘Very high cycle fatigue of a high strength steel under sea water corrosion: A strong corrosion and mechanical damage coupling’, *International Journal of Fatigue* **74**, 156 – 165.
- Perkins, K. and Bache, M. (2005), ‘Corrosion fatigue of a 12%Cr low pressure turbine blade steel in simulated service environments’, *International Journal of Fatigue* **27**(10-12), 1499–1508.
- Petit, J. and Sarrazin-Baudoux, C. (2006), ‘An overview on the influence of the atmosphere environment on ultra-high-cycle fatigue and ultra-slow fatigue crack propagation’, *International Journal of Fatigue* **28**, 1471–1478.
- Pfeil, L. (1926), ‘The effect of occluded hydrogen on the tensile strength of iron.’, *Proceedings of the Royal Society of London A* **112**, 128–195.
- Pfennig, A., Wolf, M., Wiegand, R., Kranzmann, A. and Bork, C.-P. (2013), ‘Corrosion Fatigue Behavior and S-N-curve of X46Cr13 Exposed to CCS-environment Obtained from Laboratory in-situ-experiments’, *Energy Procedia* **37**, 5764–5772.
- Ravichandran, K. and Larsen, J. (1997), ‘Effects of crack aspect ratio on the behavior of small surface cracks in fatigue: Part II. Experiments on a titanium (Ti-8al) alloy’, *Metallurgical and Materials Transactions A* **28a** (1), 157–169.

- 
- Reimer, L. (1998), *Scanning Electron Microscopy: Physics of Image Formation and Microanalysis*, Springer, ISBN 978-3-642-08372-3.
- Ritchie, R. (1977), ‘Influence of impurity segregation on temper embrittlement and on slow fatigue crack growth and threshold in 300-M high strength steel, Met. Trans. 8A, 1977, 1131-39’, *Metallurgical Transactions A* **8**, 1131–1139.
- Rosenfeld, I. (1974), ‘Localized corrosion’, *Proceedings of fifth international congress on metallic corrosion, NACE* p. 53.
- Sakai, T., Harada, H. and Oguma, N. (2006), ‘Crack Initiation Mechanism of Bearing Steel in High Cycle Fatigue’, *Fracture of Nano and Engineering Materials and Structures* pp. 1129–1130.
- Sakai, T., Sato, Y. and Oguma, N. (2001), ‘Characteristic SN property of high carbon Chromium bearing steel under axial loading in long life fatigue’, *Proceedings of international conference on fatigue in the Very High Cycle Regime (later named VHCF-2)* pp. 51–57.
- Sawert, W. (1943), ‘Verhalten der Baustähle bei Wechselnder Mehrachsiger Beanspruchung, 87, Nr 39/40, 2 Okt 1943’, *Zeitschrift des Vereins Deutscher Ingenieure* **87**, 609–615.
- Schijve, J. (1978), ‘Internal fatigue cracks are growing in vacuum’, *Engineering Fracture Mechanics* **8** (4), 575–581.
- Schneider, K. (1983), Corrosion fatigue behaviour of turbine blade materials, in ‘Pergamon Press’.
- Schönbauer, B. M., Perlega, A., Karr, U. P., Gandy, D. and Stanzl-Tschegg, S. E. (2015), ‘Pit-to-crack transition under cyclic loading in 12%Cr steam turbine blade steel’, *International Journal of Fatigue* **76**, 19–32.
- Schönbauer, B. M. and Stanzl-Tschegg, S. E. (2013), ‘Influence of environment on the fatigue crack growth behaviour of 12% Cr steel’, *Ultrasonics* **53**(8), 1399–1405.
- Sedriks, A. (1979), *Corrosion of Stainless Steels*, Wiley, New York, chapter 7, p. 282.
- Shamsaei, N., Fatemi, A. and Socie, D. (2011), ‘Multiaxial fatigue evaluation using discriminating strain paths’, *International Journal of Fatigue* **33**, 597–609.
- Shiozawa, K., Morii, Y., Nishino, S. and Lu, L. (2006), ‘Subsurface crack initiation and

- 
- propagation mechanism in high-strength steel in a very high cycle fatigue regime', *International Journal of Fatigue* **28** (11), 1521–1532.
- Shiozawa, K., Shimatani, Y., Nakada, T., Yoshimoto, T. and Koshi, M. (2010), 'Very high cycle fatigue properties of high speed steel developed by basis on internal failure mechanism', *Nihon Kikai Gakkai Ronbunshu, A Hen/Transactions of the Japan Society of Mechanical Engineers, Part A* **76**, 1689–1697.
- Sines, G. (1959), 'Behavior of metals under complex static and alternating stresses', In 'Metal Fatigue' (Eds G. Sines and J. L. Waisman), McGraw-Hill, New York pp. 145–169.
- Sivaprasad, S., Tarafder, S., Ranganath, V. R., Tarafder, M. and Ray, K. K. (2006), 'Corrosion fatigue crack growth behaviour of naval steels', *Corrosion Science* **48**(8), 1996–2013.
- Smith, K., Watson, P. and Topper, T. (1970), 'A stress-strain function for the fatigue of metals', *Journal of Materials Science* **5** (4), 767–776.
- Socie, D. (1987), 'Multiaxial fatigue damage models', *Journal of Engineering Materials and Technology* **109**, 293–298.
- Socie, D., Waill, L. and Dittmer, D. (1985), 'Biaxial fatigue of inconel 718 including mean stress effects. In: Miller KJ, Brown MW, editors', *Multiaxial fatigue, ASTM STP 853. Philadelphia: ASTM* pp. 7–36.
- Stewart, A. (1980), 'The influence of environment and stress ratio on fatigue crack growth at near threshold stress intensities in low-alloy steels', *Engineering Fracture Mechanics* **13**, 463–478.
- Strauss, B., Schottky, H. and Innueber, J. (1930), 'Die Carbidausscheidung beim Gluehen von Nichtrostenden, Unmagnetischen Cr-Ni Stahl', *Zeitschrift für anorganische und allgemeine Chemie* **188**, 309–324.
- Sunder, R. and Ilchenko, B. V. (2011), 'Fatigue crack growth under flight spectrum loading with superposed biaxial loading due to fuselage cabin pressure', *International Journal of Fatigue* **33**(8), 1101–1110.
- Suresh, S. and Ritchie, R. (1982), 'A geometric model for fatigue crack closure induced by fracture surface roughness', *Metallurgical Transactions A* **13** (9), 1627–1631.

- 
- Suresh, S., Zamiski, G. and Ritchie, R. (1981), ‘Oxide-induced crack closure: an explanation for near-threshold corrosion fatigue crack growth behavior’, *Metallurgical Transactions A* **12** (8), 1435–1443.
- Susmel, L. (2008), ‘Multiaxial fatigue limits and material sensitivity to non-zero mean stresses normal to the critical planes’, *Fatigue & Fracture of Engineering Materials & Structures* **31**, 295–309.
- Tanaka, K., Hoshide, T., Yamada, A. and Taira, S. (1979), ‘Fatigue crack propagation in biaxial stress fields’, *Fatigue & Fracture of Engineering Materials and Structures* **2**(2), 181–194.
- Uhlig, H. and Cook, E. (1969), ‘Mechanism of Inhibiting Stress Corrosion Cracking of 18-8 Stainless Steel in  $MgCl_2$  by Acetates and Nitrates’, *Journal of Electrochemical Science* pp. 173–177.
- Uhlig, H. and Lee, H. (1972), ‘Corrosion Fatigue of Type 4140 High Strength Steel’, *Metallurgical Transactions* **3**, 2949–2957.
- Van Der Sluys, W. and Emanuelson, R. (1986), Overview of data trends in cyclic crack growth Results in LWR environments, *in* ‘Proceedings of the Second IAEA Specialists Meeting on Subcritical Crack Growth’, Vol. 1, pp. 199–218.
- Vansovich, K., Yadrov, V. and Beseliya, D. (2015), ‘The Effect of Stress State Characteristics on the Surface Fatigue Cracks Growth Rate Taking into Account Plastic Deformations’, *Procedia Engineering* **113**, 244 – 253.
- Varvani-Farahani, A. and Topper, T. (1997), ‘Crack growth and closure mechanisms of shear cracks under constant amplitude biaxial straining and periodic compressive overstraining in 1045 steel’, *International Journal of Fatigue* **19**, 589–596.
- Vasudevan, A., Sadananda, K. and Holtz, R. (2005), ‘Analysis of vacuum fatigue crack growth results and its implications’, *International Journal of Fatigue* **27**, 1519–29.
- Verreman, Y. and Espinosa, G. (1997), ‘Mechanically short crack growth from notches in a mild steel’, *Fatigue & Fracture of Engineering Materials and Structures* **20** (2), 129–142.
- Vetter, K. and Strehblow, H. (1970), *Berichte der Bunsengesellschaft fr physikalische Chemie* **70**, 1024–1035.

- 
- Voce, E. (1948), 'The relationship between stress and strain for homogeneous deformation', *Journal of the Institute of Metals* **74**, 537–562.
- Vosikovski, O. (1975), 'Fatigue-Crack Growth in an 1-85 Line-Pipe Steel at Low Cyclic Frequencies in Aqueous Environments', *Journal of Engineering Materials and Technology* **75-Mat-T**.
- Vu, Q. H., Halm, D. and Nadot, Y. (2010), 'Multiaxial fatigue criterion for complex loading based on stress invariants', *International Journal of Fatigue* **32**(7), 1004–1014.
- Wang, Q., Kawagoishi, N. and Chen, Q. (2003), 'Effect of pitting corrosion on very high cycle fatigue behavior', *Scripta Materialia* **49**, 711–716.
- Yuuki, R., Akita, K. and Kishi, N. (1989), 'The effect of biaxial stress state and changes of state on fatigue crack growth behaviour', *Fatigue & Fracture of Engineering Materials & Structures* **12** (2), 93–103.
- Zenner, H. and Richter, I. (1977), 'Eine Festigkeitshypothese für die Dauerfestigkeit bei beliebigen Beanspruchungskombinationen', *Konstruktion*, *29* **1**, 11–18.
- Zenner, H., Simbürger, A. and Liu, J. (2000), 'On the fatigue limit of ductile metals under complex multiaxial loading', *International Journal of Fatigue* **22** (2), 137–145.
- Zhang, X.-Y., Li, S.-X., Liang, R. and Akid, R. (2013), Effect of corrosion pits on fatigue life and crack Initiation, *in* '13th international conference on Fracture, June 16-21'.
- Zhang, Y. and Edwards, L. (1992), 'The Effect of Grain Boundaries on the Development of Plastic Deformation Ahead of Small Fatigue Cracks', *Scripta Metallurgica et Materialia* **26**, 1901–1906.
- Zhu, M. and Xuan, F. (2009), 'Effect of microstructure on appearance of near-threshold fatigue fracture in Cr-Mo-V steel', *International Journal of Fracture* **2009**, 111–120.
- Zouani, A., Bui-Quoc, T. and Bernard, M. (1999), 'Fatigue Life Parameter for Type 304 Stainless Steel Under Biaxial-Tensile Loading at Elevated Temperature', *Journal of Engineering Materials and Technology* **121** (3), 305–312.

**Titre :** Fatigue et fatigue-corrosion d'un acier au Cr-Mo en tension-biaxiale

**Mots clés :** acier, fatigue, fatigue-corrosion, tension-biaxiale, contrainte moyenne

**Résumé:** Les connecteurs clips utilisés pour assembler les tubes de riser pour le forage pétrolier subissent un chargement cyclique de tension biaxiale en phase avec de fortes contraintes moyenne dans la zone critique de la structure. L'objectif est donc de caractériser séparément ces deux effets.

Pour étudier les effets contrainte moyenne, des essais de fatigue uniaxiale ont été menés sur un acier Mo-Cr avec différents rapports R. Les durées de vie diminuent avec l'augmentation de R, et la limite d'endurance suit la parabole de Gerber.

Pour étudier l'effet d'un taux de biaxialité, des essais cycliques de tension et pression interne combinées ont été effectués. Un taux de biaxialité modéré a un effet bénéfique, alors que la tension équilibaxiale a un effet légèrement nuisible. Des facettes intergranulaires révélatrices de fragilisation par l'hydrogène ont été observées sur les surfaces de rupture.

Plusieurs critères de fatigue échouent à décrire toutes les données de cette étude et un nouveau critère de fatigue a été proposé, qui décrit bien les effets combinés d'une contrainte moyenne et d'un taux de biaxialité positif.

Pour étudier l'influence d'un milieu corrosif (3,5% NaCl), des essais de tension et pression interne combinées ont été conduits sous corrosion libre et protection cathodique.

En corrosion libre, l'eau salée réduit fortement les durées de vie et supprime la limite d'endurance. Les durées de vie en fatigue uniaxiale et biaxiale sont presque les mêmes, malgré des mécanismes de fissuration différents.

La protection cathodique annule l'effet néfaste de l'eau salée pour tous les taux de biaxialité, en dépit d'un net accroissement de la fragilisation par l'hydrogène des joints de grains.

**Title :** Fatigue and corrosion-fatigue in Cr-Mo steel in biaxial tension

**Keywords :** steel, fatigue, corrosion-fatigue, biaxial tension, mean stress

**Abstract:** The clip connectors used to join the riser tubes for offshore oil drilling undergo cyclic loading with in-phase biaxial tension in its critical areas along with high mean stresses. This study investigates separately the mean stress and biaxiality effects.

Uniaxial fatigue tests were run on Cr-Mo steel with various R ratios to investigate the mean stress effect. The fatigue lives were found to decrease with increasing R, and the endurance limit to follow Gerber's parabola.

To study the effect of biaxial tension, combined cyclic tension and internal pressure tests were run on tubular specimens, at a fixed R ratio. Moderate stress biaxialities had a beneficial effect on fatigue lives, while equibiaxial tension had a slightly detrimental effect. Intergranular facets associated with temper and hydrogen embrittlement were observed on the fracture surfaces.

Several popular fatigue criteria failed to describe all fatigue data and a new fatigue criterion has been proposed that captures both mean stress effect and biaxiality effect.

To investigate the influence of corrosive medium (3.5% NaCl) combined cyclic tension and internal pressure tests were run under free corrosion and cathodic protection.

In free corrosion, salt water strongly reduced the fatigue lives and suppressed the endurance limit. Fatigue lives in uniaxial and biaxial tension were nearly the same, although the crack growth mechanism was different.

Cathodic protection cancelled the detrimental effect of salt water for all biaxialities, in spite of a clear enhancement of H-induced embrittlement of the grain boundaries.

